Gravitational Effects on Defect Formation in Melt Grown Photorefractive Materials: Bismuth Silicate

by

Michaela E. K. Wiegel

B.S. in Mechanical Engineering
Case Western Reserve University (1995)

M.S. in Mechanical Engineering
Case Western Reserve University (1997)

Submitted to the Department of Mechanical Engineering in
Partial Fulfillment of the Requirements for the Degree of

Doctor of Philosophy
in Mechanical Engineering
at the
MASSACHUSETTS INSTITUTE OF TECHNOLOGY
February 2003

Signature of Author: _____
Department of Mechanical Engineering
September 12, 2002

Certified by: _____
August F. Witt
Professor of Material Science and Engineering
Thesis Supervisor

Accepted by: _____
Ain A. Sonin
Professor of Mechanical Engineering
Chairman, Committee on Graduate Studies

Gravitational Effects on Defect Formation in Melt Grown Photorefractive Materials: Bismuth Silicate

by

Michaela E. K. Wiegel

Submitted to the Department of Mechanical Engineering on
December 19, 2002 in Partial Fulfillment of the Requirements for
the Degree of Doctor of Philosophy in Mechanical Engineering

ABSTRACT

Photorefractivity is the modulation of index of refraction due to nonuniform illumination, and numerous applications have been demonstrated utilizing this nonlinear optical property. However, commercial production is seriously impeded by the inability to produce bulk material with the homogeneity of opto-electronic properties that is required for device applications. Bismuth Silicate, $Bi_{12}SiO_{20}$, (BSO) is a photorefractive material with outstanding properties including a fast response time and high sensitivity is studied. Its photorefractivity is due to a native defect whose exact nature and origin have not been unambiguously determined.

Motivation for current research arose from unexplained optical variations observed in BSO that implicate convective interference as playing a role in native defect formation. Microgravity growth experiments are proposed in order to establish a controlled, convection-free environment to study the origin and nature of the critical native defect. This work aims at resolving critical aspects of performing quantitative microgravity growth experiments that include the interaction of BSO melts with its confinement material; development and characterization of a vertical Bridgman-Stockbarger growth system with a quantifiable, reproducible, and controllable thermal environment; and Bridgman-Stockbarger growth experiments. A comparative analysis of crystals was done in order to establish the relationship between variations in opto-electronic properties as a function of changes in growth conditions.

Wetting experiments revealed the sessile drop method to be inappropriate for the BSO-platinum system due to grain boundary pinning. No fundamental difference between the wetting behavior in a terrestrial and a low gravity environment was observed.

Results from the comparative analysis indicate a lower defect concentration in Bridgman-Stockbarger material as compared to Czochralski material. The ambient atmosphere during processing and high temperature annealing was found affect material response, including removal of the photochromic response and decrease of carrier lifetime. The lack of the critical defect in hydrothermal BSO, and its existence in all melt grown material indicates that the melt plays a fundamental role in its formation. Clustering in the melt is implicated in the literature from nonlinear melt properties. It is therefore hypothesized that these clusters in the melt act as precursors for native defect formation and subject to gravitationally induced convection.

The support of the National Aeronautics and Space Administration is gratefully acknowledged.

Thesis supervisor:August F. Witt
Title:Ford Professor of Engineering, MacVicar Faculty Fellow

ACKNOWLEDGEMENTS

I dedicate this thesis to Prof. August F. Witt - his contributions in the field of crystal growth for over 40 years were as great as the pivotal role he played in so many students' lives. His passing is a profound loss to everyone who knew him. I cannot express the difference he made in my life - I respected, feared, and loved him. His uncompromising expectation of quality in my work, his encouragement for critical and creative thinking, and his advice in times of difficulty have allowed me to grow as both a researcher and as an individual.

I am deeply indebted to Piotr Becla for all of his help. Throughout the years, he was always willing to lend a hand, explain a concept, or think of ways to test a theory. His patience in teaching me about the solid state physics aspects of this work was unbelievable, and I am grateful for all of the time he spent with me. I thank my fellow students, especially Yu Zheng and Nick Allsop, for their help in the lab, their ideas, and their friendship.

I would like to thank Prof. Jon Dantzig, Prof. Al Sacco, Dr. Shari Motakef and Dr. Matthew Overholt for sharing their resources and knowledge with me. I am honored to have had the interaction not only on a professional level but also on a personal level.

I owe the MIT Central Machine Shop a huge thanks (and a couple of pitchers of libations) for their quality work, their advice and for helping me out of a few jams. I would also like express my appreciation to John DiFrancesco, Fred Wilson. and Guenter Arndt for their help. A special thanks to Gene Nelson at UAH for his incredible glass blowing and for making Huntsville more enjoyable.

Life is not just about work, and I want to thank all of my friends for helping me keep sight of that fact. They were a tremendous source of support to me as well as providing some welcome diversions from this research. A heartfelt thanks to Chris for reminding me of who I am, for listening, and for sharing. The GISC and its members hold a special place in my heart. They have my eternal gratitude for their incredibly generous help in editing this thesis and in preparing for the final presentation. I also would like to thank the regulars at the Muddy Charles Pub for putting up with me on my bad days, for having fun with me on my good days, and for always tipping generously.

Corny suffered through the trials and tribulations of this thesis with me more than anyone else. I cannot express how much his steadfast love and support helped me survive MIT. I will never forget all that he did for me and all of the love he gave me.

My family - their unconditional love and belief in my ability to succeed has been with me no matter what the undertaking. By example, they have shown me the rewards of working hard and not giving up on goals. I cherish my family - they are my biggest fans and I am theirs.

Lastly, I want to thank NASA for continual funding of this work, for my Graduate Student Research Fellowship, and for support of KC-135 flight experiments.

TABLE OF CONTENTS

LIST OF FIGURES

LIST OF TABLES

CHAPTER 1: INTRODUCTION

As with so many great scientific advances, photorefractivity was first observed unexpectedly as an anomaly in the light transmission of optical crystals. In 1966, Ashkin[1] stated "This effect although interesting in its own right, is highly detrimental to the optics of non-linear devices based on these crystals." in reference to the time dependent light scattering observed from laser illuminated $LiNbO_3$ and $LiTaO_3$. This effect, now known as photorefractivity, is the modulation of the index of refraction due to non-uniform illumination. In order for a material to be photorefractive, it must be both photo-conductive as well as electro-optic. Incident illumination causes photo-ionization (1) of carriers into the conduction band. The carriers then diffuse and/or drift (2) and finally are trapped (3). This in turn creates an internal electric field (4) which results in a change in the index of refraction due to the electro-optic effect[2]. This process is shown in Figure 1-1.

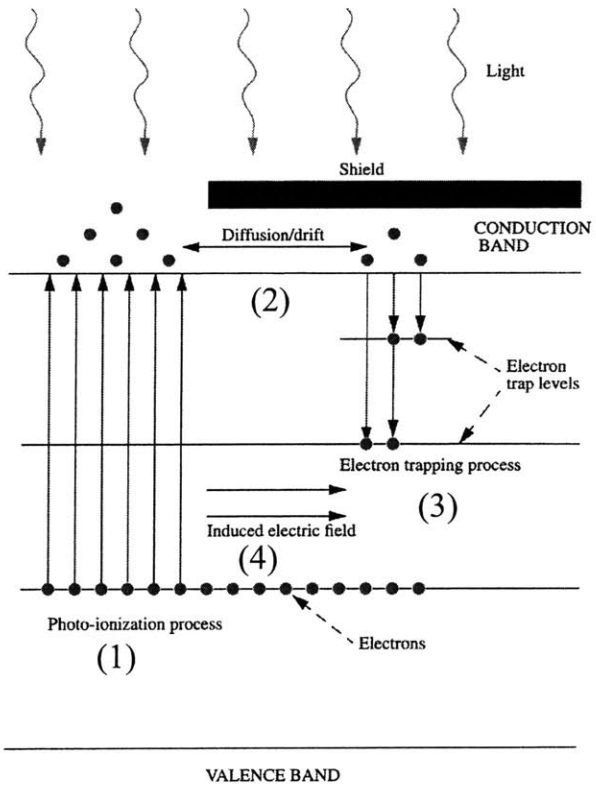

Figure 1-1: Photo-refractive effect: (1) photo-ionization (2) drift/diffusion (3) trapping of electrons (4) electric field induced by space charge redistribution.

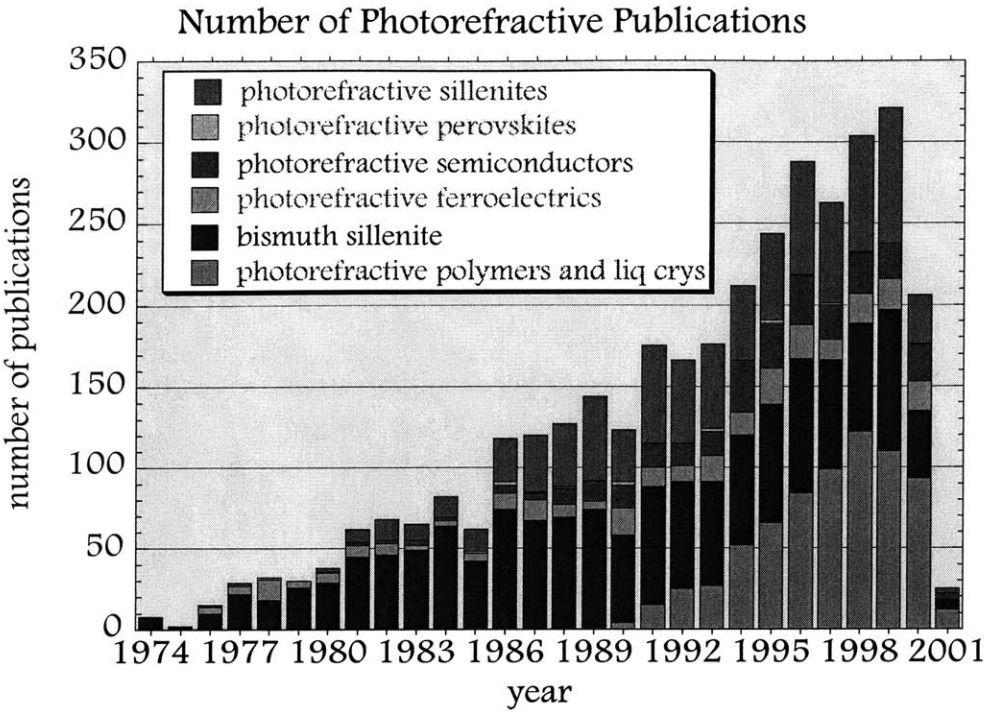

Figure 1-2: Number of research publications concerning photorefractive materials (data from mid-2001)[3].

In the last 30 years, research into photorefractivity of nonlinear optical materials has produced a large body of literature (see Figure 1-2). Many potential applications have been demonstrated for photorefractive single crystals, including volume holographic storage, dynamic holography, phase conjugation, wave modulation, and image amplification[2,4,5,6,7]. In stark contrast, only a single device, narrow band interference filters, is actually produced commercially. This discrepancy between 'possibility' and 'reality' arises due to the inability to produce bulk crystals with the crystalline perfection, on both the micro and macroscale, that is necessary for these devices[2,7].

Table 1-1 summarizes some of the known photorefractive materials, as well as their relevant photorefractive properties. With so many photorefractive materials to choose from, $Bi_{12}SiO_{20}$ (BSO) stands out because of its outstanding sensitivity and excellent response time. Additionally, its relatively low melting point allows the use of conventional heat-pipes in growth apparatus.

The photorefractive effect is not an intrinsic property in BSO; it is a result of a native defect that is introduced during growth. The current hypothesis is that it is a Bi_{Si} anti-site

defect. The fact that the exact nature and origin of this critical native defect has yet to be unambiguously identified, has greatly impeded progress in controlling growth induced imperfections. Consequently, despite 40 years of extensive research, there is a need for an improved understanding of the mechanism of critical defect formation.

Material	Electro-optic Coeff. x 10^{-12} (cm/V)	Crystal Structure	Sensitivity (cm^2/J)	Response time (msec)	T_c (°C)
$Bi_{12}SiO_{20}$	$r_{41} = 5$	cubic	4×10^{-5}	~ 1-10	-
$Bi_{12}GeO_{20}$	$r_{41} = 5$	cubic	5×10^{-5}	-	-
$LiNbO_3Fe$	$r_{33} = 31.8$	trigon.	7×10^{-5}	~ 2000	1150
$LiNbO_3Rh$	$r_{33} = 31.8$	trigon.	7×10^{-3}	~ 2000	1150
$BaTiO_3$-doped	$r_{51} = 802$	cubic		-	120
$KNbO_3Mn$	$r_{42} = 380$	ortho			
$KNbO_3Fe$	$r_{42} = 380$	ortho		< 100	480
$Ba_2NaNb_5O_{15}$ (Mo or Fe)	$r_{33} = 57$	ortho	$\sim 8 \times 10^{-3}$	~ 2000	580
SBNCe	$r_{33} = 420$	tetrag.	9.5×10^{-3}	~ 80	72
SBN	$r_{33} = 420$	tetrag.	3.2×10^{-5}	~ 1000	75
BBN	$r_{33} = 1350$	tetrag.	5×10^{-4}	-	56

Table 1-1: Photorefractive materials and properties[3].

In order to realize the technological potential of photorefractive materials, effective defect engineering is necessary. Defect engineering refers to the controllable incorporation of a homogenous density and distribution of application specific defects during melt growth. A deeper understanding of the fundamental origin and nature of the defect we aim to control must be gained before this goal can be achieved.

CHAPTER 2: LITERATURE REVIEW

2.1 Introduction

The group of compounds that is now known as sillenites was first discovered by Sillen in 1937[8]. Interest in these materials grew substantially starting in the 1960's. Although initially they gained attention for their piezoelectricity and electro-optic activity[9,10], their photorefractive property soon became the primary effect of interest. The three primary sillenites are bismuth silicate ($Bi_{12}SiO_{20}$, BSO), bismuth germanate ($Bi_{12}GeO_{20}$, BGO), and bismuth titanate ($Bi_{12}TiO_{20}$, BTO). The sillenite of choice for this work is BSO because it melts congruently (unlike BTO) and has a lower melting point than BGO. Its thermophysical properties are given in Table 2-1.

Physical Properties	Temperature (°C)	
melting point	895	
density (solid)	20	9.206 g cm^{-3}
density (liquid)	950	7.63 g cm^{-3}
linear expansion coeff.		1.6 x 10^{-7} K^{-1}
volume expansion coeff.		7 x 10^{-5} K^{-1}
specific heat (solid)		2.7 J cm^{-3} K^{-1}
specific heat (liquid)		3.0 J cm^{-3} K^{-1}
thermal conductivity (solid)	700	0.19 W m^{-1} K^{-1}
	800	0.18 W m^{-1} K^{-1}
	895	0.16 W m^{-1} K^{-1}
thermal conductivity (liquid)	895	0.27 W m^{-1} K^{-1}
viscosity (liquid)	900	0.22 dyn cm^{-2}s
breaking strain		2 x 10^{-4}
latent heat	895	460 J cm^{-3}

Table 2-1: Thermophysical properties of bismuth silicate (BSO)[11].

2.2 Sillenite Phase formation and Crystal Structure

2.2.1 Bi_2O_3 - MO_2 Phase formation

In early phase formation investigations, Differential Thermal Analysis (DTA) and X-ray analysis were used almost exclusively. Speranskaya produced early phase diagrams for BSO and BGO[12, 13] but only the 6:1 and 2:3 Bi_2O_3:MO_2 compounds were represented. Aurivillius et al.[14] investigated yet another compound of the form Bi_2MO_5 (M= Ge, Si) and identified a two layer structure consisting of deformed $Bi_2O_2^{2+}$ layers and MO_3^{2-} chains with a Bi_2O_3:MO_2 ratio of 1:1. These early papers disagreed with each other[15,16] as to whether sillenites were true compounds or merely isomorphous mixtures.

In an effort to resolve discrepancies about the nature of the phases formed within the sillenite structure, Kargin et al.[17] investigated the physiochemical nature of 23 different sillenite compounds. Compounds were formed using solid phase reactions and single crystals were grown either by the Czochralski method or hydrothermal method. They found that only group IV elements (Si, Ge, Ti) formed constant composition compounds. Compounds synthesized using group II, III, V, and VI elements exhibited varying compositions, with randomly distributed ions of two or more elements. Additionally, they concluded that the sillenite structured bismuth oxide (the γ-phase) should more correctly be considered a separate phase with the composition $Bi_{25}^{3+}Bi^{5+}O_{40}$ rather than a metastable γ-modification of Bi_2O_3.

Takamori[18] studied the Bi_2O_3 rich side of the phase diagram and came up with modifications of the diagram based on DTA and x-ray diffraction studies of water quenched melts. Brice[19] proposed the diagram shown in Figure 2-5 based on his bulk growth experiments. Recently, Fei[20] studied the Bi_2O_3 - SiO_2 system and developed both stable and metastable diagrams that are shown in Figure 2-1.

2.2.2 Sillenite Crystal Structure

The sillenite crystal structure and atomic arrangement were determined by Abrahams et al.[9] using x-ray diffraction to examine bismuth germanate spheres. They confirmed the

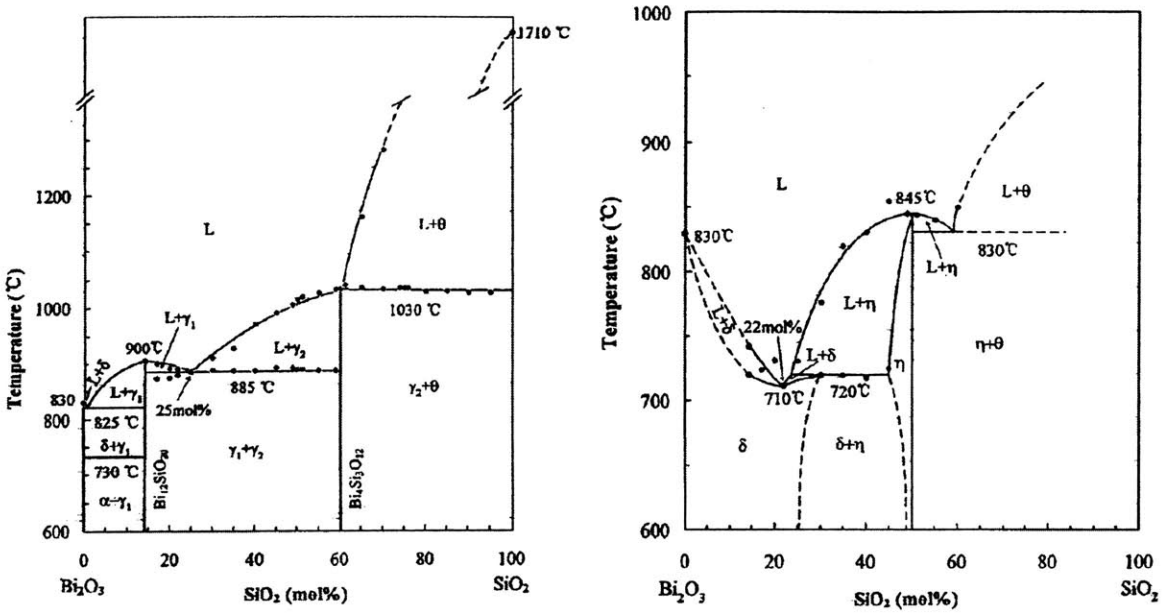

Figure 2-1: BSO Phase diagrams after [20]. Stable phase diagram shown on the left and metastable diagram shown on the right (note temperature scales).

space group choice of Sillen[8] to be I23. They also determined an occupancy factor of 91.1% for Ge in its tetrahedral sites. In subsequent work on BSO[21], they determined atomic coordinates, interatomic distances, and an occupancy factor of 87% for the Si atom. Figure 2-2 shows a unit cell of BSO[22]. The M atom (Si, Ge, Ti, etc.) is tetrahedrally coordinated with 4 oxygen atoms, and the tetrahedron sits in the BCC positions. The bismuth is heptacoordinated with oxygen[21] and its configuration is shown in Figure 2-3.

Work by Babonas et al.[23] focused on identifying the atom groups that had natural oscillations that do not depend on the rest of the crystal and could therefore be identified in the vibrational spectra of the sillenites. Their analysis of the unit-cell structure and nature of the chemical bonds indicated three different groups. They found that their calculated vibrational frequency of the $O_{(2)}Bi$ group agreed with published Raman spectra for BSO and BGO.

Radaev and co-workers[24,25,26] worked extensively on the structure of the sillenites. They looked at the mechanisms for the isomorphous substitutions and concluded that the effective valence of the M cation is not necessarily 4^+ as it is for Si and Ge. They found that in all sillenites the M position is partly occupied by Bi atoms. Lastly, they also find that the mineral sillenite (*i.e.* γ-phase Bi_2O_3) fits into the sillenite group as $Bi_{12}Bi_{0.80}O_{19.20}$.

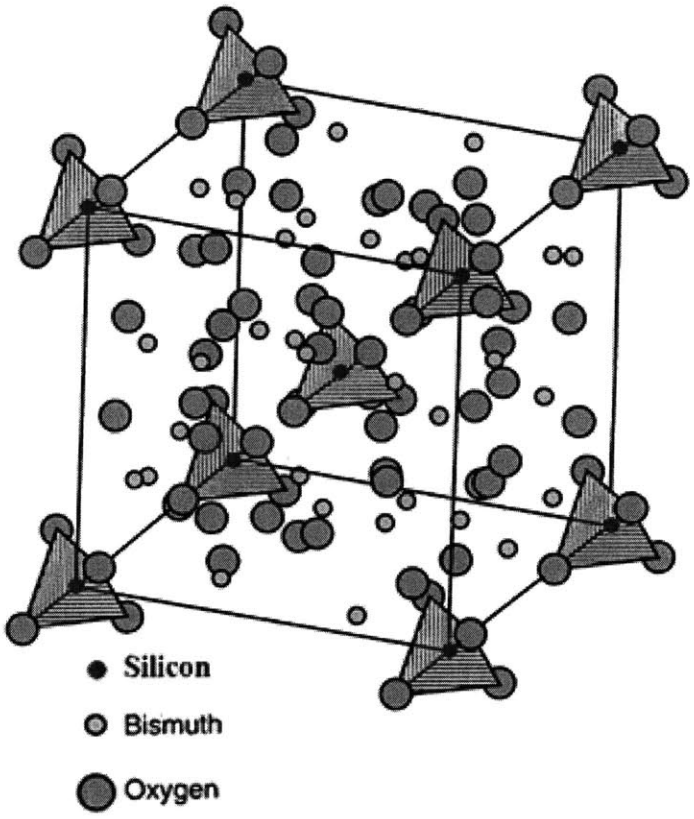

Figure 2-2: Unit cell of BSO[22].

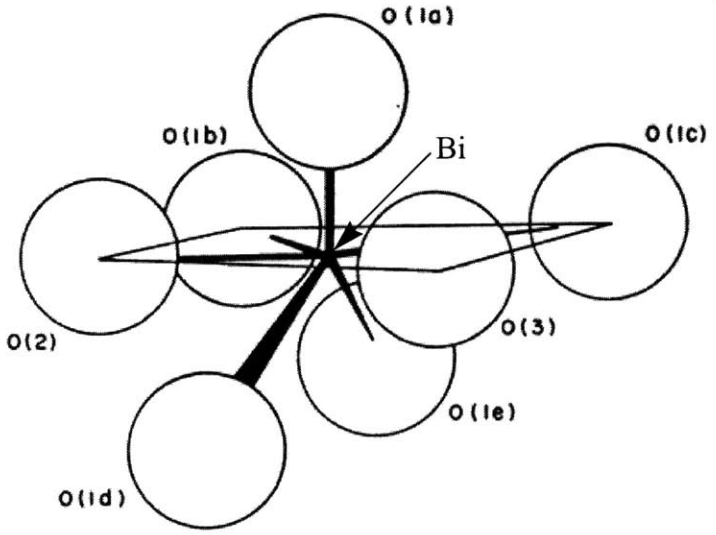

Figure 2-3: Bismuth - oxygen configuration in sillenite structure[9].

2.3 Czochralski Crystal Growth Technique

The production of sillenite single crystals can be accomplished by a number of different techniques. The most prevalent method, as with semiconductors, is growth from the melt using the Czochralski (CZ) technique. In CZ growth, a seed crystal is dipped into the melt and then pulled slowly upwards. Melt is pulled up with the seed due to surface tension. The temperature above the melt is lower, and the raised melt solidifies. By continuing to raise the seed, more melt is pulled up and solidifies, and the crystal is grown. A typical CZ system is shown in Figure 2-4. Advantages of this technique include the ability to produce large crystals and growing with a free surface (and thus avoiding confinement related stresses). However, due to the destabilizing thermal gradient and complex hydrodynamic interactions, crystals tend to have non-uniform optical/electrical properties. They may also contain macroscopic defects such as voids, inclusions, and cracks. An overview of the research on Czochralski growth is presented with a focus on heat transfer, hydrodynamic effects and defect formation.

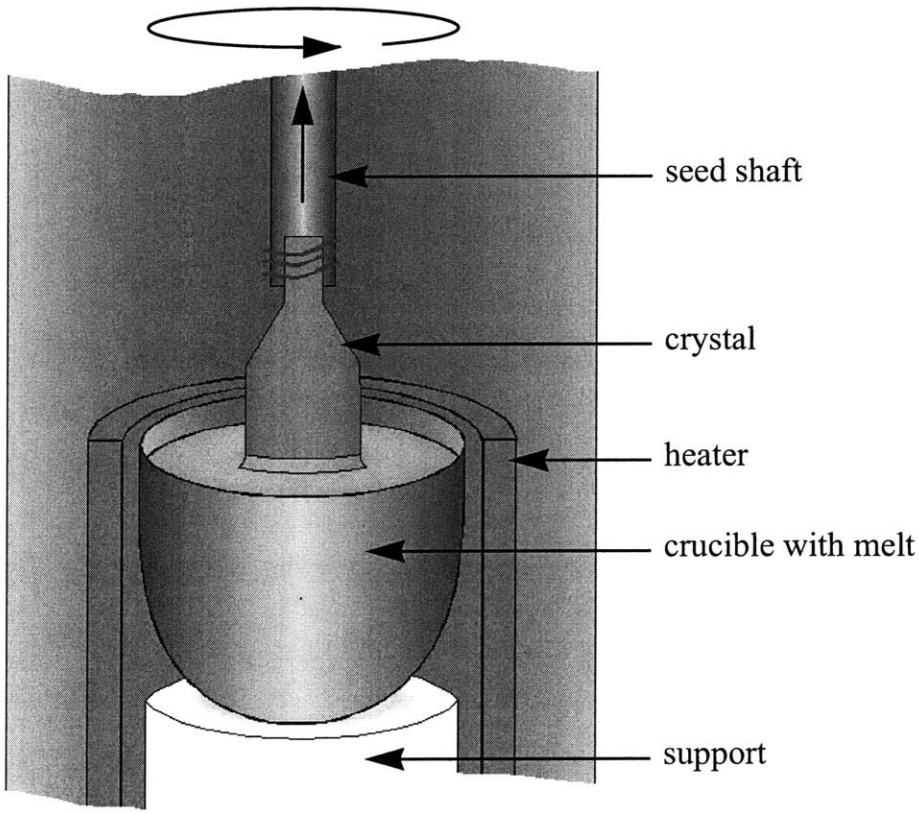

Figure 2-4: Schematic of Czochralski crystal growth process.

Sillenites were first grown by the Czochralski technique in 1967 by Ballman[27]. He was able to grow single crystals at pulling rates of up to 10 mm/hr using a rotation rate of 50 rpm. He reported that one of the prime contaminants was platinum inclusions, and that their appearance was induced by a sudden change in the melt temperature. Although he was primarily concerned with $Bi_{12}GeO_{20}$, he also grew $Bi_{12}SiO_{20}$, $Bi_{12}TiO_{20}$, and $Bi_{12}GaO_{20}$.

Brice and co-workers[19,28,29,30,31] studied BSO extensively in the 1970's with a focus on determining the growth parameters that would enable production of large BSO single crystals. Describing BSO as $Bi_xSiO_{1.5x+2}$, they found that crystals could be grown from melts with composition in the range of x = 10-14 by using low growth rates. The starting with a melt composition had little effect on the composition of the resultant crystal[19,29]. Growing from a melt with composition at either minimum or maximum amount of Bi_2O_3 of the existence region produced crystals that were less strained and had little axial composition variation. Figure 2-5 shows a portion of the phase diagram, and these compositions at the extrema of the existence region are indicated. Because the tangent of the solidus line is vertical at these

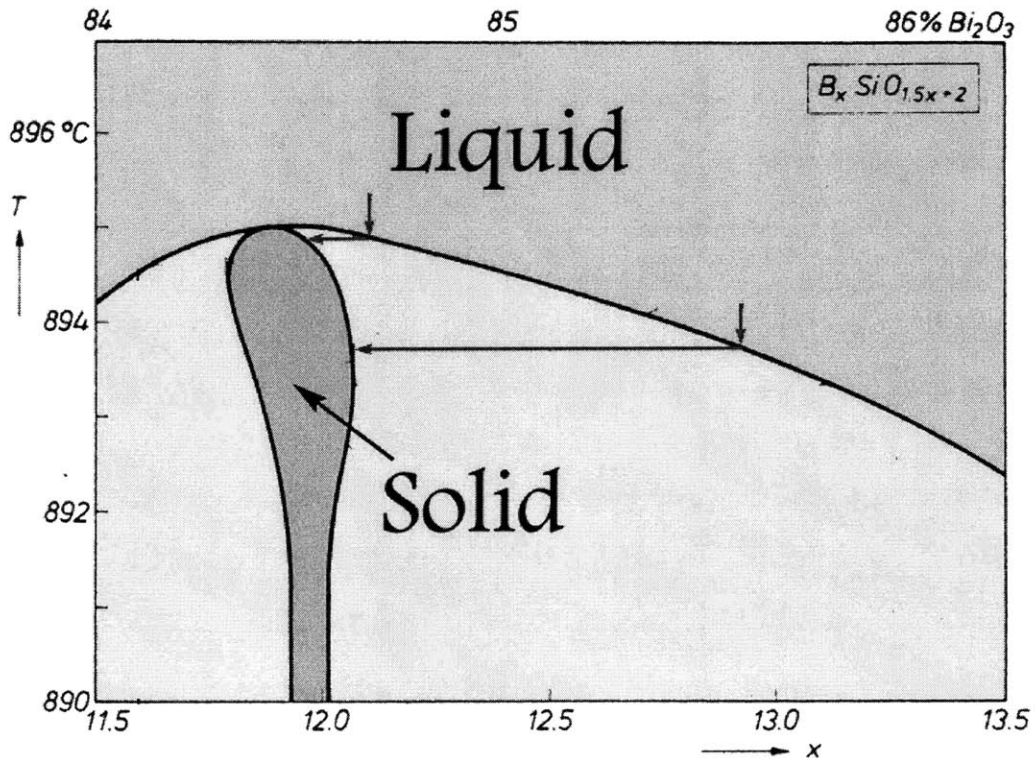

Figure 2-5: The existence region of the solid (from Brice et al.[19]).

instances, the composition in the crystal only varies minimally for large variations in the melt composition.

They also found that the maximum permissible growth rate was found to be inversely proportional to the square root of the crystal radius ($R^{-1/2}$). Additionally, large diameter crystals were also limited by temperature gradients across the boule that could lead to cracking if it became too large. This limits the growth rate of larger crystals to be proportional to $R^{-2/3}$ for radii larger than 1.5 cm[19].

Other growth conditions that affect the growing crystal are ambient atmosphere[32], rotation rate of the crystal, system geometry, and thermal gradients. These will be discussed in subsequent sections. The addition of dopants to the melt also necessitates a reduction in the pulling rate[33]. The effect of doping is discussed in Section 2.8.4 in reference to electro-optical properties of sillenites.

2.3.1 Heat Transfer Effects

Heat transfer plays a critical role in growth of crystals by the Czochralski method. The interplay between conduction, convection, and radiation as well as the phase transformation boundary makes analysis of CZ systems a complex problem. There has been a significant amount of research that has been done on CZ growth, mostly driven by semiconductor industry. In oxide systems, such as BSO, a complication arises due to the semi-transparent nature of the solid which makes it a radiatively participating medium. Moreover, the high Prandtl number of most oxide melts means that there will be significant distortion of the temperature field due to convection.

The rate of removal of latent heat of transformation during solidification limits the maximum permissible growth rate[19]. The energy that is produced must be conducted away through the solid crystal. If the growth rate is too high, not all of the latent heat can be conducted away, and the crystal loses contact with the melt[19,34] as the interface temperature increases. Kravchenko et al.[34] also found that the rate of removal of latent heat influences the types and relative sizes of facets that appear on the growth interface.

Radiative heat transfer between the melt, crystal, and surroundings changes throughout the growth process[35]. The radiative exchange between the melt and the furnace

affects the radial gradients at the surface of the melt. As the crystal increases in size, it obstructs the interaction between melt and furnace. Additionally, as melt depth decreases, radiative losses to the crucible vary due to the changing system geometry and crucible temperature. Furthermore, there is an increase in the surface area of the crystal that is within the interaction zone for radiative exchange. The increase in radiative heat transfer means a decrease in the conductive component leading to a change in the interface shape from flat to concave[34].

One distinguishing feature of oxide melts that make them very different from semiconductor melts is their high Prandtl number[36]. The thermal field within the melt will be significantly affected by the flow structures present. For example, it has been shown that at the boundary between natural and forced convection cells, there is a conduction layer while the temperature within the vortices is almost uniform due to significant mixing[37].

2.3.2 Hydrodynamic Effects

The fluid-flow behavior in the melt during crystal growth is a critical factor in determining the resultant crystal properties and has thus stimulated a significant amount of research in the area. Three main approaches are used to study the flow behavior:

1. growth experiments involving removal of the crystal at various instances
2. experimental simulations of the growth process, and
3. numerical modeling

Temperature gradients induce natural convection while crystal and/or crucible rotation induce forced convection. These two opposing influences are the driving forces in the melt. The shape of the growth interface is controlled by the dominant convection mode. The transition from one mode to the other can induce large temperature variations in the melt at the interface, and this can lead to non-steady temperature variations, increased defect incorporation, and/or catastrophic failure of the crystal due to cracking and sudden changes in the diameter[28,38,39,40,41,42].

Carruthers and Nassau[43] recognized early on that forced flow due to rotation of the crystal and/or crucible could be analyzed as a Taylor-Proudman cell. With crucible rotation, the outer portion of the liquid rotates as an almost solid body. For a crucible rotation of zero,

they found that fluid is drawn up at the center axis and flung outward at the crystal surface. They note that stagnation surfaces exist in all cases except when crucible rotation is zero or very small. They suggest that crucible rotation could be used to control dopant levels in the melt and/or reducing crucible attack due to decreased mixing in the melt.

Carruthers[44] compares the two convective driving forces in the melt using the ratio of Grashof number and Reynolds number. He normalizes with respect to viscosity as given by:

Equation 2-1 $$\mathrm{Gr} = \mathrm{Re}^2$$

The form of the Reynolds number is slightly different from its usual definition in that it accounts for the fact that the linear melt flow velocity is related to the total area.

Equation 2-2
$$\mathrm{Gr} = \frac{g\beta\Delta T R^3}{\nu^2}$$
$$\mathrm{Re} = \frac{\pi\omega d^2}{\nu}$$

where β = coefficient of thermal expansion (K^{-1})
ΔT = temperature difference (K)
g = acceleration due to gravity (m sec^{-2})
R = crucible radius (m)
ν = kinematic viscosity (m^2 sec^{-1})
ω = crystal rotation rate (rad sec^{-1})
d = crystal diameter (m)

Using Equation 2-1, and inserting the definitions for Grashof and Reynolds numbers given by Equation 2-2, he solves for the critical diameter where the two driving forces balance each other:

Equation 2-3 $$d = \frac{\left[g\beta\Delta T R^3/\pi^2\right]^{0.25}}{\omega^{0.5}}$$

Carruthers notes that the aspect ratio of the melt affects the type of thermal convection flows that occur. The gradual shifts in interface morphology depicted in his work corroborate this suggestion.

Kobayashi published a series of papers computationally analyzing the flow in a crucible in the mid to late seventies[36,45,46]. Initially, only forced convection was considered but both crystal and crucible rotation was taken into consideration. Subsequently, he analyzed the same geometry but looks at the effect of changing the Grashof number for a fixed Reynold's number in both low and high Prandtl number cases. Of importance is the conclusion that for high Prandtl numbers the temperature distribution, and hence interface shape, depend on the flow. He notes that the transition from one regime to the other depends mainly on Equation 2-1, although his definition (Equation 2-4) of both the Reynolds and the Grashof numbers differ from Carruthers.

Equation 2-4

$$\mathrm{Gr} = \frac{g\beta\Delta T d^3}{\nu^2}$$

$$\mathrm{Re} = \frac{\omega a^2}{\nu}$$

where d = height of melt (m)
a = crystal radius (m)

Brice et al.[28] were the first to discern the effect of rotation rate on growth specifically in sillenites. They found that above a critical rotation rate growth became unstable and a dark region or regions appeared in the melt around the periphery of the crystal and slowly precessed. Analyzing various Reynolds and Taylor numbers they found no statistically significant correlation with the Rayleigh number.

Further investigation of this rotational instability[30] used a platinum disk to simulate the rotating crystal on BSO melt. They found that the flow within the melt is due to purely natural convection with no rotation (see Figure 2-6a). With increased rotation, flow changed to a configuration with a Taylor Proudman column underneath the disk and radial flow still existing in an outer annulus (Figure 2-6b). Above a critical rotation rate, flow became purely rotational (Figure 2-6c). The appearance of a darkened extrusion on the melt surface marks the transition from the Taylor-Proudman configuration to the purely rotational flow. The rotation rate was also found to have a significant effect on the temperature distribution in the melt. Whiffin et al.[30] conclude that rotational instabilities are due to coupling between the rotationally induced flow and natural convection.

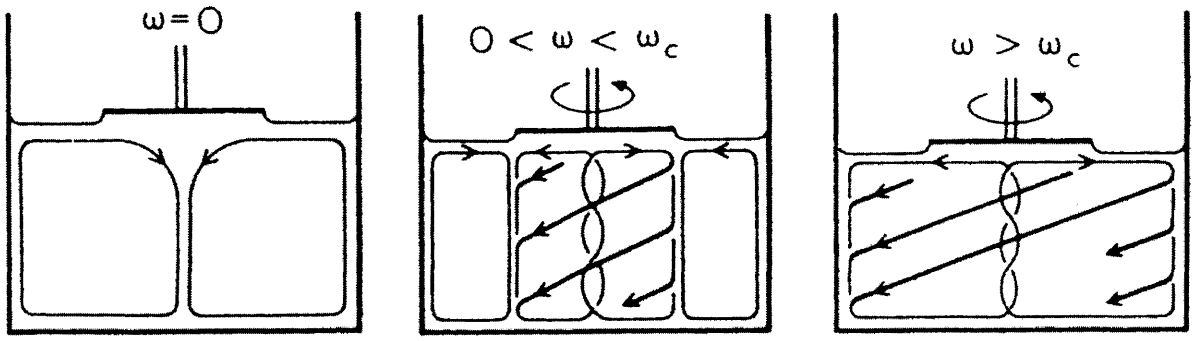

Figure 2-6: Fluid flow modes as a function of rotation rate[30].

Kimura[47] used tetradecane ($C_{14}H_{30}$) to simulate BSO melts in studying the effects of rotation rate on fluid flow modes. The critical physical properties of $C_{14}H_{30}$ are similar to those of BSO melts, as is the Prandtl number. This makes tetradecane a good material to use for flow simulations. Kimura's results agreed qualitatively with those of Whiffin et al.[30] for melt surface features and temperature variations. He also found turbulent flow for very high rotation rates; a result that had not been observed in simulations using water or water-glycerin as simulation fluids.

In the late 80's and early 90's, Nikolov and coworkers published a series of papers[38,48,49,50] on the role of convection in the melt in Czochralski systems. They recognized that other researchers had proposed a number of different criteria for the critical Reynolds number at which flow transitions occur. Using a water-glycerin mixture in flow visualization experiments, they analyzed the effect of parameters including the melt aspect ratio (h/D), the crystal to melt aspect ratio (d/D), the Prandtl number, and the Grashof number on the critical rotation rate for flow transition. Using data from other publications, as well as their own simulations, they determined an empirical relationship (Equation 2-5) between the system parameters and the critical Reynolds number.

Equation 2-5 $$\mathrm{Re}_{crit} = 3.18\left[\mathrm{Gr}\left(\frac{d}{D}\right)^{2.1}\left(\frac{h}{D}\right)^{0.35}\right]^{0.44}$$ and also

Equation 2-6

$$N_{crit} = \frac{3.18\left(g\beta\Delta T\right)^{0.44} D^{0.245} h^{0.155} \nu^{0.12}}{d^{1.08}}$$

where β = coefficient of thermal expansion (K^{-1})
D = crucible diameter (m)
h = melt height (m)
d = crystal diameter (m)
ν = kinematic viscosity ($m^2\ sec^{-1}$)
ΔT = temperature difference in the melt (K)
N_{crit} = critical rotation rate ($rad\ sec^{-1}$)

They suggested that the parameter space they inspected covered the different ranges used by other researchers and could thus can account for variations observed in their relationships.

Iliev et al.[38] also found that temperature fluctuations in the melt are mainly due to the interaction between natural and forced convection. Using water-glycerin mixtures of varying viscosities as well as a wide variety of experimental configurations, they concluded that the fluctuations are mainly localized at the boundary between the two types of flow, with the Reynolds and Grashof numbers determining the location of the boundary. The amplitude of the fluctuations is controlled by the temperature difference between the crystal and the crucible. The period depends on the Grashof number and the crucible diameter. The amplitude and period of the fluctuations are also dependent on how close the system is to the critical rotation rate. Above 0.4-0.5 N_{crit} up to 1 N_{crit} periodic oscillations occur with the maximum amplitude appearing around 0.8-0.9 N_{crit}.

As computational capabilities have increased in recent years, numerical modeling has become a more viable method for analyzing melt flows in Czochralski systems. Since non-axisymmetric flows are common in CZ systems, Xiao and Derby[37] used a type of finite element numerical method to achieve high spatial resolution in a three-dimensional model. A flat interface is the main assumption that differs considerably from real growth systems. Their steady axisymmetric solution shows natural convection in an outer annulus and rotationally driven flow underneath the crystal that does not extend to the crucible bottom. The azimuthal velocity is confined to near the crystal and decays as $Re^{-1/2}$ (Reynolds number is based on crucible radius). They analyzed a short time transient solution and a long time solution, both

of which displayed a three-dimensional nature with an annular vortex structure and four fold symmetry. Like Whiffin et al.[30], they conclude that the baroclinic instability theory does not apply. One mechanism they propose is that the breakdown of the Stewartson layer (the boundary between the two opposing meridional flows) into non-axisymmetric structures.

Santos et al.[51] did simultaneous experimental and computational work. They found that the flow patterns determined the shape of the interface and size of the core. The experimental portion of their work examined the development of the shape of the interface in relationship to the temperatures within the melt. They observed the interface by either withdrawing the crystal from the melt at various points during growth or by examining axial slices. They divided the growth process into four different zones, as seen in Figure 2-7: the shoulder (A), and the body with a sigmoidal interface (B), a flat interface (C), and a concave interface (D). Their theoretical modeling of the flow and temperatures fields were obtained by solving the modified Laplace and Navier-Stokes equations using experimental boundary conditions. The numerical model used experimental conditions as well as material specific physical properties. They showed that for a given melt height, the interface depends on the crystal diameter, and that at small melt heights the interface becomes concave.

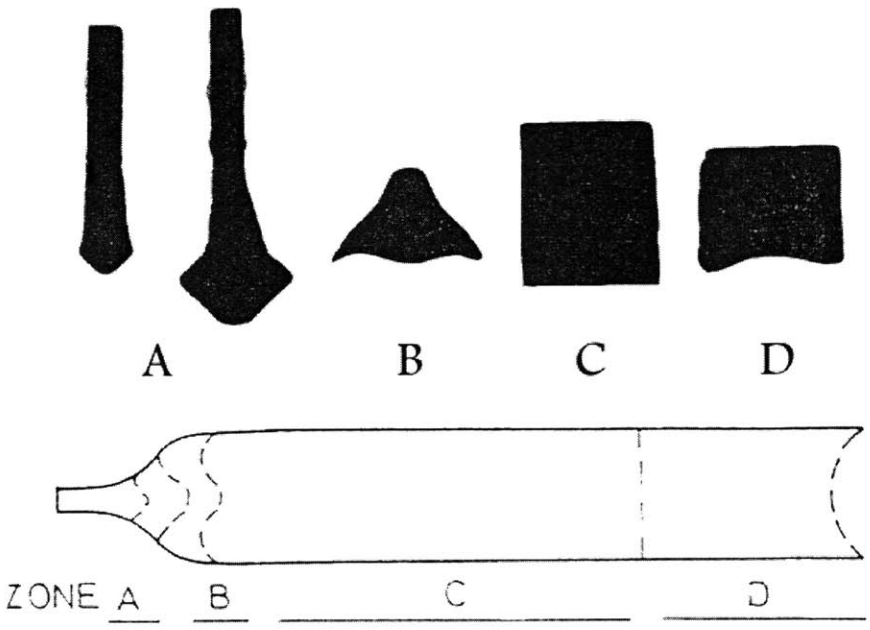

Figure 2-7: Interface shapes observed by Santos et al.[51].

2.4 Bridgman-Stockbarger Growth

Other methods that have been employed for sillenite growth are directional solidification, hydrothermal growth, float-zone growth, laser heated pedestal growth, and sol-gel technique. A thorough review of the work done in directional solidification is presented since the main thrust of this thesis concerns Bridgman-Stockbarger growth of BSO. A conventional Bridgman-Stockbarger (B-S) furnace is shown in Figure 2-8. It consists of two heaters separated by a gradient zone. The solid/melt interface is located in the gradient zone. The hydrothermal technique is also of importance since crystals grown by this technique do not exhibit photorefractivity. This lack of photorefractivity suggests suggests that the origin of the native defect is fundamentally related to growth from the melt.

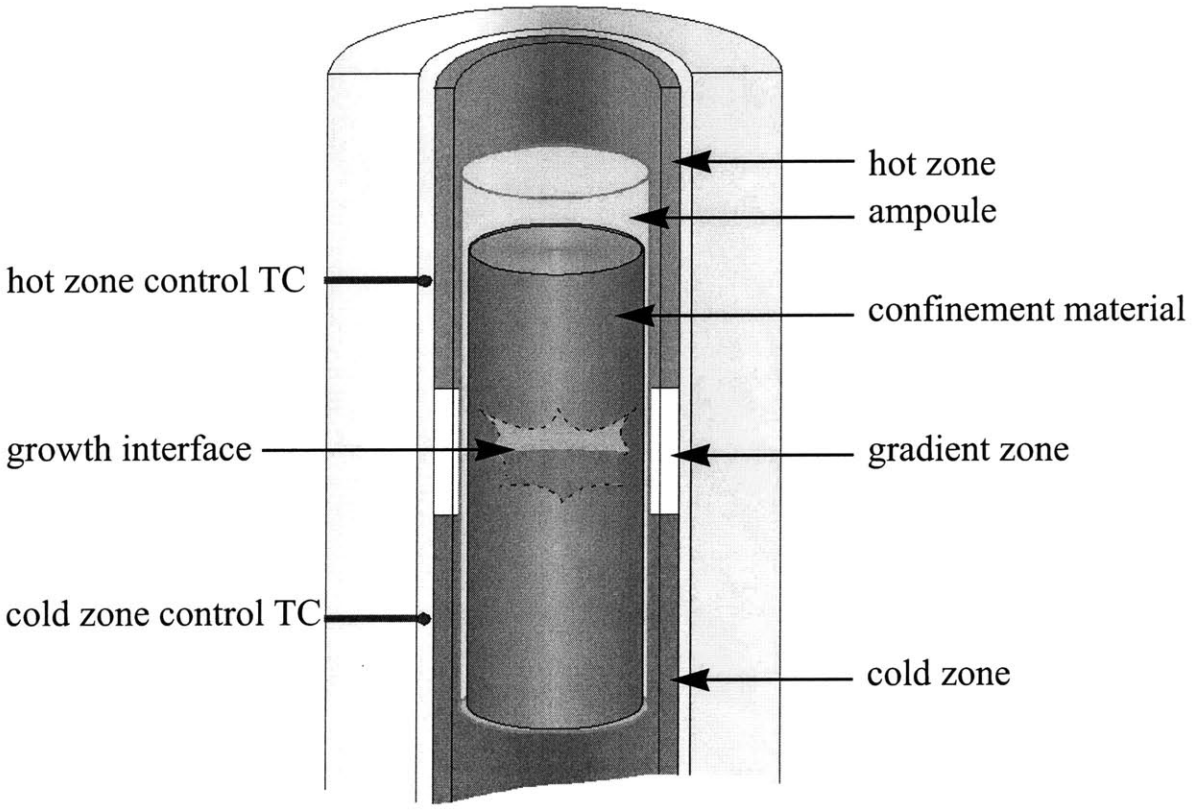

Figure 2-8: Schematic of conventional Bridgman-Stockbarger configuration.

2.4.1 Numerical Modeling

Starting in the early 90's, modeling of oxide growth using directional solidification was done that accounted for internal radiative transport in the crysta and/or melt. Earlier modeling research[52,53,54,55,56,57,58,59] was geared toward growth of metals and semiconductors and thus has limited applicability to oxide growth. The importance of radiative heat transfer effects had already been recognized in modeling Czochralski growth[59].

Brandon, Derby, and coworkers[60,61] were the first to analyze the effects of internal radiation on directional solidification of oxides. They presented a model for the growth of semitransparent crystals in which three-dimensional radiative transport is coupled rigorously to two-dimensional heat flux. The crystal was modeled as a non-scattering, participating medium with uniform properties, and the melt was assumed to be opaque. Initially, it was assumed that convection was negligible and the ampoule walls are thin, grey, and diffuse[60]. They used an idealized three zone furnace with a heat-pipe geometry and allow for a three-dimensional, curved interface. They analyzed the effect of varying the absorption coefficient in the solid and also the emissivity of the inner and outer surfaces of the ampoule. In subsequent work, they included the effects of convection in the melt, finite ampoule dimensions, and furnace design considerations[61]. They found that for intermediate values of the absorption coefficient, there was a monotonic increase in the curvature with decreasing coefficient value, and that the additional conductive heat transfer through the ampoule increased the severity of the effect. As the radiative heat flux in the solid became stronger, increasing the overall heat flux, the thermal gradient steepened in the melt in order to balance the total axial heat flux. Convection did not influence the shape or position of the interface significantly. Lastly, decreasing the thermal conductivity of the ampoule flattened the interface as well as raising it in the gradient zone.

Lin and Motakef[62] focused on modeling directional solidification in BSO. Unlike Brandon and Derby, they modeled radiation in the solid using a two-band model. At wavelengths less than 6 μm, the crystal was assumed to be completely transparent; while for longer wavelengths, it was assumed to be totally opaque. The semi-transparency of the solid led to the convex interface shape, and they found that the interface deflection increased with ampoule wall thickness. The radiative heat flux dominated in the solid due to the low thermal

conductivity, and was greatest in the center. Unlike Brandon and Derby, they found that convection affected the shape of the interface through enhanced mixing between edge and center thus reducing the deflection of the interface by about 20%. They also examined several different furnace configurations. Increasing the length of the gradient zone to 4 cm, decreased deflection by about 10%. Similarly, using an adiabatic zone with multiple gradients, also decreased the deflection by about 10%. However, removing the heat pipes decreased the deflection by 40%.

The assumption that the melt is opaque is based on the finding that there is a large increase in the absorption coefficient upon melting of sapphire[63,64]. However, in practice, this is not always true, and consequently Vizman et al.[65] accounted for conduction and radiation in all portions of the crystal. They used an idealized three zone furnace but allowed for thermal gradients in the heater regions. They employed the diffusion approximation for thermal conductivity (Equation 2-7) to account for radiation.

Equation 2-7
$$k = k^{mol} + k^{rad} = k^{mol} + \frac{16n^2\sigma T^3}{3Ro}$$

where k = thermal conductivity (W m^{-1} K^{-1})
k^{mol} = molecular thermal conductivity (W m^{-1} K^{-1})
k^{rad} = approximation for radiation contribution to thermal conductivity (W m^{-1} K^{-1})
n = refractive index
σ = Stefan-Boltzman constant (W m^{-2} K^{-4})
T = temperature (K)
Ro = Rosseland mean absorption coefficient (m^{-1})

They compared three cases: (1) the crystal and melt were both opaque, (2) the crystal and melt were both transparent, and (3) the melt was opaque but the crystal was transparent. Transparency in both phases flattened the interface and shifted it upwards in the gradient zone (compared to the totally opaque case), and this effect became more pronounced as the fraction solidified increased. These changes were explained by the fact that when radiation is taken into account, it increased the total axial heat flux which shifted the interface upwards and flattened it. Since absorption was higher in the melt, the increased flux was accommodated by a steeper gradient in the melt. In contrast to Lin and Motakef[62], they found that a thicker ampoule decreased interface deflection.

Nicoara et al.[66] use the same model as Vizman et al. to look at the effect of furnace configuration. They found that the growth rate did not affect the interface shape but that the fraction solidified did. The length of the gradient zone also affected the interface position. A two centimeter gradient zone was found to be too short because the interface moved into the hot zone. They concluded that for a large diameter crystal a steep gradient and long gradient zone furnace configuration is preferable.

Because machining of oxide crystals can be both costly and difficult, Virozub and Brandon[67] modeled the growth of slab-shaped semitransparent crystals. They found a qualitative difference in the shape of the interface for slab shaped crystals as compared to the cylindrical counterpart. The interface was severely deflected as well as shifted towards the hot zone. They attributed these differences to the large change in the viewing angle of the interface and the cold zone. These changes substantially increased the radiative axial heat flow which in turn drove the interface towards the hot zone and increased its curvature. They concluded that the adverse increase in interface curvature in slab shaped crystals may make this approach ineffective for producing high quality crystals.

More recently, Lu[68] used a boundary element modeling (BEM) technique to analyze the heat transfer in semi-transparent crystals. BEM offers advantages in both memory and computation requirements over finite difference and finite element methods. Additionally, it can handle the moving boundary calculations associated with the interface motion. He found that as solidification proceeds the curvature initially decreases and then increases. At the top of the crystal, however, the interface eventually inverts to concave due to the boundary effect.

As computational capabilities increased, the ability to handle more complex situations became possible. Vizman et al.[69] used finite volume method to investigate the effects of temperature asymmetry and tilting of the ampoule on the convection in the melt. They accounted for radiative flux using the diffusion approximation in both the solid and the melt. In accordance with modeling oxides, they chose a Prandtl number of 17.6. They found that the flow structure in an aligned case changed from a single torroidal flow to a two cell-structure if the gradient in the hot zone was non-constant but did not induce three-dimensional flow. Comparing both opaque and transparent cases they observed much higher Reynolds numbers in the semitransparent melt due to the increased radial gradients. Tilting the ampoule

even by one degree caused the right flow cell to become stronger in a semi-transparent melt. Superposition of non-constant gradient and tilting caused significant deviation from symmetry in the flow. Again, the effect was more pronounced in the semitransparent melt than in the opaque melt. For a five degree tilt the flow changed such that it flowed upwards on the right side and down along the left side. Neither tilting nor non-constant gradients affected the shape of the interface. However, since a semi-transparent melt is more sensitive to tilting and non-constant temperatures, the solute segregation will also be more significantly influenced as a result.

The fundamental problem of modeling results is that the basic data base of properties is not complete, boundary conditions of real systems are often difficult to determine, and the necessary idealization of boundary conditions in modeling can not readily be realized experimentally. Therefore, modeling can produce not be expected to produce absolute data. Nevertheless, much qualitative inisight can be gained that can be used to help analyze experimental results.

2.4.2 Directional Solidification of BSO

Only two groups have reported Bridgman growth of BSO. The first reports were by Xu et al.[70,71] who reported the ability to grow BSO boules in the <111> or <112> direction that were core-free. Growth along the <100> or <110> direction resulted in a darkened core similar to the core found in CZ grown crystals. They also grew doped BSO crystals that were reported to be inclusion and core free. They analyzed the distribution of dopants using the diffusion limit but conclude that it was invalid. In reviewing the analysis technique, it is concluded that in using only the top and bottom portions of the crystals (as Xu did), one would not use adequate number of data points to make a viable analysis for the axial distribution. Additionally, x-ray fluorescence is not a very sensitive technique for accurately determining doping levels, and this further brings into question the validity of their conclusion that solute transport regime is diffusion dominated.

The only other research on directional solidification was done by Zheng and Witt[72]. Successful growth of BSO was performed in a heat pipe based Bridgman-Stockbarger furnace. However, platinum embrittlement was found to occur in samples processed in a

sealed ampoule. Additionally, some sample contained fibrous inclusions that were found to be Bi deficient. The current research is a direct extension of this work.

2.5 Hydrothermal Growth and other methods

Hydrothermal growth of BSO is also of significance because it provides low temperature growth conditions involving aqueous solutions. Undoped[73,74] and doped[75,76] BSO was grown from solution at ~400 °C and pressures in excess of 4500 psi. Hydrothermal BSO is clear and no longer exhibits photorefractivity. The critical native defect responsible for photorefractivity is missing in these crystals. The extended absorption shoulder present in melt grown material (centered around 2.6 eV) and responsible for the characteristic yellow-yellow-orange color is also absent. The absorption shoulder reflects the true band edge of 3.4 eV. Harris[75] used mass spectrometry to compare impurity levels in hydrothermal and CZ material and found no difference in low level (ppma) impurities. Additionally, no photochromic response was observed in the undoped hydrothermal material in contrast to undoped CZ grown material[74,76]. These results indicate that the deep donor responsible for the absorption shoulder is the critical native defect that is responsible for the photorefractive response and photochromism. Moreover, it is implicated that the defect's origin is fundamentally related to growth from the melt.

Larkin et al.[76] investigated using dopants to 'tailor' the response of hydrothermal samples. Interestingly, hydrothermal BSO doped with excess Bi showed the characteristic absorption shoulder of CZ samples as well as exhibiting photorefractivity. This result supports the hypothesis that the critical native defect is a bismuth anti-site defect that is occupying the silicon tetrahedral position (discussed further in subsection 2.7.2). Preliminary results from co-doped hydrothermal samples also showed a similar response to CZ material. Co-doping with chromium and phosphorous enhanced IR absorption at the expense of blue absorption, while co-doping with chromium and aluminum had the opposite effect. The ability to tailor the photorefractive response to specific wavelengths has not been pursued further in the literature.

The sol-gel technique has also been investigated for producing BSO films[77,78]. Results indicate that films are crystalline and have optical properties in agreement with bulk crystals.

Like hydrothermal growth, the sol-gel technique does not involve growth from the melt. It involves the deposition of thin films through chemical hydrolysis of alkoxides. Bismuth nitrate and tetraethyl orthosilicate were used as the precursors. X-ray diffraction was used to identify the structure as BSO with some Bi_2O_3 present as well. Although the authors present absorption data, it is hard to tell if it has the characteristic absorption shoulder associated with the native defect. Since it is not a melt-growth technique, the native defect could be absent. Unfortunately, no photorefractivity measurements were made by the authors on BSO produced by the sol-gel technique.

Another technique that has been employed is float zone growth[79,80,81,82]. Although the method has the advantage of avoiding confinement related contamination, the size of crystals produced in a terrestrial environment is limited. Cracking is a serious problem in float zone growth of sillenites due to the large temperature gradients. An improved float zone technique employing an infrared heater to reduce the thermal stress in the grown crystal was developed by Fu and Ozoe[82]. Quality and maximum growth rate were both increased by this method. Computational modeling[79] of the float-zone process to investigate maximum bridge size and growth rate agree well with experimental work.

Microgravity conditions are ideal for the float zone process since one of the major problems in a terrestrial environment is deformation of the molten zone due to gravity. Experimental[83,84] and computational[85] work was done on BGO float zone growth in microgravity. Experimental results reveal a lower dislocation density and a slightly wider wavelength region. However, numerous macro and micro cracks are present as well as pores. Full three-dimensional computational treatment of non-uniform temperature environments revealed strong convective interference for the terrestrial case and showed that microgravity greatly reduces convection and stabilizes the float zone. However, the microgravity environment is subject to g-jitters and numerical modeling reveals that they affect the temperature and flow fields in the float zone.

If the source rod is moved through the heater rather than the heater traveling along the source rod (as with the float-zone method), the technique is referred to as laser heated pedestal method[86,87,88,89]. Growth rates are lower than float zone growth approximately an order of

magnitude. Limits for axial gradients and maximum growth rates are imposed in order to avoid cracking.

Finally, there are several other methods that have been used to grow sillenites, but they have received little attention in the literature. Thin plates were grown using the EFG method[90], and it was found that in order to achieve stable growth, the die needed to be concave rather than planar. Modeling of growth of BGO by the heat exchanger method was done[91], but there does not seem to be any experimental verification of this work. BSO has also been grown using the pulling down method[92], and good quality crystals were produced that had no cracks or inclusions as long as the starting charge was Bi rich.

2.6 Macroscopic Defect Formation in Melt-Grown Sillenites

2.6.1 Bubbles and Inclusions

One of the major defects found in Czochralski grown sillenites is bubbles (voids)[93,94,95,96,97]. Several researchers have studied the mechanisms for formation of bubbles in oxide crystals. Cockayne[98] found six modes of void formation:

I. Entrapment of impurity-rich liquid in cell boundary or solute trail which contracts upon freezing
II. Segregation of gaseous impurities directly
III. Entrapment of escaping volatile impurities
IV. Capture of gas bubbles displaced from the melt
V. Condensation of vacancies
VI. Solidification with a limited supply of liquid

In oxide growth, mechanisms I-IV are assumed to occur, with mechanisms I and II predominant[98]. Possible sources of bubbles in oxides that are also mentioned by Cockayne include: an imbalance in oxygen in the ambient atmosphere and the oxygen vapor pressure at the melting point; a separation of oxygen from complex ions within the melt by reaction with impurities; a change in solubility of gaseous components due to the phase transformation; and an evolution of gases which have been absorbed or trapped during melt preparation.

Miyazawa[96] studied the effect of fluid flow on gas-bubble entrapment for Czochralski grown oxide crystals. Because the solid-liquid interface is the source of the gasses dissolved in the melt in mechanisms I-IV, the capture of gas bubbles can be avoided by decreasing the pulling rate. Results indicated that both diameter and rotation rate affected the formation of bubbles, and that the boundary between bubble and bubble-free growth conditions coincided with the macroscopically flat interface. The bubbles appeared for convex interfaces around the central axis of the boule. Using the Grashof number to characterize natural convection and the Reynolds number for forced convection, he found a linear relationship between the diameter and the reciprocal of the square root of the rotation rate ($\omega^{-1/2}$) for the boundary between bubble and bubble-free growth. Dissolved gas in the melt due to rejection upon solidification can lead to supersaturated liquid. This liquid will be either concentrated underneath the crystal due to natural convection and nucleated bubbles are likely to become trapped, or the supersaturated liquid is removed from the interface due to forced convection and bubbles are not incorporated in the crystal. However, crystal rotation rate is not the only parameter that affects bubble entrapment as was noted by him in earlier work[97] where decreasing the growth rate also decreased bubble incorporation.

Similar work was done by Kobayashi[99] with the conclusion that the primary determinant for bubble inclusion is the growth rate. Because of conflicting reports on the effect of rotation rate on bubble formation, he analyzed the fluid flow in terms of the Grashof and Reynolds number. The crystal diameter was used as the characteristic length for both dimensionless numbers, whereas Miyazawa[96] (and most others) use the crucible diameter as the characteristic length for the Grashof number. Kobayashi found a relationship for the critical transition between flow regimes:

Equation 2-8
$$f = \frac{\mathrm{Re}^{2.5}}{\mathrm{Gr}}$$

where f is a constant on the order of 10. Because of the difficulties in determining parameters such as temperature differences, he suggested that the critical Reynolds number should scale as the diameter to the 1.2 power:

Equation 2-9
$$\mathrm{Re} = A(2a)^{1.2}$$

where a = diameter of the crystal, and

Equation 2-10 $$A = \left(\frac{fg\beta\Delta T}{4\nu^2} \right)^{0.4}$$

where f = constant as given by Equation 2-8
g = acceleration due to gravity (m sec^{-2})
β = thermal expansion coefficient (K^{-1})
ΔT = temperature difference between crystal and crucible (K)
ν = kinematic viscosity (m^2 sec^{-1})

2.6.2 Facets and Coring

A core in a crystal is due to the formation of a central facet during growth. Facets form on the solid-liquid interface during growth when the curved interface intersects a singular face[100]. Jackson[101] found that a surface could be either atomically rough (i.e. non-faceted) or atomically smooth (i.e. faceted) and that the Jackson factor (α) determines in which regime an interface lies:

Equation 2-11 $$\alpha = \frac{\Delta H}{T_m R}\xi$$

where ΔH = enthalpy of phase transformation (J mol^{-1})
T_m = melting point during growth (K)
R = gas constant (J K^{-1} mol^{-1})
ξ = fraction of total binding energy which binds a molecule in a layer parallel to the plane face to other molecules in the layer

If $\alpha < 2$, an atomically rough interface is predicted and growth is continuous. For small values of ΔT, the growth rate can be approximated to be proportional to ΔT.

The kinetics of facet growth are substantially different than those of non-faceted growth; facet growth requires much greater supercooling. The size of the facet depends on the growth rate, the radius of curvature of the interface (R), and the thermal gradient (G) near the interface. The supercooling (ΔT) is also related to the growth rate and becomes larger as the growth rate increases. The radius of the facet (b) can be approximated by the relationship[100]:

Equation 2-12 $$b^2 = \frac{2\Delta TR}{G}$$

The composition of the crystal does not vary markedly between facet and off facet material, but the facet does have a slightly larger lattice constant as well as being darker in color[19,98]. The size of the central core, and hence facet face, can vary from as little as one to two percent of the cross-section, to covering the entire growth interface. Because of the difference in lattice constant of the core, a strain develops at the facet edge. This strain is a function of the ratio of the facet area to the total area, and in the case of a large facet can lead to substantial additional strain in the crystal[102]. Cockayne[98] states that the most likely cause of the change in lattice parameter is oxygen segregation. He suggests that the entrapment of oxygen vacancies on the facets occurs due to the high lateral growth rates involved in facet formation and the small relative diffusion constant of oxygen with respect to the cations present.

One of the first publications to study the central core in detail was by Picone[103]. Crystals were grown in the <110> direction, and core formation was suppressed at rotation rates higher than 35 rpm. The central core contained an unusual microstructure consisting of bands that did not correlate with the period of rotation, computer control loop period, or thermal response. He attributed the striations to thermal fluctuations arising from convective instabilities.

Aggarwal et al.[104] grew undoped and Fe-doped crystals in the <100> and <111> directions. Using energy dispersive x-ray (EDX) measurements, they found that there was essentially no difference in composition between core and off-core material. They observed a silicon deficiency in all samples (Si content measured at 0.5 wt% as compared to stoichiometric value of 0.98 wt%). Unfortunately, the sensitivity of the EDX technique is only 0.5 wt%, and the authors acknowledge that a more sensitive technique is necessary before any conclusions about the compositional variations can be made.

Santos et al.[105] also use EDX to study the core in BSO and BGO. They found that the Bi/Ge is larger in the core area, in agreement with Tu[106]. However, the difference in ratios is small: 11.6 for core compared to 11.2 for off-core. Converting this atomic ratio to weight percent, the ratios correspond to 86.24% and 86.35% respectively, and this 0.1% difference

falls below the 0.5 wt% sensitivity of EDX. Electron paramagnetic resonance (EPR) and fluorescence measurements revealed the Fe^{3+} impurity concentration in the core to be three times higher. The EPR results also indicate a higher strain in the core, and it is attributed to the presence of a greater number of imperfections. The authors conclude that the higher Bi/Ge ratio in the core is due to a larger number of Fe atoms occupying the germanium tetrahedral position. Lastly, they find that cores have a slightly different index of refraction as observed with interferograms. The optical activity (OA), however, does not vary between core and off-core material. This finding is in conflict with Gospodinov et al.[107] who observed a 7-8% decrease of OA in the core.

2.7 Point defects

In sillenites, point defects are critical because it is a native point defect that is responsible for the photorefractive effect. Point defects lead to interband states (traps) that affect the electro-optic properties of the material. They have been studied extensively, but no clear consensus has emerged. The inconsistencies between various studies are mainly due to the variability of crystal quality and residual impurities that plague sillenite bulk growth. Nevertheless, there are several observations that have been verified by a number of different authors.

2.7.1 Energy Gap Trap levels

Common techniques for studying trap levels are thermally stimulated current (TSC), photoconductivity, photo- and thermo- luminescence, and optical absorption. Hou, Lauer, and Aldrich[108,109,110,111] were among the first to characterize the electro-optical properties and determine trap levels of BSO and BGO. As a result of this work, they came up with the phenomenological band diagram shown in Figure 2-9.

Photoconductivity measurements are commonly used to investigate interband states[108,109,112,113,114,115,116]. Illumination excites carriers out of interband levels that then drift under an applied field, thereby producing a current in the crystal. Photoconductivity depends on the ratio of filled to empty trap, and it determines the speed of photorefractive build-up as well as the decay of modulation of the index of refraction (Δn)[117]. Photocurrent is dominated

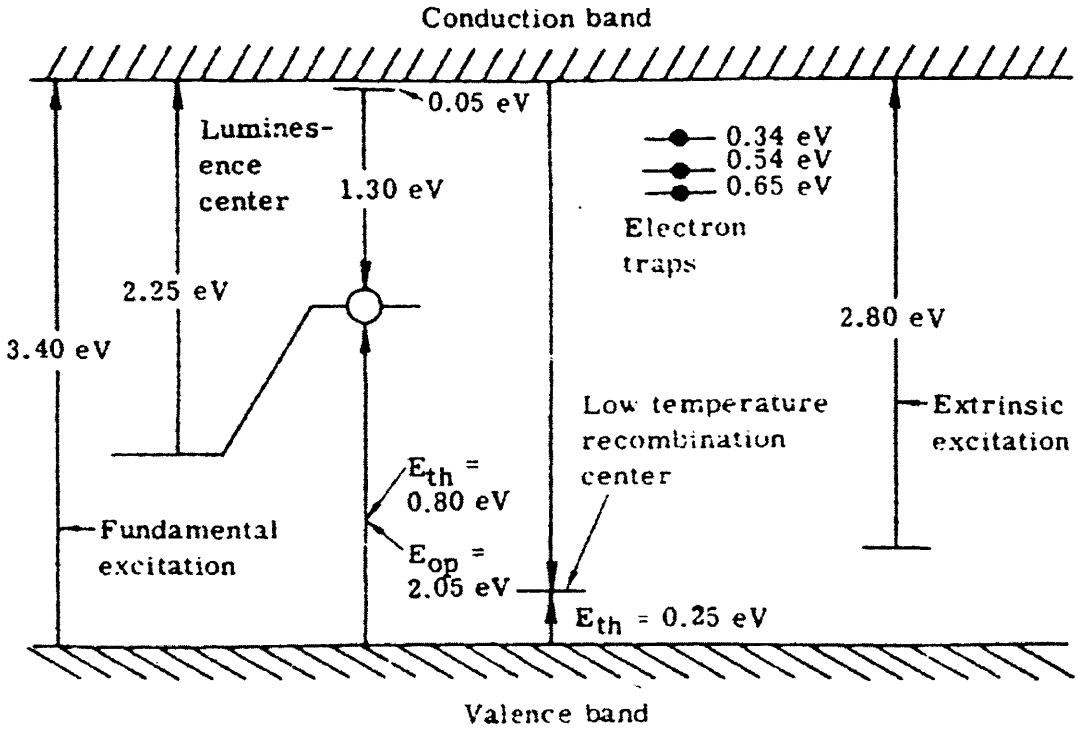

Figure 2-9: Phenomenological band diagram for BSO at 80 K, after [108].

by electrons, and it is larger than hole photocurrent by about an order of magnitude[109,115]. Thermal activation and quenching of photo current, as well as the spectral dependence of photocurrent[108,112,114,115], were used to postulate trap and recombination center levels. Most authors agree that there are several types of traps present in these materials[112,113,114,118]. One modification of photoconductivity is the time of flight (TOF) technique that uses short pulses of light to generate a sheet of carriers that drift under the influence of an external field. TOF[119,120] has been used to measure charge carrier mobility.

Thermally stimulated current (TSC) has been used extensively to investigate shallow traps in sillenites[110,121,122,123,124,125,126,127]. This technique can be used to identify traps that lie up to 1.5 eV below the conduction band. However, since residual impurities often create levels in this range, much variability is observed in TSC results. Table 2-2 lists results from Takamori without (0 kV/cm) and with (1.35 kV/cm) a bias voltage as well as results from several authors as given by Takamori[122]. He found that trap levels varied even from boule to

boule in his own work. There is also no agreement whether the majority traps are for electrons[69,112] or holes[124]. Nevertheless, there is general agreement that there are at least two different types of trapping centers - usually described as 'fast' and 'slow' traps.

0 (kV/cm)	1.35 (kV/cm)	from [108, 111]	from [162]	from [125]
	0.15			
0.28	0.33	0.34	0.25	0.26
			0.35	0.38
0.64	0.64	0.54	0.47	0.45
			0.55	0.50
0.82	0.83	0.65	0.58	0.60
0.96	0.93		0.66	0.74
	1.41		0.72	

Table 2-2: Trap levels determined from TSC measurements[122].

Optical absorption behavior is quite well characterized for the sillenites because absorption is often measured in conjunction with other measurements. The main feature is a broad shoulder extending from about 2.2 eV up to the band edge (3.4 eV), and it is generally accepted that it is due to the critical native defect[116]. In sillenites, the energy required for optical absorption is greater than the energetic distance from the interband level to the bottom of the conduction band due to the indirect bandgap and momentum conservation constraints. Therefore, absorption energies do not correlate directly with position within the energy gap. Absorption behavior is modified by dopants[116] as well as stoichiometry[117,128,129,130,131] as is shown in Figure 2-10 and Figure 2-11. As mentioned earlier, hydrothermal BSO is neither photorefractive nor does it have this characteristic absorption shoulder[73], thus suggesting that the critical native defect is responsible for the shoulder.

2.7.2 Nature of Intrinsic Defect

Lauer et al.[111] were the first to speculate on the nature of the defects leading to the observed trap levels. Citing the work of Abrahams et al.[9,21] on the occupation of the tetrahedral position, they speculated that a silicon vacancy complex, $[V_x V_O]^{-2}$, was a suitable

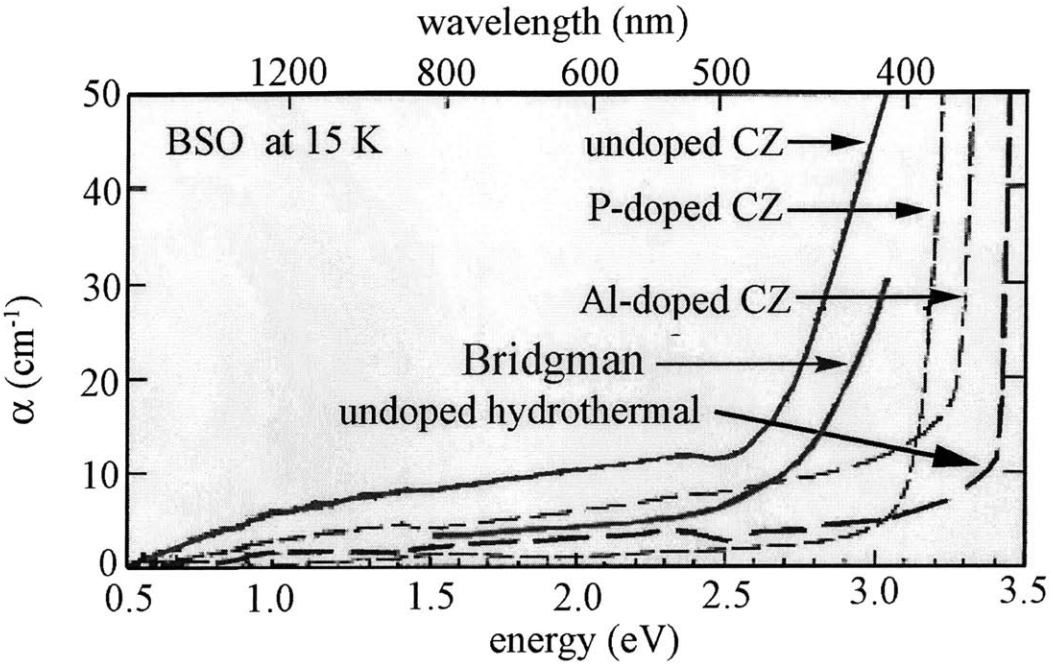

Figure 2-10: Comparison of optical absorption behavior for undoped and doped Czochralski, Bridgman, and hydrothermal BSO.

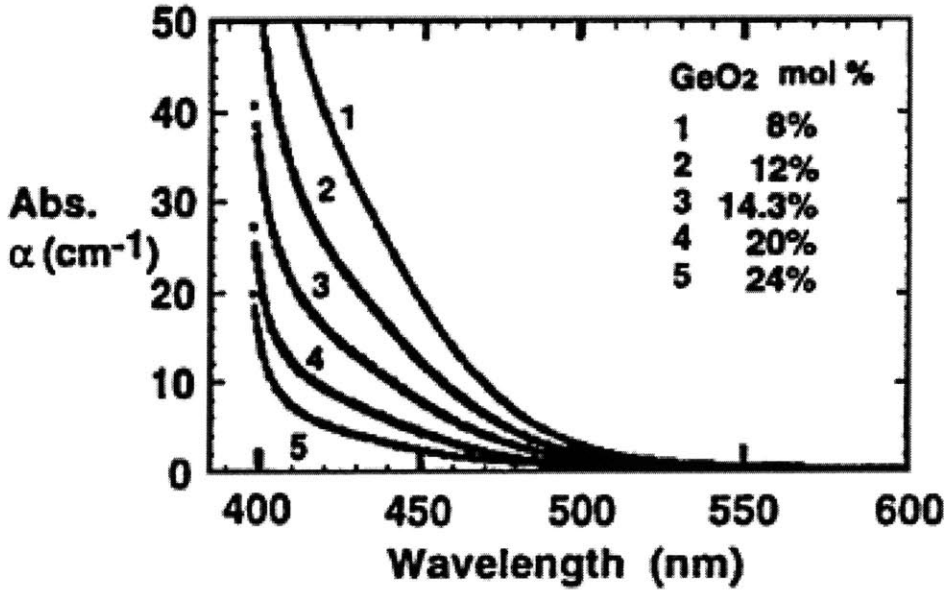

Figure 2-11: Effect of stoichiometry on optical absorption[131].

candidate for the luminescence center. This center lies at 2.25 eV when occupied by an electron and at 1.30 eV when occupied by a hole. They concluded that this trap is completely different in nature from the major luminescence peak found at 1.95 eV[105] for several reasons:

1. Although it responds to band edge excitation (3.4 eV), it can also be excited by energy that peaks at 2.25 eV.
2. 1.30 eV emission can be enhanced by IR light.
3. The 1.30 eV peak is present in thermoluminescence.

These facts led to the conclusion that the 1.30 eV trap participates in the charge transfer process. Additional photoconductivity and optical absorption data is presented in [108] and they conclude that the broad absorption shoulder is due to a silicon vacancy complex 2.6 eV below the conduction band.

It was not until work by Oberschmidt[116] that this theory was questioned. Based on his observation of absorption, photoconductivity, mass densities, and annealing, he discussed different types of possible defects. The tetrahedral position is normally occupied by the M atom ($Bi_{12}MO_{20}$, M= Ge, Si, Ti). The author considers included impurity substitution on the M site, vacancy of the M site, or bismuth on the M site. He concluded that it must be a well adapted atom rather than a vacancy due to the small ΔG value and the lack of diffusion. Using the relationship between the lattice constant and the ionic radii of the M atom as further support, he proposed the hypothesis that the critical defect is an antisite defect where Bi occupies the M position. More specifically, he proposed a Bi_M^{3+} + hole scheme. This hypothesis has become the accepted explanation throughout literature. More recently, magnetic circular dichroism (MCD) and optical detection of magnetic resonance (ODMR) studies[132,133] have further confirmed this theory.

2.8 Electro-Optic Properties

Bismuth silicate is of technological interest because of its electro-optic properties. Initial interest in the sillenites was for their piezo-electric property as observed by Ballman[27] but their photorefractivity is now the primary property of interest. A summary of properties for BSO is given in Table 2-3.

Electrical/ Optical Properties	
Dark resistivity	5×10^{13} (Ω cm)
Dielectric constant	56
Loss tangent	0.0015
Transmission range	0.45 – 7.5 (μ)
Bandgap	3.25 (eV)
Dark conductivity majority carriers	p-type
Photo-induced majority carriers	Electron
Optical activity	'+' and '-'
Electro-optical coeff. (Pockels)	5.0×10^{-10} (cm V^{-1})
Δn_{max}	10^{-5}
Response time at 1 W cm^{-2}	$10^{-4} - 10^{-3}$ (sec)
Writing energy density	10^{-2} – 1 (mJ cm^{-2})

Table 2-3: Electro-optic properties of BSO.

2.8.1 Electro-optic Effect

The linear electro-optic effect (Pockel's effect) refers to the change in refractive index due to an electric field. This can be expressed as

Equation 2-13 $$\Delta n = \frac{1}{2} n^3 r_{41} E$$

where n = refractive index
r_{41} = electro-optic coefficient (cm/V)
E = electric field (V/cm)

Lenzo et al.[134] measured optical activity and electro-optic effect in sillenites. They observed that application of an electric field produced both linear birefringence (electo-optic effect) and circular birefringence. They found that the optical rotary power of BGO was a function of wavelength and that the rotation was right-handed in all samples. In contrast, Feldman et al.[10] found that all of their BGO crystals were left-handed.

Values for the electro-optic coefficient for BSO were also determined by Aldrich et al.[109] as part of the investigations mentioned previously. More recently, measurements of the

electro-optic (EO) coefficient were made[135] that agreed with Aldrich's BSO value of r_{41} = 5.0 x 10^{-10} cm/V but are 20% higher for BGO than Lenzo's values (r_{41} = 4.1 x 10^{-10} cm/V vs. r_{41} = 3.4 x 10^{-10} cm/V). Lemaire et al.[136] found smaller values of r_{41} for both BSO and BGO in their work, but they also reported values that varied strongly from sample to sample. Differences in values for the EO coefficient can be explained by losses at surface contacts and internal nonuniformities in conductivity[135]. Since conductivity of samples can be affected by unintentional impurities, as well as inhomogeneities in intrinsic defect levels, it is not surprising that different crystals yield different coefficients.

2.8.2 Photorefractivity

Photorefractivity is the modulation of the index of refraction as a result of non-uniform illumination, and it is a 3 step process. First, illumination causes photoionization, the excited carriers then diffuse and/or drift, and they are finally trapped. This in turn creates an internal electric field which results in a change in the index of refraction because of the electro-optic effect. Figure 2-12 shows how photorefractivity can be used to generate a grating in a material.

There are a number of different possibilities as to the type and number of donors, traps, and carriers as shown in Figure 2-13[137]. The simplest model is a single donor that also acts as the trap of a single carrier (e.g. either hole or electron) as is suggested by Vogt et al.[117]. For BSO, there are two competing model for the mechanism of photorefractivity. In the first model, carriers diffuse or drift in the conduction band[138,139,140]. Only one charge carrier (electrons) is assumed in this model. The second model uses charge hopping for carrier motion. Attard[126,141,142,143,144] postulates that charge exchange happens in a 'hopping/ communication' band that requires several sources of defect/impurity levels. He found that both holes and electrons act as charge carriers. This result was also concluded by a number of other investigators[145,146,147].

The most common experimental set-up for photorefractivity measurements is the four-wave mixing configuration. Two write beams (split from a single laser source) form an interference pattern in the crystal. This pattern is 'read' by another beam and the diffracted

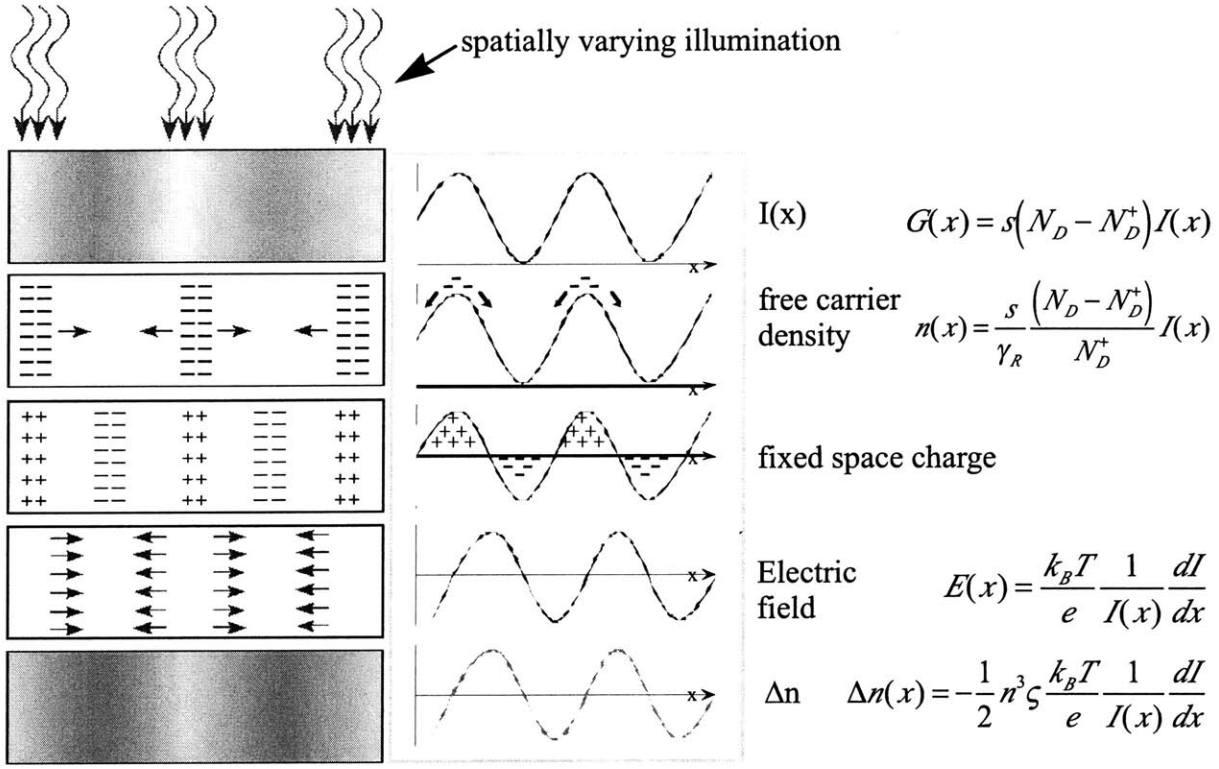

Figure 2-12: Schematic of using photorefractivity to produce grating in a material.

signal is measured. A schematic is shown in Figure 2-14. A similar set-up using only 2 beams is also sometimes employed[130,141,146,148]. The four beam configuration allows a number of properties such as diffraction efficiency[117,147], effective trap density[117,130,145,148,149], carrier mobility[133], and diffusion transport length[148,149] to be measured using grating response and decay characteristics. Low temperature studies[118,147,149] as well as investigations on the effect of doping[118,147,149] have also been performed. Several authors have found that the photorefractive response varied not only from boule to boule[146,147] but also between samples taken from the same boule[123].

2.8.3 Photochromism

Photochromism refers to changes in the absorption behavior of a material as a result of illumination. Like photorefractivity, the exact mechanism for photochromicity is still subject to controversy[150,151]. Chromium and manganese are two dopants that are particularly

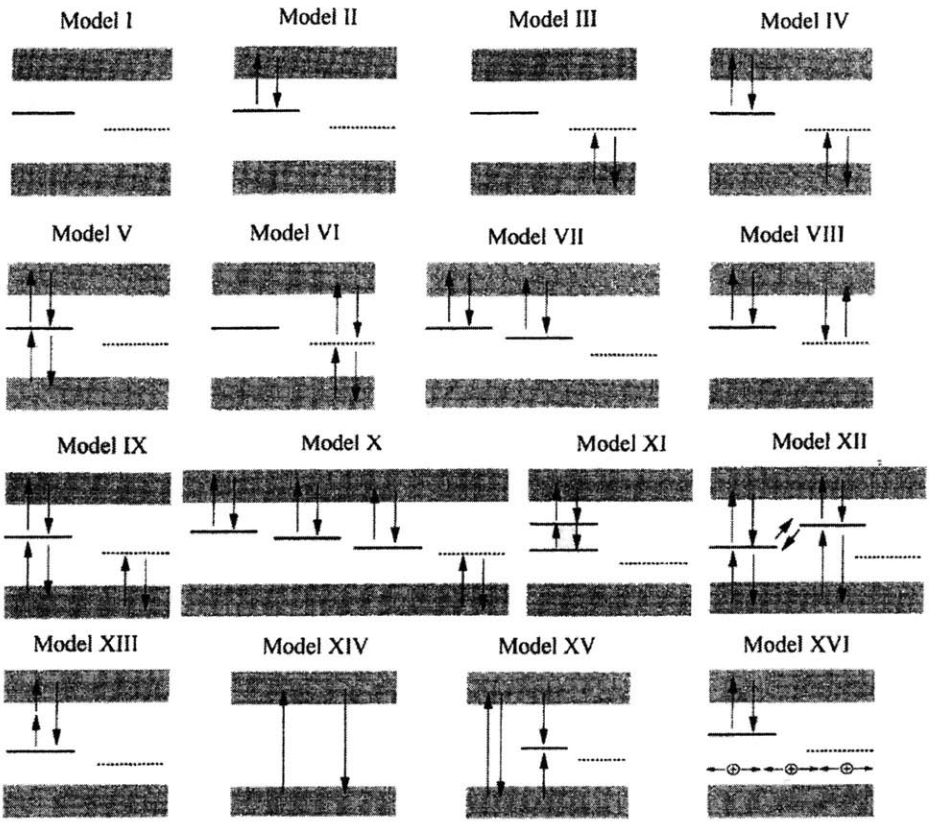

Figure 2-13: Models as proposed by Solymar[137] for charge donor/trap levels and carrier action.

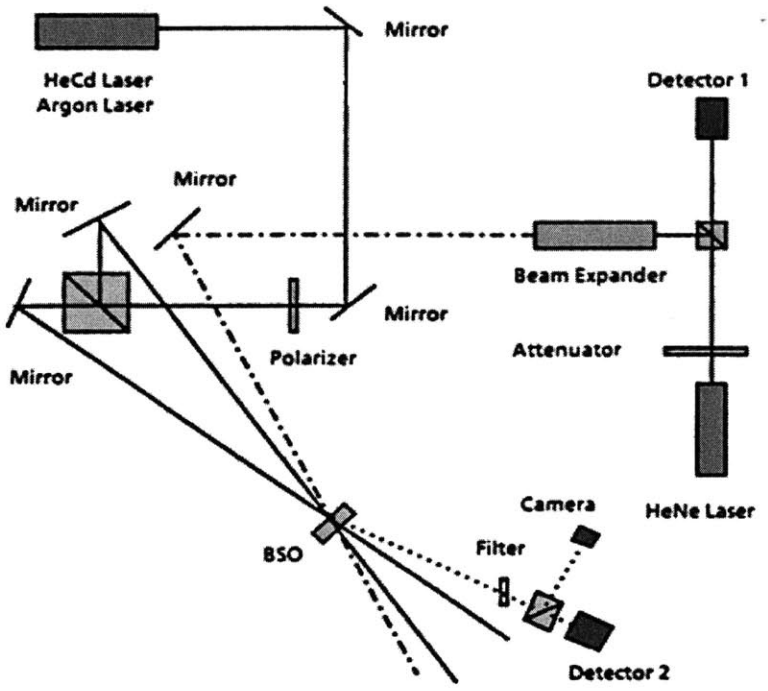

Figure 2-14: Schematic of photorefractive FWM mixing setup[143].

effective in increasing the photochromic response. Photochromic materials are desirable for memory applications where minimal decay of holographically 'written' information is important[152].

It was known early on that trace impurities could affect the color of the crystal and induced photochromism. Brice et al.[19] found that crystals containing more than one ppm of either chromium or iron darkened while those containing less than one ppm of those species stayed light-colored. Likewise, Tanguay et al.[153] reported that some crystals grown turned dark upon removal from the furnace and exposure to room light. They found a correlation between this photosensitivity and particular batches of Bi_2O_3. These crystals were analyzed using emission spectrograph and atomic absorption analysis and no impurity level exceeded the one to two ppm range. The photochromic response of BSO is therefore extremely sensitive to impurity incorporation. Low temperature photochromism was observed by numerous investigators in both doped and undoped sillenite crystals[151,154,155,156]. Doped materials have also been observed to exhibit photochromism at room temperature[152,157,158,159,160].

Other illumination induced effects result from the emptying and filling of traps prior to taking measurements such as TSC and photoconductivity. One method to thermally empty traps is to heat and then cool samples while they are not exposed to light[161]. Pre-illumination with 833 nm light was found to decrease photoconductivity by an order of magnitude[161] while pre-illumination with 650 nm and shorter wavelength light restored photoconductivity to near its initial value. Illumination also markedly affects TSC and TL measurements, and the widely varying TSC results found in literature may in part be explained by varying initial illumination conditions in addition to varying crystal quality.

2.8.4 Doping Effects

Intentional addition of small amounts of impurites, referred to as doping, affects the electro-optical properties by changing the electronic transitions due to additional interband states that act as donors, acceptors, and/or traps. Dopants can bleach crystals, as seen with Al, P, Ga, Ca, or Zn[162,163,164,165,166,167]. They can also increase absorption, as seen with Cr, Mn, and Co[33,165,168,170]. Doping with Cr, Mn, Cu, Co, and Fe also increases the photochromic

effect (PCE)[150,165,171]. Additional trapping levels are created by the presence of dopants[163,170], and they decrease photoconductivity. The effects of doping on TSC[126], Raman spectra[171], and optical activity[172,173,174] have all been studied. The effects of different dopants, or combination of dopants, provides the possibility of tailoring crystals for specific wavelength response[165].

Dopant	Absorption	Effect
Fe	red or blue shift, incr and decr α	lowers concentration of shallow traps
Cr	red shift, incr α, PCE	increases OA, photorefractivity
Mn	red shift, incr α, PCE	decreases OA
Zn	bleach, blue shift	raises concentration of shallow traps
Cu	red-shift, PCE	
Co	red shift, incr α,	slight increase of OA
Ni	minor bleaching, blue shift	
Ca	bleach, blue shift	
V	red or blue shift, incr and decr α	
Al	bleach, blue shift	act as acceptors
P	bleach, blue shift	act as donors
Ga	bleach, blue shift	act as acceptors
Cd	increase	

Table 2-4: Dopants used with sillenites and their effect

2.8.5 Conclusion

It is clear from the literature that crystal quality and purity has severely complicated the study of the electro-optic properties and the full spectrum of interactions of interband states in sillenites. However, in general, the literature seems to point to a multi-carrier, multi-level (both shallow and deep traps) mechanism for photorefractivity. Although not unambiguously identified, the preponderance of the data supports the hypothesis that the Bi_M antisite is the critical native defect. Lastly the effect of doping is well understood in terms of donor and acceptor behavior.

CHAPTER 3: MOTIVATION AND EXPERIMENTAL APPROACH

3.1 Motivation

To date, the commercial development of a large number of BSO based devices is strongly impeded by the difficulties in controlling the density and distribution of the defects responsible for the photorefractive behavior in BSO[35,75,92,153,175] on both a micro and macro scale. The situation is primarily due to the fact that the exact chemical and/or crystalline nature and origin of these defects are as yet unknown. Research focused on identification and control of the full spectrum of energy levels in the bandgap (caused by defects generated during melt growth) is complicated by the following factors

(a) convective interference with heat and mass transfer during growth

(b) confinement related contamination of the melt, and stress in the solid

(c) kinetic undercooling effects associated with facet growth

The use of a microgravity environment as a means of reducing gravity related effects has yielded insight in fields as diverse as crystal growth, combustion, and fluid physics. In crystal growth, the microgravity conditions reduce the gravitationally induced driving forces for convection by up to six orders of magnitude, as reflected in the Rayleigh number:

Equation 3-1
$$\mathrm{Ra} = \frac{g\beta\Delta T l^3}{\nu\alpha}$$

where g = acceleration due to gravity (m sec^{-2})
β = volumetric coefficient of thermal expansion (K^{-1})
ΔT = temperature difference (K)
l = characteristic length (m)
ν = kinematic viscosity (m^2 sec^{-1})
α = thermal diffusivity (m^2 sec^{-1})

Microgravity growth experiments make it possible to study effects and properties otherwise masked or skewed by convective interference. Thus, experiments are expected to facilitate the study of the formation of the critical native defects during growth of BSO. In order to maximize data obtained from microgravity experiments, accompanying ground based

work is critical. The influence of gravity on critical defect incorporation must be established under quantifiable, reproducible, and measurable boundary conditions. Additionally, terrestrial experiments also serve as a basis for comparative analysis with microgravity experiments. For the last 10 years, NASA sponsored research on BSO has been conducted at MIT with the ultimate goal of performing quantitative microgravity experiments aboard the International Space Station. These experiments are aimed at determining the nature and origin of the critical native defect in bismuth silicate.

3.2 Objectives of Research

This thesis is directed at resolving specific issues that are critical to ground-based research as well as industrial production of melt-grown BSO. The following areas are addressed in this work:

1. analysis of the interaction of BSO with confinement material
2. reproducible and quantifiable growth of BSO by the Bridgman-Stockbarger method
3. development of analytical approaches to the identification of defects of concern
4. investigation of the relationship between growth conditions and the density and distribution of the critical native defect due to gravitationally induced convection.

3.3 Experimental Approach

Minimizing contamination and stress due to the confinement material is desirable. To assess the feasibility of quasi-containerless processing, the interaction of BSO with its confinement material is studied using the sessile drop method for contact angle measurements and solidification experiments in both a terrestrial and a low gravity environment. In order to establish reproducible Bridgman-Stockbarger growth capabilities, a crystal growth system is designed, implemented, and thermally characterized. Czochralski growth is used to produce bulk material for Bridgman-Stockbarger experiments. Additionally, since this material is grown in an environment with strong convective interference, it can be used in the analysis of the effect of growth conditions on defect incorporation. Analysis of the optical properties of grown BSO samples is used to study both macro- and micro-segregation of the critical native defect. Based on the results, a hypothesis is to put forward as to the origin of the native defect.

CHAPTER 4: INTERACTION OF BSO MELT WITH PLATINUM CONFINEMENT MATERIAL

One of the fundamental issues in Bridgman growth of any material, and BSO in particular, is the interaction with the confinement material. If the confinement material and the solidified crystal have different thermal expansion coefficients, the crystal cannot contract during cooling and this leads to stresses in the crystal. These stresses can be avoided by using a non-wetting confinement material or one with similar thermal expansion properties. Unfortunately, the corrosiveness of the BSO melt does not provide many material choices, and platinum has been used exclusively for growth from the melt. Throughout the literature, it is documented that molten oxides, including BSO, will attack platinum labware[27,176-187]. It is therefore necessary to study the interaction between BSO and the confinement material.

4.1 Ground-based Sessile Drop Experiments

Previous sessile drop experiments of molten BSO on platinum indicated that the contact angle depended on the oxygen content of the ambient atmosphere[72]. For pure platinum in a 0.1% oxygen with argon balance atmosphere, the contact angle was measured to be 41°. In this work, platinum-5%gold was considered as an alternate material because it is known that several glasses do not wet this material[188].

4.1.1 Background

Sessile drop theory is based on the equilibrium state of the contact line that results from the balance of solid, liquid, and vapor phase interfacial tensions. Figure 4-1 shows a schematic of a sessile drop and the interfacial tensions. The balance of forces acting on the drop governs the shape of the sessile drop. Gravity tends to flatten the drop while surface forces tend to make it spherical. The balance of these forces is given by Young's Equation:

Equation 4-1
$$\cos\theta_E = \frac{\gamma_{s/v} - \gamma_{s/l}}{\gamma_{l/v}}$$

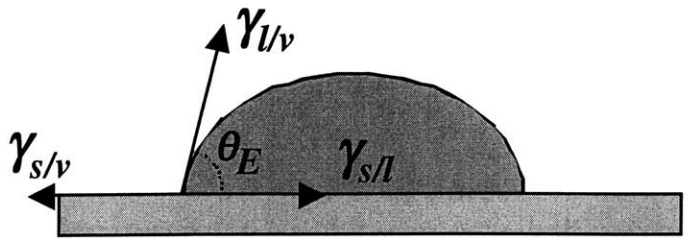

Figure 4-1: Surface tension forces in a sessile drop configuration.

where: θ_E = equilibrium contact angle

$\gamma_{l/v}$ = liquid/vapor interfacial energy (mJ m^{-2})

$\gamma_{s/v}$ = solid/vapor interfacial energy (mJ m^{-2})

$\gamma_{s/l}$ = solid/liquid interfacial energy (mJ m^{-2})

The Laplace equation of capillarity is the mechanical balance of forces and is given in Equation 4-2[189]. It relates the pressure difference across a curved interface to the surface tension and curvature of the interface. For two homogeneous fluids that are separated by an interface, the Laplace equation is the mechanical equilibrium condition:

Equation 4-2 $$\gamma(\frac{1}{R_1}+\frac{1}{R_2})=\Delta P$$

where R_1, R_2 = principal radii of curvature (m)

ΔP = pressure difference across interface (N m^{-2})

γ = interfacial tension (mJ m^{-2})

If no other forces are present, the change in pressure can be expressed as a linear function of elevation (Equation 4-3):

Equation 4-3 $$\Delta P=\Delta P_0+(\Delta\rho)gz$$

where ΔP_o = change in pressure at a reference plane (N m^{-2})

$\Delta\rho$ = change in density (kg m^{-3})

g = acceleration due to gravity (m sec^{-2})

z = vertical height of drop measured from the reference plane (m)

4.1.2 Experimental Methods

The furnace used for the sessile drop experiments is shown in Figure 4-2. The heating element consisted of Fe-Cr-Al windings embedded in alumina-silica insulation (Watlow, 700W). A quartz tube was placed through the furnace cavity; it was fitted with endcaps that allowed for imaging from one end and control of ambient composition from the other. A bubbler with glycerin was used to ensure a constant pressure within the tube that was slightly above atmospheric pressure. Copper tubing was used to cool the quartz tube in order to avoid overheating of the o-ring on the endcap. The alumina (Rescor 960, Cotronics) sample holder, shown in 4-3, was mounted on a ceramic tube used for insertion of the sample into the center of the furnace.

Platinum-5%gold sheets (0.25 mm) were ordered with a mirror finish for use as the substrate for the sessile drops. However, the 'as delivered' substrates had uniform scratches. They were polished with a colloidal silica solution (0.02-0.05 μm, pH 10) on a long nap pad

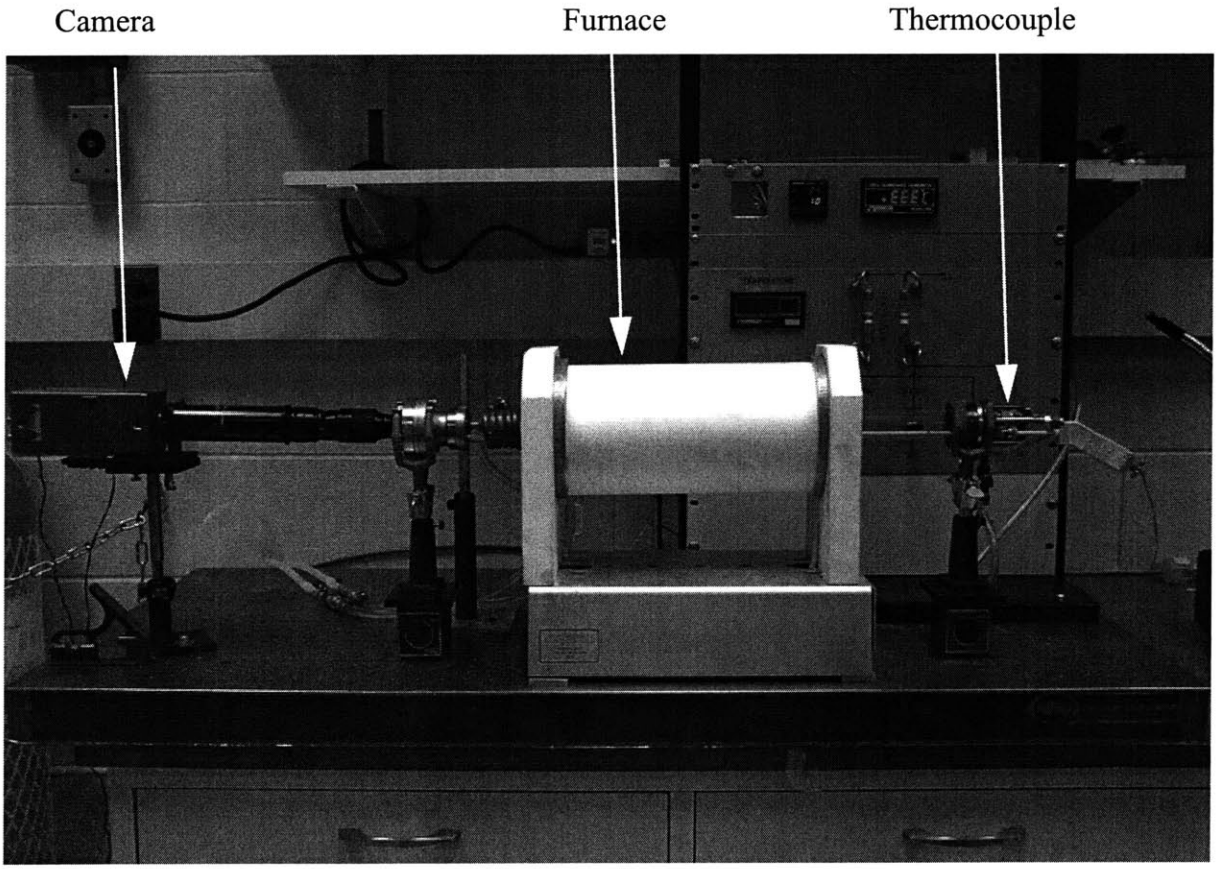

Figure 4-2: Experimental setup for sessile drop experiments.

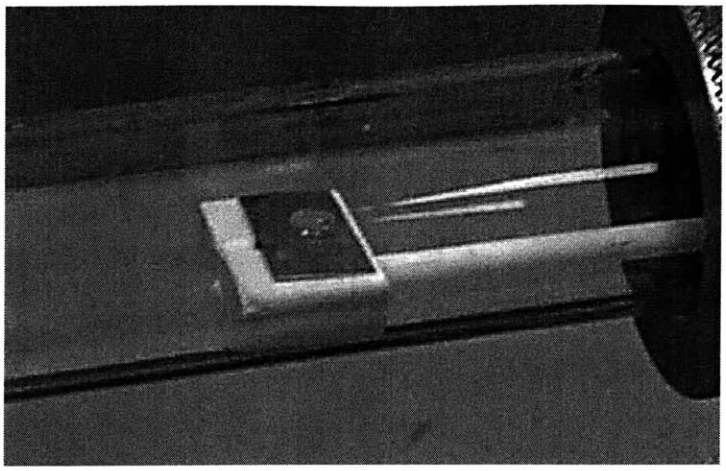

Figure 4-3: Sample holder with platinum foil and BSO sample.

(S Deman cloth, Struers). A pressure of 30 N and rotation rate of 50-100 rpm were used for all samples. Surface variations were measured with a profilometor. Finally, the sheet was cleaned with DI water and heated to a 1000 °C for 30 minutes prior to the experiment. A micrograph of a polished sample is shown in Figure 4-13(c).

The substrate and sample were inserted into the furnace and aligned with the horizontal using digital images. The tube was purged for 10 minutes with gas (0.1% oxygen, balance argon), and the sample was then heated to the melting point and images of the drop were taken using either an analog CCD camera (Panasonic VW-BD404) or a digital camera (DC290, Sony). Temperature was monitored using a thermocouple that was inserted into the ceramic support rod for the sample holder.

4.1.3 Analysis

Captured drop images were enhanced using image processing techniques in order to obtain a sharp contrast between the background and the drop such that the edge detection method could recognize the boundary. A variety of image processing techniques were investigated as some images required more processing than others depending on the camera and lighting conditions. Images were first converted to gray scale mode from RGB. The best results were obtained by applying an 'unsharp' filter, a 'hybrid median' filter, and adjusting the gray levels. All processed images were compared with the unprocessed image to ensure that the drop shape and dimension had not been altered.

Initially, edge detection was achieved using either a 'canny' or 'zerocross' method in Matlab® (Mathworks, Inc.). Edge images were cleaned up in Photoshop® (Adobe) to contain only the drop outline, and edge coordinates were extracted (Matlab®). An alternative edge detection scheme, which gave superior drop edges, used the contour filter in Photoshop after the hybrid median step to yield the drop edge from which coordinates could be extracted (Matlab). The contour filter was used with images from sample 4. Figure 4-4 shows (a) the initial image, (b) the processed image, and (c) the extracted edge of the drop.

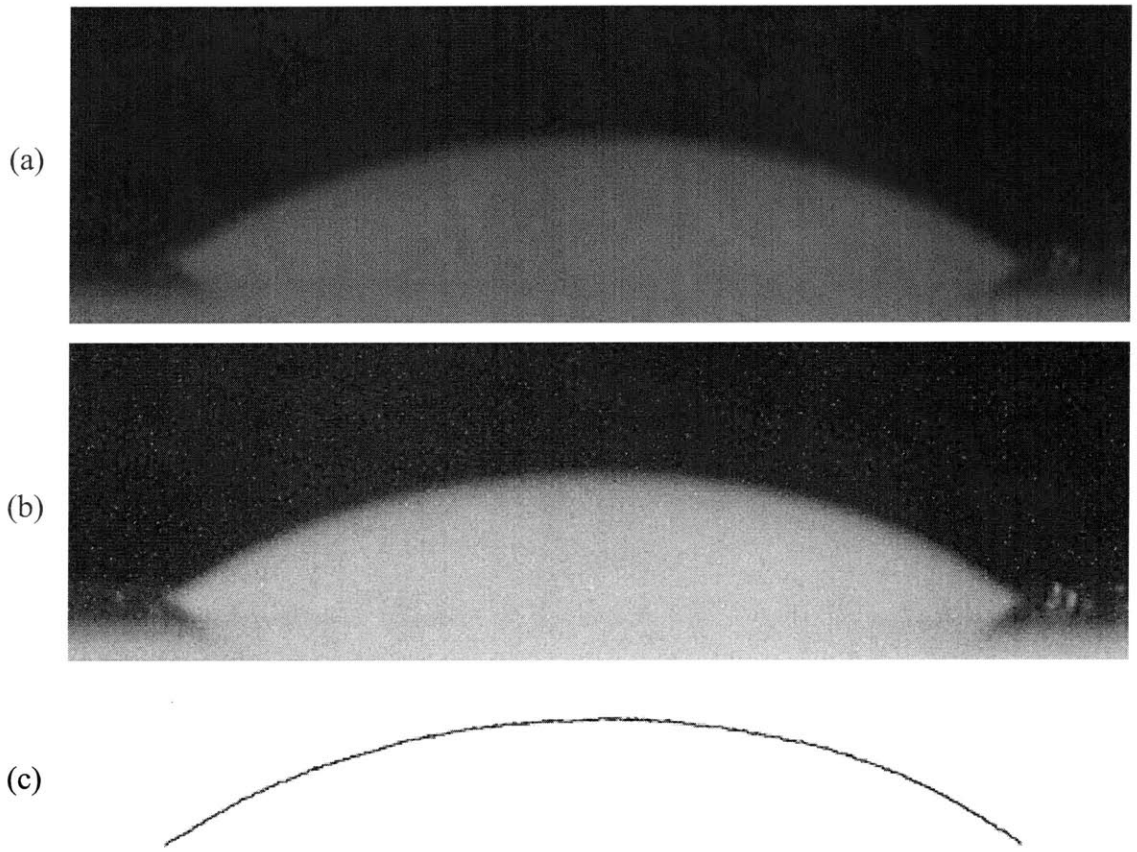

Figure 4-4: Image processing procedure (a) unprocessed image (b) enhanced image (c) edge profile.

Generally, integration of the Laplace Equation is difficult for all cases except when one of the principal radii of curvature is zero (cylindrical meniscus). However, numerical schemes do exist for the integration of axisymmetric drops. Referring to Figure 4-5, the principal radius of curvature is related to the arclength by Equation 4-4:

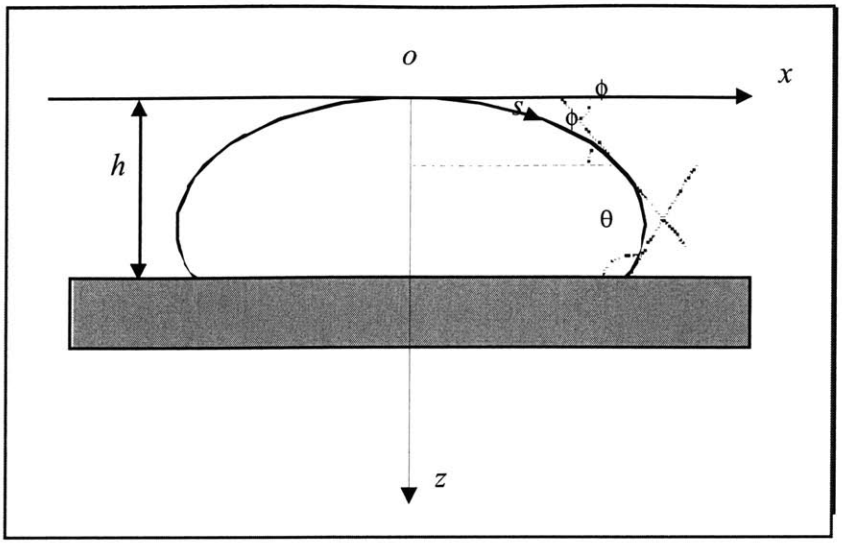

Figure 4-5: Sessile drop geometrical parameters.

Equation 4-4 $$\frac{1}{R_1} = \frac{d\phi}{ds}$$

The secondary radius of curvature is given by:

Equation 4-5 $$\frac{1}{R_2} = \frac{\sin(\phi)}{x}$$

At the droplet apex, the two principal radii of curvature are equal (defined as R_o). Combining Equation 4-4 and Equation 4-5 yields:

Equation 4-6 $$\frac{d\phi}{ds} = \frac{2}{R_0} + cz - \frac{\sin\phi}{x}$$ where

Equation 4-7 $$c = \frac{(\Delta\rho)g}{\lambda}$$ is known as the capillary constant

Equation 4-6 and the geometrical relations below form a set of first order differential equations that can be numerically integrated.

Equation 4-8 $$\frac{dx}{ds} = \cos\phi$$ and

Equation 4-9 $$\frac{dz}{ds} = \sin\phi$$

Surface tension values were determined from the drop shapes using numerical optimization code written for Fortran. A Laplacian curve was fitted to the data using four parameters: the x- and y- coordinates of the apex of the drop, the radius of curvature at the apex, and the capillary constant (c). The Laplacian curves were generated by numerically integrating the differential equations using a fourth order Runga-Kutta scheme. The best-fit parameters were obtained by minimizing the deviation between the Laplacian curve that was computed using the current estimate for the parameters and the experimentally measured drop shape. The optimization was performed using a BFGS (Broyden-Fletcher-Goldfarb-Shanno) algorithm, as coded in DOT® (VMA Engineering). Output from the code included the computed profile, the optimized parameters, the root-mean-square (RMS) deviation, and the angle at all of the points of the profile. Figure 4-6 shows the computational curve superimposed on the experimental curve for the image from Figure 4-4. The surface tension value was extracted from the optimized capillary constant.

Contact angles were directly measured using two different manual approaches. The first method found contact angles by drawing tangents at the contact point and measuring the angle between the tangent and the substrate on printed copies of the drop images. The second method used the 'measure tool' in Photoshop® to obtain values for the contact angle by directly measuring them on the computer monitor.

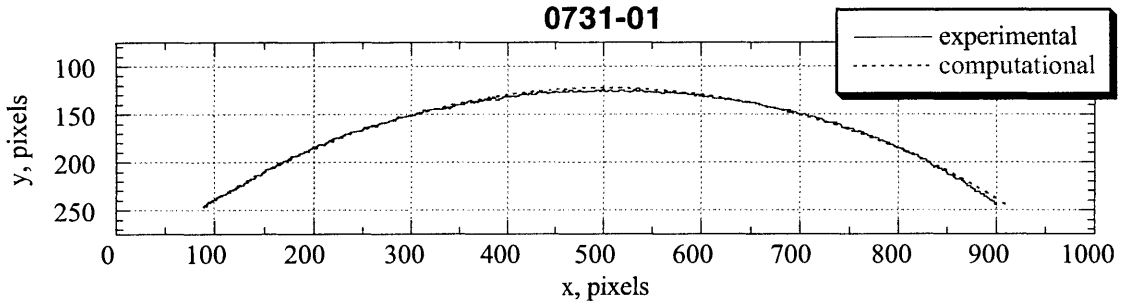

Figure 4-6: Computational curve fit of drop shape.

4.1.4 Results and Discussion

The contact angles that were both manually measured and computed for four experiments are shown in Figure 4-7 through Figure 4-9. Data was found to have a large variance between different samples as well as a temperature dependence. Images from the

third substrate were not able to be measured accurately enough due to poor contrast between the drop and background, and they were therefore not analyzed. For the first experiment (Figure 4-7), the sample became liquid at a thermocouple reading of 920 °C. Temperature was increased in 20 degree increments to 1000 °C. It was then lowered to 900 °C by decreasing in 20 °C decrements. Images from the second substrate (Figure 4-8) were analyzed several times with different types of image processing techniques to ascertain the effect on the contact angle measurement. The drop in the second set (numbered as 0718) followed a similar procedure, but in addition it had been melted and subsequently resolidified in a procedure to test camera equipment. An image of the solidified drop before it was remelted for the 0718 experiment was acquired and analyzed. The image was analyzed twice, and the data are labeled 0718-pm and 0718-pm-2 in Figure 4-8. All the other images of that experiment were obtained at 930 °C. It was noted that the contact angles for the second drop were lower than in previous tests.

The last experiment (Figure 4-9) analyzed the effects of temperature and the thermal history of the drop (specifically, whether it was being melted for the first or second time). In order to remove influences from pre-processing, a drop was melted, solidified, and remelted during one experiment. Figure 4-10 shows the drop diameter with relation to temperature. The drop first melted at a thermocouple reading of 750 °C. The diameter varied up 18% from the initial value. The data at the minimum in temperature corresponds to the last measurement before the drop solidified, and the subsequent data point is for the first value at which it became liquid again. The data in Figure 4-10 clearly show that the diameter is larger the second and third time a drop becomes molten as compared to the initial diameter of the drop.

This experiment also revealed that the drop was being pinned by non uniformities in the substrate. For all other experiments the images were acquired without additional illumination because the molten drop made a clear image against the dark background. At the lower temperatures, the drop was not as distinct from the background. When back illumination was added from outside of the quartz tube, it could be seen that the edge of the drop was not smooth but dimpled. Figure 4-11 shows a back illuminated drop image as well as an image of a solidified drop for comparison. The discontinuous change in the diameter can also be explained by the grain boundary pinning. The drop cannot assume its equilibrium shape and the diameter readjusts stepwise as the force on the liquid due to pinning is overcome.

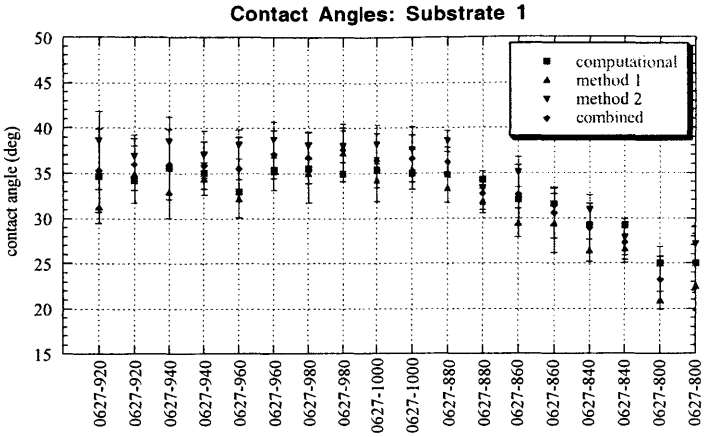

Figure 4-7: Substrate #1 contact angles. Each drop image (label format: date-temp) has 2 data points representing the left and right contact angles.

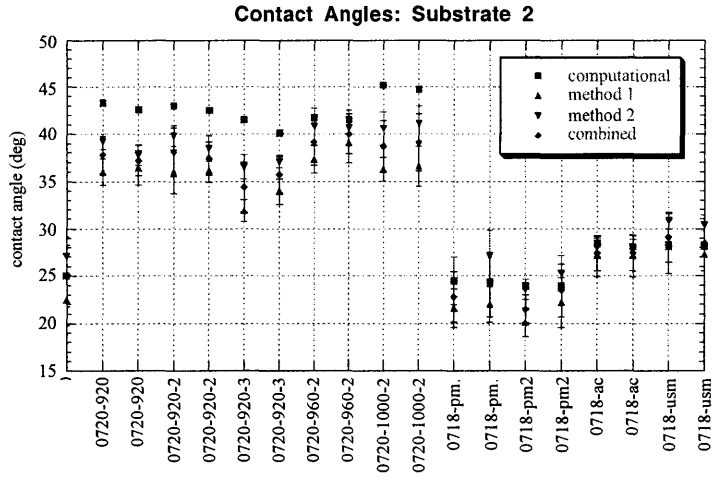

Figure 4-8: Substrate #2 contact angles. Each drop image (label format: date-temp-meas #) has 2 data points representing the left and right contact angles.

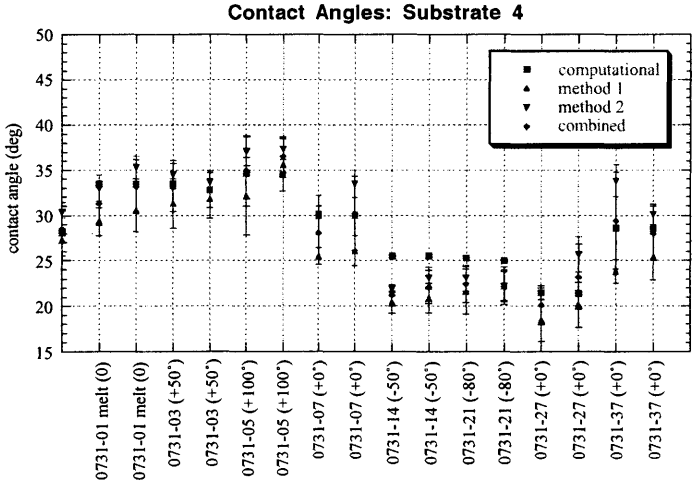

Figure 4-9: Substrate #4 contact angles. Each drop image (label format: date-meas # (ΔT)) has 2 data points representing the left and right contact angles.

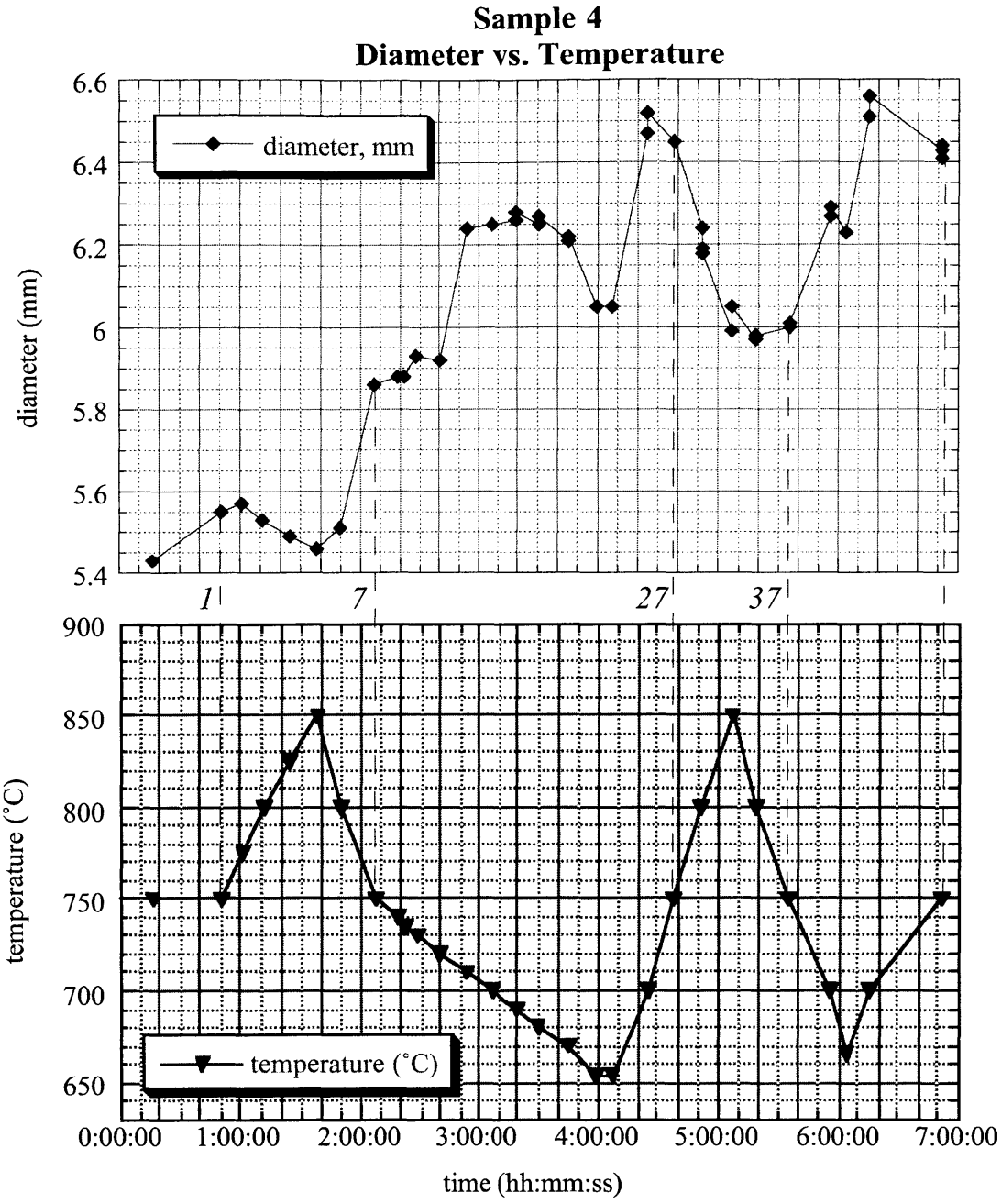

Figure 4-10: Diameter of sessile drop as a function of temperature. Shaded areas correspond to solid drops.

The initial sessile drop experiment (substrate 1) was performed on an unpolished substrate. The contact angle was not markedly different from the other samples, and no distortion of the geometric drop shape or of the drop edge was observed due to the scratches as can be seen in Figure 4-12. It is important to note that the scratches were of a particular

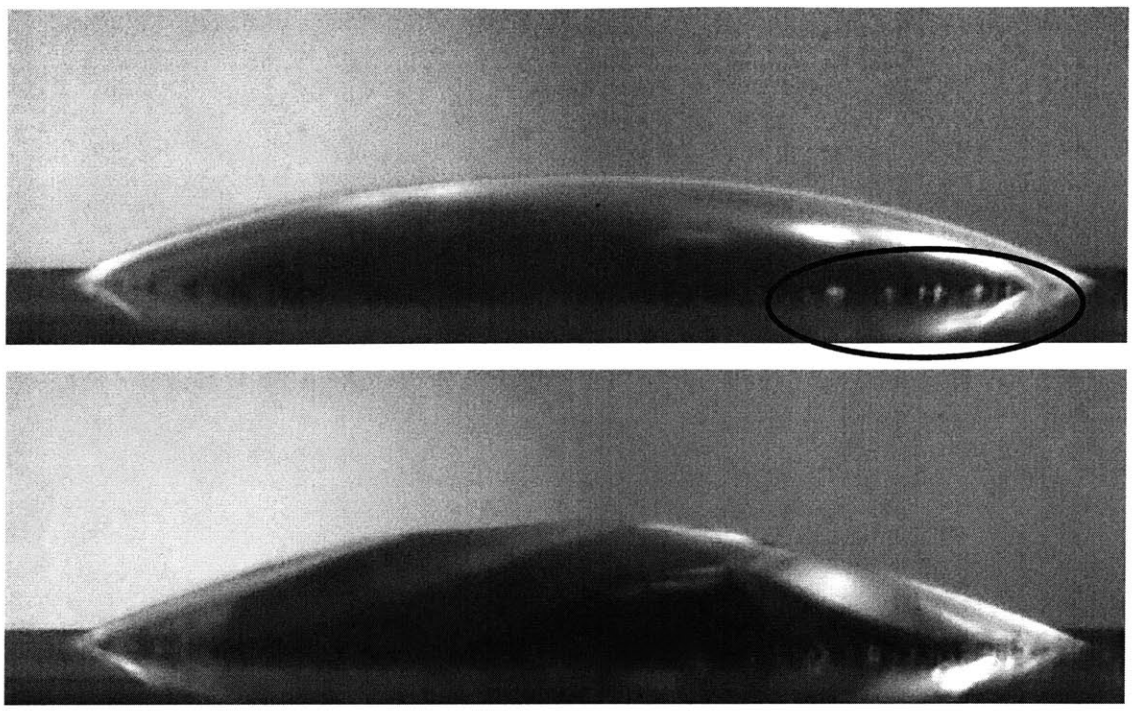

Figure 4-11: Back illuminated sessile drop showing pinning of the melt/substrate interface. (a) molten drop (b) solidified drop.

amplitude (+/- 0.5 μm) and that, in general, the roughness of the substrate can have an effect[190,191,192] on wetting behavior. Profilometry of unpolished and polished samples revealed that although polishing removes scratches, there are grains that are more resilient to polishing than other grains. This effect is attributed to an orientation dependent hardness and leads to elevation differences between grains as shown in Figure 4-13.

During the experiment, evaporation and condensation of the liquid occurred and covered the surrounding substrate in small drops as observed with optical microscopy. The condensation is also seen in the macroscopic images in Figure 4-12. The final position and shape of the drop before solidification could be identified because upon solidification the drop contracted and left a zone around the drop that was devoid of condensation. Micrographs of the condensation and denunded area corroborate that the pinning of the drop occurs at grain boundaries as can be seen in Figure 4-14. In both polished and unpolished samples, the melt follows the grain boundaries of the substrate.

The bulk of the BSO drop could be removed from the platinum with little or no effort indicating only weak adhesive forces. In some cases, the vibration due to handling the

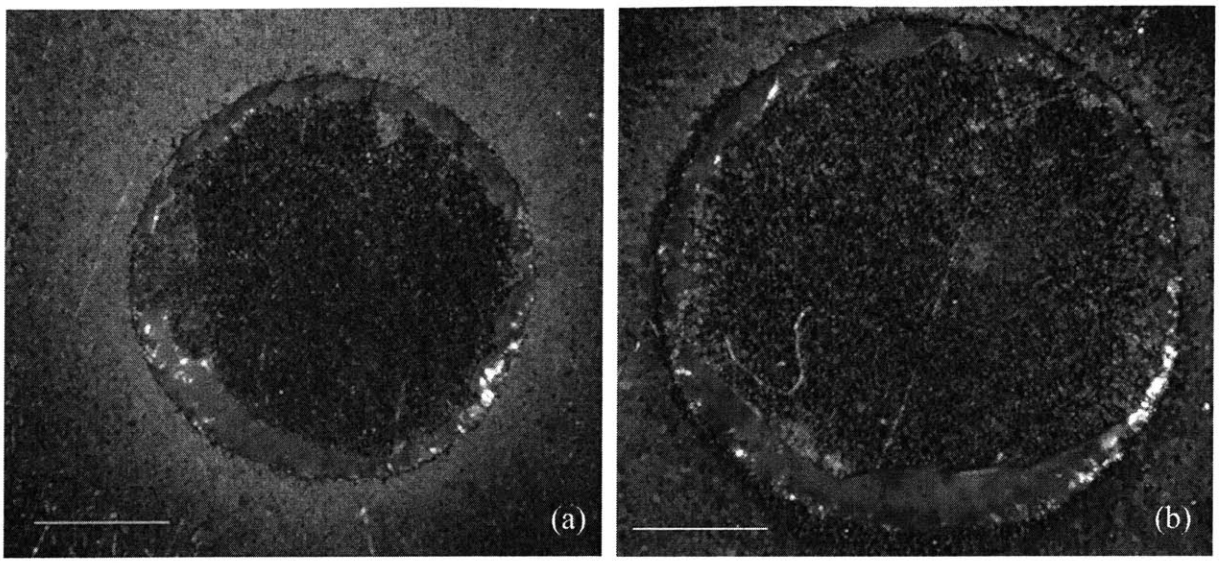

Figure 4-12: Scale bar for both images is 2 mm. Geometry of solidified drop on both (a) unpolished and (b) polished substrate is non circular and irregular. Light colored discoloration of substrate is condensation from drop.

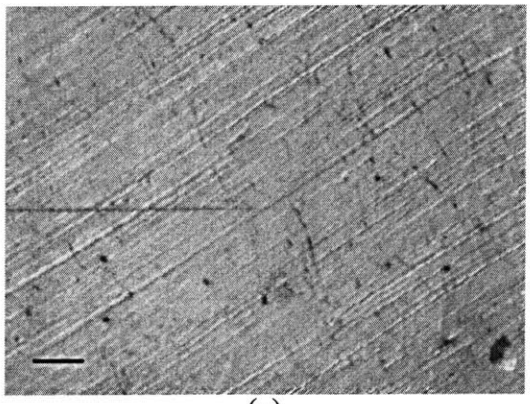

(a)

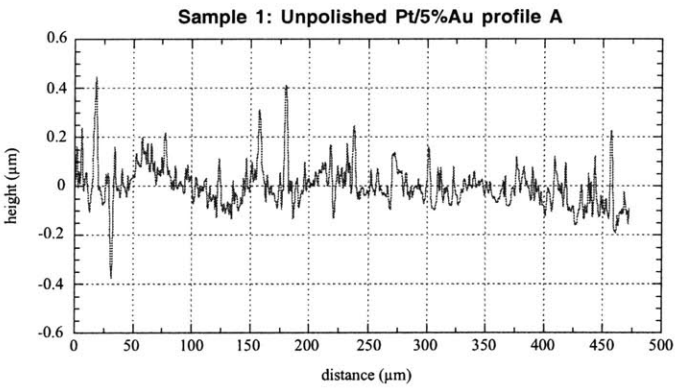

(b)

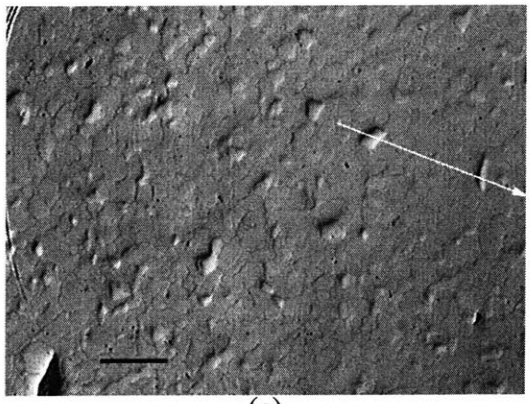

(c)

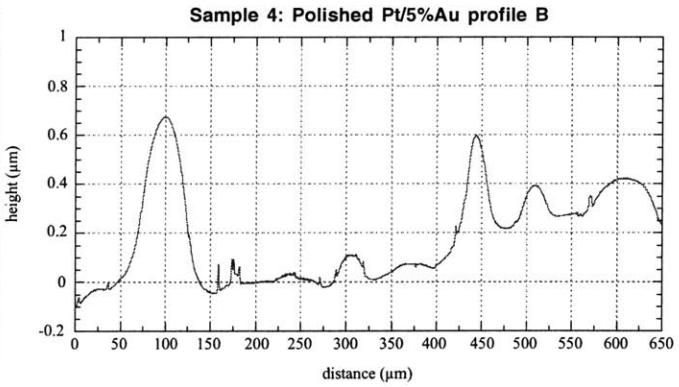

(d)

Figure 4-13: (a) micrograph of 'as delivered', unpolished Pt/5%Au. Scale bar = 200 μm. (b) Profilometry of unpolished sample taken perpendicular to the scratches. (c) Micrograph of polished sample. Scale bar represents 200 μm. (d) Profilometry of polished sample as indicated by arrow in (c).

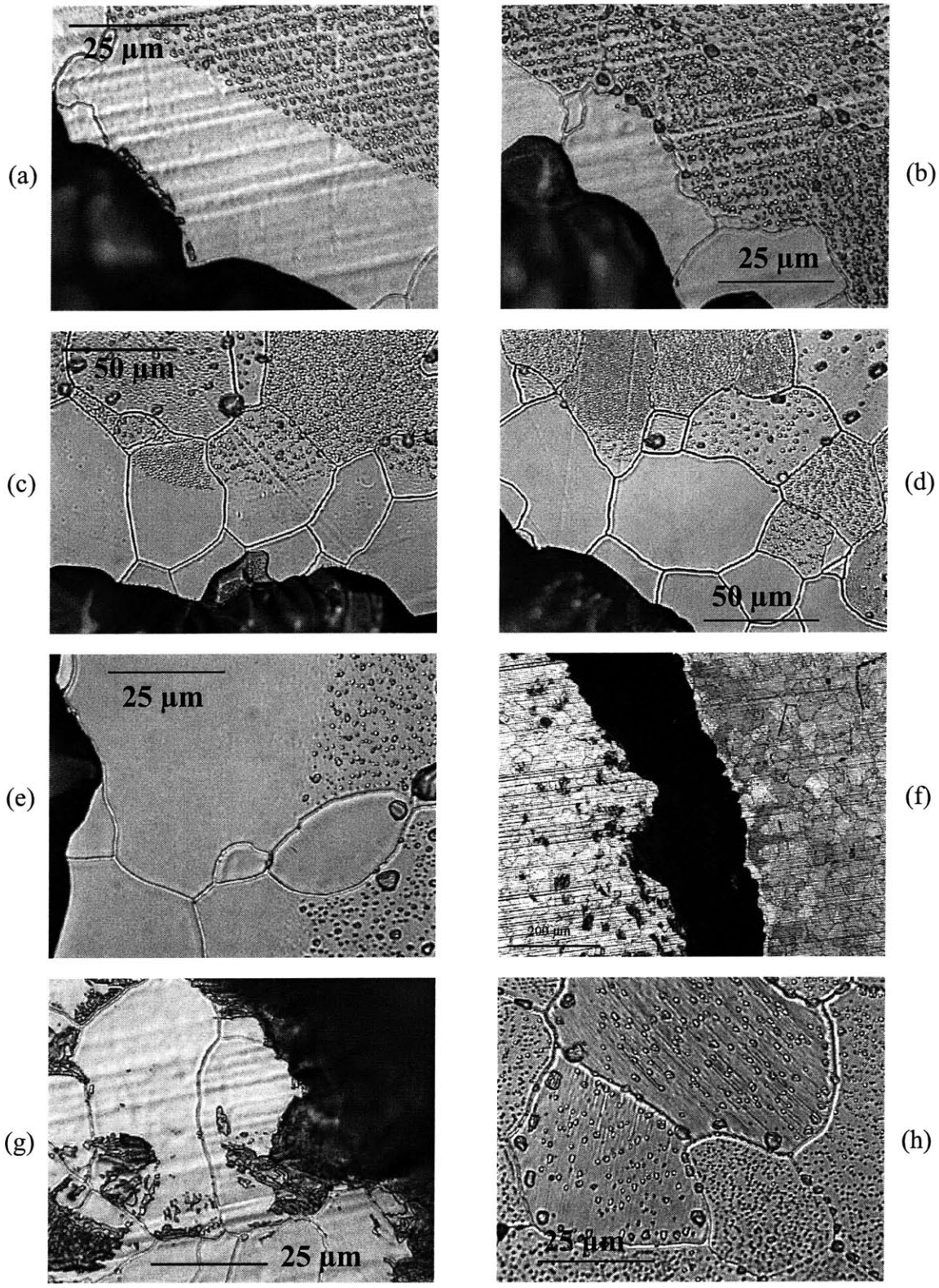

Figure 4-14: Micrographs of residual BSO and condensation. Unpolished substrate: (a) no pinning and (b) GB pinning of melt. Polished substrate: (c) no GB pinning and (d) GB pinning of melt (e) avoidance of grain by melt (f) remnant BSO ring (g) adhesion of BSO inside drop (h) grain dependent condensation.

substrate was sufficient to cause the drop to become loose. In all cases a residual ring of BSO remained attached to the substrate. SEM images (Figure 4-15) of the residual ring show that the inner edge adheres to the surface while the outer edge does not. The area in the center of the drop only contains small patches of residual BSO. This indicates that there is no strong adhesion of solidified BSO to the platinum-gold substrate except in isolated areas.

Table 4-1 summarizes the contact angle data as well as the calculated surface tension values. All of the contact angle determination methods were self-consistent and were in

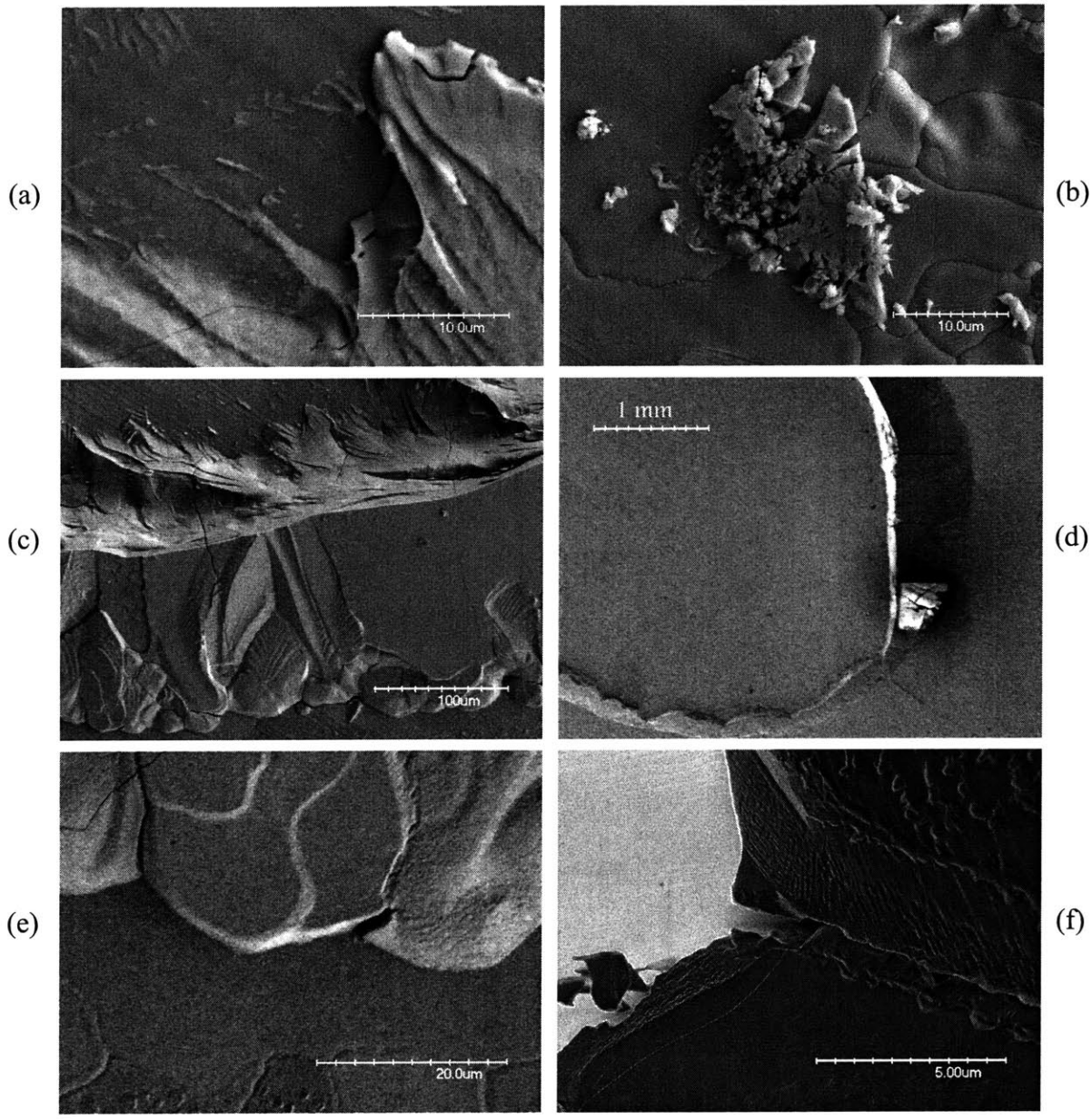

Figure 4-15: SEM images of residual BSO ring. (a) inside edge (b) remnant material inside ring (c) close-up (d) ring (e) outside edge (f) close-up of outside edge.

general agreement with the other methods. The computational results for the surface tension, however, have little consistency between data points. There are several factors that could contribute to the wide range of values. First, the pinning of the drop introduces a distortion in

image	subst rate	temp (°C)	drop side	computed cont. ang.	RMS (pixels)	method 1 cont. ang.	st. dev	method 2 cont ang.	st. dev	combined cont. ang.	st. dev	*srf. tens. (mJ/m2)*
0627-800	1	800	left	25.0	3.40	20.9	0.99	25.0	1.79	23.2	2.57	***361***
			right	25.0		22.5	2.73	27.1	2.05	25.0	3.27	
0627-840	1	840	left	29.2	1.85	26.4	1.19	30.9	1.64	28.9	2.73	***383***
			right	29.2		26.6	1.60	27.9	2.02	27.3	1.90	
0627-860	1	860	left	32.0	1.28	29.5	1.60	35.1	1.66	32.6	3.28	***302***
			right	31.6		29.4	3.27	31.3	2.12	30.5	2.77	
0627-880	1	880	left	34.8	1.99	33.3	1.58	38.5	1.16	36.2	1.59	***260***
			right	34.3		31.9	1.37	33.3	1.88	32.7	1.78	
0627-920	1	920	left	34.6	1.67	31.3	1.89	38.6	3.19	35.3	4.59	***457***
			right	34.2		34.9	3.18	36.9	2.34	36.0	2.85	
0627-940	1	940	left	35.6	1.54	32.9	2.85	38.5	2.70	36.0	3.93	***429***
			right	35.1		34.4	1.79	37.1	2.59	35.9	2.62	
0627-960	1	960	left	32.9	1.51	32.2	2.10	38.2	1.58	35.5	3.53	***422***
			right	35.4		35.2	2.07	38.7	1.99	37.1	2.65	
0627-980	1	980	left	35.5	1.56	35.0	3.25	38.1	1.49	36.7	2.83	***503***
			right	34.9		37.3	3.21	38.0	1.76	37.6	2.45	
0627-1000	1	1000	left	35.4	1.65	34.3	2.43	38.2	2.14	36.4	2.98	***537***
			right	35.0		35.4	2.20	37.6	2.51	36.6	2.58	
0720-920	2	920	left	43.3	3.18	36.0	1.41	39.2	0.82	37.8	1.95	***109***
			right	42.6		36.4	1.85	37.8	1.09	37.2	1.61	
0720-920-2	2	920	left	43.0	2.81	36.0	2.33	39.8	1.15	38.1	2.57	***110***
			right	42.5		36.1	1.25	38.5	1.35	37.4	1.75	
0720-920-3	2	920	left	41.5	4.24	31.9	1.13	36.5	1.29	34.4	2.62	***137***
			right	40.1		33.9	1.36	37.1	0.64	35.7	1.92	
0720-960-2	2	960	left	41.7	3.44	37.3	1.44	40.8	1.96	39.2	2.46	***156***
			right	41.5		39.1	2.17	40.7	1.86	40.0	2.11	
0720-1000	2	1000	left	45.2	4.51	36.3	1.28	40.6	1.76	38.7	2.71	***106***
			right	44.8		36.6	2.13	41.1	1.85	39.1	2.99	
0718-pm.	2	800	left	24.5	4.04	21.6	2.06	24.5	2.51	22.8	2.65	***384***
			right	24.4		22.0	1.88	27.1	2.74	24.1	3.41	
0718-pm2	2	800	left	23.9	2.97	20.1	1.49	23.6	1.06	21.5	1.47	***366***
			right	23.9		22.2	2.66	25.3	1.85	23.5	2.78	
0718-ac	2	930	left	28.4	2.94	27.1	2.17	28.0	0.98	27.4	1.84	***370***
			right	28.1		27.1	2.20	27.9	0.97	27.4	1.85	
0718-usm	2	930	left	28.3	2.35	28.1	2.82	30.8	0.82	29.1	2.63	***345***
			right	28.1		27.3	3.22	30.4	0.65	28.5	2.95	
0731-01	4	inital melt (temp in Δ)	left	33.5	3.50	29.3	1.53	33.0	1.44	31.3	2.35	***725***
			right	33.4		30.6	2.43	35.3	1.26	33.2	3.00	
0731-03	4	50	left	33.5	3.71	31.3	2.71	34.5	1.56	33.1	2.66	***726***
			right	32.8		31.8	2.12	33.7	1.22	32.8	1.90	
0731-05	4	100	left	34.6	3.43	32.1	4.25	37.1	1.59	34.9	3.93	***737***
			right	34.5		35.6	2.92	37.3	1.11	36.5	2.23	
0731-07	4	0	left	29.9	3.64	25.5	0.93	30.1	2.07	28.1	2.87	***802***
			right	30.0		26.1	1.64	33.5	1.53	30.2	4.07	
0731-14	4	-50	left	25.5	3.89	20.4	1.19	21.9	0.42	21.2	1.15	***930***
			right	25.5		20.9	1.64	23.1	1.22	22.1	1.80	
0731-21	4	-80	left	25.3	7.00	21.6	2.45	23.1	1.44	22.4	2.02	***804***
			right	25.0		22.2	2.07	22.2	1.59	22.2	1.76	
0731-27	4	0	left	21.5	4.78	18.4	2.32	21.4	0.63	20.1	2.16	***1298***
			right	21.4		20.1	2.46	25.7	1.92	23.2	3.58	
0731-37	4	0	left	28.6	3.20	23.8	1.31	33.8	1.73	29.4	5.32	***875***
			right	28.5		25.4	2.50	30.1	1.15	28.0	3.00	

Table 4-1: Contact angle data and computed surface tension values.

the profile of the drop at the end where it contacts the surface. Lahooti et al.[189] analyzed the effect of the accuracy of individual data points on the resultant surface tension value and they found that an inaccurate data point had a larger effect if it was located further away from the apex. The distortion due to the pinning would affect a number of the data points near the contact line and would therefore affect the calculated surface tension value. Secondly, the image analysis procedure and edge detection scheme could also affect the results by producing a contour that had points that were not on the actual contour. Lastly, because of the low contact angle of BSO with platinum/gold, only a small portion of the Laplacian curve is available for curve fitting. For this reason, the sessile drop method is not usually used when the contact angle is less than 90 degrees[193].

4.1.5 Summary and Conclusions

Contact angle measurements made manually by two different methods showed good reproducibility within each method and exhibited general agreement between the two methods. Contact angles were also obtained from numerical curve fitting of the experimental data. Computational results were within error limits (one standard deviation) for almost all images. No significant difference between the contact angle of BSO on Pt-5%Au found in this work and the contact angle of BSO on pure platinum[72] found in previous work was observed. Computed surface tension values varied drastically between experiments and within a given data set. It was suggested[193] that computational modeling using of sessile drop is inappropriate for contact angles significantly less than 90°. This is due to the fact that too little of the Laplacian curve is available for curve fitting and related errors become too large.

Uniform scratches, with an amplitude approximately +/- 0.5 μm, were found on the 'as delivered' substrate but did not affect the geometry of the drop. These scratches were on the same order as grain height variation on polished samples. Drop diameter and contact angles showed a temperature dependence and a hysteresis effect. Repeated melted and solidification of a drop on the same substrate resulted in a variation in drop diameter and contact angle. Behavior of the melt contact line was seen to be dominated by pinning at the grain boundary as shown by micrographs of the substrate and in situ images. Assumptions in the sessile drop technique that could not be satisfied in the experiments include

(a) that the surface is homogenous and smooth

(b) that no other forces besides surface tension and gravity are present.

Therefore it is concluded that the sessile drop technique is inappropriate for studying the wetting behavior of BSO melts on platinum and platinum-5%gold substrates. Although contact angle data and surface tension values could not reliably determined in this work, the discovery of grain boundary pinning is important because it helped identify the deficiencies associated with this method for the BSO-platinum and BSO-platinum/5%gold systems. Future wetting work on any system with a polished metal surfaces will need to analyze the effect of grain boundaries to ensure that assumptions made in modeling a sessile drop are met.

4.2 Reduced Gravity Wetting Experiments: KC-135

Witt et al.[194] reported that in microgravity some systems exhibit a different wetting behavior than on the ground. Early proposed designs for ampoule configurations were aimed at minimizing contact between the melt and the confinement material in an effort to establish a free solid-liquid interface. Such designs would have allowed for interface demarcation using current pulses. However, these designs depended on certain wetting behavior between the melt and the confinement material. In order to investigate the effect of gravity on the wetting behavior of BSO on platinum and platinum/5%gold, reduced gravity wetting experiments were conducted in the KC-135. The scope of the KC-135 experiments was a phenomenological comparison of the melting and re-solidification behavior of BSO in a reduced gravity (10^{-2} g) environment versus on in a terrestrial (one g) environment.

The reduced gravity environment is achieved by flying the KC-135 airplane along a parabolic trajectory. At the top of the parabola, approximately 20 seconds of reduced gravity (on the order of 10^{-2} g) are experienced by all objects and persons inside the aircraft. Each flight typically consists of forty such parabolas. Figure 4-16 shows a schematic representation of the flight path.

4.2.1 Experimental Setup and Ampoule Design

Design of experiments for KC-135 was largely constrained by the geometry of the furnace and the relatively short duration of the low gravity environment (~20 sec.). In order to

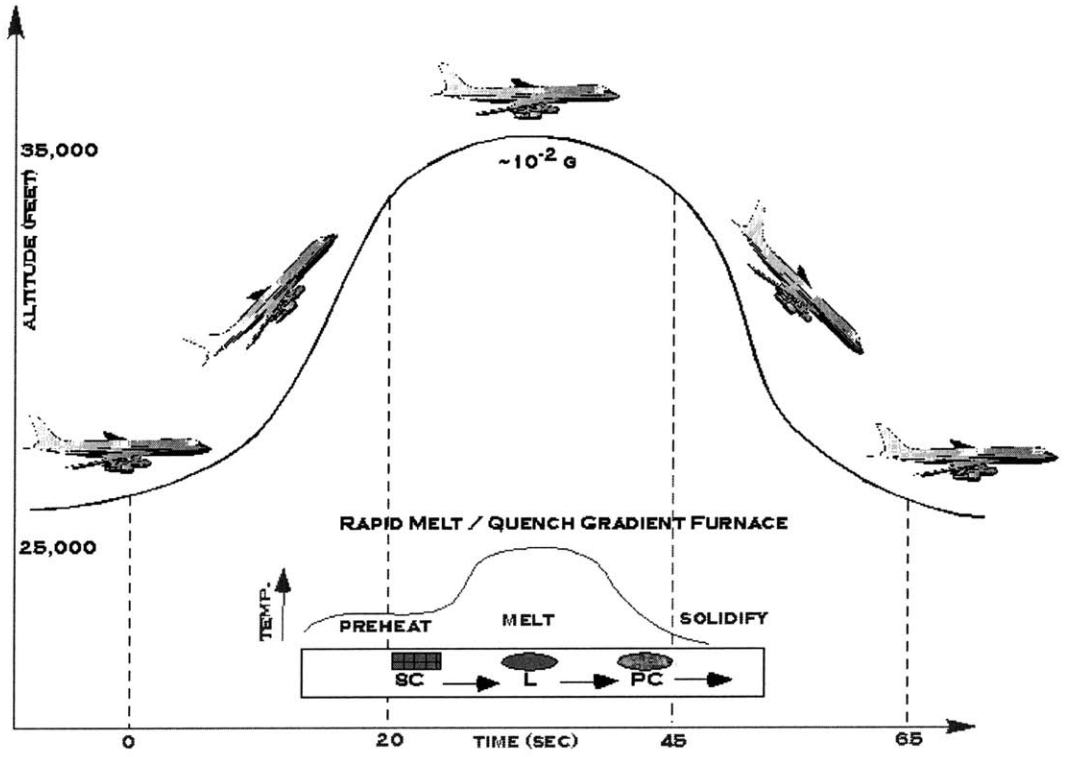

Figure 4-16: Parabolic flight path of KC-135.

accomplish melting and solidifying of a sample during one low gravity period, the existing Rapid Melt/Rapid Quench (RMRQ) NASA furnace was used (shown in Figure 4-17). The RMRQ furnace was specifically designed for use on the KC-135 and consisted of a three zone furnace: a preheat zone, a rapid melt zone, and a quench zone. Samples were stationary while the furnace moved upwards over the ampoule. A furnace profile is shown in Figure 4-18(a). Temperature was measured by the stinger thermocouple (located at bottom of ampoule), except for profile labeled as being taken on the Pt/Au fin. Data from the flight was measured with the stinger thermocouple. Distance (in cm) is relative to the starting position of the furnace (ampoule is in preheat zone).

The KC-135 confinement geometry was based on one of the proposed designs for the space flight experiments. In-situ observation of the melt contact angle was not possible; it was therefore decided to support the sample by a number of fins so that the molten BSO would form angles at several points. Figure 4-19 shows the sample and confinement foil configuration. Each BSO sample was a cylinder 5 mm in diameter and 15 mm in length. Quartz ampoules were fabricated by Gene Nelson at the University of Alabama, Hunstville.

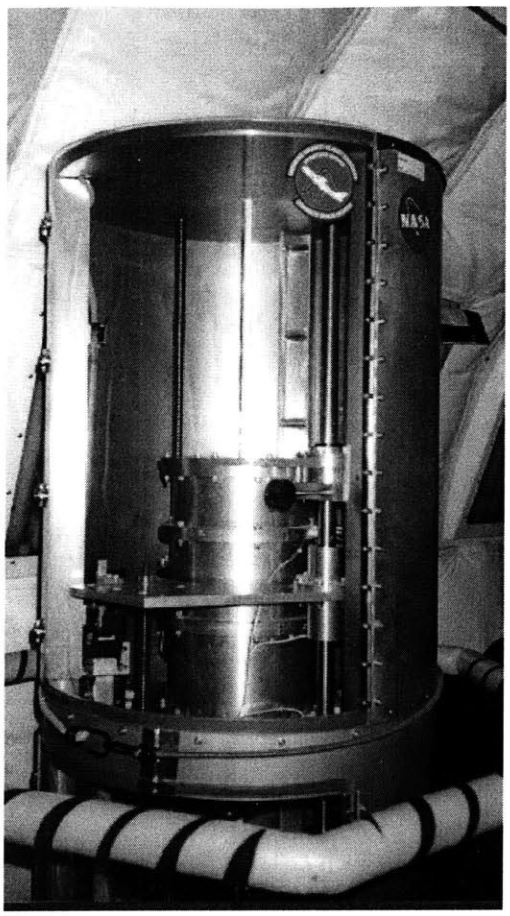

Figure 4-17: RMRQ furnace in the KC-135.

All Pt/Au pieces were sandblasted with 27 μm Al_2O_3, cleaned ultrasonically, and rinsed in methanol, and finally DI water. Ampoules were assembled as shown in Figure 4-20. Before sealing the ampoules, they were evacuated to $5x10^{-5}$ atm. and back filled to 0.3 atm. with the desired gas as per Table 4-1.

Ampoule	Atmosphere,
1-4	Ar
5-8	1% O_2
9-12	20% O_2
13	0.1% O_2
14	Ar (Pt foil)

Table 4-1: Atmospheres for the KC-135 samples. Balance gas is argon.

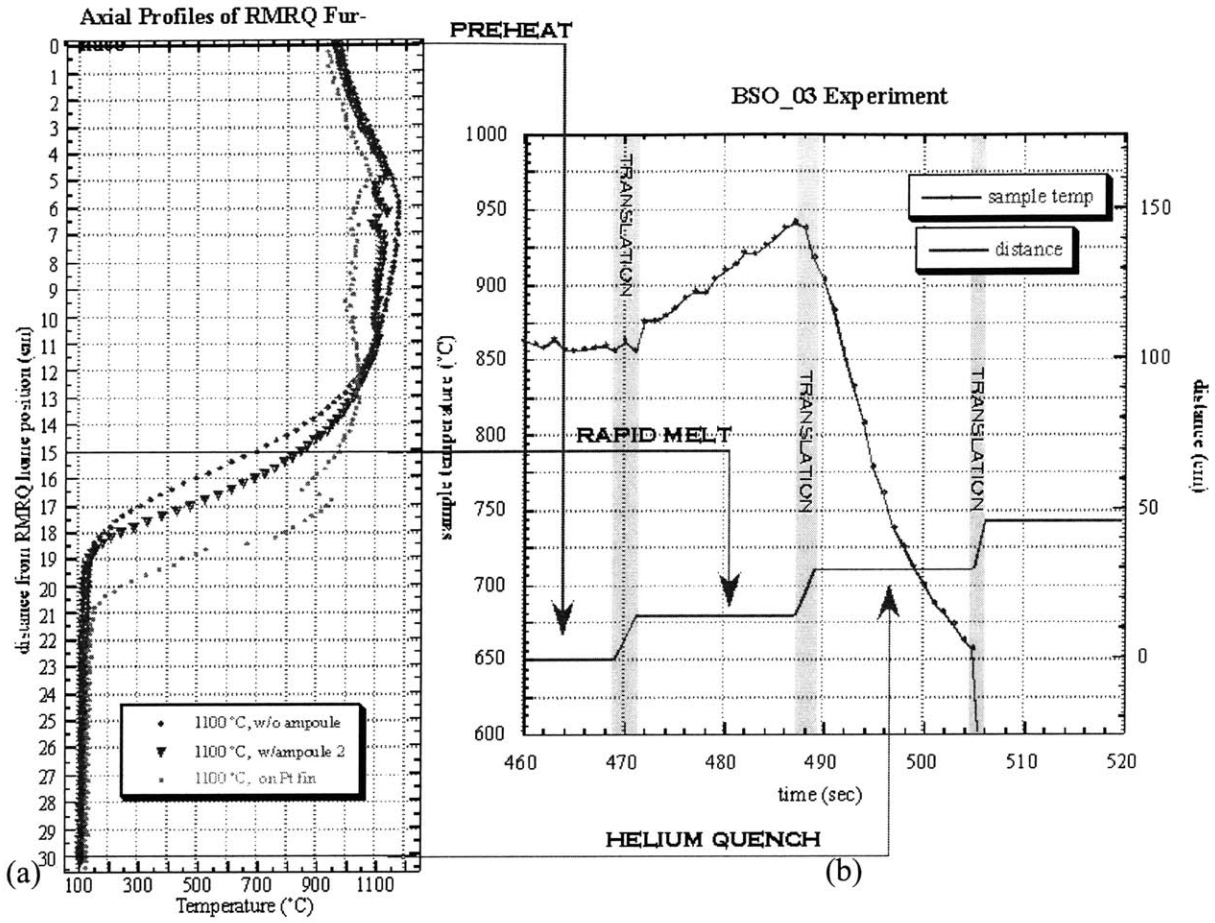

Figure 4-18: (a) Axial profile as measured by the stinger thermocouple except for profile labeled 'on Pt fin' (b) Experimental temperature and translation profile.

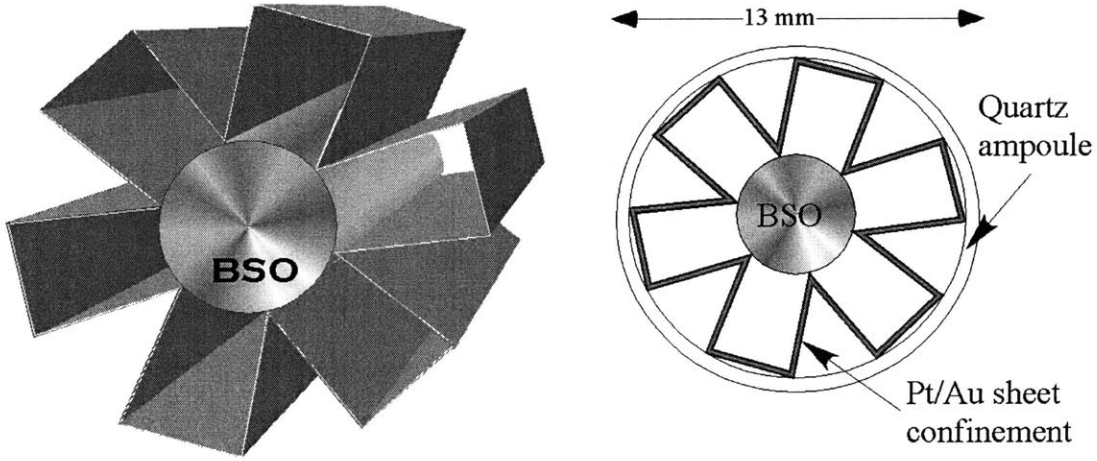

Figure 4-19: Sample and confinement material configuration.

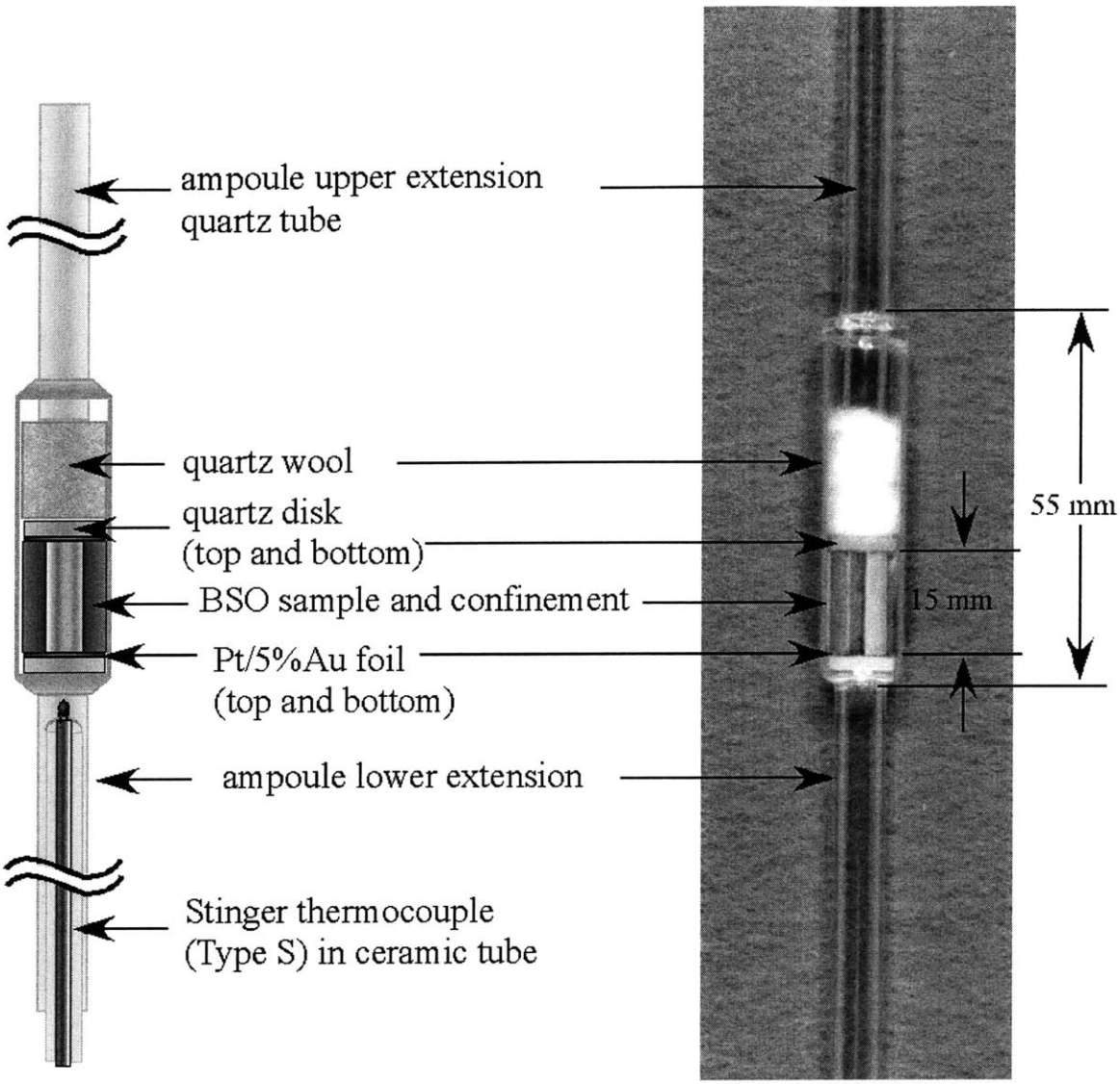

Figure 4-20: Schematic and picture of ampoule for KC-135 experiments.

4.2.2 Experimental Procedure

The first ampoule was loaded once the plane had taken off. The furnace was then ramped to the correct setpoints. Samples were heated to 850 °C in the preheat zone. As the plane entered the low gravity period of the chosen parabola, the ampoule was translated into the rapid melt zone for 15 seconds and quenched with a helium quench after rapid translation out of the heater. The temperature profile is shown in Figure 4-18(b). Ampoules could not be removed from the furnace until the plane was flying level, and this occurred every 8-10 parabolas for about 5 minutes. During this time, the processed ampoule was removed and a new ampoule was loaded.

4.2.3 Results and Conclusions

Samples that were processed successfully melted partially and solidified before the low gravity period ended. A number of samples were not quenched properly due to hardware deficiencies. Although no quantitative contact angle measurements can be made, there is no qualitative difference in the fundamental wetting behavior in low gravity as compared to terrestrial conditions. The acceleration environment for the sample is shown in Figure 4-22. The spike present 15 seconds into the low gravity period is due to the motion of the furnace from the hot zone to the quench zone. Due to residual acceleration, molten material flowed to one or the other end where it solidified. As an example, top and bottom views of sample #3 after processing are depicted in Figure 4-21. The bottom view (b) clearly shows how the melt solidified in contact with the Pt/Au. Most of the samples did not stay vertical in the confinement material. Thermal asymmetry in the furnace caused melting to occur on one side first, causing the sample to tilt slightly. Once contact was lost with the Pt fin, the conduction heat path was lost, and the sample did not have enough time to melt on that side as a consequence of the reduction in heat flux (see Figure 4-23). The need for thermal symmetry is therefore critical for processing in a partially confined manner and suggests the use of heat pipes in the furnace in order to achieve radial uniformity of the thermal environment. It is also clearly seen that there is no adhesion between the BSO and Pt as seen by the smooth surface of the BSO in Figure 4-23(b).

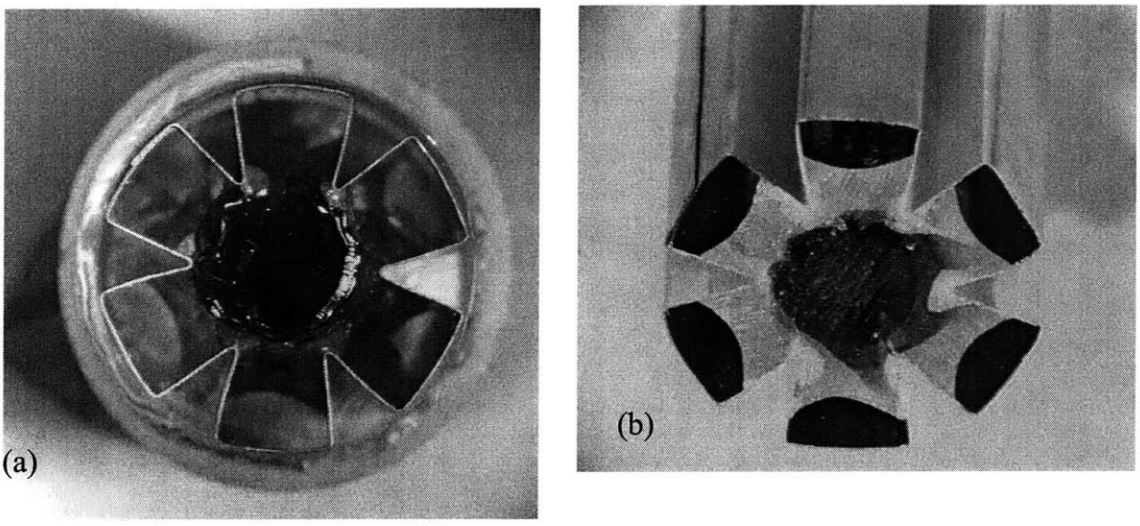

Figure 4-21: Processed KC-135 sample #3 (a) top view (b) bottom view.

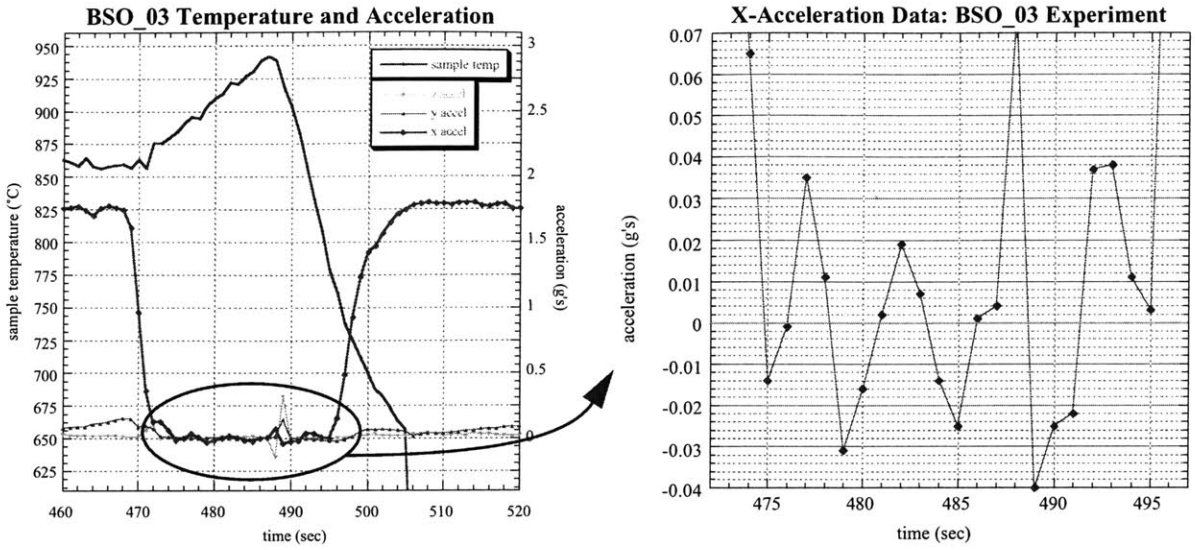

Figure 4-22: Acceleration data for sample #3 showing residual and vibrationally induced acceleration.

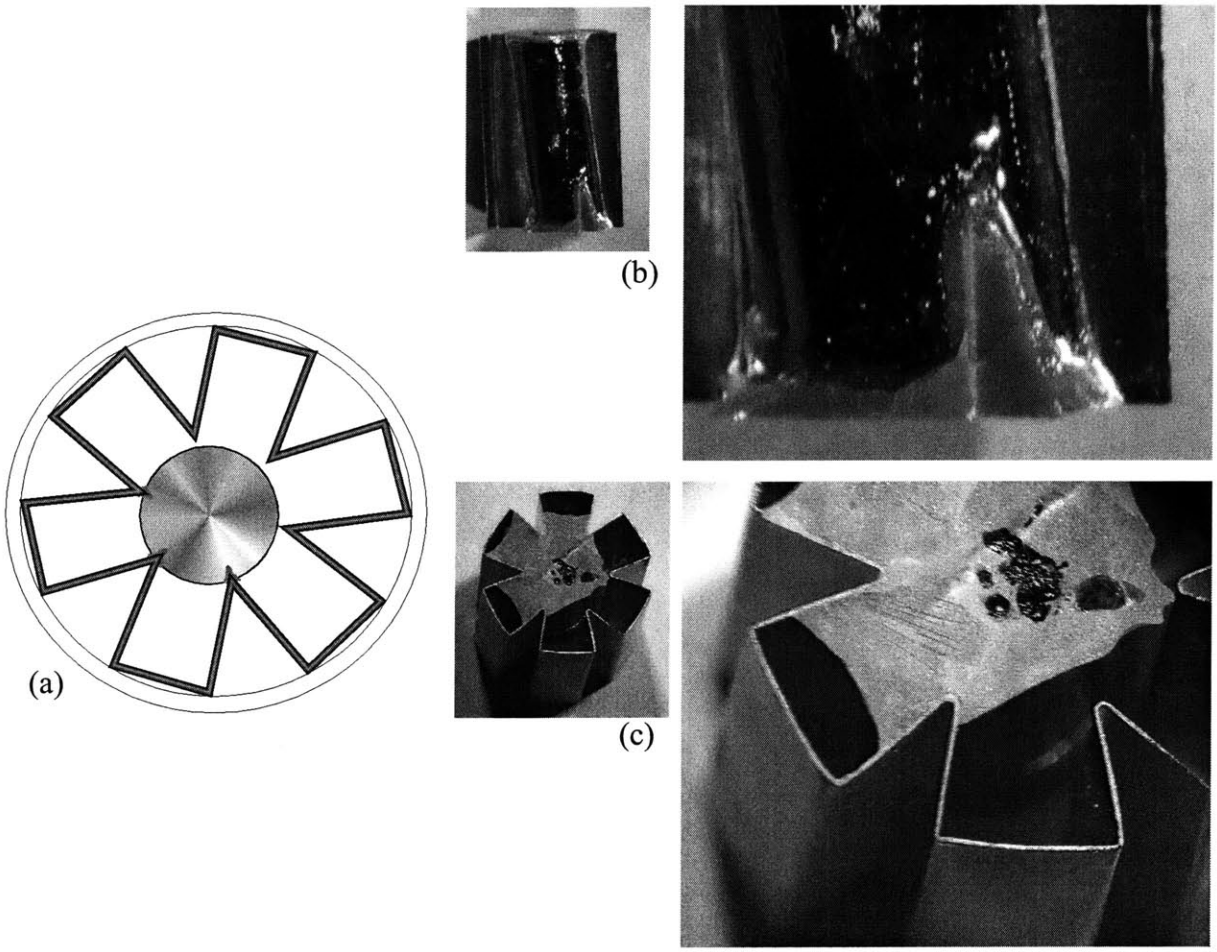

Figure 4-23: (a) schematic of how uneven melting leads to tilting of sample and loss of conduction heat transfer at some of the fin tips (b) side view of sample #5 and close-up showing no adhesion (c) bottom view of sample #5 and close-up.

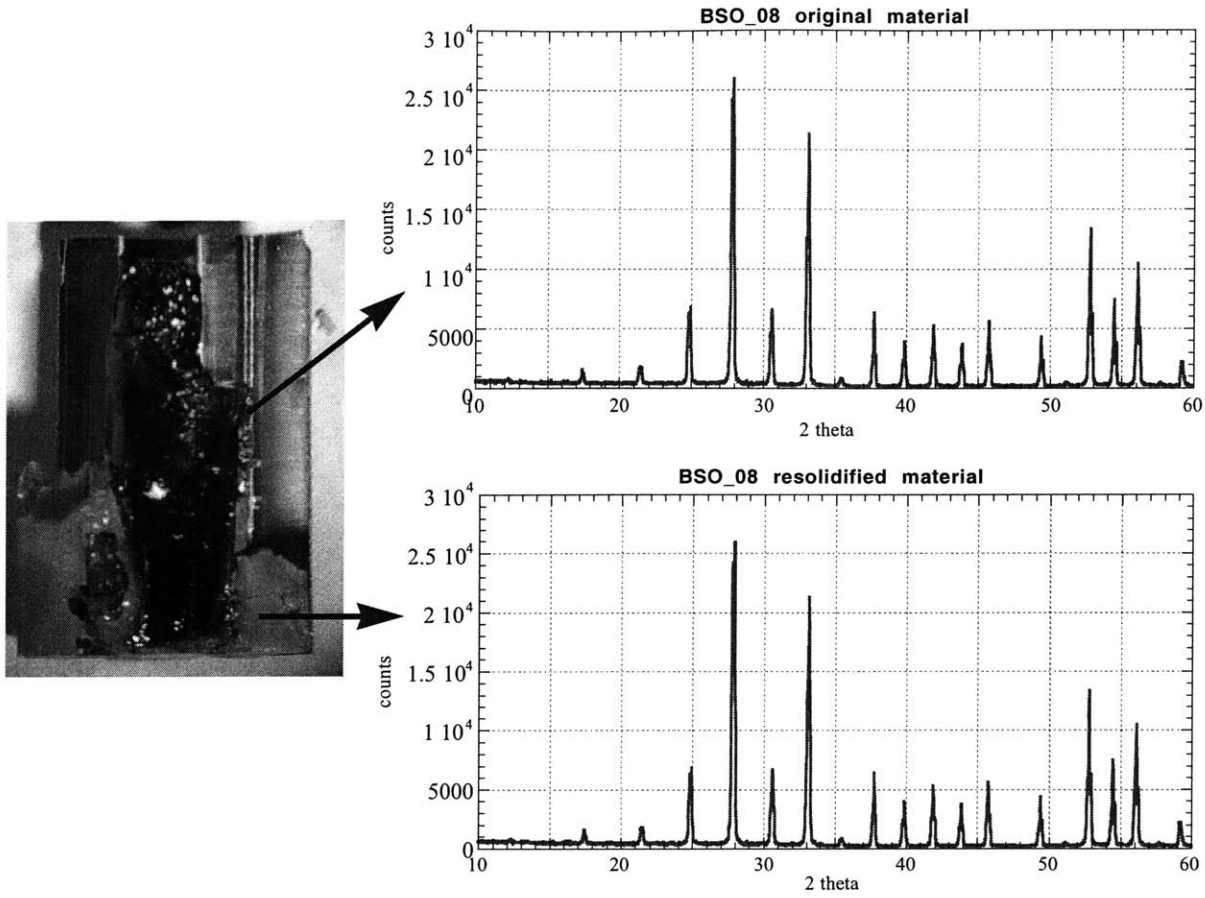

Figure 4-24: X-ray diffraction patterns for original and resolidified material showing both to be of the sillenite structure.

The unmelted BSO turned very dark due to the processing while the resolidified BSO had the characteristic light orange color. Analysis using powder x-ray diffraction showed both original material and resolidified material to have the sillenite structure, as can be seen in Figure 4-24. The change in absorption (*i.e.* color) is attributed to stress induced points defects that were generated as a result of the rapid quench.

4.3 Embrittlement of Platinum

Corrosion of the platinum is another serious concern related to the confinement material's interaction with BSO. Embrittlement was first observed in these studies while trying to grow samples for the KC-135 experiments. Crucible failure was observed when trying to grow Czochralski BSO in an atmosphere of 10^{-4} O_2 (balance argon). Embrittlement was also observed by Yu Zheng[72] in his second Bridgman growth experiments. The normally

ductile platinum foil was found to be extremely brittle when it was used to contain BSO in a sealed ampoule (see Figure 4-25). It is critical to solve the platinum embrittlement issue for the design of the microgravity ampoule since it is not possible to have a 'open' or 'flowing' environment on the space station.

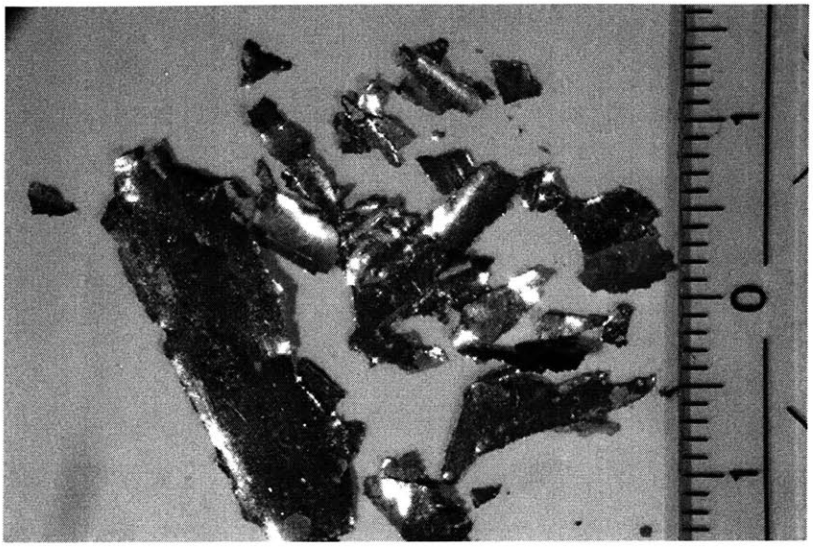

Figure 4-25: Embrittled platinum after processing BSO in a sealed environment.

4.3.1 Experimental work

Since this effect is rarely seen in 'open' systems, and on observations of the embrittled platinum foil, it was hypothesized that bismuth vapor was attacking the platinum. In order to test this hypothesis, BSO was wrapped in platinum foil along with several other foil pieces and processed by melting the BSO for 5-10 minutes. The ampoule was fabricated such that the foil pieces were kept separate from the melt. The configuration is shown in Figure 4-26.

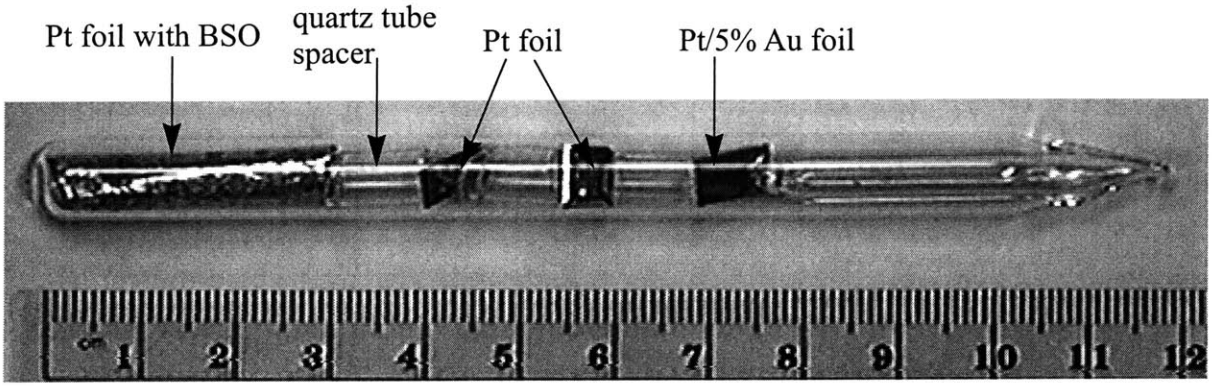

Figure 4-26: Ampoule design used for embrittlement experiments.

4.3.2 Analysis and Discussion

Both the confinement foil and the separated foil were found to be brittle after processing the ampoule by melting the BSO for 10 minutes. Fracture in embrittled platinum (Bridgman, CZ, foil samples) occurs along grain boundaries, as shown in Figure 4-27 and Figure 4-28. One form of intergranular corrosion is the attack of high melting point metals by low melting point metals[195]. The reduction of bismuth oxide vapor to metallic bismuth would occur if there is not enough oxygen in the system.

In order to verify the hypothesis that bismuth vapor is responsible, elements present in the grain boundaries were analyzed using Auger spectroscopy. Initial results were inconclusive, but fracturing the platinum under vacuum in the Auger chamber gave results

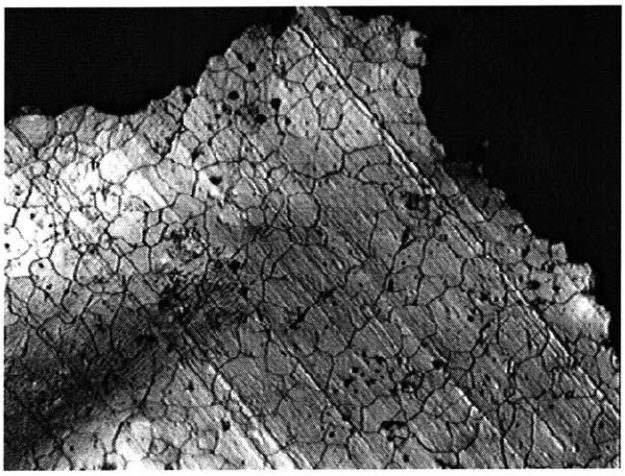

Figure 4-27: Micrograph of embrittled platinum showing grain boundary fracture.

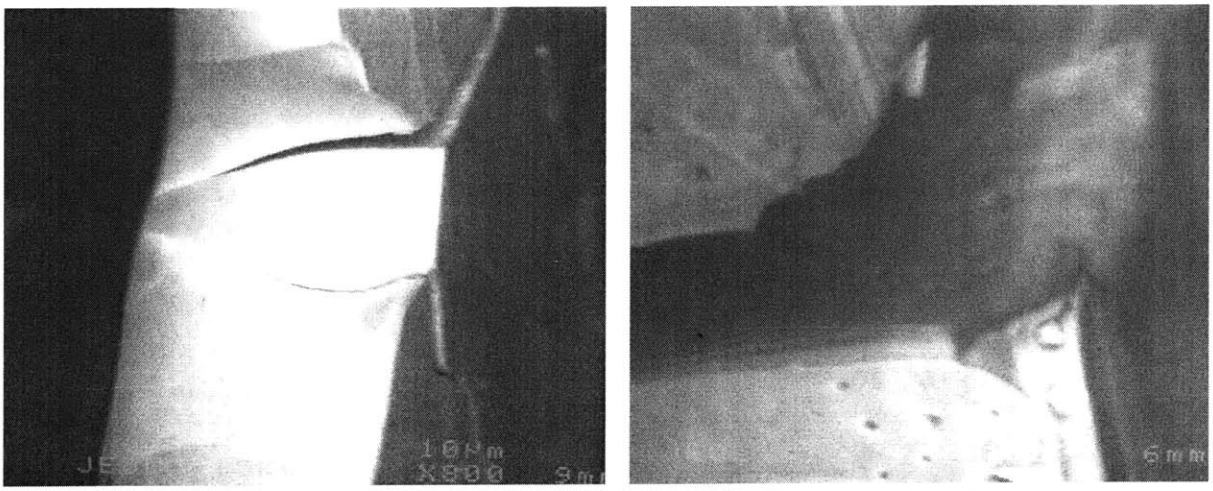

Figure 4-28: SEM micrographs of embrittled foil showing grain boundary fracture.

that strongly suggest metallic bismuth to be present. The Auger spectra is shown in Figure 4-29. There is a strong peak at 107 eV, however the main peak for bismuth is at 101. Small shifts in the spectra are known to occur[196]. Additionally, other elements with peaks in the vicinity of 101 eV are unlikely to be present in the system (Gd, Eu, Sm, Y, Sr, Rb, Be). Therefore, it is concluded that vapor transport of bismuth containing species plays a role in intergranular corrosion of platinum.

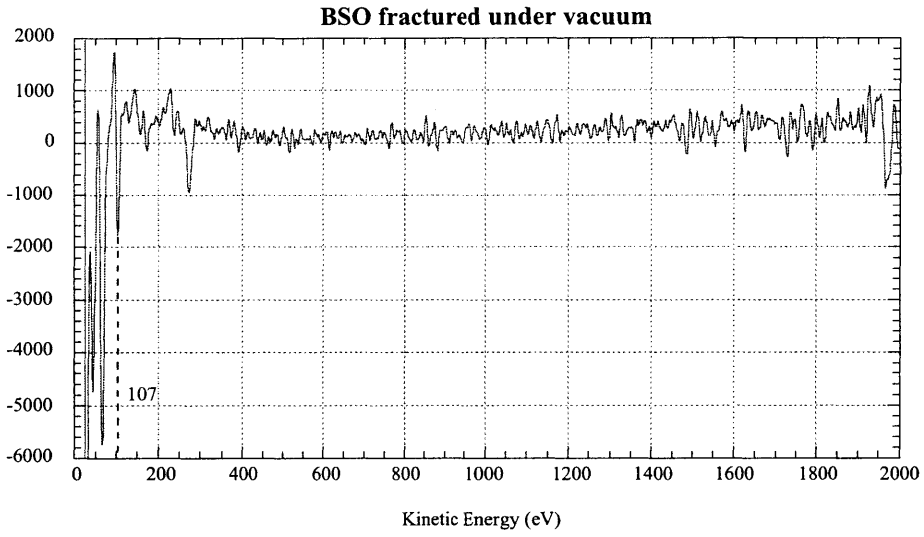

Figure 4-29: Auger spectra of platinum grain boundary fractured under vacuum.

CHAPTER 5: DESIGN AND IMPLEMENTATION OF THE VERTICAL BRIDGMAN-STOCKBARGER CRYSTAL GROWTH SYSTEM

5.1 Introduction

Directional solidification using the vertical Bridgman-Stockbarger technique provides a means to grow crystals in a thermally stable environment. Unlike in a Czochralski configuration, the Bridgman -Stockbarger (B-S) geometry is such that the hotter melt is on top of the colder crystal. This reduces the driving force for natural convection. Since in practice a flat interface is rarely achieved, the curvature of the interface still induces some density driven flows.

Idealized and more realistic B-S thermal profiles are shown in Figure 5-1. In order to approach the idealized situation as closely as possible, heat pipes can be employed in the hot and cold zones. Development and characterization of such a heatpipe based furnace for growth of semiconductors was carried out in the late eighties to mid nineties[197,198,199]. Heat pipes not only help to reduce azimuthal variations in the thermal environment but, they also allow accurate boundary conditions to be established for use as inputs in modeling calculations.

In a conventional B-S system, the control thermocouples for the hot and cold zone heaters are located in close proximity to the heaters. However, this leads to variations in the gradient zone thermal environment due to coupling between the heaters and the translating ampoule (known as end effects). As the ampoule moves through the furnace, the heat flux through the crystal changes continuously, and this in turn causes changes in both the location and the shape of the interface. One of the key developments from the work mentioned in the previous paragraph is the practice of using the thermocouples positioned in the gradient zone for controlling the heaters. This provides a near linear thermal profile in the vicinity of the interface. A modified Bridgman-Stockbarger configuration is shown in Figure 5-2 along with the thermal profile.

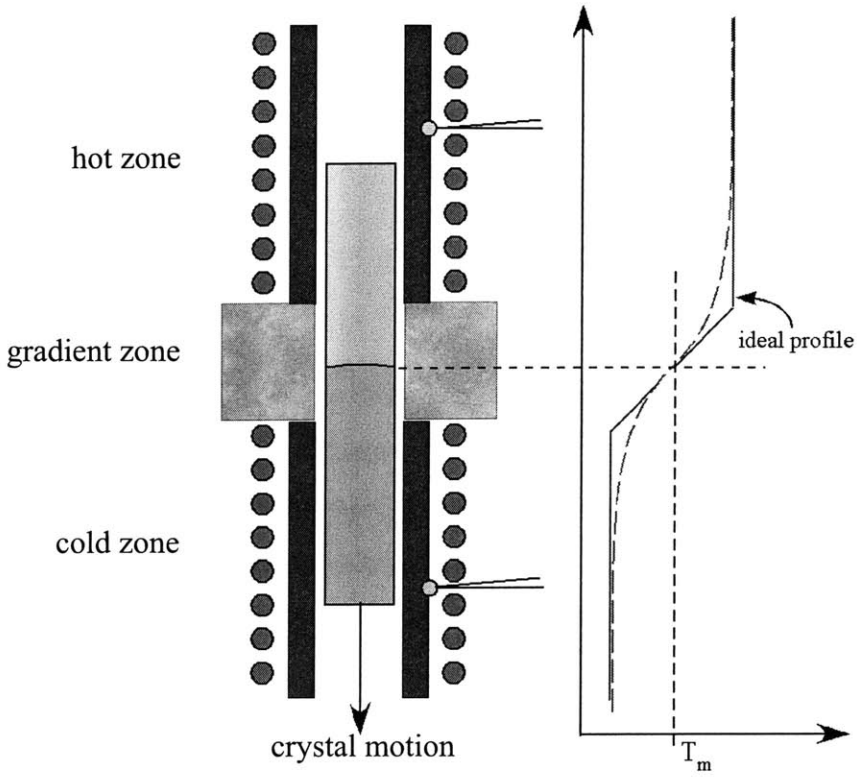

Figure 5-1: Conventional control of Bridgman-Stockbarger furnace with control TC's in heater zone. Ideal and realistic thermal profile on right.

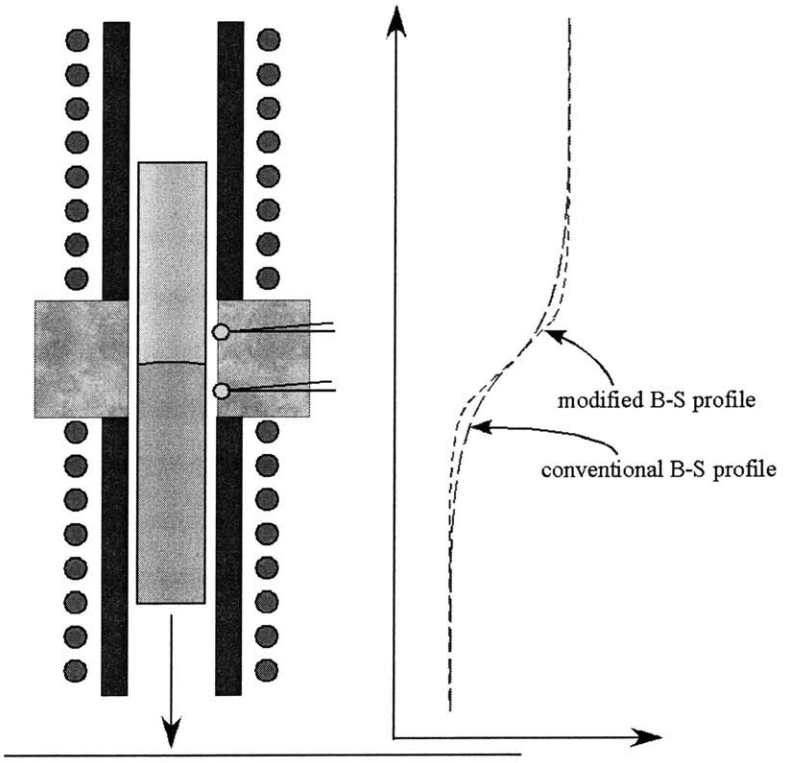

Figure 5-2: Modified Bridgman-Stockbarger with control TC's in the gradient zone. Profile on right shows modified versus conventional thermal profile.

5.2 Design and Implementation of New Furnace

The existing vertical Bridgman-Stockbarger furnace was found to be in need of a significant redesign and rebuild. After years of minor modifications from different users, the insulation and heaters were ill-matched and physically disintegrated. Additionally, no method of ensuring proper alignment between the hot and cold zones was available. Of primary concern in designing new components was the axial alignment between the hot, cold, and gradient zones to ensure radial symmetry. Additionally, disassembly, maintenance, and reassembly of the furnace in an efficient and reproducible manner was deemed necessary in order to avoid changes in the thermal characteristics of the furnace after disassembly for maintenance.

5.2.1 Heater and insulation package

The previous system consisted of a resistance heater encased in ceramic with separate alumina insulation. As can be seen in Figure 5-3, the insulation and heaters were not well matched. The new system consists of an integrated heater and insulation package that eliminates dead space and creates a protected cavity for the gradient zone insulation. The heating element consists of a helically wound iron-chrome-aluminum wire that is embedded

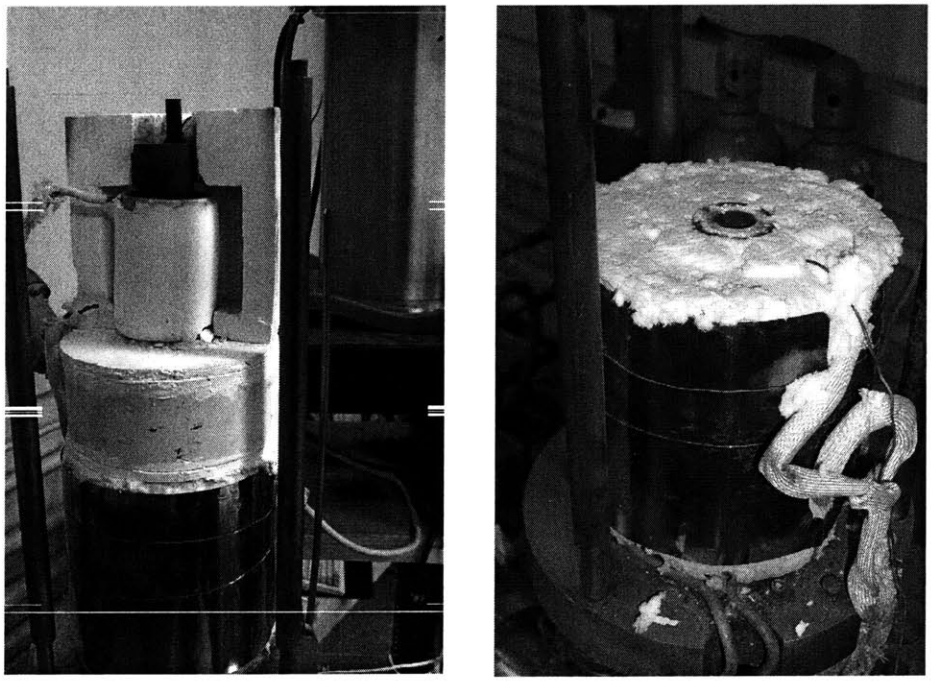

Figure 5-3: Old furnace heater and insulation (left). Cold zone shown on the right.

in a vacuum formed ceramic fiber insulation package (Thermcraft, Inc., Fibercraft VF360-25-5-V, 450 W). A black coating on the inner surface increases the radiative heat transfer, and a protective coating on the outside increases durability.

5.2.2 Gradient Zone Insulation

Ideally, the gradient zone in a Bridgman-Stockbarger furnace is adiabatic. However, this cannot realistically be achieved since there will always be a finite thermal conductivity for any gradient zone insulation. In order to minimize radial losses, the gradient zone should consist of an extremely low thermal conductivity material. The old system used ceramic microspheres encased in a refractory shell. The thermal conductivity of these spheres is 0.09 W/m K at room temperature. Unfortunately, these spheres are no longer manufactured, and an alternate insulation material had to be found. Zirconia insulation (Zircar Zirconia, type ZYFB-3) was originally chosen (thermal conductivity 0.09 W/m K at room temperature, 0.11 W/m K at 800 °C) as gradient zone insulation. A schematic of the heaters and gradient zone insulation is shown in Figure 5-4 (a).

5.2.3 Gradient Zone Inserts

The critical region for the Bridgman-Stockbarger configuration is the gradient zone because this is where the interface is located. In previous work at MIT[72,199] the feasibility of controlling the hot and cold zone heaters from thermocouples located in the gradient zone was shown to be advantageous for achieving the stability of the melt/solid interface. Four high temperature, low noise type K thermocouples (#HGKMQIN-040U-24, Omega Engineering) are located in the gradient zone for this purpose. The thermocouple insert, shown in Figure 5-5, was the same as used in previous work[72] but it was found that the cold zone control thermocouple was too far removed from the cold zone. The lag between the output of the heater and the response of the thermocouple (located ~25 mm away) was too great. A new insert with thermocouple grooves located closer to the cold zone was machined, and control was achieved with both of the bottom two thermocouples (C and D).

The thermocouple insert fits inside an alignment piece designed to ensure that the heat pipes were axially aligned with each other and the gradient zone (see Figure 5-4(b) and Figure

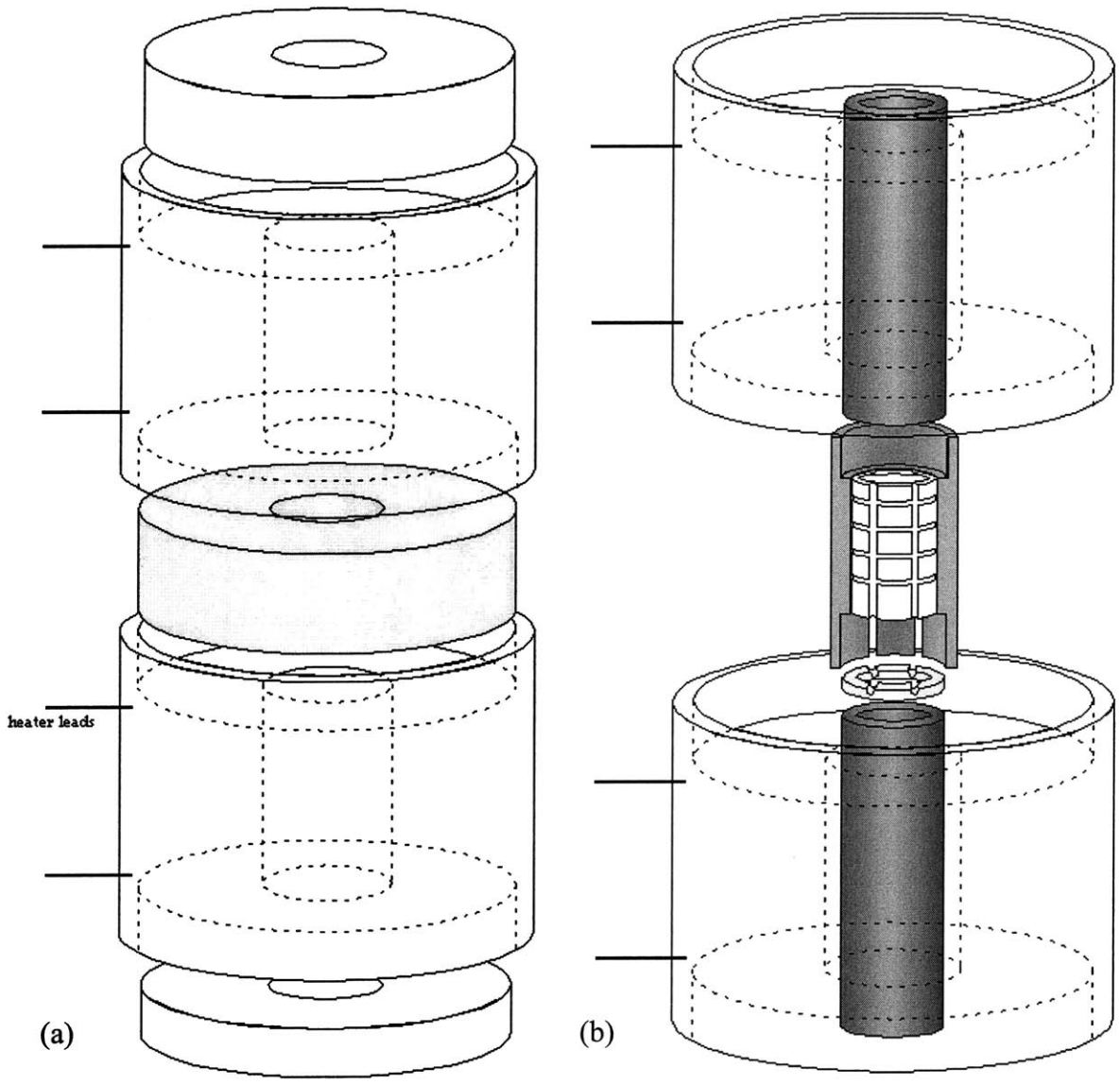

Figure 5-4: Schematics of new furnace design. (a) heaters and gradient zone insulation (b) heaters, heat pipes, and gradient zone inserts.

5-6). The gradient zone insulation surrounds the inserts, and axial alignment of the heaters with the heatpipes is achieved through the tight fit of the heater/insulation packages around the gradient zone. A schematic of the furnace cross-section with the location of the thermocouples is seen in Figure 5-7(a), and an image of the assembled furnace is seen in Figure 5-7(b). Abbreviations in the subsequent discussion are as follows: thermocouple = TC, hot zone = HZ, and cold zone = CZ. The letters A-D refer to the thermocouples in the gradient zone with A located closest to the hot zone and D located closest to the cold zone.

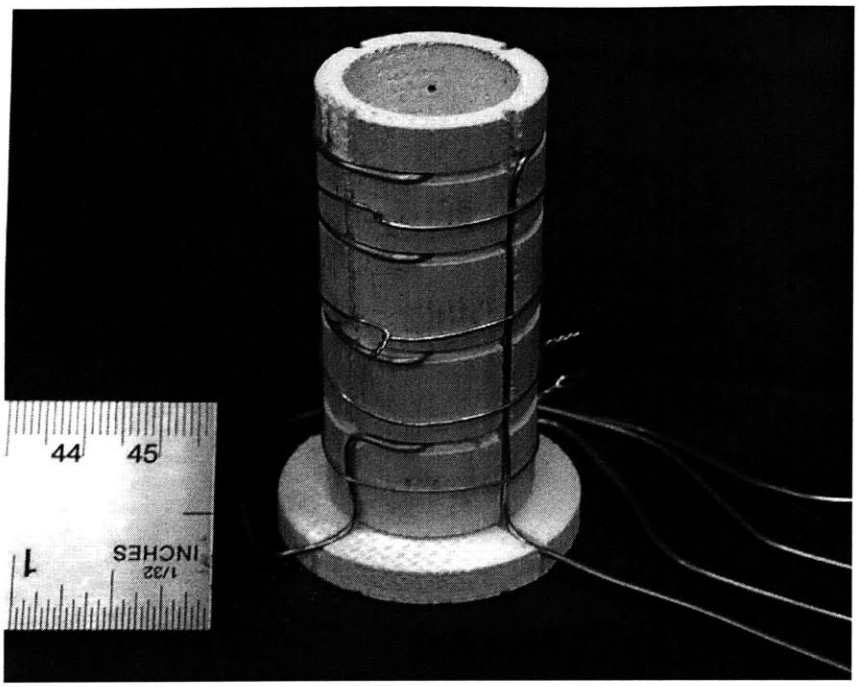

Figure 5-5: Thermocouple insert shown with 4 thermocouples in place.

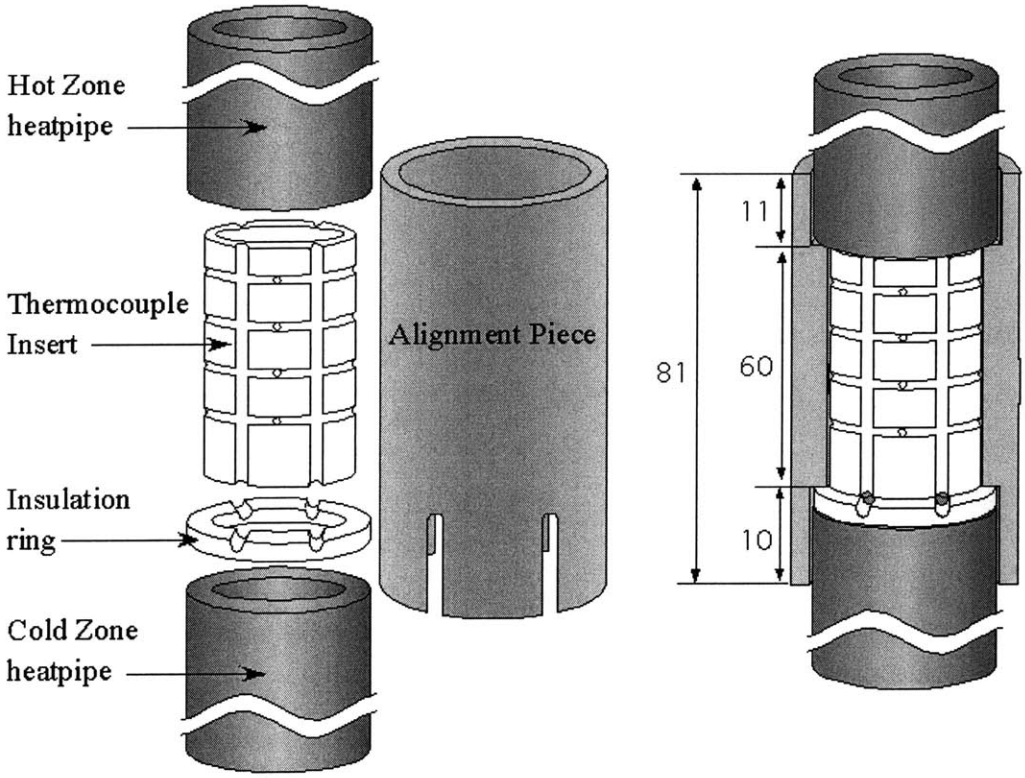

Figure 5-6: Exploded and assembled views of alignment pieces designed for gradient zone. Dimensions in millimeters.

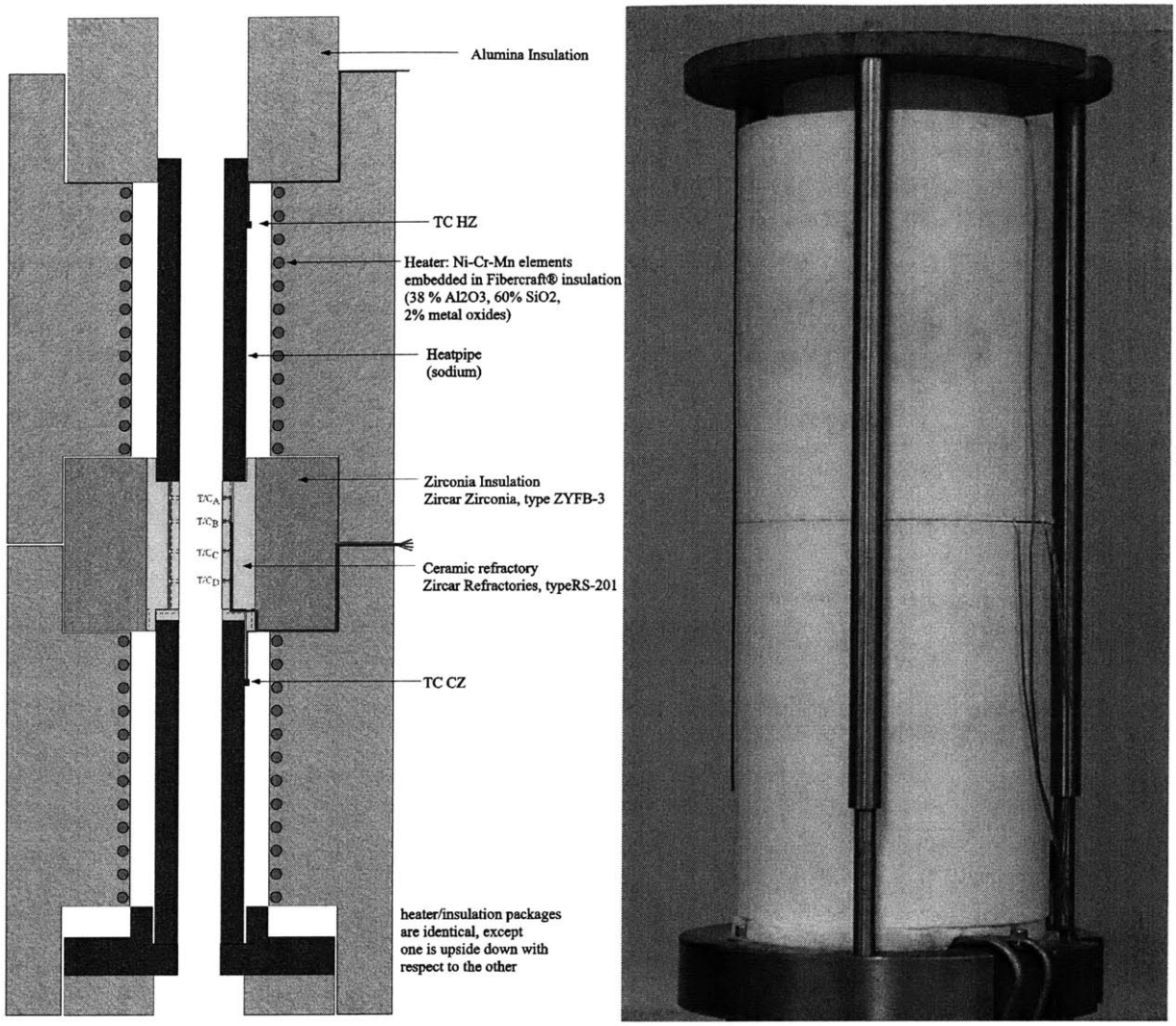

Figure 5-7: (a) cross-section of furnace (b) image of assembled furnace.

5.3 Data Acquisition and Control – Hardware

The existing hardware system had been in use for a number of years and was in need of refurbishment. The hardware rack was completely rewired in order to remove old wires with cracked insulation, dangerous connections, and incorrect wire gauges. The DC power supplies (SCR 80-28-0V, Electronic Measurements, Inc.) and linear amplifier for motor control (LA 5600, Reliance Electric) did not need to be exchanged. Limit switches were installed in order to avoid damage to the motor in case of accidental excessive translation in either direction. The crystal growth facility is shown in place in Figure 5-8.

The computer hardware as well as the software for data acquisition and furnace control were upgraded. In order to run the most current version of the National Instruments

software, Labview 6i, a 400 MHz Pentium II machine (Dell) with Windows 2000 operating system was used. A 24-bit, high precision temperature and voltage data logger (NI 4351, National Instruments) was purchased in order to assure accurate temperature data. An 8 channel, 12-bit, isolated analog output board (PCI 6308V, ADLink Technology, Inc.) was purchased for controlling the power supplies as well the motor. Previously, the motor control signal was obtained via a 4-bit home-built D/A board which only allowed for 16 discrete speeds. The new system allows for 256 speeds which was a significant improvement of the system.

5.4 Data Acquisition and Control – Software

The new hardware and upgrade in control software made it necessary to write a completely new data acquisition and control program. Main components included temperature display and logging, control of the power supplies (either in a manual mode or using PID control), translation control through set speed and distance, as well as emergency shut-down of power supplies. Because of the lengthy nature of crystal growth experiments, the furnace cannot be monitored continuously, and it is therefore paramount to ensure that failure of a thermocouple does not result in a catastrophic meltdown of the furnace or heatpipes. In order to avoid accidental overheating of the furnace, several safety checks were written into the code. A thermocouple failure results in an open-loop signal results in the form of a very large negative reading. This could be detrimental for a control thermocouple since it would result in full power being applied to the heaters in response. The other danger is overheating of the heat-pipes which have a working limit of 1100 °C. In the Labview program, the temperatures of the control thermocouples as well as the thermocouples located on the heat pipes are checked to see if they are less than 0 °C (open-loop) or greater than 1100 °C (overheating). If either scenario is true, control is switched from PID to manual and power output set to zero.

5.4.1 Heater control

One of the most critical functions of the program is the control of the heaters. Three different modes were implemented. A manual mode allowed for specification of the output control voltage (0-5 V corresponds to 0-80V output from the power supply). The other two

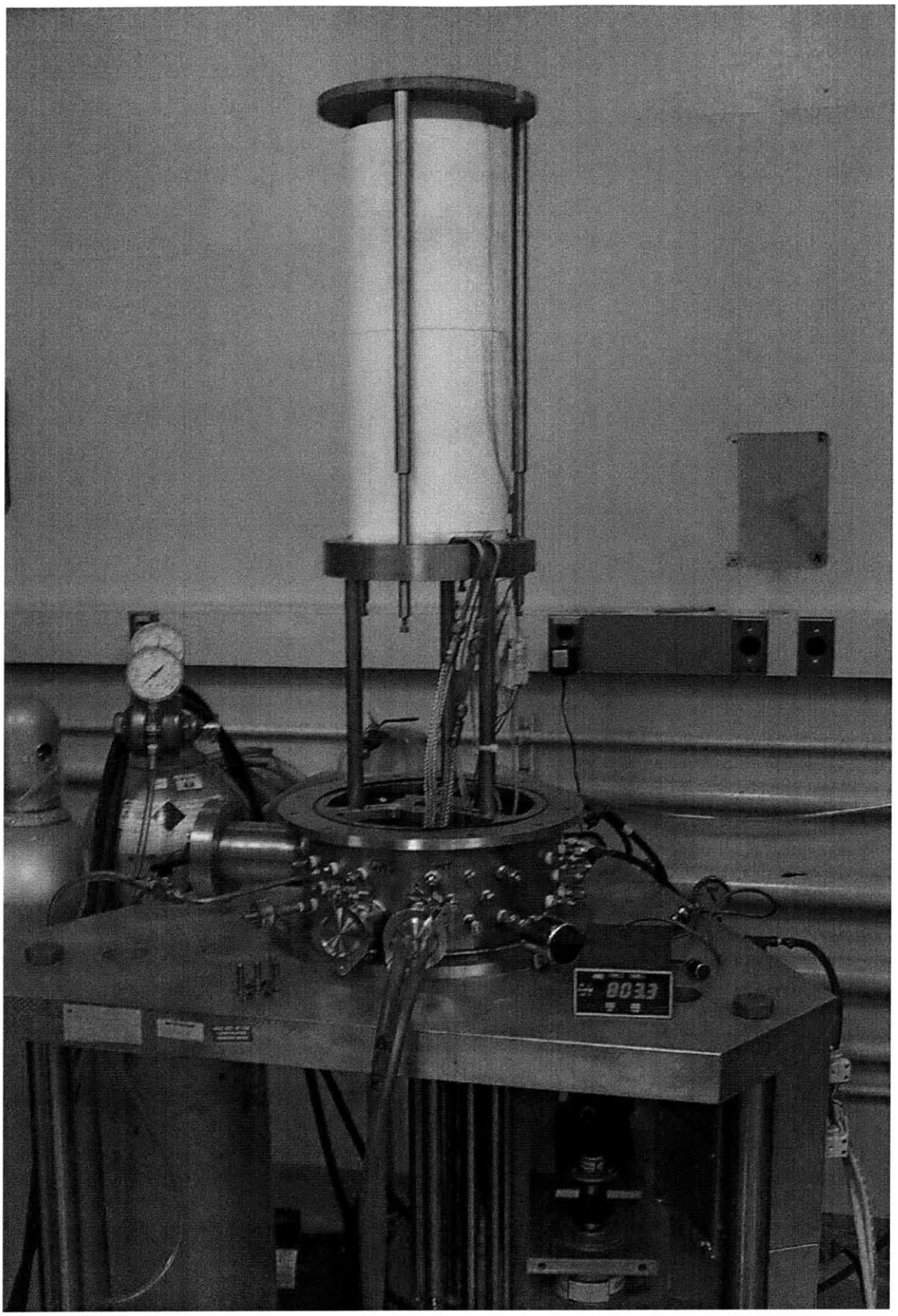

Figure 5-8: Bridgman-Stockbarger Crystal Growth Facility.

modes are PID controlled - one for the heating cycle and one for the cooling cycle. The control thermocouple, PID constants, setpoint, and ramp rate are all adjustable real time.

Tuning of the heaters was attempted using the Ziegler-Nichols method. However, it was found that the calculated constants from this method did not yield a stable system. It was necessary to adjust the parameters experimentally. Typical adjustments included reducing the integral (I) and derivative (D) parameters by at least a factor of five.

If the heaters were controlled by the thermocouples located on the heat pipes, manual tuning of the heaters was straightforward. In Figure 5-9, a typical heater response is shown with PID parameters as calculated via the Ziegler-Nichols method and then subsequent manual adjustment of the derivative and integral control in order to obtain stable heater response. Figure 5-10 shows the heater response to a 5 °C/minute ramp rate with the HZ thermocouple controlling the heater.

Once control was attempted with one of the gradient zone thermocouples, determining the appropriate control parameters became more difficult due to the long lag between heater output and subsequent thermocouple response. This lag time can be seen in Figure 5-11. It was found that increasing the loop delay to 60 seconds in the software enabled determination of appropriate PID constants. Control using an intermediate delay of 30 seconds is shown in Figure 5-12. Ramp rates of 0.5 to 1 °C/minute resulted in little or no overshoot for these delay times. Initially, control of the cold zone heater with a gradient zone thermocouple was not possible due to the distance of these thermocouple from the heater. A new gradient insert with TC C and TC D located much closer to the cold zone was implemented. Table 5-1 gives experimentally determined parameters for various control thermocouples and loop delays.

zone	control TC	loop delay (sec)	P	I	D
HZ	HZ	15	0.2	0.004	3.0
CZ	CZ	15	0.2	0.004	1.0
HZ	A	40	0.089	0.0008	30
HZ	A	60	0.06	0.0005	35
CZ	C	40	0.135	0.0004	62
CZ	D	60	0.09	0.0006	36

Table 5-1: PID constants for various heater, control TCs, and loop delays.

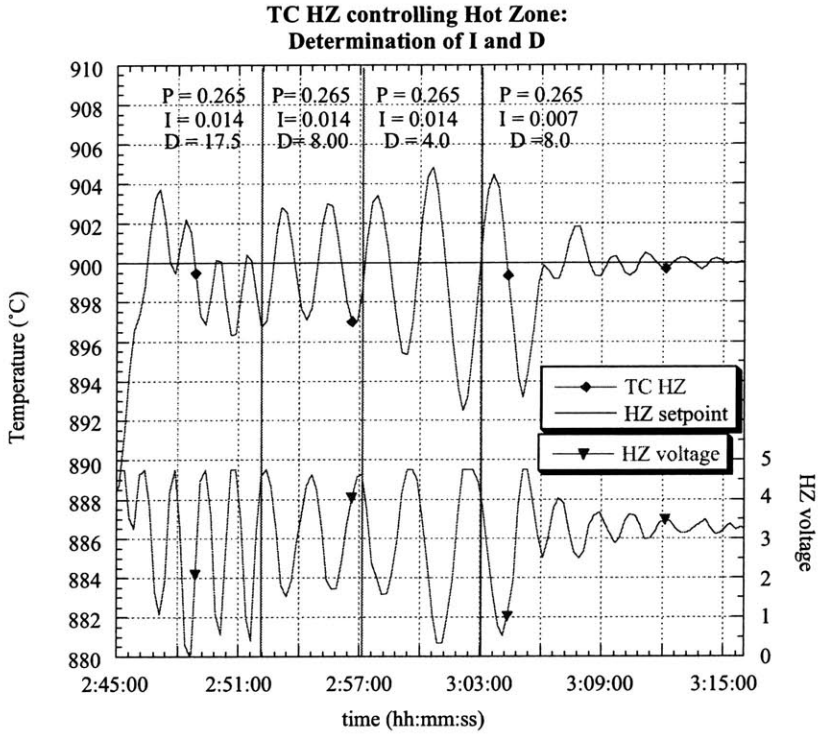

Figure 5-9: Initial PID parameters as determined by Ziegler-Nichols method. Also shown are subsequent modifications of I and D to obtain stable system.

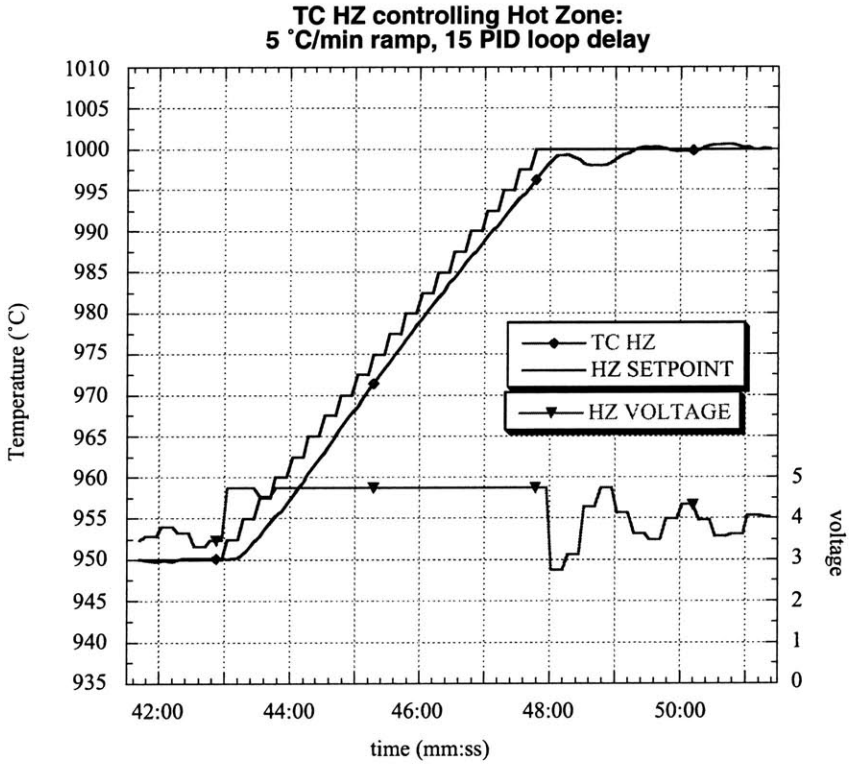

Figure 5-10: Tuned HZ heater response for a 5 °C/min ramp when it is controlled by TC HZ.

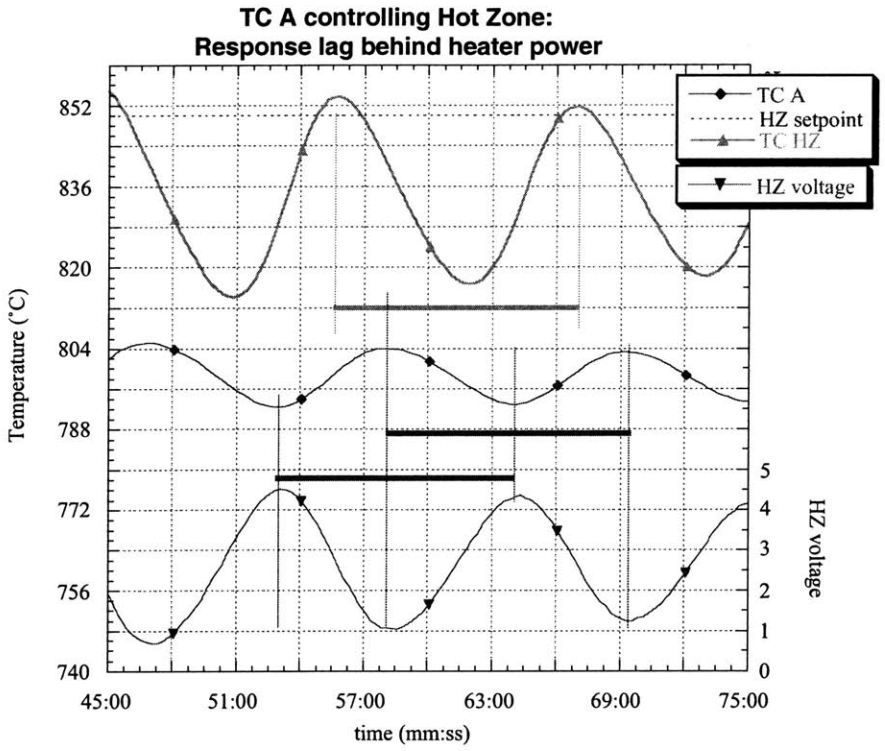

Figure 5-11: Lag in gradient zone thermocouple response to heater output.

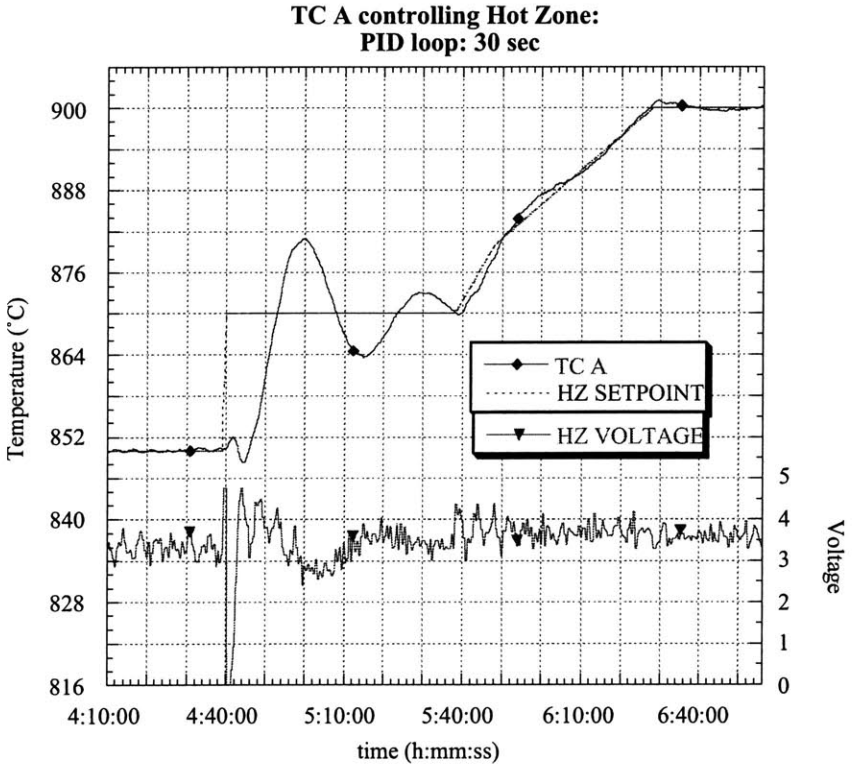

Figure 5-12: Nominally good control of hot zone using TC A with increased time delay between PID control calculations.

5.4.2 *Motor control*

It was necessary to establish a relationship between control voltage output and translation speed in order to be able be able to specify the desired growth rate during experiments. Initial tests revealed poor linearity in the translation speed as a function of control voltage as can be seen in Figure 5-14. It was found that a small voltage offset (~8.6 mV) was present from the output channel that was less than the resolution of the board. It could therefore not be compensated for by using the software. A voltage divider was implemented in order compensate for the offset voltage. A schematic of the circuit is shown in Figure 5-13. Additionally, it was found that a ground loop existed within the screw terminal for the board. After eliminating the ground loop voltage, an essentially linear relationship between control voltage and resultant translation was found and is shown in. The y-intercept, however, was still not zero unless it was specified as such Figure 5-15 during the linear fit. As a result, average translation speeds (based on total distance and total time) were calculated for all of the thermal characterization runs.

Based on the data presented in Figure 5-14 and Figure 5-15, it was concluded that it was not possible to specify the desired speed accurately enough by assuming a linear speed per volt relationship. In addition, the varying loads on the motor also affected the speed. As a result, a position encoder was implemented on the motor to control the speed using feedback control. In order to acquire the TTL signals from the encoder, a counter/timer board (PCI-6601, National Instruments) was purchased. The translation rate is directly calculated from the encoder rotation rate information as shown schematically in Figure 5-16.

PID was not used for controlling the motor rotation speed because the control loop introduced oscillations that were unacceptable in the translation rate response. To avoid this

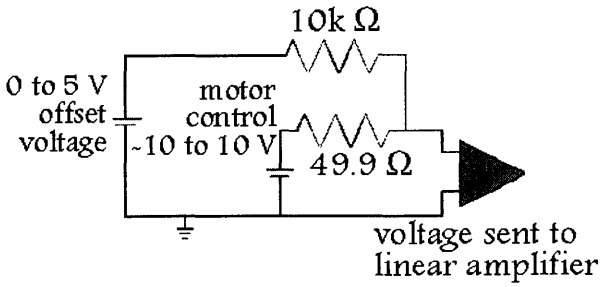

Figure 5-13: Schematic of circuit designed to compensate for small voltage offset from the output board.

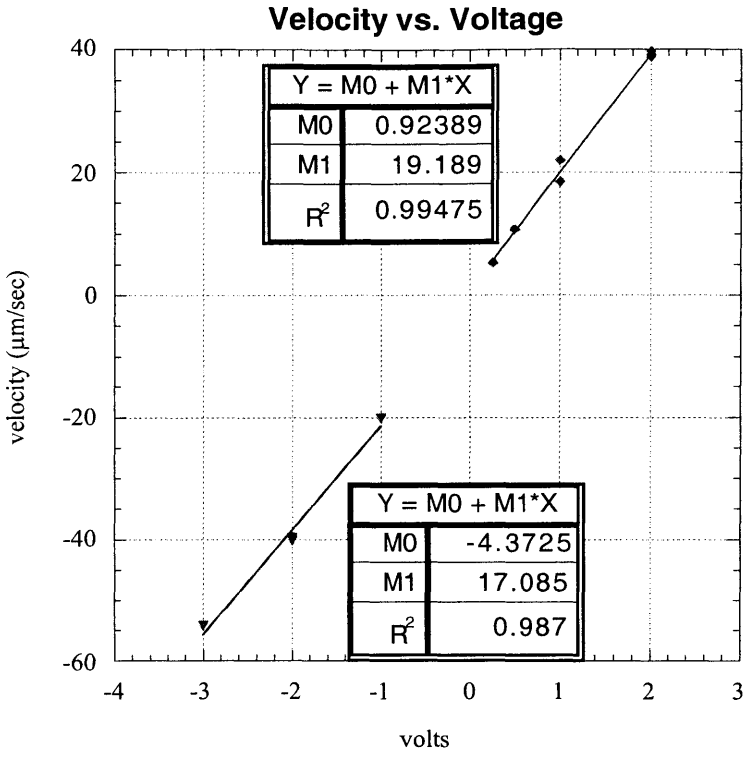

Figure 5-14: Uncorrected velocity versus voltage for translation control.

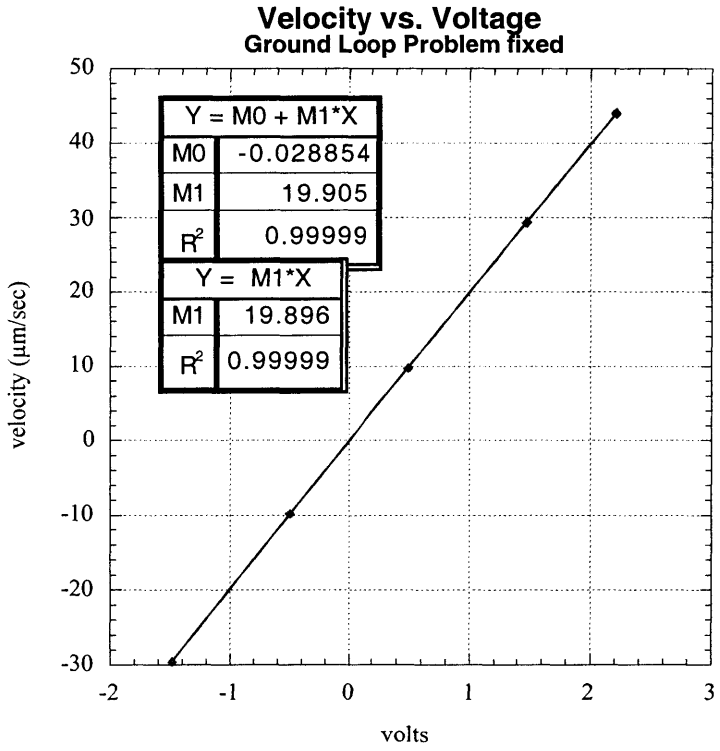

Figure 5-15: Velocity versus voltage signal with compensation for background voltage signal and ground loop problem fixed.

$$\frac{1\ in}{8\ rev} * \frac{1\ rev}{1.7\ rev} * \frac{1\ rev}{X\ rev} * \frac{1\ rev}{100\ rev} * \frac{25{,}400\ \mu m}{1\ in} * \frac{1\ \min}{60\ \sec} * \frac{1.556e^{-3}\ \mu m/s}{1\ rpm} = A$$

lead screw | belt | gear box | gear reducer

$$Velocity\ (\mu m/sec) = A * RPM$$

Figure 5-16: Correlation used to calculate actual translation speed from rotation rate information obtained from the encoder.

problem, the velocity vs. voltage relationship obtained in Figure 5-15 was used to obtain a first approximation for the voltage output in response to a step change in the translation rate setpoint. Adjustments to the control output voltage that were proportional to the error between the actual translation rate and the setpoint were then used to settle in on the correct translation rate.

5.5 Summary

A new Bridgman-Stockbarger crystal growth system was designed and implemented for conducting growth experiments. Design requirements for the new furnace included (1) axial alignment capabilities for the hot, cold zone, and gradient zones; (2) ease of disassembly and maintenance; and (3) compatibility with the existing furnace hardware. Combined heater and insulation packages were used for the hot and cold zones. The gradient zone was redesigned to included an alignment piece that ensured axial alignment of the hot cold, and gradient zones. The gradient zone insert design was not altered except for the position of the thermocouples. For data acquisition and control, Labview 6i was implemented and a new program and user interface was developed. New hardware to interface the furnace to the computer was purchased that increased the resolution of the thermocouple data as well as the motor control signal.

Implementation of the new furnace components and integration with the software was successful. Assembly was found to be reproducible and simple to accomplish and thus satisfied the first design requirement. Axial alignment of the different zones was also successful through the alignment piece used in the gradient zone. Control of the heaters using the gradient zone thermocouples was found to be significantly more difficult than controlling

with the heat pipe thermocouples. Nevertheless, PID parameters for stable heater response could be determined manually. In order to obtain accurate translation speed information, an encoder was used to measure the revolution rate of the motor and convert that data directly into the ampoule translation speed. Overall, the crystal growth facility was significantly improved by redesigning the furnace components and updating the control hardware and software.

CHAPTER 6: THERMAL CHARACTERIZATION AND MODELING OF THE BRIDGMAN-STOCKBARGER FURNACE

6.1 Introduction

After the successful implementation of the new growth system, the thermal environment was fully characterized. It is desirable to be able to control both the location and the shape of the interface during growth. An ideal B-S furnace has no radial heat flow in the gradient zone (*i.e.* adiabatic) such that the heat flux is purely in the axial direction from hot zone to cold zone. In practice however, the gradient zone can have considerable radial heat losses that will affect the ability to control the interface shape and location. Thus, before successful growth experiments could be performed, it was vital to characterize the thermal environment as well as determine thermocouple setpoints that would yield the desired interface shape.

6.2 Thermal Characterization I

6.2.1 Dummy charge considerations

Based on previous work at MIT[72], the thermal behavior of the new furnace was characterized using a dummy charge that housed a thermocouple on the periphery and one in the center of the charge. Initial thermal profiles were measured with no platinum confinement by using the same dummy charge as used in the previous work[72]. The dummy charge body consisted of a quartz rod and is shown in Figure 6-1. As discussed in Chapter 2, internal radiation plays an important role in the growth of BSO due to a radiative heat flux component in the solid. BSO exhibits an IR cut-off frequency of 6 microns at room temperature and a low thermal conductivity. Both of these properties vary considerably from those of quartz as can be seen in Table 6-1. Since the thermal conductivity of quartz is an order of magnitude larger than that of BSO, and it has a lower IR frequency cut-off, it is expected that thermal profiles obtained with the quartz dummy will underestimate the role of radiation heat transfer.

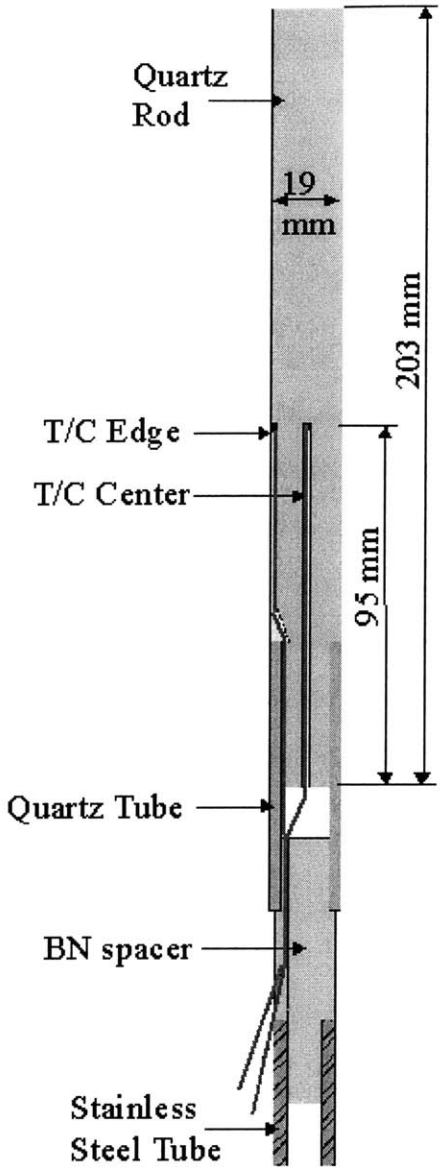

Figure 6-1: Original dummy charge used for initial thermal profiles.

In order to assess the accuracy of the isotherms, the agreement between the center and edge thermocouples was analyzed. The accuracy of low noise, type K (Chromel-Alumel) thermocouples is listed as 1.1 °C or 0.4% (whichever is greater), and at 900 °C the accuracy error is therefore 3.6 °C. In order to assess the discrepancy between two individual thermocouples at the same temperature, they were wrapped in a stainless steel sheet and inserted halfway into the hot zone heat pipe. The stainless steel sheet wrapped around the tips of the thermocouples ensured not only close contact of the thermocouples, but also

surrounded them with a high thermal conductivity material to eliminate any temperature variations in the thermocouple environment. The heat pipe was then ramped up in temperature using TC HZ. This was done for several sets of thermocouples, and Figure 6-2(a) show an example of the temperature difference between thermocouples 1 and 2 as a function of thermocouple 1 temperature. At lower temperatures the behavior was nonlinear and different for each thermocouple pair. However, at higher temperatures, the difference was fairly constant with a maximum discrepancy of 0.5 °C. The difference in thermocouple readings was also dependent on the hot zone heater output as seen in Figure 6-2(b). Since the maximum discrepancy observed was 0.5 °C when the hot zone heater was at temperature, this was taken as the uncertainty in the calculated isotherms.

Material	Thermal Conductivity (W/m K)	Cut-off frequency in IR range
BSO (solid)	0.19 @ 973 K 0.18 @ 1073 K 0.16 @ 1168 K	6 micron @ 298 K
BSO (liquid)	0.27 @ 1168 K	N.A.
Fused silica	1.8 @ 973 K 2.0 @ 1073 K	4 micron @ 298 K

Table 6-1: Comparison of thermal conductivity and IR cut-off frequency for BSO and quartz[72].

Isotherms were calculated by fitting a circular arc through the center and edge thermocouple data at the same temperature. The peripheral data point could be used twice by assuming thermal symmetry. In previous work[72], it was found that the shape of the interface could not be inverted from concave to convex when there was no confinement material present around the dummy charge. This was found not to be the case with the new furnace design indicating that thermal losses in the hot zone were less than in the previous system.

A new dummy charge was fabricated for use with platinum confinement as shown in Figure 6-3. The new quartz dummy was machined with the same diameter as the samples (15 mm). The new dummy was also shortened in order to more closely resemble the sample dimensions. Since the confinement material of the ampoules is quartz, this extra layer outside of the platinum foil was added as well. Because the new dummy charge was shorter than the original dummy, it was possible that the thermocouple readings were not steady state values.

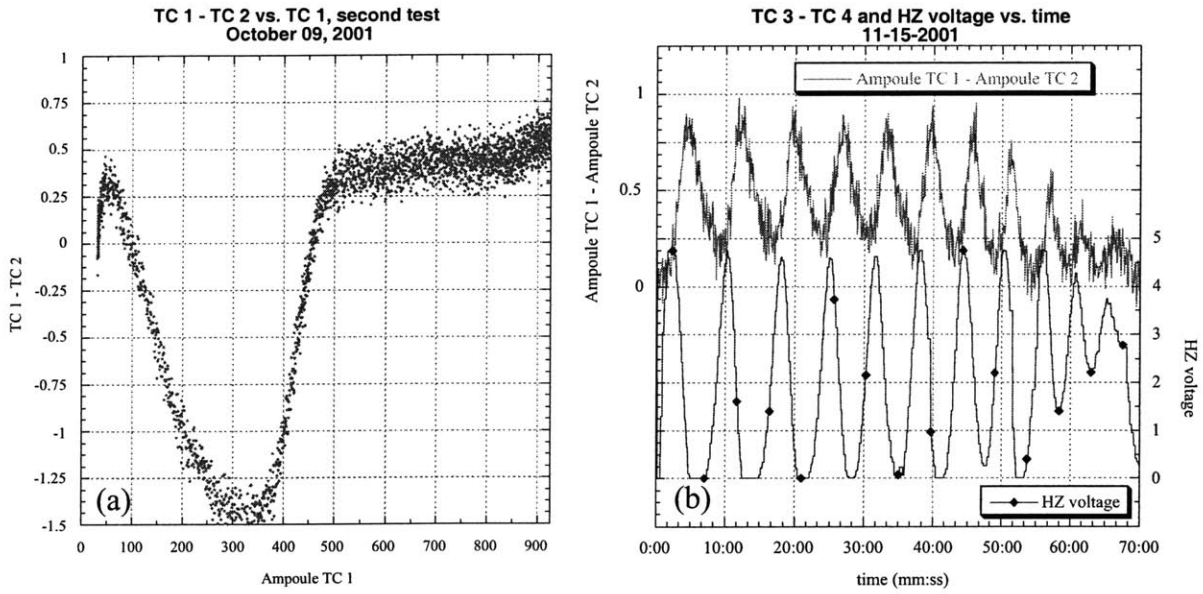

Figure 6-2: (a) Example of non linear nature of discrepancy observed for a thermocouple pair (b) interdependence of TC discrepancy and heater output.

A profile was obtained during which at several instances translation was halted for 5-10 minutes. Figure 6-4 shows clearly that the temperatures of neither the center nor the peripheral thermocouple change when translation stops. This test verified that for one μm/sec. translation rates, the dummy charge has sufficient time to equilibrate for steady state temperature readings.

6.2.2 Thermal Profiling Results

A number of different conditions were explored during the thermal characterization. As an initial baseline, a profile was obtained with the setpoints of the TC A and TC D at 900 °C and 800 °C, respectively. This profile was acquired in an argon atmosphere of approximately 1 atm. using the original dummy charge. The temperature of the edge and center thermocouples as a function of position is shown in Figure 6-5. The furnace thermocouples are also shown, and their values can be read for any given ampoule thermocouple position by drawing a horizontal line at the desired height. On the right are the isotherms calculated from the thermal profile. It is noted that the planar isotherm (the point where the edge and center thermocouples are at the same temperature) sits very high in the gradient zone; in fact, it is located above the control thermocouple (TC A). Additionally, the

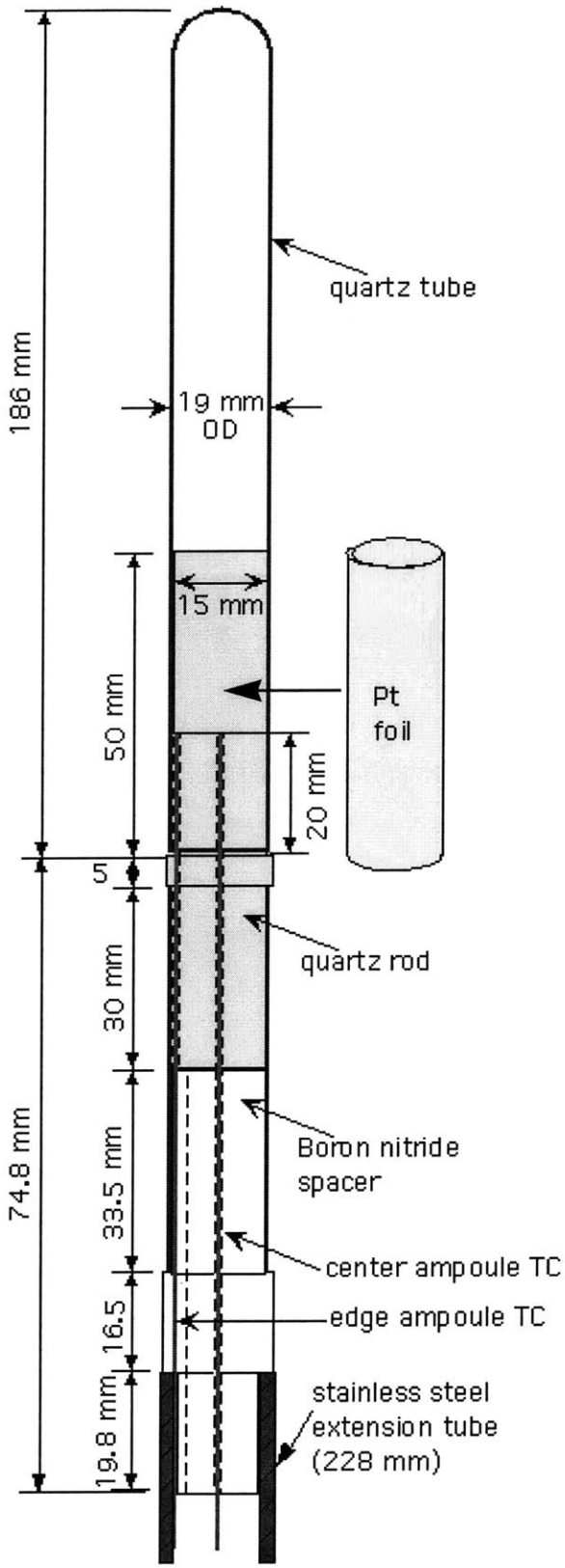

Figure 6-3: New dummy charge designed to more accurately emulate the ampoule configuration.

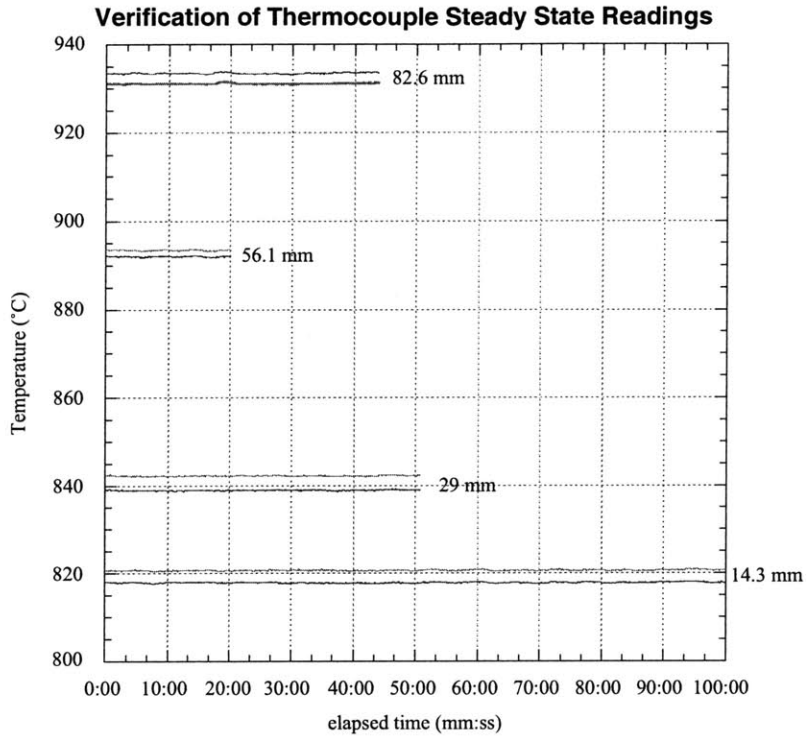

Figure 6-4: Time evolution of thermocouple readings after translation arrests in dummy charge motion.

895 °C isotherm (melting point) is slightly concave - this is undesirable and indicates the need to use different setpoints.

Figure 6-6 shows the initial case (a) and two different sets of thermocouple setpoints, (b), (c). Increasing both the hot and cold zone control setpoints lowered the melting point isotherm in the gradient zone, but also made it more concave. Although a more centralized location of the interface is desirable, the concave shape is not. Decreasing the temperature gradient did not have a significant effect on the shape of the interface. For all cases, there was no confinement material and the atmosphere was approximately one atmosphere argon.

The effects of using a low pressure atmosphere as well as the effect of increasing the translation speed were also investigated. Neither parameter had a significant impact on the thermal profile as can be seen in Figure 6-7. The differences from the increase in translation speed are due to the fact that the thermocouples no longer reaching steady state.

In the old growth system, it was found that thermal profiles obtained without confinement had isotherms to the inability to change the interface from concave to convex[72].

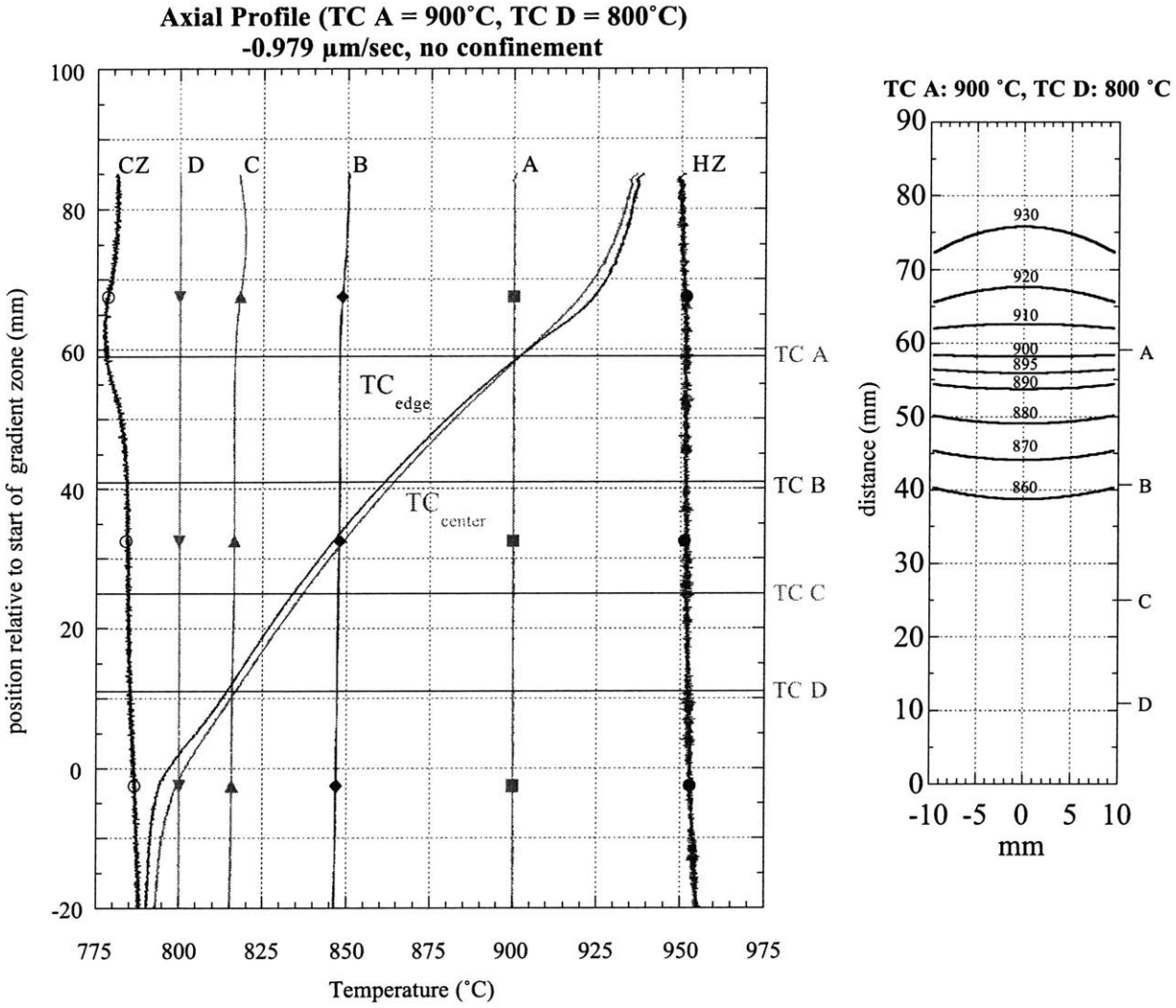

Figure 6-5: Thermal Profile with TC A = 900 °C and TC D = 800 °C. Old dummy was used with no confinement and argon atmosphere.

The results presented above are fundamentally different because in all cases an interface shape inversion was present. This indicates a much better thermal environment in the hot zone region of the furnace than in the old system (less radial heat flow). Since all crystal growth experiments were to be done with platinum confinement, thermal profiling using a dummy charge with a platinum liner generated more relevant data than the initial profiles without confinement.

Figure 6-8 presents a comparison of isotherm data from profiles with and without platinum confinement. The platinum liner acts to decreases the curvature of the isotherms

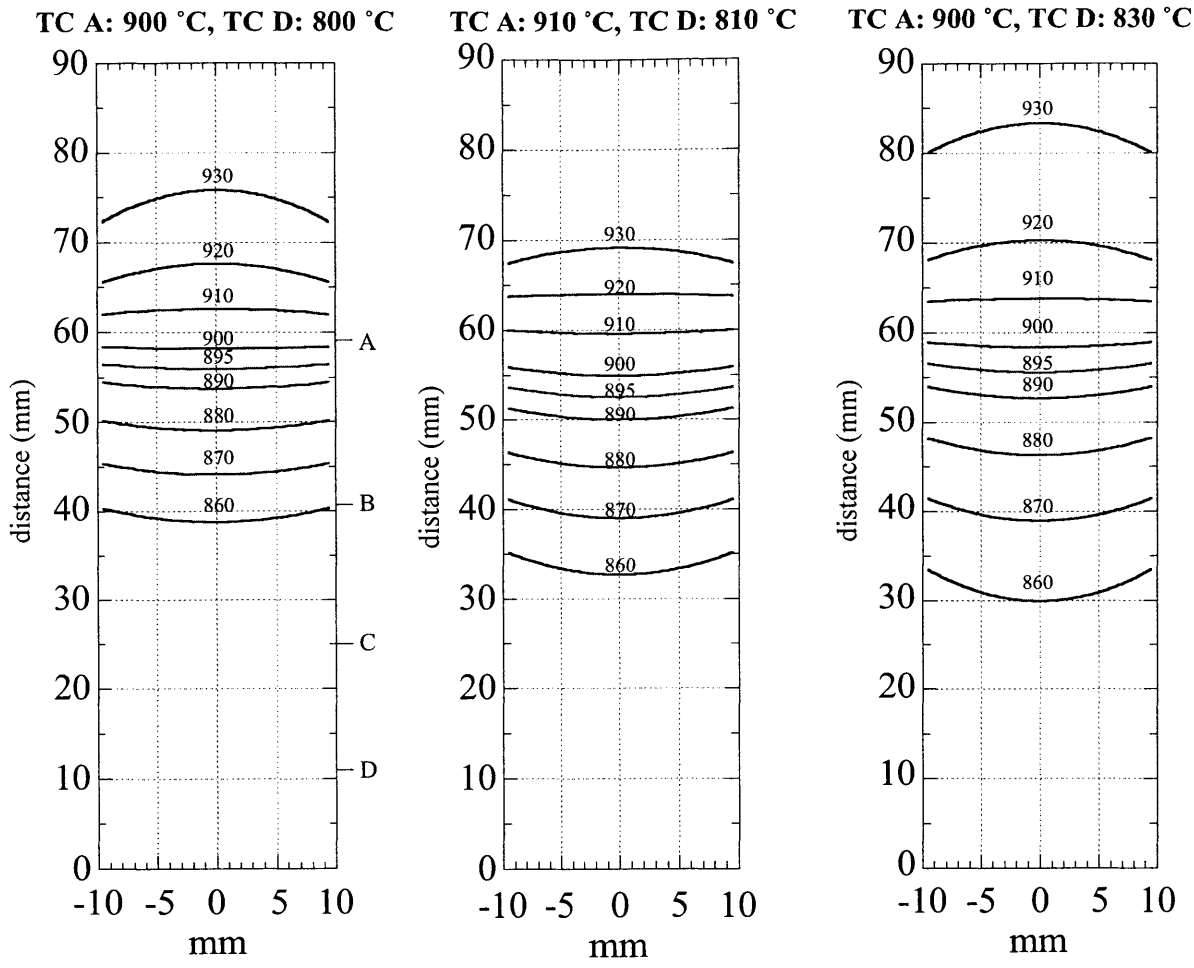

Figure 6-6: Isotherms for different setpoints of TC A (controls hot zone) and TC D (controls cold zone).

compared to the unconfined profile but it does not change the melt isotherm location considerably. Due to the high thermal conductivity of platinum, the axial heat flux component increases compared to the radial heat flux. The axial profile also becomes more linear with the presence of the platinum liner. Nontheless, the 895 °C isotherm is still concave in shape.

Since a convex interface is desired, it was attempted to adjust the hot and cold zone temperatures to increase axial heat transfer and determine setpoints that would lead to a convex interface shape at any location in the gradient zone. It was found that changing the setpoints had little to no effect on the shape of the isotherm located at the height of TC A as can be seen in Figure 6-9 and Figure 6-10. The temperature difference between the center and peripheral thermocouples varies only slightly indicating that the isotherm is essentially unaltered.

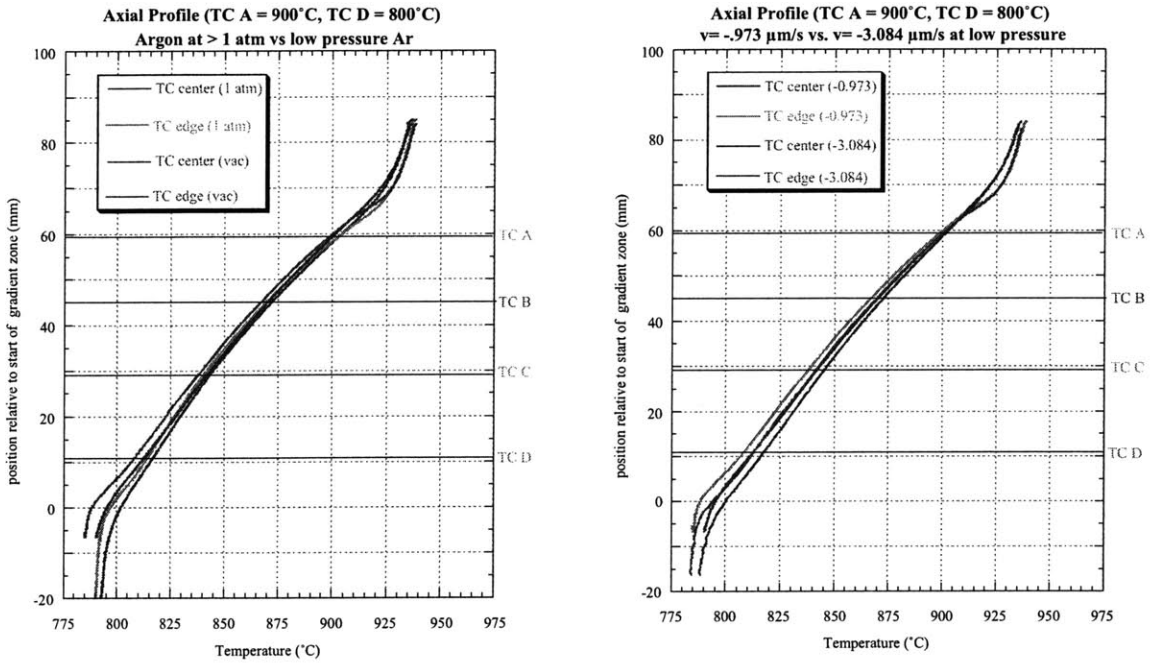

Figure 6-7: Comparison of profiles for (a) 1 atm. Ar vs. low pressure, 1 µm/sec. (b) low pressure, 1 µm/sec. vs. 3 µm/sec. For all cases the setpoints were TC A = 900 °C and TC D = 800 °C.

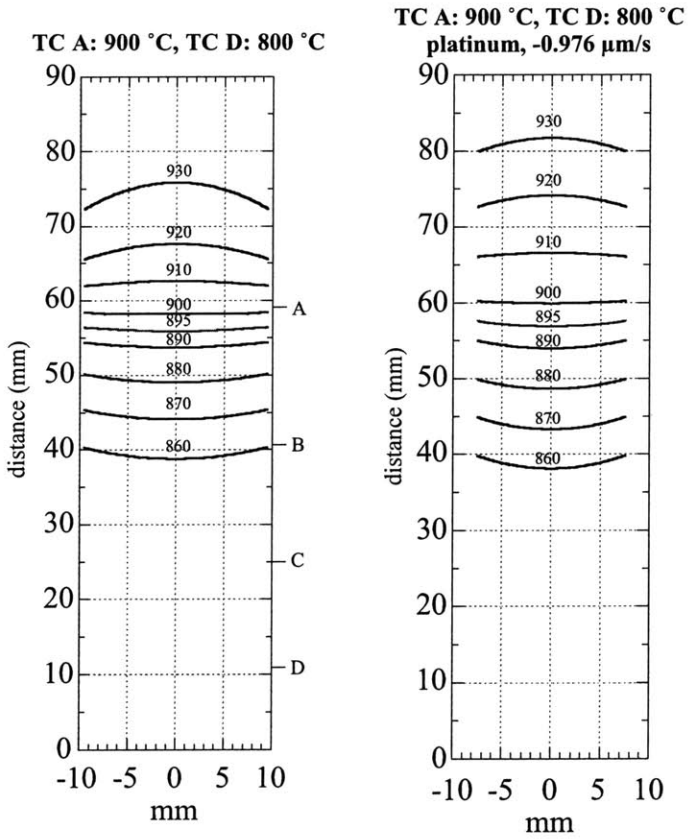

Figure 6-8: Comparison of isotherms (a) without platinum confinement (b) platinum confinement. Setpoints for both are TC A = 900 °C and TC D = 800 °C.

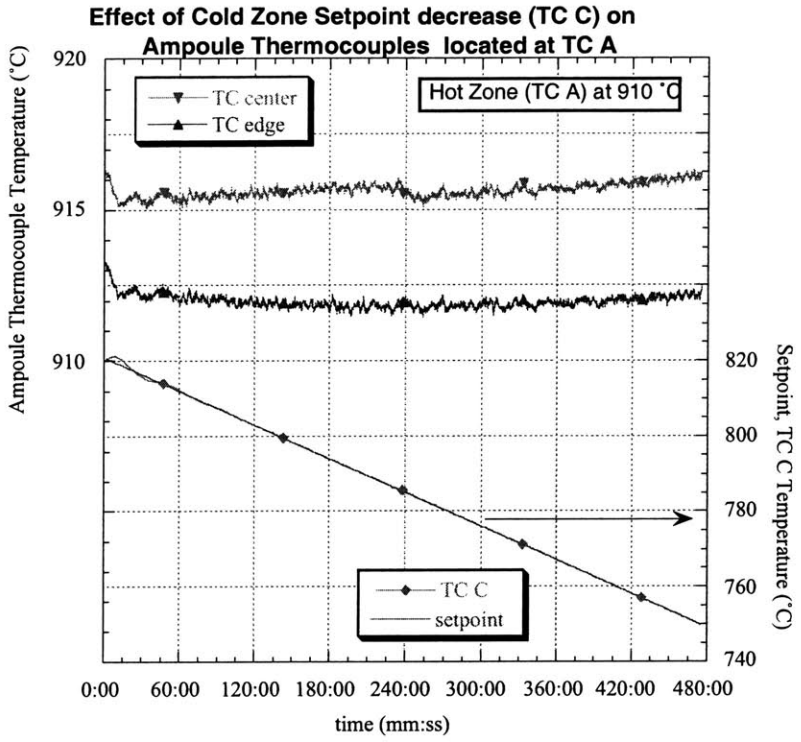

Figure 6-9: Cold zone setpoint decrease from 810 °C to 750 °C. Ampoule thermocouples located at the same height as TC A, near the top of the gradient zone.

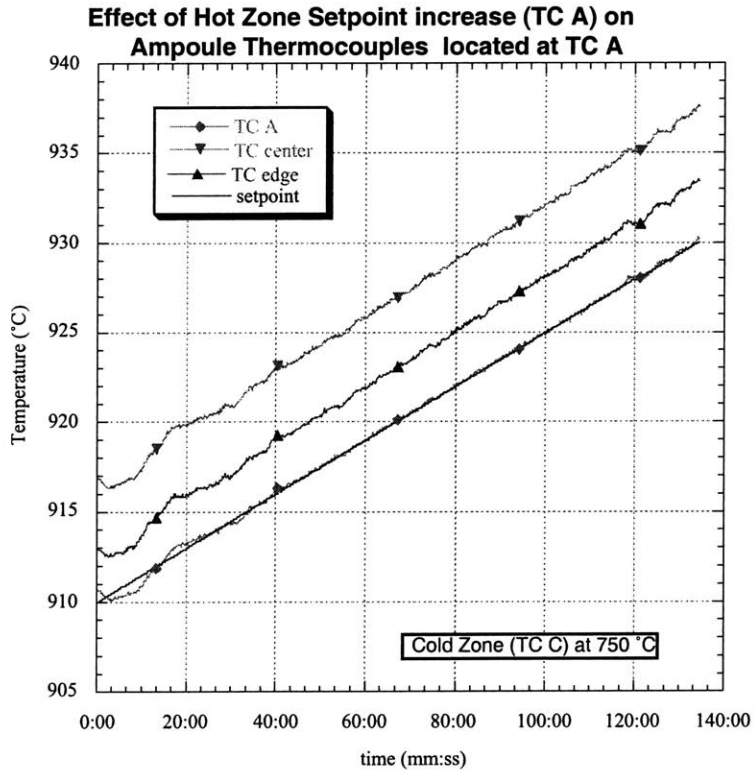

Figure 6-10: Hot zone setpoint increase from 910 °C to 930 °C. As with the CZ setpoint decrease, the isotherm shape at TC A does not change.

It was concluded that the radial heat loss in the gradient zone must be dominating the heat transfer processes. In order to assess the magnitude of the heat loss, both the hot and cold zones (controlled by TC HZ and TC CZ, respectively) were set to 890 °C and a thermal profile was obtained (shown in Figure 6-11). The temperature drop in the gradient zone is of the order of 20 °C as can be seen from the gradient zone thermocouples (TC B and TC C). Looking at Figure 6-11, it was also observed that when the ampoule thermocouples were at the same height as a gradient zone thermocouple, there was a discrepancy between the temperature readings. The gradient zone thermocouples are sheltered by the insert while the ampoule thermocouples are exposed in the chamber. Therefore, the contribution from radiative heat transfer will be greater for the ampoule thermocouples due to different view factors. In order

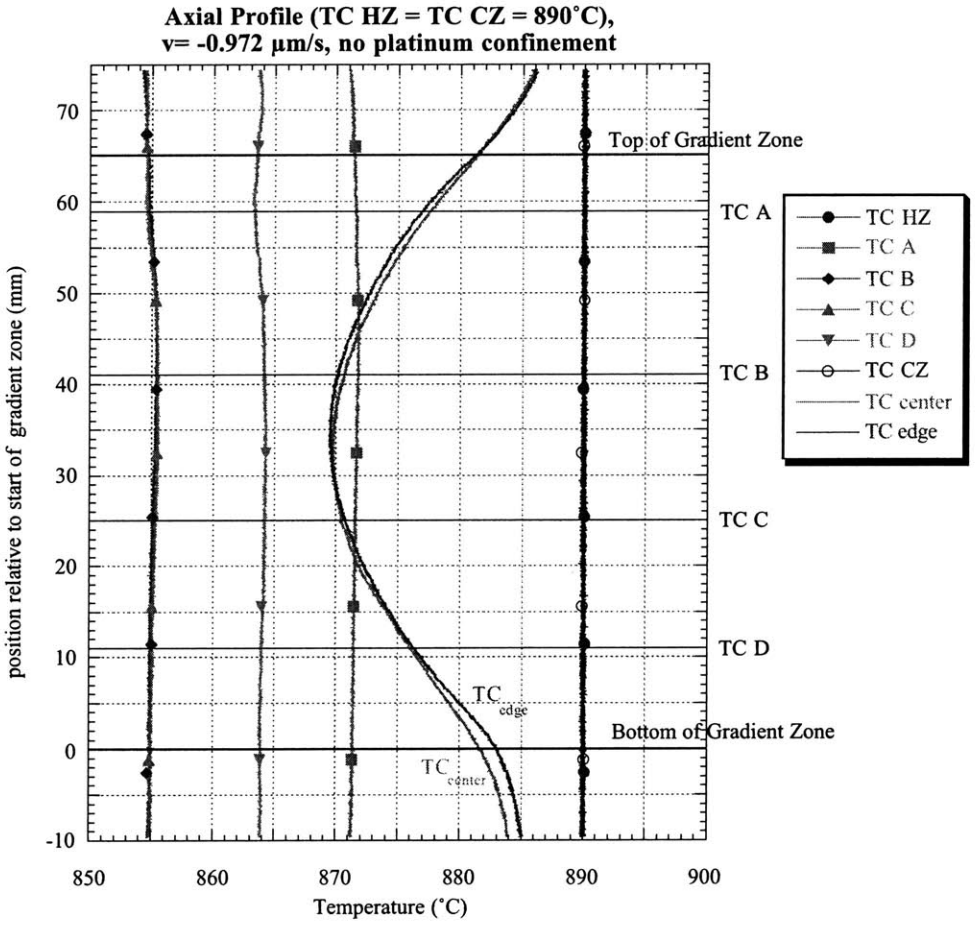

Figure 6-11: Axial profile used to assess radial losses in the gradient zone. TC HZ = TC CZ = 890 °C. Temperature drop in gradient zone over 20 °C.

to analyze different possible changes to the system that would reduce the radial losses as well as increase axial heat transfer, it was decided to simulate the furnace using a numerical model.

6.3 Thermal Modeling Background

Initially, a one dimensional analysis of the conductive heat loss in the gradient zone was performed. Figure 6-12 shows the geometry of the gradient zone and a schematic of the resistance model for heat flux. Using the model to look at the thermal resistance as a function of insulation conductivity and thickness, it was determined that a new gradient zone insulation could increase the thermal resistance of the gradient zone by a factor of three. For one dimensional heat flux through a composite cylindrical shell, the heat flux is given by Equation 6-1.

Equation 6-1 $$\dot{Q} = \frac{(T_1 - T_2)}{R_{total}}$$ where the total resistance is given by:

Equation 6-2 $$R_{total} = \frac{\ln\left(\frac{r_2}{r_1}\right)}{2\pi k_{RS200} L_{RS200}} + \frac{\ln\left(\frac{r_3}{r_2}\right)}{2\pi k_{ZYFB-3} L_{ZYFB-3}} + \frac{\ln\left(\frac{r_4}{r_3}\right)}{2\pi k_{htr} L_{htr}}$$

where R_{total} = total resistance (Ω)
T_1 = inner temperature (K)
T_2 = outer temperature (K)
r_i = inner radius (m)
r_{i+1} = outer radius (m)
k = thermal conductivity (W m^{-1} K^{-1})
L = thickness (m)

In order to assess whether changing the gradient zone insulation would enable control of the shape and location, it was decided to set up a 2 dimensional finite element model of the furnace. Model design, implementation, and execution was done by Matthew Overholt of CapeSim, Inc. The commercial software package, CapeSim was used to define the grid of the furnace and perform the simulations.

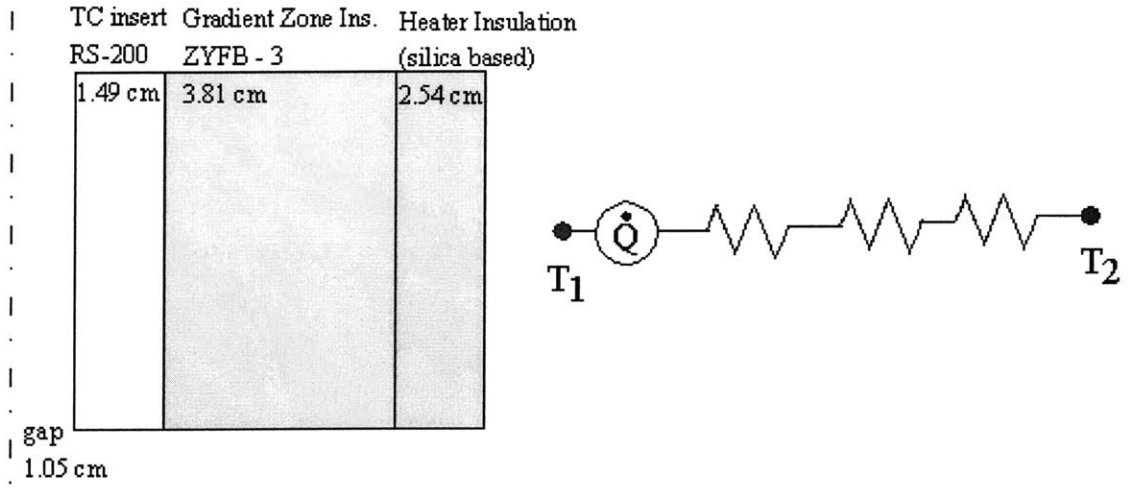

Figure 6-12: One-dimensional heat loss approximation. By comparing the overall resistance to heat flux for different geometries, the optimum solution was found.

6.3.1 Governing Equations

Flow of incompressible laminar fluids are governed by the Navier-Stokes Equations. For the axisymmetric cylindrical geometry, the equations for the stress-divergence are in the following form:

Equation 6-3

$$\rho\left[u_r\frac{\partial u_r}{\partial r}-\frac{u_\theta^2}{r}+u_z\frac{\partial u_r}{\partial z}\right]=\frac{1}{r}\frac{\partial}{\partial r}\left(r\sigma_{rr}\right)-\frac{1}{r}\sigma_{\theta\theta}+\frac{\partial\sigma_{rz}}{\partial z}$$

$$\rho\left[u_r\frac{\partial u_\theta}{\partial r}-\frac{u_r u_\theta}{r}+u_z\frac{\partial u_\theta}{\partial z}\right]=\frac{1}{r^2}\frac{\partial}{\partial r}\left(r^2\sigma_{r\theta}\right)+\frac{\partial\sigma_{z\theta}}{\partial z}$$

$$\rho\left[u_r\frac{\partial u_z}{\partial r}+u_z\frac{\partial u_z}{\partial z}\right]=\frac{1}{r}\frac{\partial}{\partial r}\left(r\sigma_{rz}\right)+\frac{\partial\sigma_{zz}}{\partial z}$$

The stress tensor components can be expanded as:

Equation 6-4

$$\sigma_{rr}=-p+2\mu\frac{\partial u_r}{\partial r}\qquad \sigma_{rz}=\mu\left[\frac{\partial u_r}{\partial z}+\frac{\partial u_z}{\partial r}\right]$$

$$\sigma_{zz}=-p+2\mu\frac{\partial u_z}{\partial z}\qquad \sigma_{r\theta}=-p+\mu r\frac{\partial}{\partial r}\left(\frac{u_\theta}{r}\right)$$

$$\sigma_{\theta\theta}=-p+2\mu\frac{u_r}{r}\qquad \sigma_{z\theta}=\mu\frac{\partial u_\theta}{\partial z}$$

Boundary conditions for the equations consist of Dirichlet (no-slip) condition at solid walls and the natural condition (tangential and normal stresses specified) at free surfaces.

The energy equation used in CapeSim is given by:

Equation 6-5
$$\frac{\partial T}{\partial t} + \rho c_p \vec{u} \cdot \nabla T = \nabla \cdot \left[\lambda \nabla T\right] + q_T + \mu\phi$$

However, the $\mu\phi$ term is usually assumed to be negligible in laminar flow conditions. Boundary conditions for the energy equations can be of the Dirichlet type (fixed temperature value), a flux boundary condition (surface has user defined heat flux), or a film boundary condition (user defined heat transfer coefficient and sink temperature). For a simple radiation boundary condition, the flux or film boundary condition can be used.

The CapeSim software has several powerful capabilities for handling radiation in cavities and enclosures. It employs the Gebhart factor method for calculating the radiative flux. Additionally, it can also handle emissivities that are temperature dependent. Cavity boundaries can be either solid or virtual which represent either a physical boundary or a gap or opening, respectively. For an opening the emissivity has a constant value of unity; however, the temperature is defined as either a constant value or as a moving value that is determined from the temperature of surrounding surfaces. Furthermore, the accuracy of the energy balance also depends on the accuracy of the geometrical factors that are used. CapeSim employs an automatic view factor calculation module.

6.3.2 Finite Elements and Solver

For the current simulations, 6-node isoparametric triangle and 9-node quadrilateral elements were used. Figure 6-13 shows the original furnace geometry with the elements used for the simulation. The Newton-Rhapson algorithm for solution of the system was employed with a convergence criteria of $1e^{-7}$.

6.3.3 Furnace Model

The final temperature could be specified at any of the thermocouple locations. The outside of the furnace was set to radiate to the inner wall of the stainless steel bell jar that was

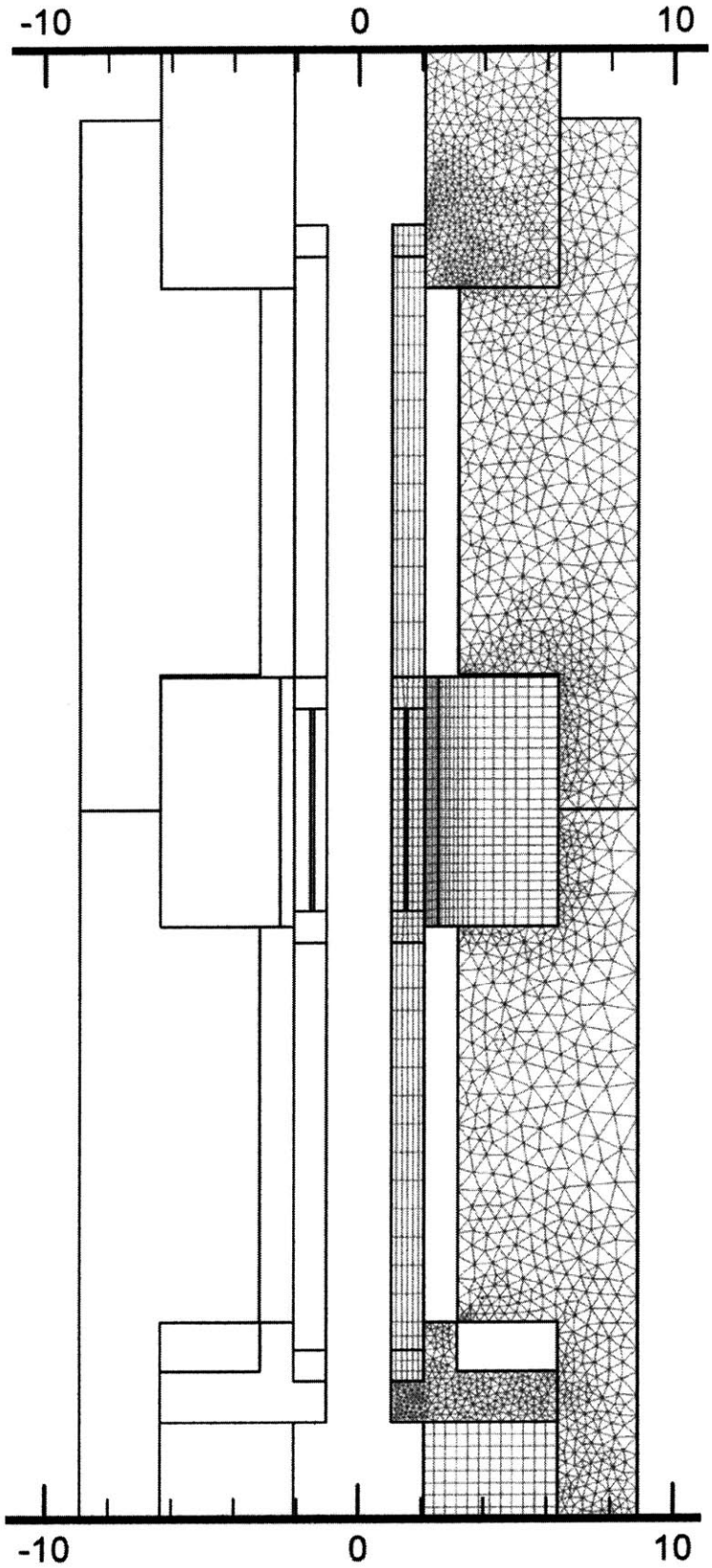

Figure 6-13: FEM grid used for numerical simulation. For clarity, the second order grid that does not include mid and center points is shown.

set to stay at a fixed temperature. For initial cases, this temperature was set at 75 °C or 80 °C. This temperature was measured experimentally to be 135 °C; however, comparing simulations where the only difference was either a 140 °C or 80 °C wall temperature, it was found that the only effect was a 0.7 °C change in the lower heat pipe temperature. Therefore, the outside wall temperature did not have a significant effect on the overall heat transfer. The bottom of the furnace is water cooled, and the temperature along the bottom of the furnace was set at a constant value of either 40 °C or 80 °C. This value was also determined experimentally to be approximately 40 °C. Running the same setpoints (TC A = 910 °C and TC C = 810 °C) with the bottom boundary condition set at 40 °C rather than 80 °C, lowered the cold zone temperature by 2-3 °C.

The heat pipes were modeled by setting the thermal conductivity to 100 W cm^{-1} K^{-1} (~25 times that of copper) so that the temperature would remain uniform along the length of the heat pipe. The ends of the heat pipe had to be modeled separately since no heat pipe action occurs there. The thermal conductivity of Inconel was used for the 0.25" (6.35 mm) end pieces. Additionally, two gaps were added to the model. The first gap is located between the gradient zone insulation and the bottom of the hot zone insulation package. The second gap is between the thermocouple insert and the gradient zone alignment piece. Both of the gaps are due to the tolerances of the fabrication processes used to manufacture the different ceramic and refractory materials. The zero reference point of the model is the bottom of the furnace. The location of the start and end of the gradient zone and the four gradient zone thermocouples is given in Table 6-2.

Location in Furnace	Thermal Profiles (height in mm)	Thermal Modeling (height in cm)
Start of gradient zone	0	19.502
TC D	11	20.602
TC C	25	22.002
TC B	41	23.602
TC A	59	25.402
end of gradient zone	65	26.002

Table 6-2: Cross reference values between experimental profiles and thermal modeling for original configuration.

6.4 Thermal Modeling of Gradient Zone Radial Losses

The first set of simulations was aimed at modeling the radial losses in the system and looking at the effect of changing the gradient zone insulation material and geometry. Thermocouples HZ and CZ (located on the heat pipes) were used as control thermocouples and set to a temperature of 1163 K (890 °C). The ambient atmosphere was helium, argon, or vacuum. Results from the vacuum case are shown in Figure 6-14(a). This was compared with the experimentally measured profile shown in Figure 6-11. The discrepancy between the model results and the temperature readings from the gradient zone is approximately 4 degrees. A plausible explanation is the fact that the presence of the ampoule is an additional axial heat conduction path that is not present in the model.

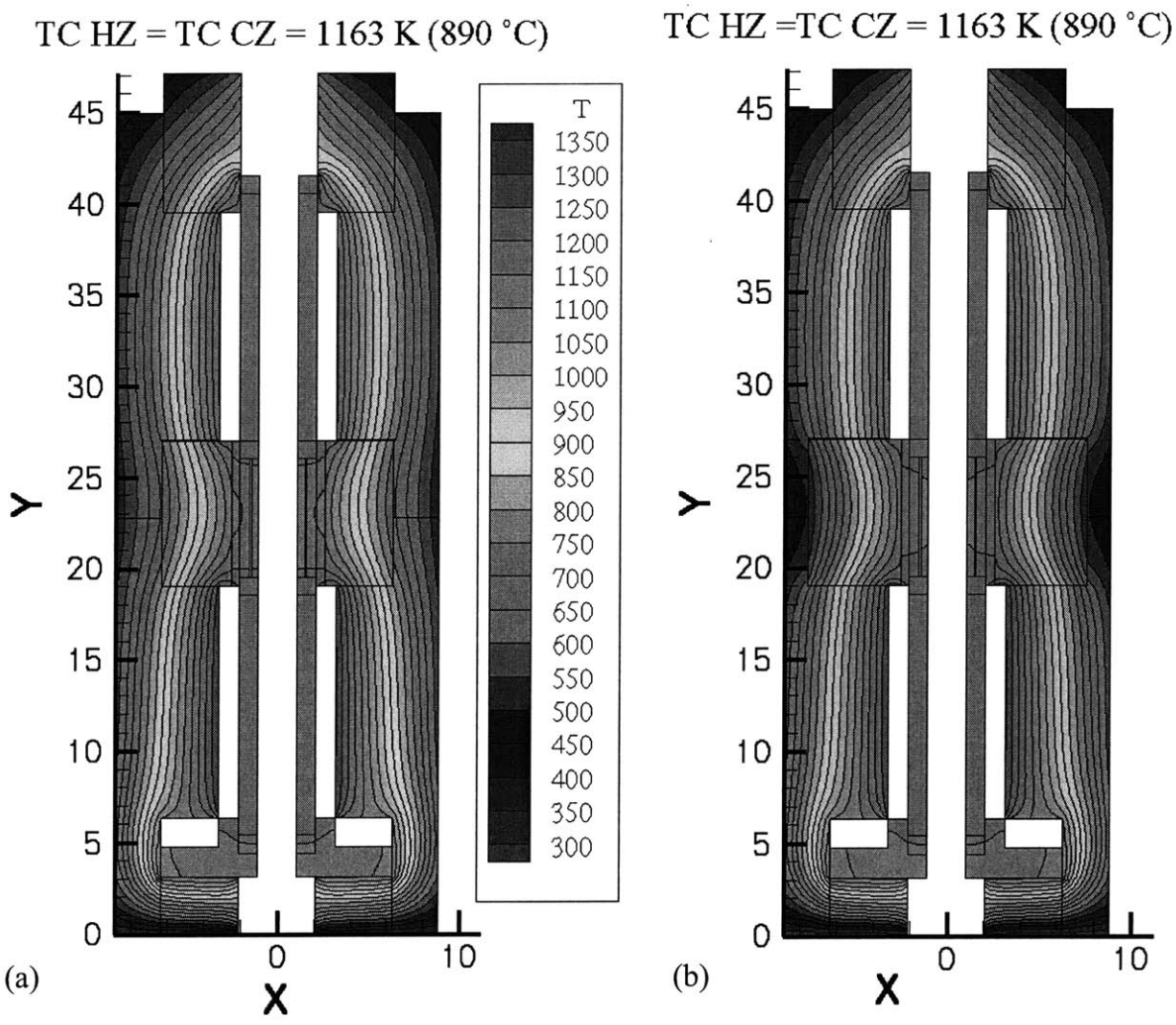

Figure 6-14: Modeling result with TC A = TC D = 1163 K for (a) old configuration and (b) new configuration. Ambient atmosphere is a vacuum.

For the next simulation, the insulation material was then changed to a new candidate, Zirpor-1 (Zircar Ceramics, Inc.), but the geometry was not altered. The setpoints were kept the same, and simulations were run for each ambient atmosphere. A marked decrease in the radial losses was observed (Figure 6-15), and this is due to the decrease in thermal conductivity from 0.11 W/m K for the ZYFB-3 to 0.042 W/m K for Zirpor. The maximum temperature drop along the inner surface decreases to 20 °C as compared to 40 °C for the original ZYFB-3 insulation.

The outer diameter of the insulation was increased so that the thickness of the vestibule walls of the heater/insulation packages was only 6 mm (~0.25"). Simulations were run with the same setpoints for all ambient atmospheres. Although the maximum loss along

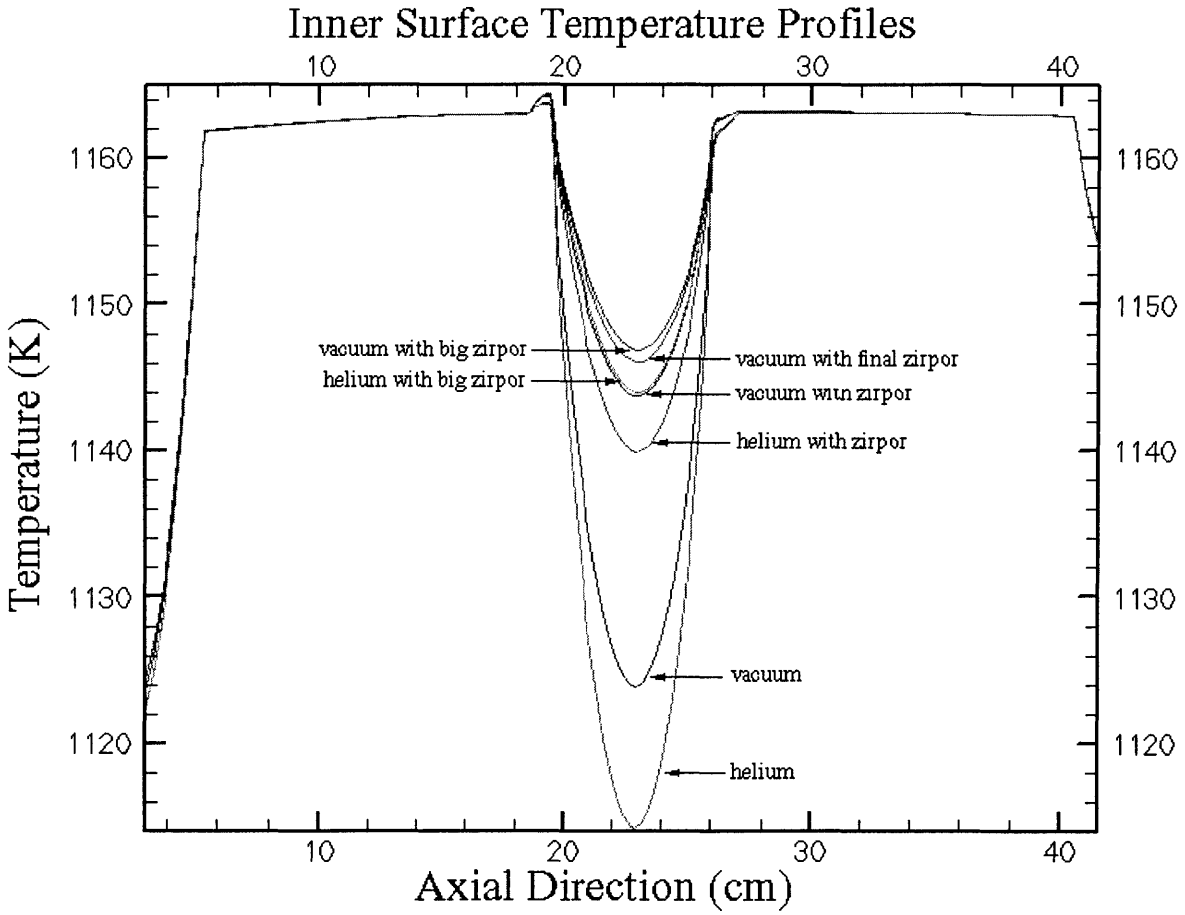

Figure 6-15: Inner surface temperature profiles for different insulation types and geometries. Setpoints of hot and cold zone are 890 °C.

the inner wall decreased to 16 °C, the change was not as significant as exchanging the insulation type. Figure 6-15 shows the profile along the inner wall for all of the cases that were simulated for setpoints of 1163 K (890 °C). Based on these simulations, it was decided to order new gradient insulation and heater/insulation packages. In order to assure mechanical stability of the vestibule walls, the final dimension for the wall was chosen to be 0.5 inches (12.7 mm) which increased the outer diameter of the new gradient zone insulation to 6 inches (152.4 mm). The new gradient zone insulation consisted of 3 separate layers of Zirpor 1 that were bonded together to get the desired thickness (83 mm). Because of the fragility of the Zirpor material, it was also coated with a hardener in order to prolong the life of the insulation. Modeling results for the isothermal case (TC HZ = TC CZ = 890 °C) are shown in Figure 6-14 for the old and new configuration in (a) and (b), respectively. The final configuration is shown in the cross-sectional view in Figure 6-16.

6.5 Additional Modeling Results

A simulation was run using setpoints of TC A = 910 °C and TC C = 760 °C without and with a platinum liner on the inside wall. The platinum liner was added in order to emulate the presence of the platinum confinement material. As with the thermal profiles obtained with the quartz dummy, the platinum had a linearizing effect on the gradient. The temperature distribution for the gradient zone without and with platinum is shown in Figure 6-17. In addition, the presence of the platinum reduced the hot zone temperature and increased the cold zone temperature as seen in Figure 6-18.

In conclusion, the thermal model was found to adequately reproduce experimental data. The agreement within the gradient zone was excellent, but the temperatures of the hot and cold zone differed considerably from experimental profiles for some cases. The discrepancies are attributed to additional losses in the real furnace that are not accounted for in the model and the fact that no ampoule is present in the model. The effect of varying the boundary conditions was to change the cold zone heater temperature by 2-3 °C, indicating the need to have accurate experimental input. Although no ampoule was present in the simulations, emulating the presence of the platinum confinement material resulted in the model more accurately predicting the cold zone temperatures.

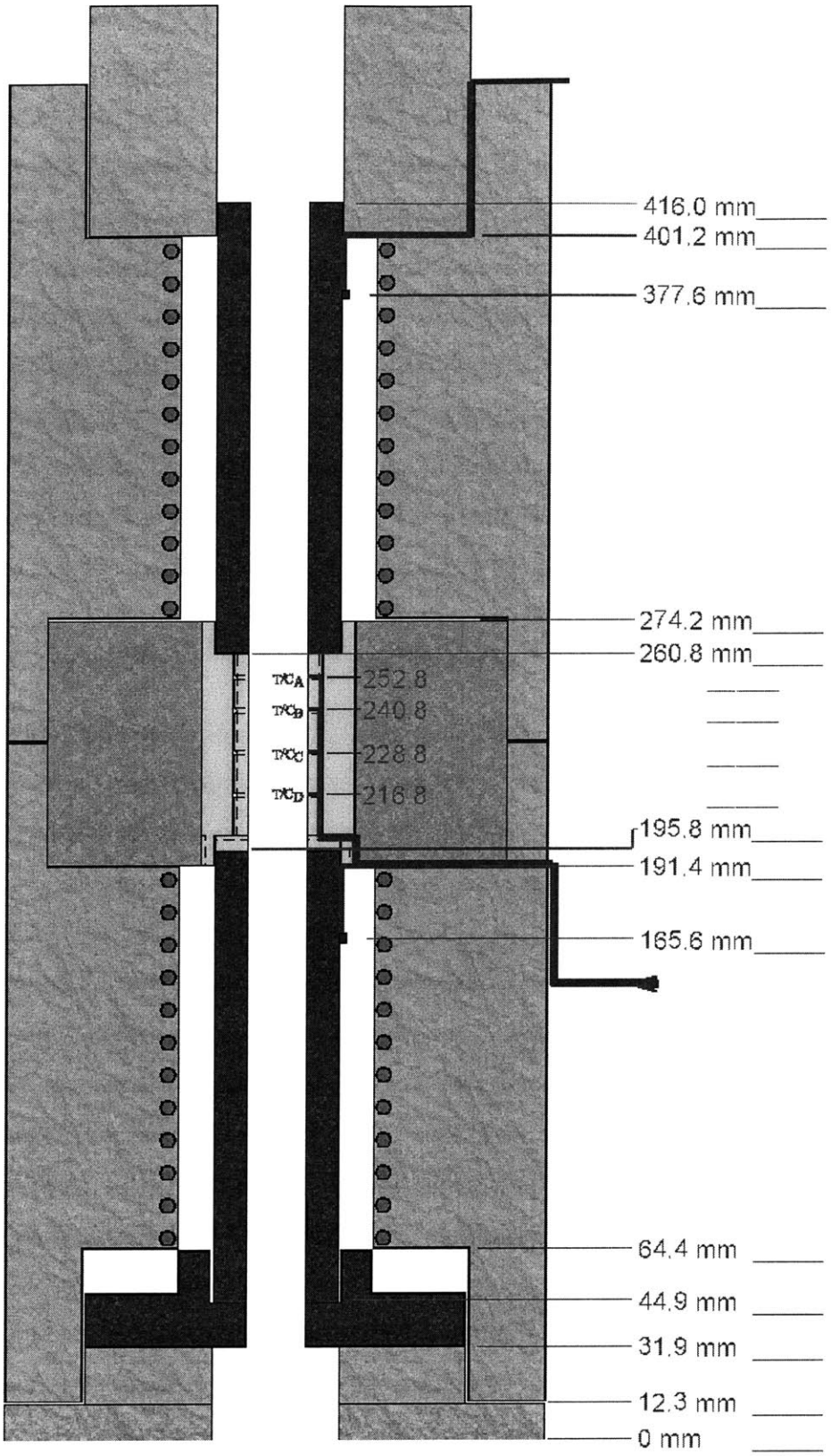

Figure 6-16: Schematic cross-section of the final furnace configuration with heights indicated.

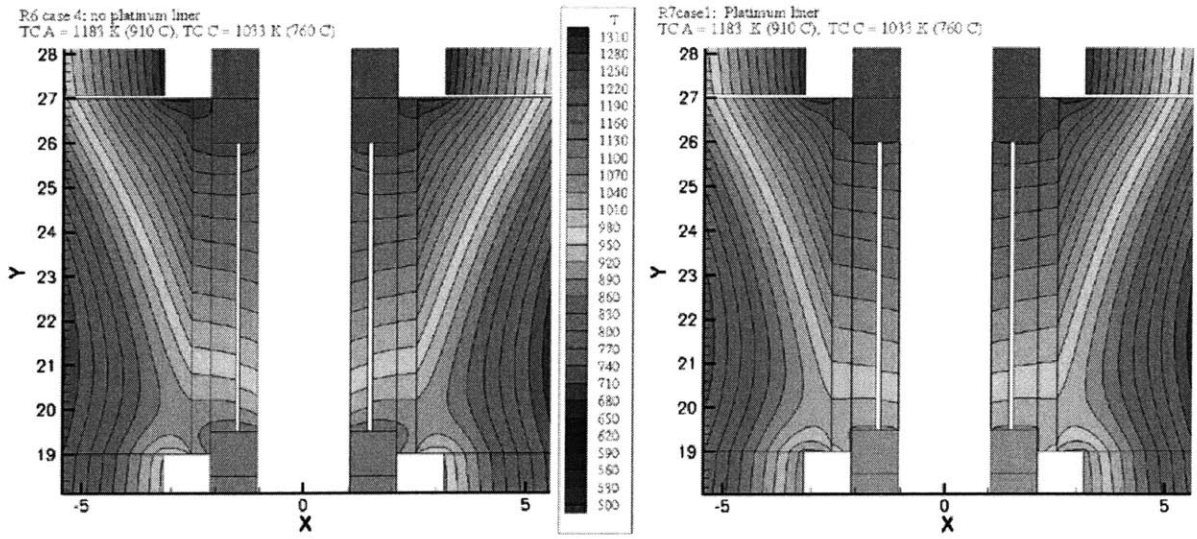

Figure 6-17: Comparison of gradient zone temperature distribution (a) without platinum liner and (b) with platinum liner.

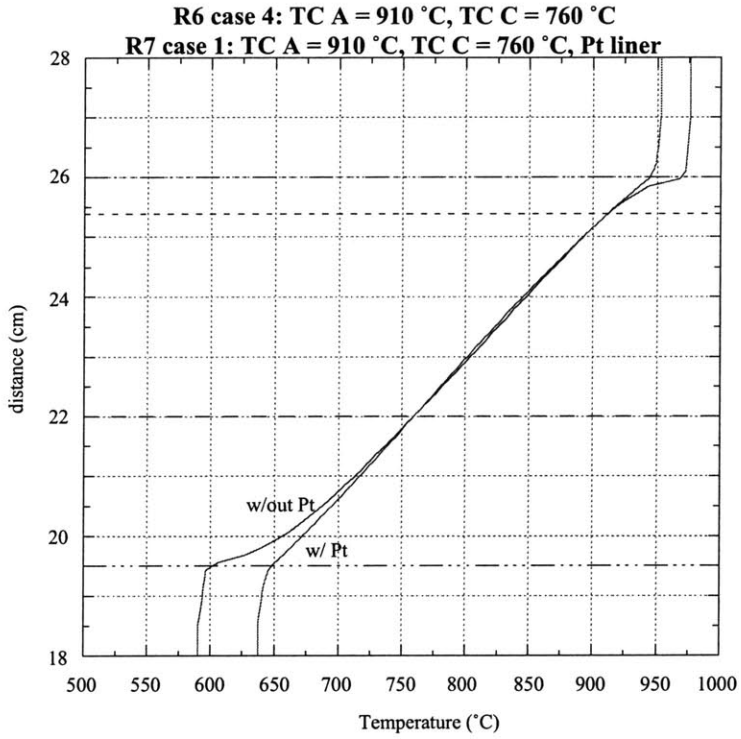

Figure 6-18: Effect of platinum liner on temperature of hot and cold zone.

CHAPTER 7: CZOCHRALSKI GROWTH EXPERIMENTS

7.1 Introduction

In order to perform growth experiments in the Bridgman-Stockbarger furnace, it was necessary to produce BSO crystals that could be used as charge material. Since a single crystal was needed for the seed in the B-S growths, several Czochralski growths were done in order to produce large boules that could be used for both seed and charge material. This work was carried out at the Air Force Research Laboratory (AFRL) on Hanscom Air Force Base because of the availability of large platinum crucibles on base (6 cm diameter and height, 1mm wall thickness). The furnace was configured with a main inner heater and an outer booster heater. The inner heater was controlled by a thermocouple at the bottom of the crucible while the outer heater was controlled by a thermocouple on the outside of the heater baffle. The furnace is depicted in Figure 7-1. Three Czochralski crystals were grown and analyzed.

7.2 Growth 1: CZ070201

The first growth run did not use a full charge and was intended mainly to establish viable growth conditions in the furnace. Starting material was 5-9's grade for both the SiO_2 and the Bi_2O_3, and the charge size was 600 g. From this growth run it was found that 3.5 mm/ hr. growth rate was too high and caused the seed to pull off the melt. A 2 mm/hr. growth was used with a rotation rate of 20 rpm based on Brice[28]. The necessary setpoints for the outer and inner heaters were established for subsequent growths.

The grown crystal is shown in Figure 7-2. The irregular shape is due in part to the proper setpoints not being known in addition to the misalignment between crucible and crystal. There are several differences between this first crystal and later crystals. First, no clear facets are visible. Secondly, the diameter of this crystal is much smaller. Lastly, the crystal stays light colored with exposure to room lights. Both of the later crystals turned dark once removed from the furnace.

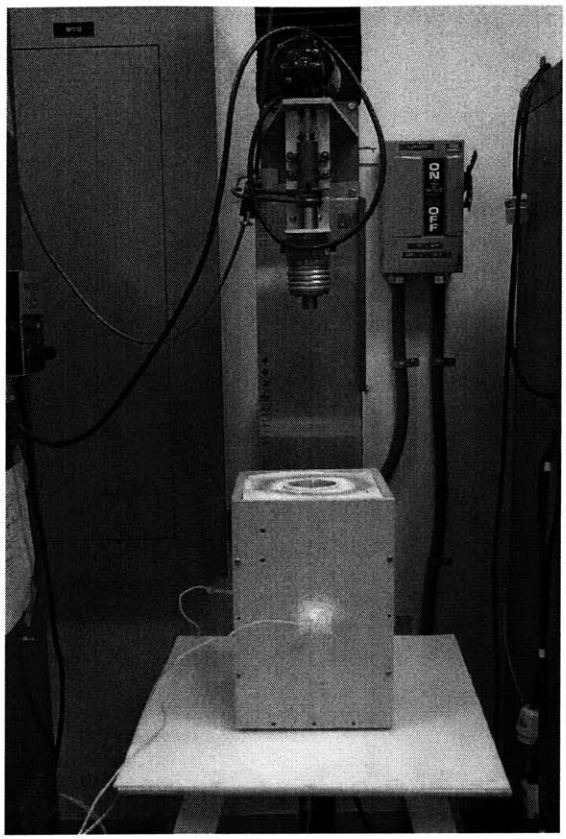

Figure 7-1: Czochralski furnace at AFRL that was used for growth of CZ crystals.

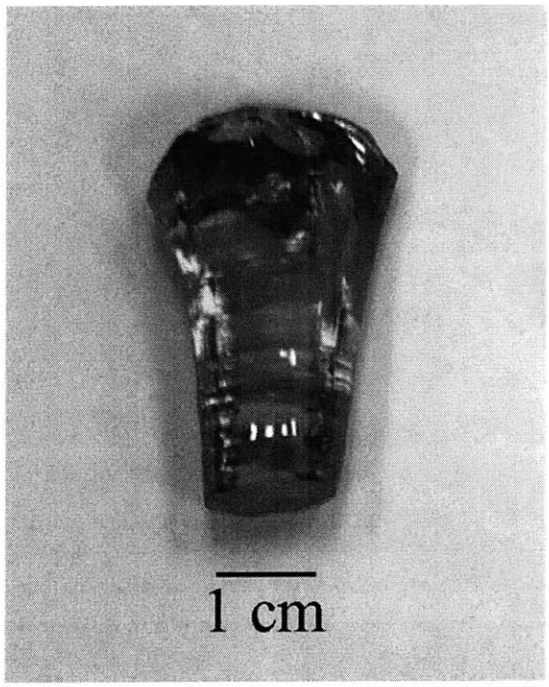

Figure 7-2: CZ072101 boule. This growth run was used to establish optimum conditions for subsequent runs.

7.3 Growth 2: CZ102301

The objective of the second growth was to produce a large boule that could provide enough charge material for several Bridgman-Stockbarger runs. The charge was pre-synthesized from 5-9's SiO_2 and 6-9's Bi_2O_3 and weighed 975 g. The crucible position was lowered by 2.5 cm in the furnace from the first run. Prior to seeding, the melt was allowed to equilibrate for several hours. The initial 6 hours of growth used a pull rate of 2 mm/hr and a rotation rate of 15 rpm. Because the diameter was increasing too rapidly after 6 hours of growth, the pull rate was increased to 2.5 mm/hr, and the rotation rate was increased to 20 rpm. This caused a sharp shoulder and subsequent decrease in the diameter of the crystal to a stable value.

Upon removal from the furnace, the crystal turned very dark with exposure to room light. It is shown in Figure 7-3. The external faceting is very pronounced for the entire length

Figure 7-3: CZ102301 boule. Top picture shows crystal after exposure to room light and resulting darkness. Backlit crystal shown on the bottom.

of the crystal. In an attempt to reduce the stresses in the crystal prior to machining, the crystal was annealed at 750 °C for 36 hours with a 0.3 °C/min. heat-up rate and a 0.2 °C/min. cooling rate. However, the crystal developed internal cracks during this process. Fortunately, this did not affect the ability to machine the crystal. The crystal was cut into several slices and then a 5/8" core drill was used to produce cylindrical pieces (14 mm in diameter) that were used for charge material in the B-S experiments. The top and bottom of the crystal contained a number of inclusions and these portions of the crystal were not used for charge material. The nature of the defects will be discussed in section 7.5.

7.4 Growth 3: CZ110501

The last growth run was very similar to the second one. Again, the objective was to produce a large boule that could provide charge material for B-S growth runs. The charge was pre-synthesized from 5-9's SiO_2 and 6-9s Bi_2O_3 and weighed 972 g. Upon melting the charge in the growth furnace, several chunks of material remained floating on the melt and could not be melted by raising the furnace temperature in excess of 100 °C. Platinum tipped tongs were used to remove this material. Analysis of the material using powder x-ray diffraction revealed that it was a mixture of eulytite and sillenite composition with a small fraction of SiO_2. The most likely source of this second phase is attributed to the pre-synthesis procedure. Growth proceeded as before for this crystal. The rotation rate was kept constant at 20 rpm for the entire run. The pull rate was changed from 2 mm/hr to 2.5 mm/hr after the first four hours of growth. This again produced a sharp shoulder with the main portion of the crystal being at an almost constant diameter. There is a slight decrease in the diameter during the second half of the boule. The grown crystal is shown in Figure 7-4.

As with CZ102301, the external faceting is very pronounced. Secondary facets on the corners are present after the shoulder but gradually disappear. The top and the bottom of the boule again contained inclusions. However, the inclusion rich portion of the crystal at the top is considerably larger than in CZ102301. The disappearance of the secondary facets coincides with the disappearance of the inclusions. Although not as pronounced as with the second crystal (CZ102301), the last crystal also turned dark upon removal from the furnace and exposure to room light.

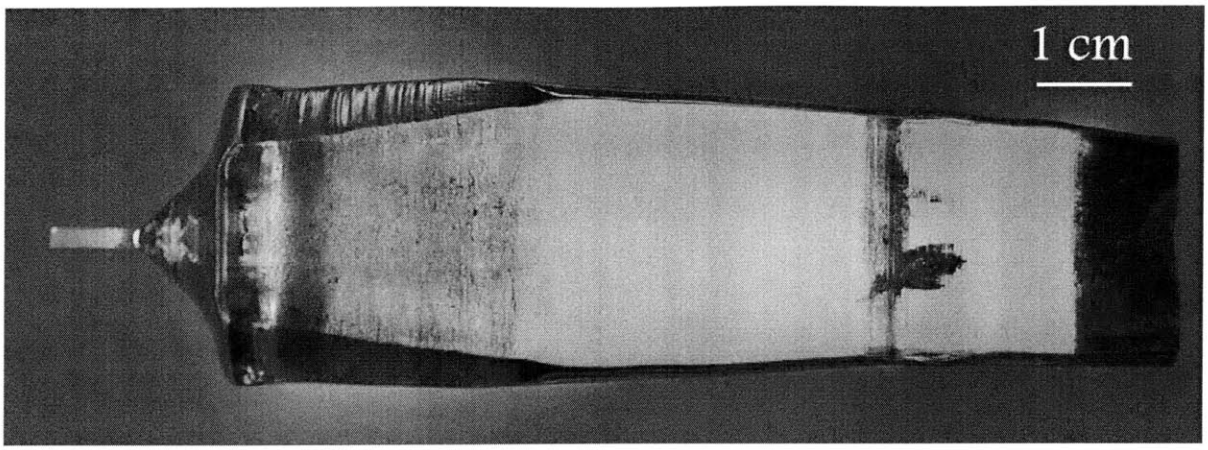

Figure 7-4: Image of CZ110501 boule. Initial portion as well as very bottom of boule contain a number of inclusions.

In an attempt to eliminate the cracking during the annealing process, the heating rate was reduced to 0.2 °C/min. and the crystal was annealed at 650 °C for 48 hours. It was cooled from 650 °C to 450 °C at 0.1 °C/min. and subsequently to room temperature at 0.2 °C/min. Unfortunately, the slower heating and cooling rates did not prevent the second boule from cracking during the annealing process. As with the second crystal, the internal cracks did not prevent the machining of samples by cutting 10-13 mm thick slice and then core-drilling 14 mm diameter cylinders from these slices.

7.5 Defect Analysis of Czochralski grown material

Since both of the large boules were subject to cracking during annealing, as well as exhibiting similar inclusion incorporation behavior, an analysis of these macroscopic defects was undertaken. An axial slice was cut perpendicular to one of the main facets. A second axial slice was cut at a 45 angle and as such was perpendicular to the secondary facet. These slices were mechanochemically polished with Syton (colloidal silica) on a Chemomet pad (Buehler). A schematic of the slice orientation with respect to the boule is shown in Figure 7-5. Prior to taking the axial slices from the CZ110501 boule, a slice was cut perpendicular to the growth axis that contained the bottom portion of the inclusions. This allowed the radial distribution of the inclusions to be observed.

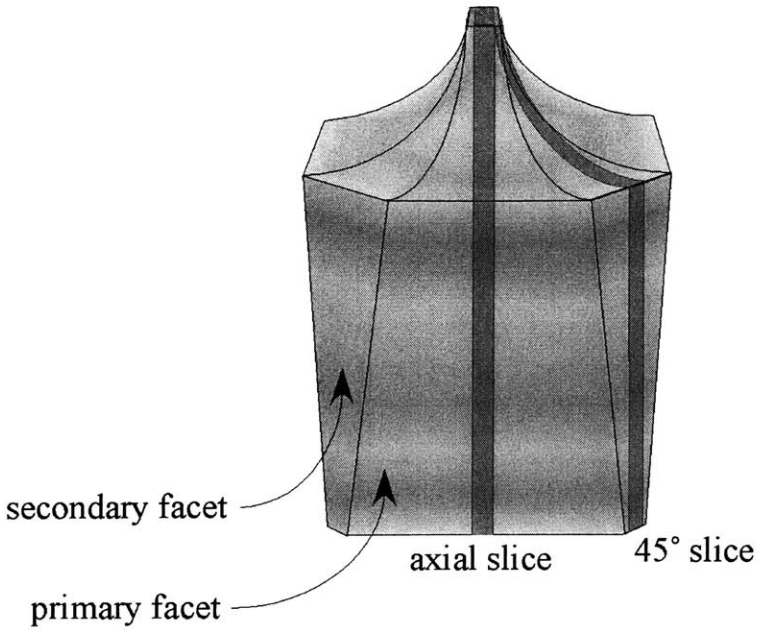

Figure 7-5: Schematic of orientation of axial slices taken out of CZ102301 and CZ110501.

7.5.1 Cracking

According to Brice[102], the maximum rate of temperature change without cracking is given by:

Equation 7-1
$$\left|\frac{dT}{dt}\right|_{max} = 8^{0.5}\frac{K}{c}\frac{\varepsilon_b}{\alpha R^2}$$

where κ = k/c, the ratio of thermal conductivity (k) to heat capacity (c)
ε_b = breaking strain (cm cm^{-1})
α = thermal diffusivity (cm sec^{-2})
R = radius of crystal (cm)

For BSO, the maximum temperature change rate is therefore 64/R^2 at the melting point and twice that near room temperature. The first CZ crystal has a maximum radius of 1.74 cm. The theoretical maximum cooling rate would therefore be 0.25 °C/min. Since the heating rate was higher than the critical rate, the crystal most likely cracked during the heat-up.

The second crystal, however, was processed below this critical rate. However, Brice[132] noted that there was an additional strain due to the existence of the facet, as given by:

Equation 7-2 $$\varepsilon_f = \alpha \Delta T_f$$

where ε_f = facet strain
β = thermal expansion coefficient (K^{-1})
ΔT = temperature difference between facet and bulk of crystal (K)

This results in a strain that is approximately ε_f times the ratio of area of the facet to area of the whole crystal. If the ratio is small, the additional strain due to facets is negligible. In CZ102301 and CZ110501, the central facet covered almost 100% of the total cross-section, and the strain at the edge of the facet would be significant. Taking Equation 7-2, even a 1 °C temperature difference adds considerable strain, since the thermal expansion coefficient is about 10% of the breaking strain. The cracking of the second crystal during the anneal is therefore attributed to a combination of the strain from the heating and/or cooling plus the strain from the existence of the facet.

7.5.2 Macroscopic Defects

The second and third crystals contained regions of defects characterized by inclusions and thin branchlike lines. As can be seen from Figure 7-3 and Figure 7-4, the defects are present at the top and bottom of the boules. They also appear at points where the crystal was disturbed from hitting the crucible wall.

Transmission optical microscopy revealed that there were two distinct kinds of defects. The first kind of defect (referred to as type I) consisted of larger amorphous structures with surface texture as well as internal structures. Figure 7-6 shows several representative micrographs. The second kind of defect (type II) consisted of thin, branchlike structures with some slightly enlarged, dark regions. The patterns formed by the 'branches' were unusual as can be seen in Figure 7-7.

In order to identify the nature of both types of inclusions, a sample was analyzed using scanning electron microscopy (SEM) and energy dispersive x-ray (EDX). The SEM clearly showed that the type I defects were voids, not inclusions. The series of images in Figure 7-8

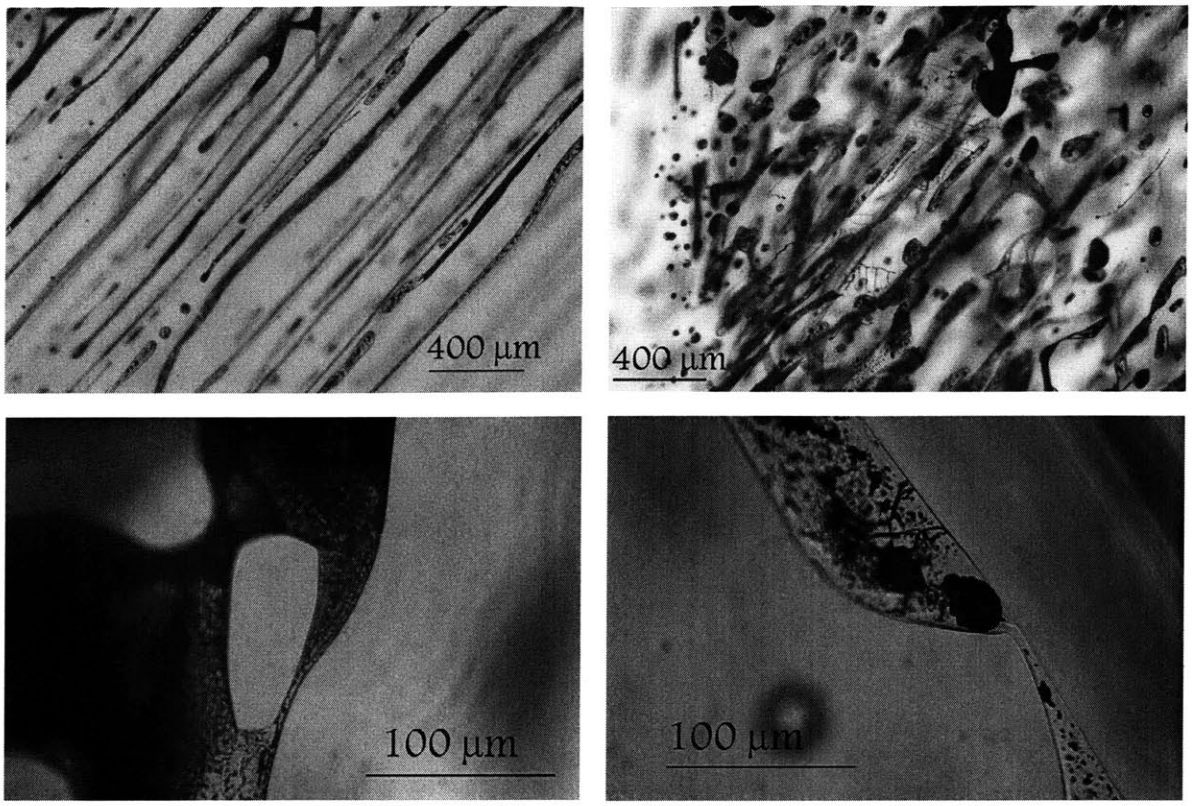

Figure 7-6: Micrographs of Type I defects found in CZ102301 and CZ110501.

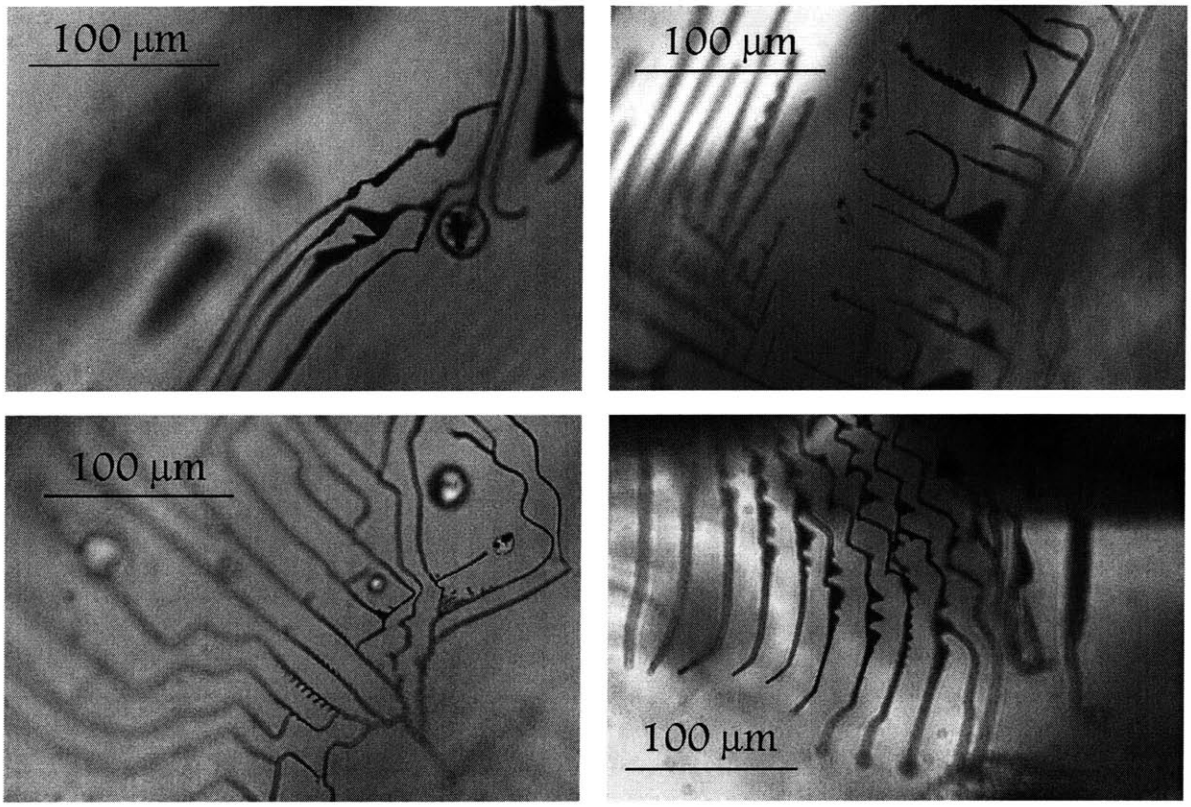

Figure 7-7: Micrographs of Type II defects found in CZ102301 and CZ110501.

correlates the SEM data with the optical data. Figure 7-8(a) is an image taken in pure reflection microscopy that shows two separate defect structures with a definite morphology. Figure 7-8(b) is an image taken in pure transmission microscopy, and it reveals that the two separate regions are actually connected and that type II defects are also present. Additionally, the type I defects are seen to be transparent in the regions that intersect the surface, *i.e.* the portions corresponding to the defects observed in pure reflection. Figure 7-8(c) is the SEM image, and it clearly shows the type I defect to be a void with a textured surface. Figure 7-8(d) is combined transmission and reflection illumination and it is observed that the type II defects were present when the voids formed since the texture observed in the SEM correlates to the location of the type II defects.

The thin branch-like defects were identified as being platinum inclusions using EDX. Optical microscopy was used to locate a type I defect that intersected the surface by comparing transmission and reflection images, shown in Figure 7-9 (a), (b), and (d). The SEM image Figure 7-9 (c) revealed the defect to be an inclusion separate from the matrix. EDX scans of both the matrix and the inclusion are shown in Figure 7-10. The EDX unambiguously identified the inclusion to be platinum. Elemental maps showed a deficiency in bismuth where the platinum is located.

7.6 Segregation

Analysis of the top portion of the boules revealed that both macroscopic and point defects were subject to non-uniform incorporation in the crystal. The distribution of the voids and the platinum was analyzed in order to establish the origin of the defects. It is well documented in literature[131,184,186,187,200] that Czochralski crystals can contain platinum inclusions.The source of platinum is from attack of the crucible by the melt. Voids are also common in oxide crystals[94,95,96,97,99,200,201].

7.6.1 Macroscopic defect segregation

A radial slice was taken from CZ110501 that contained the defects from the top of the boule and is shown in Figure 7-11. As mentioned earlier, two cross-sectional slices were also cut from each boule and polished on both sides: the first perpendicular to one of the main

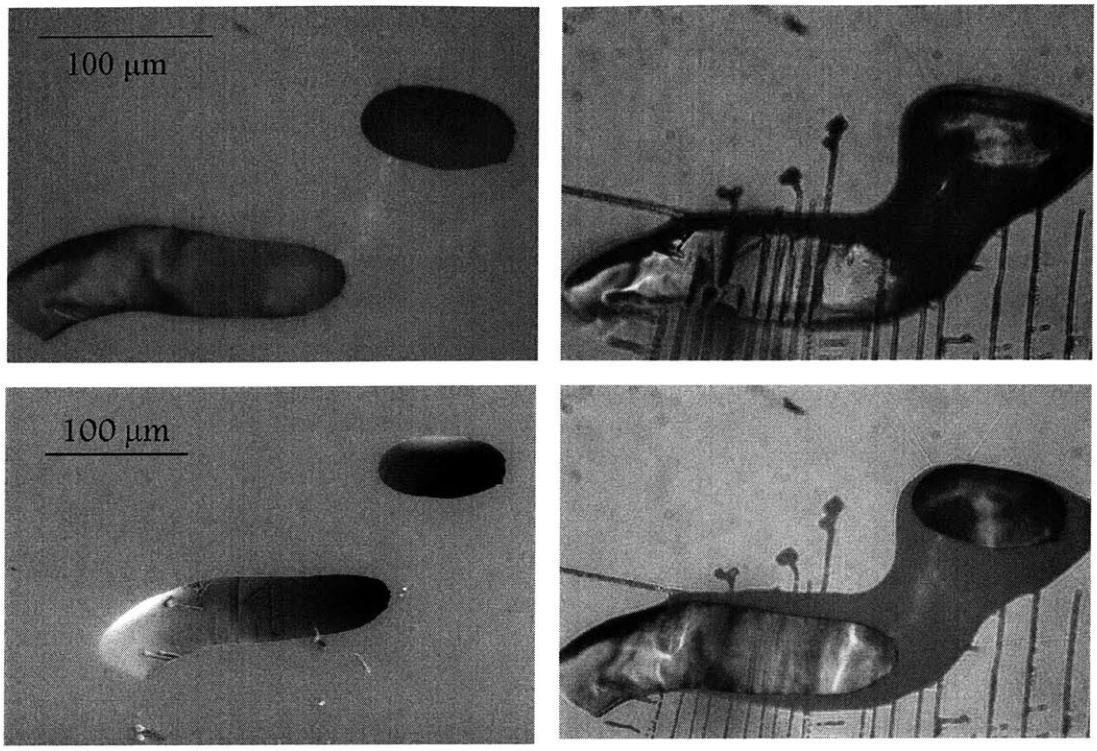

Figure 7-8: Sequence for identifying defect of type I as a void. (a) pure reflection (b) pure transmission (c) SEM (d) transmission and reflection.

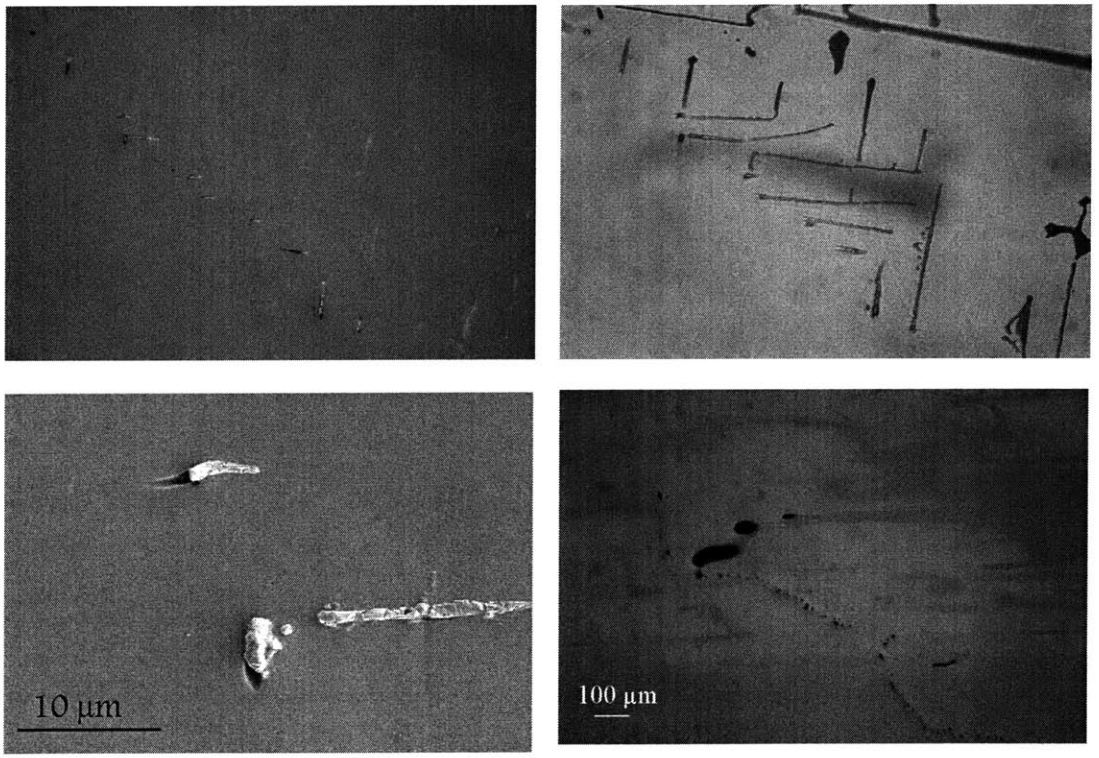

Figure 7-9: Sequence for identifying defect of type II as platinum. (a) pure reflection (b) pure transmission (c) SEM (d) transmission and reflection of analysis area.

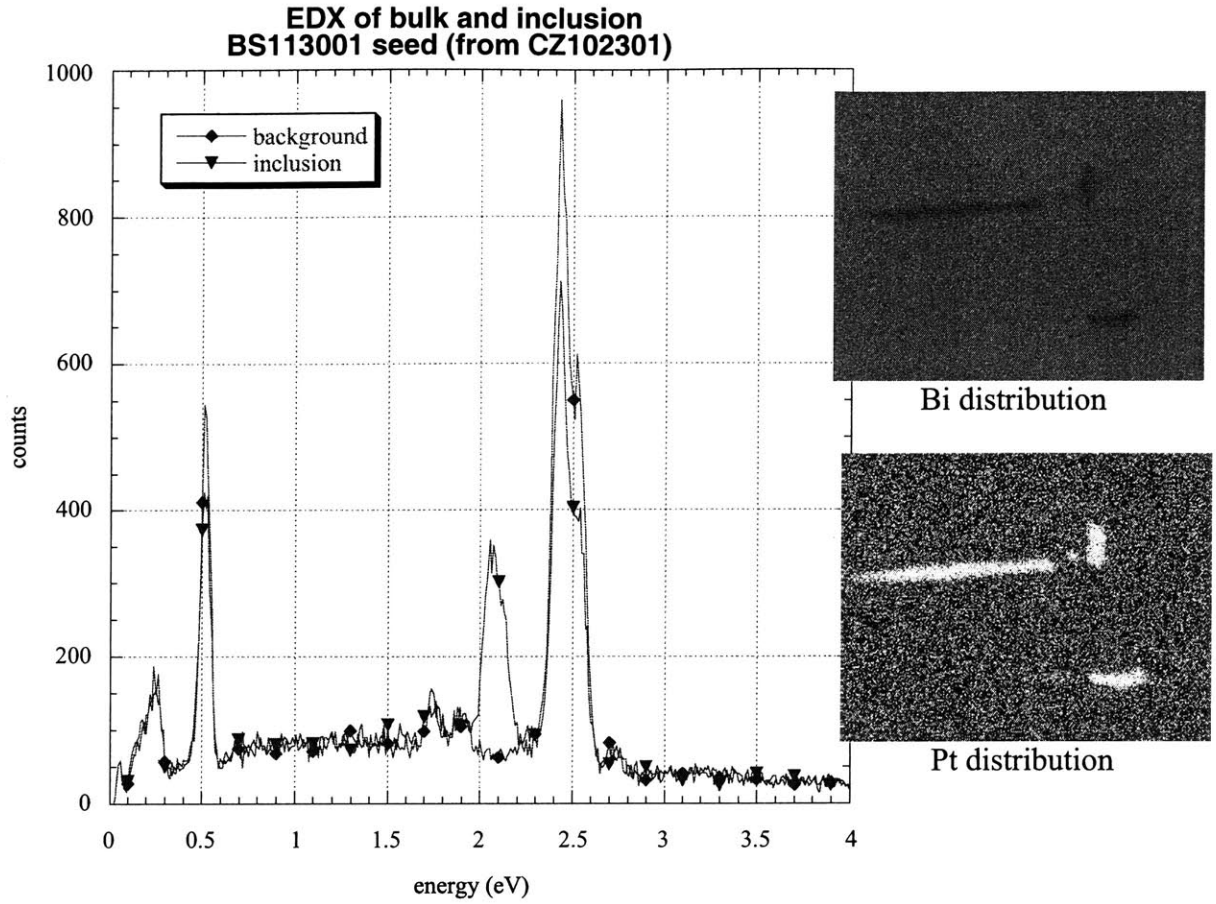

Figure 7-10: EDX of inclusion and surrounding bulk (on left). Elemental distribution maps for bismuth and platinum (on right).

external facets and the second one on a 45° diagonal from the first slice such that it was perpendicular to the secondary external facet. These slices are shown in Figure 7-12 and Figure 7-13 for CZ102301 and CZ110501, respectively.

The axial distribution of defects can be seen clearly in Figure 7-12 and Figure 7-13, and both crystals exhibit a similar pattern. Faceting is extremely prominent in both crystals. A darkened, central core can be seen to develop immediately, and it is due to the <100> facet. The shape of the interface is deeply convex, and growth is completed faceted. It appears that non-faceted material contains the highest density of voids and inclusions. It is not possible to unambiguously determine the mode of growth in this area of dense voids; however, the tendency for faceted material to be darker in color would also indicate that this high defect area was not growing as faceted material. The <100> facet does not support void formation as

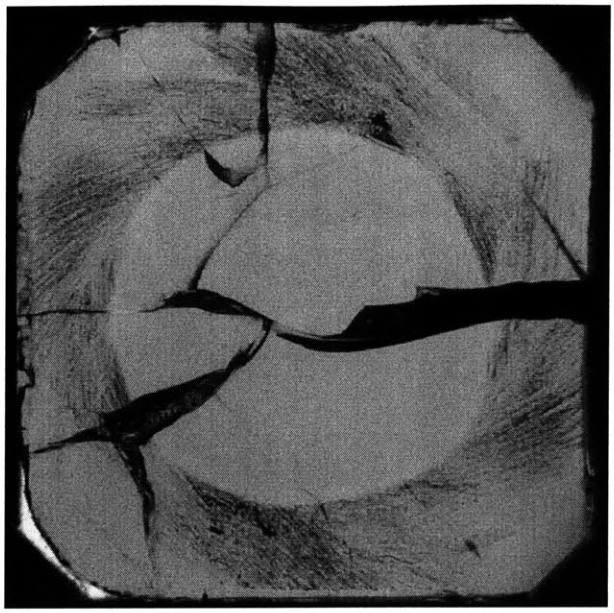

Figure 7-11: Radial slice from CZ110501 boule that includes inclusions (taken from top of boule at point where inclusions disappear).

can be seen clearly from the clean central core present in both crystals and from the pattern of void incorporation in the micrographs of Figure 7-13. The interface is faceted, alternating between <100> and <110>, and the voids form on the <110> facets but not on the <100> facets. Bubbles are no longer present in either crystal when the interface became a single, large <100> facet. The growth direction and mechanism therefore play a critical role in determining whether these defects were incorporated.

The general consensus in the literature is that for low growth rates, bubbles are not incorporated; for high growth rates, bubbles are incorporated; and that for intermediate growth rates, the fluid flow determines whether or not bubbles are swept in towards the center or outwards to the edge of the crystal. Miyazawa[96] and Kobayashi[99] both analyzed bubble entrapment as a function of fluid flow, and they concluded that bubbles were swept towards the center and incorporated when natural convection is dominant. Looking at the axial and radial slices, it is observed that the defects appear only on the periphery and the central core is free of these defects. Additionally, since the prominent bubble entrapment occurred after the interface inversion, bubble entrapment in CZ102301 and CZ110501 was not due to fluid flow transport of bubbles. It is therefore concluded that the growth rate must be too high to allow for sufficient diffusion of gaseous constituents away from the interface[94,95,99]. The defects are

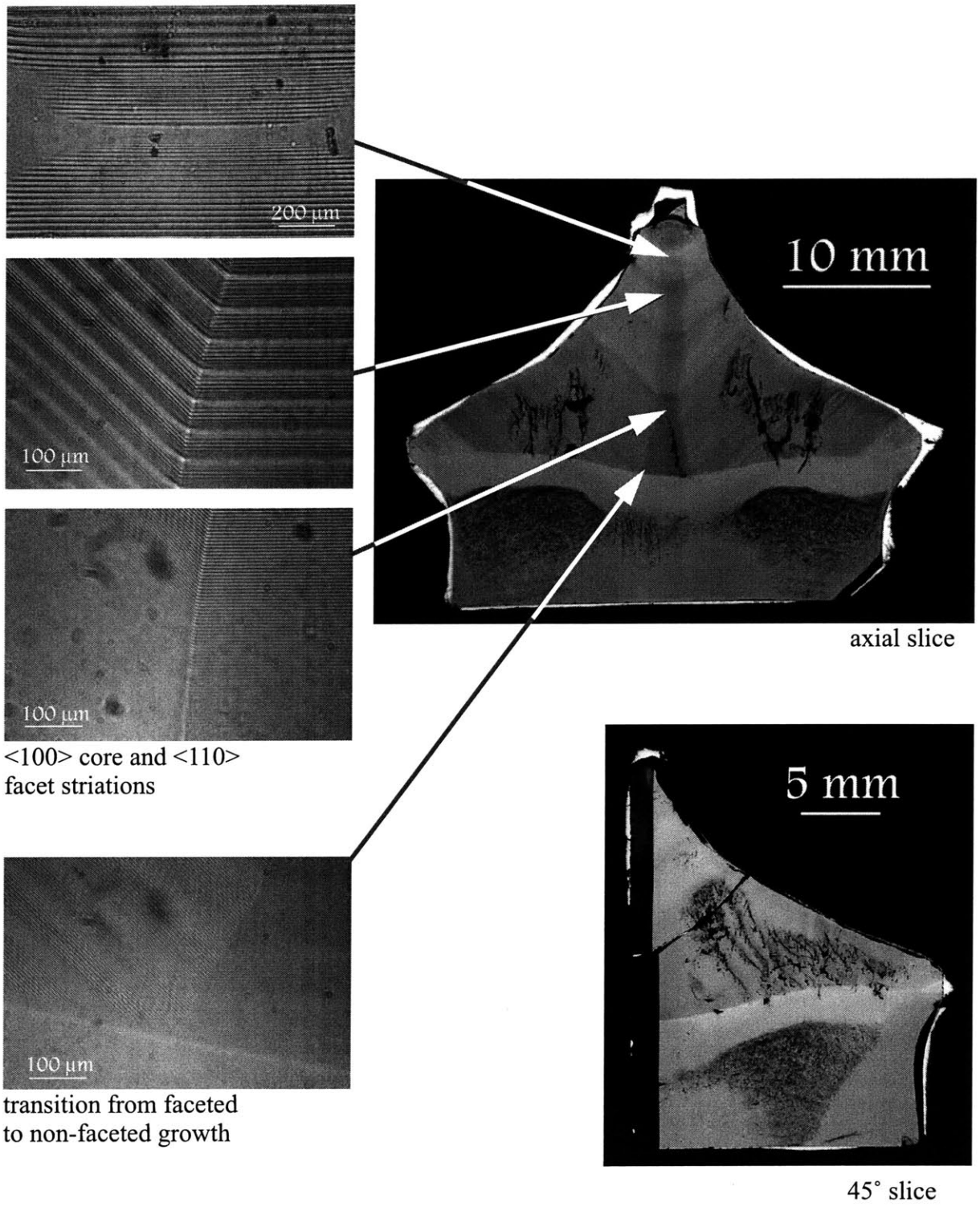

Figure 7-12: Axial slices of CZ102301 boule with micrographs of striations seen in the facet, as well as the transition between facet and non-faceted growth.

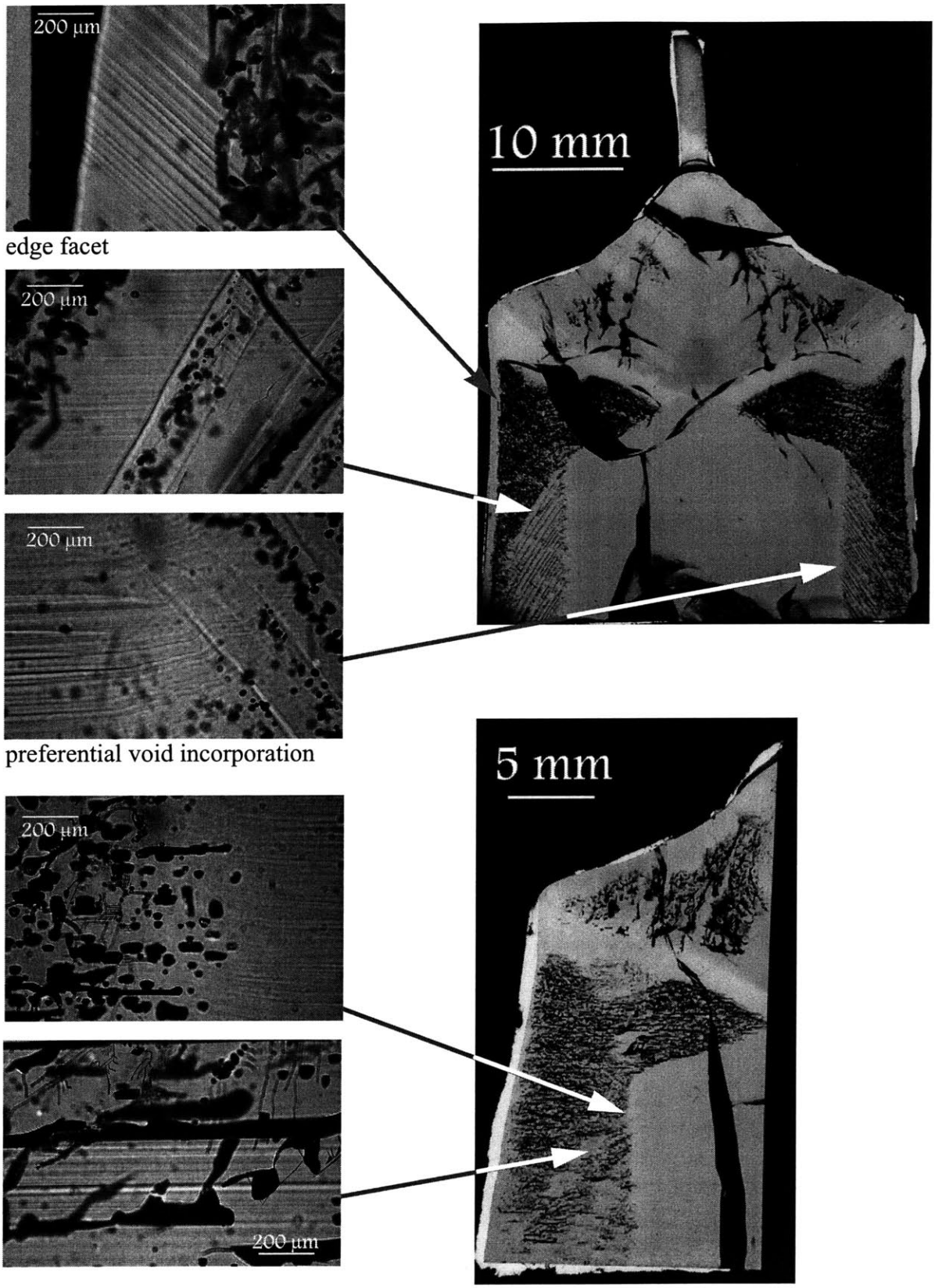

Figure 7-13: Axial slices of CZ110501 boule. Adjoining micrographs show extreme faceting, preferential void incorporation and facet to non-facet transition.

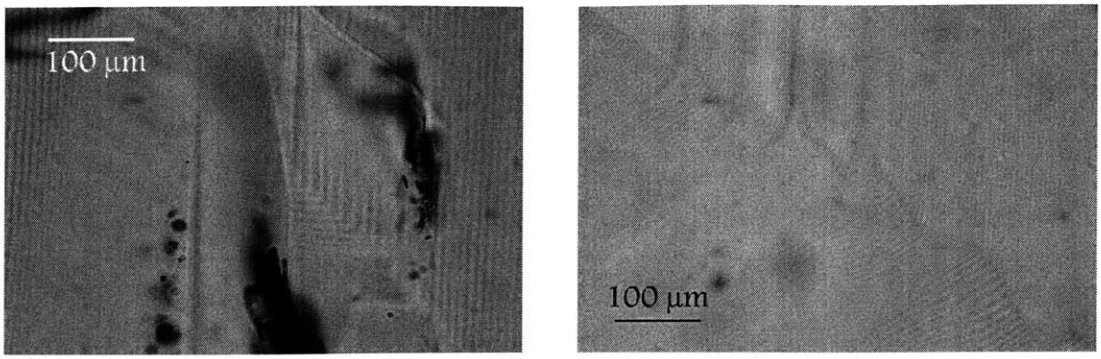

Figure 7-14: Images from the 45° slice of CZ110501 boule that shows the strong tendency towards faceting. as well as the fact that voids interrupt facet growth.

oriented in straight lines that rotate around the central core in a stepwise manner. The melt underneath the crystal is rotated by the crystal, and the voids are swept along with the fluid prior to being incorporated. This explanation is in agreement with the statements by Miyazawa that once bubbles are nucleated they grow as the crystal grows. Lastly, the portion of the crystal contain the highest density of bubbles corresponds to the periods where fluid flow transitions from being controlled by natural convection to being controlled by forced convection. It is postulated that since the fluid flow during this period is random, no clear pattern is observed in the bubble incorporation.

7.6.2 Point defect segregation

The macroscopic images capture quite well the problem of segregation of point defects. Variations in the optical absorption of BSO are due to changes in the concentration of the point defects responsible for the absorption behavior of BSO. Faceted growth results in material that is darker, and it is therefore assumed to have a higher concentration of point defects. Several authors mention the preferential incorporation of photochromic centers in the facets[19,108,153]. It is also known that the faceted material has a slightly different lattice constant[19,98] and is postulated that this effect might be due to preferential absorption of defects. Comparing growth from different facets, the <100> facet is the darkest, followed by the <110> facet and then by the non-faceted grown material which is lightest and more yellow in color. Chemical analysis of facet versus non-facet material was not pursued since the bulk material that was used in the current work came from regions that were completely faceted.

However, the presence of the darker core and faceted material, as well as the presence of striations, is in line with the documented literature about CZ growth.

Examining the phase diagram near the composition of BSO in, it is seen that there is a small existence region for the solid. This existence region is one explanation of the observed segregation. If the composition of the melt varies due to convection, the solid that is formed will also vary. The classic analysis of Burton, Prim, and Schlichter[202] gives the composition of the solid as a function of both the composition of the melt as well as the growth rate as given by:

Equation 7-3

$$C_s = \frac{C_l k_o}{k_o + (1 - k_o)\exp(-V\delta/D)}$$

where C_s = composition of the solid
C_l = composition of the liquid
k_o = distribution coefficient
V = solidification rate
d = boundary layer thickness
D = diffusion coefficient

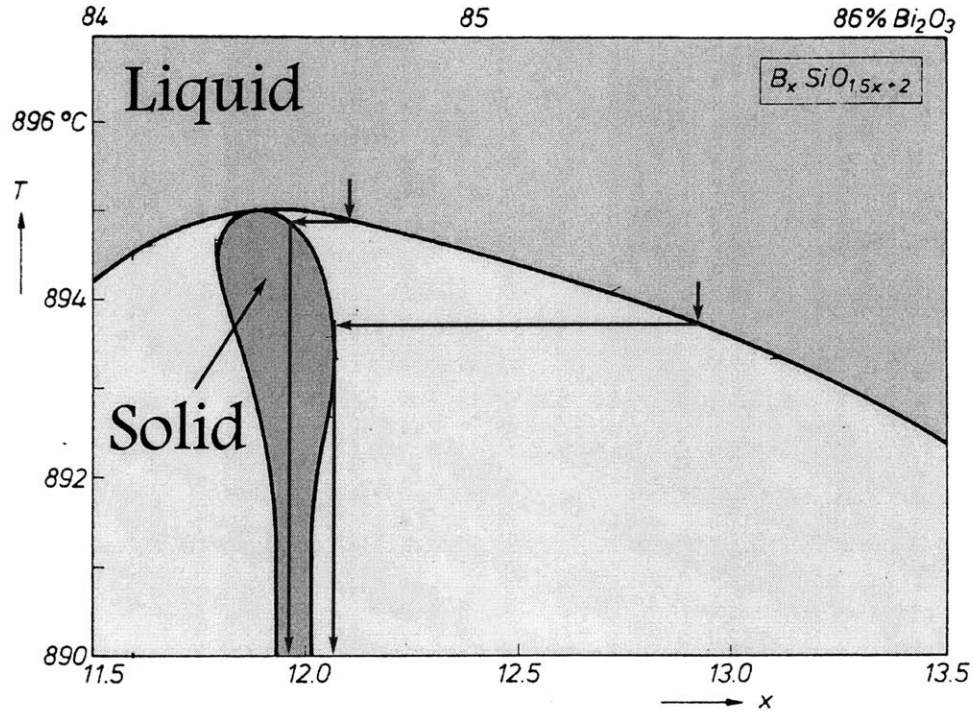

Figure 7-15: Phase diagram of BSO showing existence region of solid[19].

Striations arise from misalignment between crystal and crucible axis and from thermal fluctuations in the melt. Variations in the actual growth rate result from localized remelting and solidification and from temperature changes at the melt interface. Analyzing the images in Figure 7-12 and Figure 7-13, striations that have a period just a little longer than predicted for rotational striations are found. Striations with a variety of longer periods, ranging from 10 to 100 seconds, are also observed. In the central core of CZ110501, rotational striations are observed, as well as variations with a period of about 30 seconds. Non rotational striations are due to variations in the microscopic growth rate resulting from thermal fluctuations in the melt underneath the crystal.

7.7 Convection

The shape of the interface, and hence defect incorporation, is dominated by the fluid flow in the melt. The observed distribution of defects in the initial part of the CZ boules can be easily explained in these terms. As detailed in the literature review, the two opposing forces in the melt are due to natural convection induced by radial temperature differences and forced convection induced by the rotating crystal. If natural convection dominates, the interface tends to be convex, while it is flat or concave if forced convection either balances or overpowers natural convection. Although the primary factor influencing the interface shape is hydrodynamics, heat transfer is also important in determining the final interface shape at any given point during growth. This aspect makes detailed analysis quite difficult – as the crystal grows, both the radiative and the conductive heat fluxes change due to the increase in crystal size, reduction in melt height, and changing view factors. Nevertheless, using the available literature, a plausible explanation linking the fluid flow and resulting interface morphologies during the CZ102301 and the CZ110501 growths can be proposed.

There are three main dimensionsless numbers that are of importance (neglecting surface tension driven convection, *i.e.* Marangoni flow). They are the Prandtl, Reynolds, and Grashof numbers. The Prandtl number is a ratio of momentum to heat diffusivity. The Grashof number is a measure of the natural convection due to the radial temperature variations, and the Reynolds number is a measure of the forced convection due to the rotation of the crystal. However, as was noted in Chapter 2, not all analyses define the parameters as given by Equation 7-4. The Grashof number is sometimes defined by using the melt height (d)

instead of the crucible radius or diameter. The length scale in the Reynolds number, shown in Equation 7-4 with the crystal diameter (d) is defined in some papers by the crystal radius, the crystal diameter times π, or even the crucible radius.

Equation 7-4

$$\mathrm{Pr} = \frac{\mu C_p}{k} = \frac{\nu}{\alpha}$$

$$\mathrm{Gr} = \frac{D_c^3 g\beta(T_c - T_m)}{\nu^2}$$

$$\mathrm{Re} = \frac{d^2\omega}{\nu}$$

where μ = dynamic viscosity (kg m^{-1} sec^{-1})
C_p = heat capacity (J kg^{-1} K^{-1})
k = thermal conductivity (W m^{-1} K^{-1})
α = thermal diffusivity (m^2 sec^{-1})
ν = kinematic viscosity (m^2 sec^{-1})
D_c = crucible radius (m)
g = acceleration due to gravity (m sec^{-2})
β = coefficient of thermal expansion (K^{-1})
T_c = temperature of crucible (K)
T_m = melting point (K)
ω = crystal rotation rate (rad sec^{-1})
d = crystal diameter (m)

Because the set-up was not intended to study the CZ growth process, one of the key parameters that was not assessed is the radial temperature variations. The Grashof number is used almost exclusively to assess the strength of natural convection in the CZ system, and one of the parameters is this temperature difference. Using a reasonable range of values for these variables gives a good approximation to when flow transitions should occur and allows comparison to experimental data.

7.7.1 Phenomenological Explanation

Figure 7-16 and Figure 7-17 represent schematics for six different stages of growth for CZ102301 and CZ110501 respectively. During the initial stages of growth, the crystal is small

and natural convection dominates. As the diameter increases, the strength of forced convection starts to increase and the interface flattens resulting in multiple, stepwise facets. At the shoulder, the rotation rate and pull rate (for CZ102301) are increased, resulting in a sudden transition that causes considerable remelting of the crystal. As the crystal continues to grow under these mixed conditions, the interface is nonfaceted. As forced convection becomes dominant, the interface becomes faceted again and is initially slightly concave. Eventually, the <100> covers the entire crystal, and the interface is flat. At the end of growth (not pictured) the interface becomes concave with inclusions as the melt depth is shallow. For CZ110501, only the pull rate is increased in the shouldering process, and the flow transition is more gradual without significant remelting of the crystal. Additionally, the interface is not concave as forced convection starts to dominate, but rather it is slightly convex with a large center <100> facet. This central facet eventually covers almost the entire crystal with the exception of a small edge facet that is present for the entire length of the inclusion-free, flat interface portion of the crystal.

7.7.2 Comparison of observed flow transition with literature

As was noted by Nikolov et al.[49], the literature presents a variety of criteria for determining the critical Reynolds number for flow transition. Since the series of papers by these authors is the most recent of the analyses, and they use an empirical fit to cover a wide range of Prandtl, Grashof, and Reynold numbers, their relationships were employed in the current analysis. In order to get a good estimate for the melt height, the starting volume of melt was calculated. Initially, the melt height does not drop significantly since the crystal diameter is small. Therefore the initial height (h_i) was used for preliminary analysis aimed at determining the radial temperature variation. The drop in melt height, as the diameter increased, was estimated by using the point when the translation rate increased. This drop is the difference between the actual crystal length and the length that would be expected from multiplying the pull rate by the elapsed time. From Nikolov et al.[49], the following empirical relationship for the critical rotation rate (rad sec^{-1}) is found:

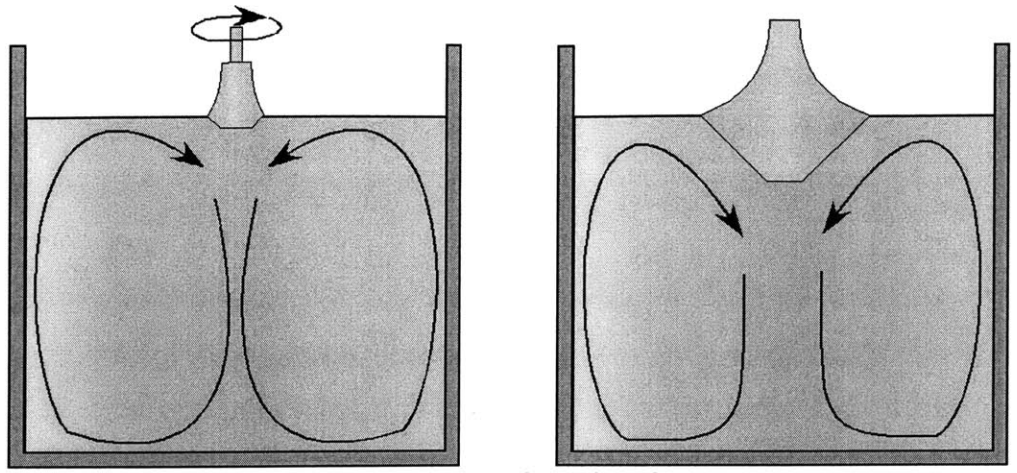

natural convection dominates

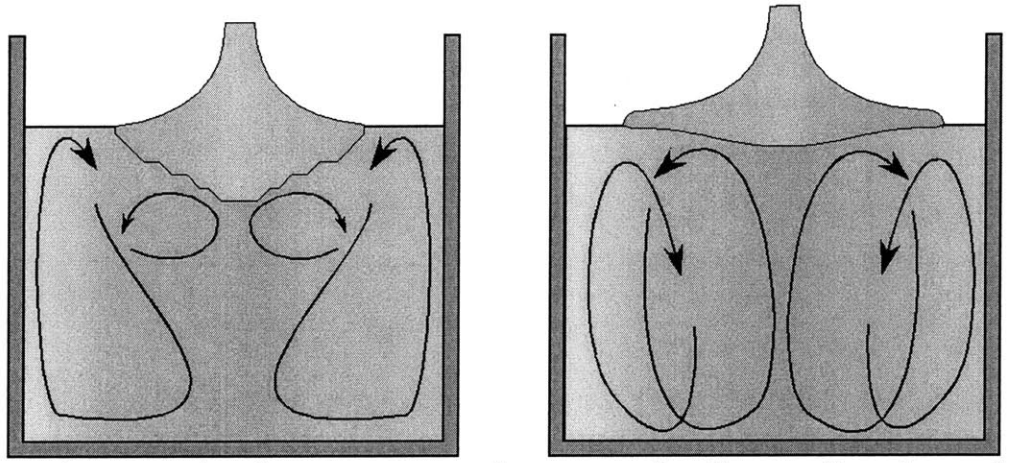

forced convection becomes more important leading to flow inversion

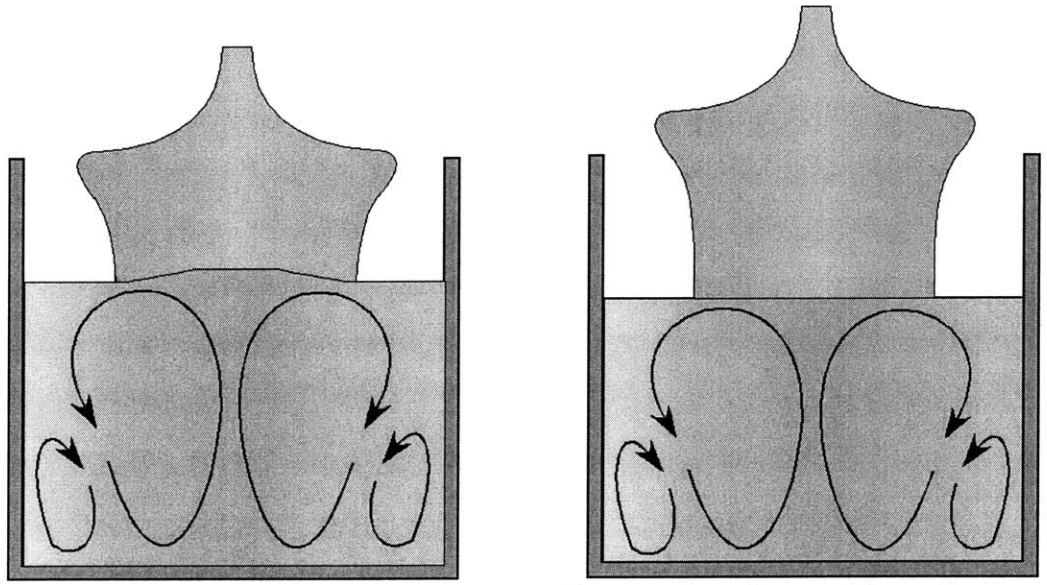

forced convection dominates leading to flat, faceted interface

Figure 7-16: Evolution of convection in melt for CZ102301.

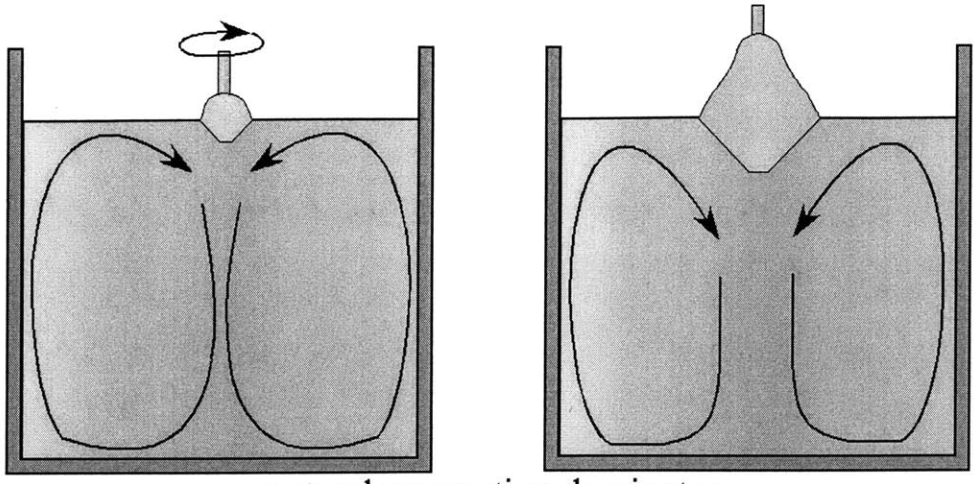

natural convection dominates

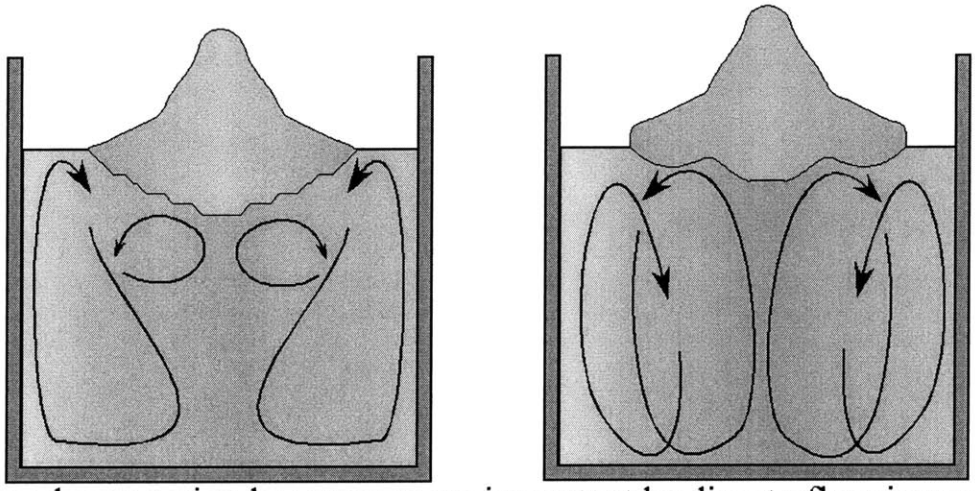

forced convection becomes more important leading to flow inversion

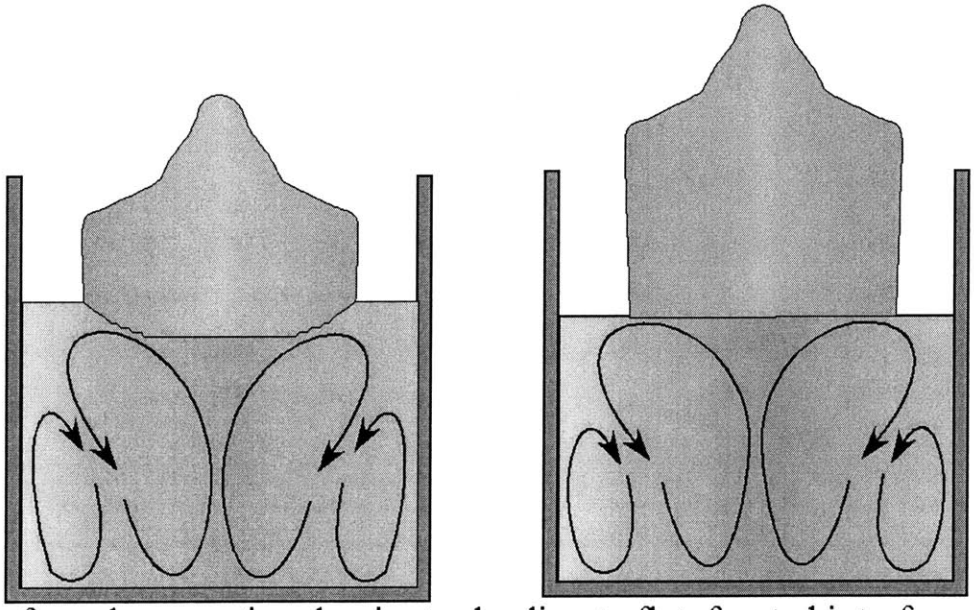

forced convection dominates leading to flat, faceted interface

Figure 7-17: Evolution of convection in melt for CZ110501.

Equation 7-5

$$N_{crit} = \frac{3.18\left(g\beta\Delta T\right)^{0.44} D^{0.245} h^{0.155} \nu^{0.12}}{d^{1.08}}$$

where N_{crit} = critical rotation rate (rad sec^{-1})

g = acceleration due to gravity (cm sec^{-2})

ΔT = temperature difference (K)

β = coefficient of thermal expansion (K^{-1})

D = crucible diameter (cm)

h = melt height (cm)

d = crystal diameter (cm)

ν = viscosity (poise)

Since the growth experiments were at either 15 or 20 rpm, the equation was rearranged to give an expression for the critical diameter based on a given rotation rate

Equation 7-6

$$d_{crit} = \left[\frac{3.18\left(g\beta\Delta T\right)^{0.44} D^{0.245} h^{0.155} \nu^{0.12}}{N}\right]^{0.926}$$

The radial temperature difference (ΔT) needed to be estimated because there was no experimental data available. In the CZ102301 growth, there is a very distinct flow transition at the point when the rotation rate was increased, and the diameter at that instant is known. Therefore, Equation 7-5 could be used as a starting point for estimating ΔT. Using ΔT values of 10, 40, and 80 K, the critical rotation rate was calculated and is plotted in Figure 7-18. The shaded region corresponds to the 15 - 20 rpm region. The diameter at the transition is approximately 3.6 cm, and from the graph, it can be deduced that the temperature gradient should lie between 40 and 80 °C. Similarly, for CZ110501, the diameter at which the transition started (between 3.5 -3.8 cm) was known, so the ΔT at which the critical rotation rate dropped below 20 rpm for that diameter was needed. As with CZ102301, the appropriate ΔT lies between 40 and 80 degrees, as seen in Figure 7-19.

Having determined that the temperature difference between crucible and crystal lies somewhere between 40 and 80 K, it was possible to use both the critical rotation rate and the critical diameter (as per Equation 7-6) to refine the estimate. Table 7-1 and Table 7-2 contain the results from these calculations for CZ102301 and CZ110501, respectively.

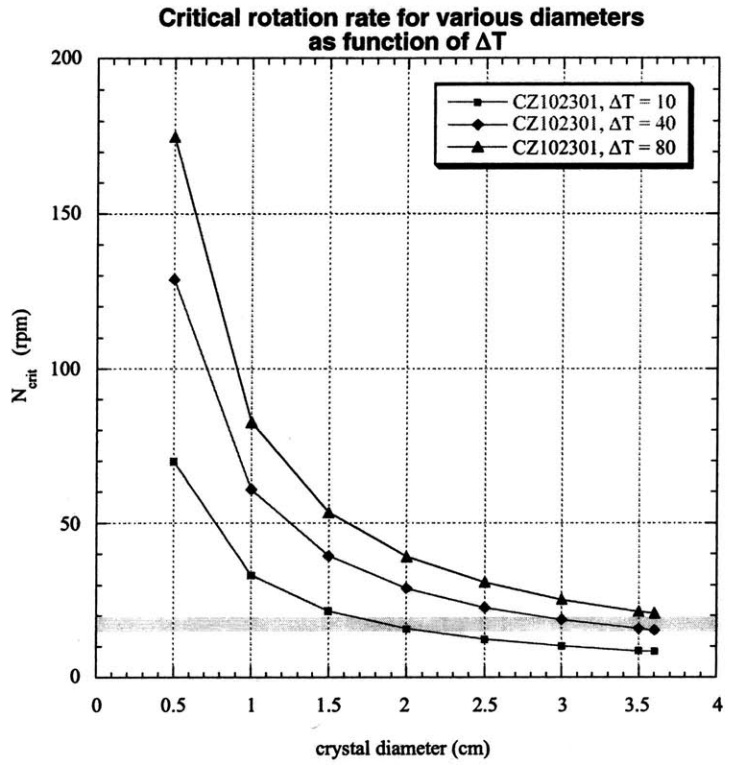

Figure 7-18: Variation of critical rotation rate as a function of crystal diameter for CZ102301.

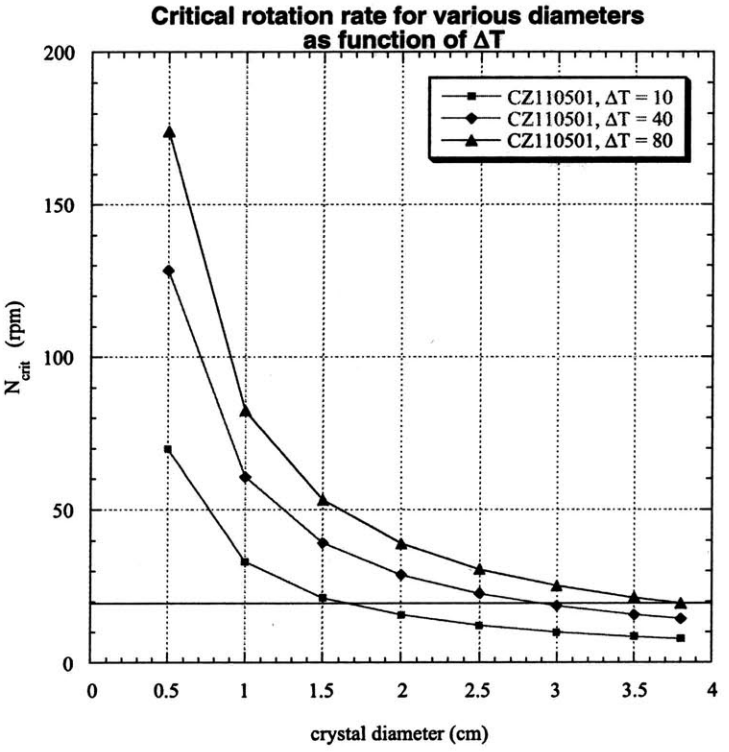

Figure 7-19: Variation of critical rotation rate as a function of crystal diameter for CZ110501.

ΔT	h	d	N	Gr	Re_{crit}	N_{crit}	d_{crit}
40	4.44	3.6	15	659232	688	15.2	3.65
40	4.44	3.6	20	659232	688	15.2	2.80
50	4.44	3.6	15	824040	759	16.8	4.00
50	4.44	3.6	20	824040	759	16.8	3.07
60	4.44	3.6	15	988848	823	18.2	4.31
60	4.44	3.6	20	988848	823	18.2	3.30
65	4.44	3.6	15	1071252	852	18.9	4.45
65	4.44	3.6	20	1071252	852	18.9	3.41
70	4.44	3.6	15	1153656	880	19.5	4.59
70	4.44	3.6	20	1153656	880	19.5	3.52
80	4.44	3.6	15	1318464	934	20.7	4.84
80	4.44	3.6	20	1318464	934	20.7	3.71

Table 7-1: Determination of ΔT for CZ102301 using N_{crit} and d_{crit}

ΔT	h	d	N	Gr	Re_{crit}	N_{crit}	d_{crit}
40	4.38	3.5	20	659232	669	15.7	2.79
40	4.38	3.8	20	659232	722	14.3	2.79
50	4.38	3.5	20	824040	738	17.3	3.06
50	4.38	3.8	20	824040	796	15.8	3.06
60	4.38	3.5	20	988848	800	18.7	3.30
60	4.38	3.8	20	988848	863	17.1	3.30
65	4.38	3.5	20	1071252	828	19.4	3.40
65	4.38	3.8	20	1071252	894	17.8	3.40
70	4.38	3.5	20	1153656	856	20.1	3.51
70	4.38	3.8	20	1153656	923	18.3	3.51
80	4.38	3.5	20	1318464	908	21.3	3.71
80	4.38	3.8	20	1318464	979	19.5	3.71

Table 7-2: Determination of ΔT for CZ102301 using N_{crit} and d_{crit}.

It was found that the height parameter did not appreciably affect the results. The heights listed are estimates based on crystal length at the time of pull rate increase. For CZ102301, the main criteria for finding ΔT was a value such that the critical crystal diameter was larger than the critical diameter for 15 rpm and smaller than the critical diameter for 20

rpm. Increasing the rotation rate from 15 to 20 rpm would then have induced the flow transition. As can be seen from Table 7-1, a ΔT value between 40 and 70 fulfills this criteria. Looking at CZ110501, the transition is more gradual and the criteria for ΔT was such that the critical diameter and rotation rate coincided with the actual diameter and rotation rate. The best fit comes from $\Delta T = 70$ degrees. It is therefore concluded that the radial temperature gradient in the CZ system is around 70 degrees and that the experimental data (*i.e.* observed interface inversion in axial slices of data) corroborate this result.

CHAPTER 8: BRIDGMAN-STOCKBARGER GROWTHS

8.1 Introduction

Bridgman-Stockbarger growth experiments were performed with the goal of investigating the effect of growth conditions on defect incorporation. The primary variable that was altered was the thermal environment via the imposed gradient. Additionally, several different growth rates were used during each growth. The initial growth was done using the Zirconia insulation and a high temperature gradient. The second growth was performed under the same conditions to test for reproducibility of growth conditions. The last growth was done with the Zirpor insulation and employing a low gradient such that the maximum melt temperature did not exceed 930 °C.

8.2 Ampoule Assembly

Ampoules were made from quartz tubes (15 mm x 17 mm). A two to three cm long quartz rod piece (15 mm diameter) was sealed into quartz tubes to provide a flat, bottom surface. The rod position was such that the bottom portion of the quartz tube mated with the boron nitride support piece. A platinum cup was used on the bottom of the sample. Platinum confinement was a thin foil (0.17 mm thick) that was wrapped into a cylinder and inserted into the cup. A schematic of the ampoule design is shown in Figure 8-1. An unassembled ampoule is shown in Figure 8-2. The following procedure was used to prepare ampoules:

1. orientation of seed with Laue X-ray
2. clean seed and charge material in methanol
3. rinse seed and charge material in DI water
4. micrographs of platinum surfaces
5. clean platinum parts in hydrochloric acid
6. rinse platinum with DI water
7. if not already annealed, heat platinum foil for 30 minutes at 1000 °C
8. measure, weigh, and photograph seed and charge material
9. assemble ampoule
10. evacuate/purge with 20% O_2 balance argon three times
11. evacuate for at least 12 hours
12. backfill to 0.3 atm. and seal

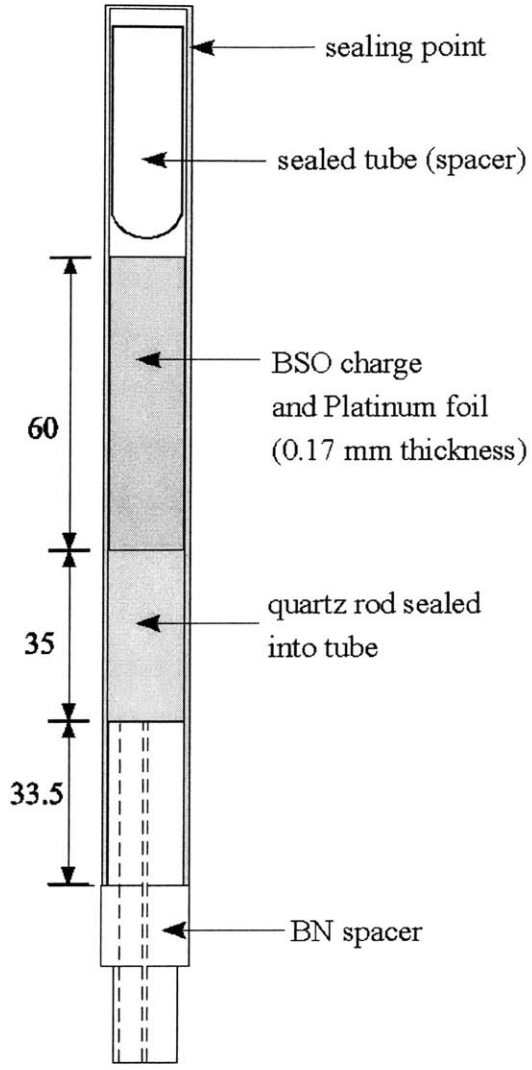

Figure 8-1: Schematic of ampoule design for Bridgman-Stockbarger experiments

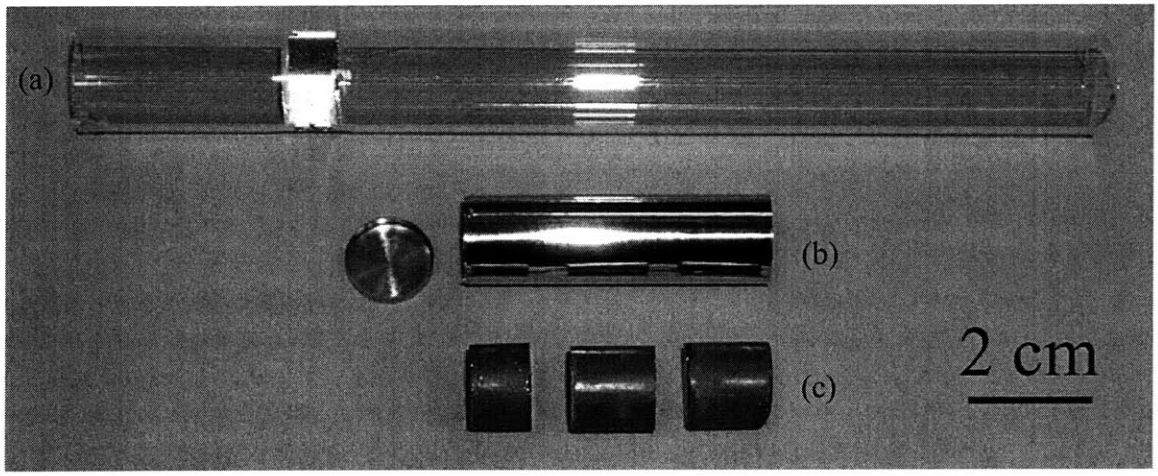

Figure 8-2: Unassembled ampoule showing the (a) quartz envelope, (b) platinum foil, and (c) BSO charge

The ampoule thermocouple was attached while loading the ampoule into the furnace. The boron nitride support and stainless steel extension rod were used to secure the thermocouple so that it did not move. The height of the thermocouple corresponded to the desired seeding interface location (+/- 1 mm).

8.3 Bridgman Stockbarger Growth #1 (BS113001)

8.3.1 Objective

The goal of the first experiment was two-fold(1) to test the ampoule fabrication procedure, experimental procedures for heat up, interface location, translation, and demarcation; (2) to use the furnace geometry with the Zirconia insulation for a growth run in order to have a basis for comparison of growths done in the new Zirpor insulation and furnace geometry.

8.3.2 Ampoule Configuration

Table 8-1 gives a summary of the ampoule and charge specifications. The ampoule after sealing is shown in Figure 8-3.

charge length	37.5	mm
charge diameter	13.9	mm
charge weight	5.7*	g
seed length	12.5	mm
seed weight	1.9*	g
dopant type	none	
dopant concentration	n/a	
quartz thickness	1	mm
platinum foil thickness	0.17	mm
wrapped thickness	0.35	mm
inside surface	reflective	
outside surface	reflective	
atmosphere	20/80 O_2/Ar	
sealing pressure	~0.2	atm.

* These weights were calculated from density and geometry data.

Table 8-1: Ampoule configuration for BS11301.

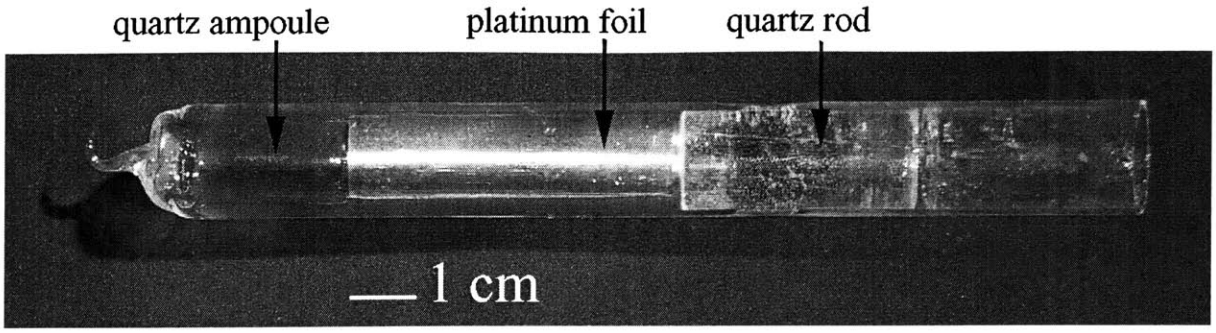

Figure 8-3: Assembled ampoule for first B-S experiment (BS113001).

8.3.3 Experimental Procedure

Accurate positioning of the ampoule relative to the furnace is critical in order to be able to control the position of the seeding interface. Height position information is obtained via an indicator attached to the translation system and a scale mounted on the frame of the furnace. The information obtained from the scale readings is correlated to the position within the furnace by a simple mapping procedure. A spreadsheet was used that calculated the needed position on the scale based on the length of the ampoule, the position of the sample thermocouple, and the desired interface location in the sample. The heights relative to the bottom of the furnace were used as the absolute reference frame. The desired interface location, determined from thermal profiles using a dummy charge, was calculated as a certain distance below a known height value (*e.g.* TC A). The height reading needed on the scale such that the seeding interface was at the correct height in the charge was then obtained by subtracting the same distance from the height reading of the ampoule from the reference point.

The ampoule was placed in the cold zone during initial heat-up to provide a more uniform thermal environment. Initially, heaters were manually controlled for the first hour. Control using the hot zone and cold zone thermocouples was initiated after the first hour. Both zones were initially ramped at 3 °C per minute. The hot zone ramp rate was incrementally increased to 5 °C/minute while the cold zone ramp rate was decreased to 2 °C/minute since it was desired that the ampoule heat up slowly. Thermal arrests at 800 °C for the hot zone and 700 °C for the cold zone allowed stabilization of the thermal environment. Heater control was switched to TC A and TC C and the temperature ramp resumed. Once TC C was approaching the final setpoint, the sample was translated at 20 μm/sec. into the gradient zone. The

translation speed was reduced as the ampoule approached the seeding interface position and the ampoule TC was monitored. The theoretical location of the seeding interface position had been determined from a thermal profile.

			distance (mm)
HZ setpoint 1	910	C	
CZ setpoint 1	810	C	
translation rate 1	-1.00	μm/sec.	
translation time 1	2:00:00	hh:mm:ss	7.2
HZ setpoint 2	910	C	
CZ setpoint 2	810	C	
translation rate 2	-4.00	μm/sec.	
translation time	0:05:50	hh:mm:ss	1.4
HZ setpoint 3	910	C	
CZ setpoint 3	810	C	
translation rate 3	-1.00	μm/sec.	
translation time 3	1:50:00	hh:mm:ss	6.6
HZ setpoint 4	910	C	
CZ setpoint 4	810	C	
translation rate 4	1.00	μm/sec.	
translation time 4	0:05:00	hh:mm:ss	-0.3
HZ setpoint 5	910	C	
CZ setpoint 5	810	C	
translation rate 5	-2.00	μm/sec.	
translation time 5	2:00:00	hh:mm:ss	14.4
			29.3

Table 8-2: Experimental timeline for BS113001

The growth conditions and translation profile for the first experiment are given in Table 8-2. The temperatures of the furnace thermocouples and the ampoule thermocouple during growth are shown in Figure 8-4. After completion of the translation profile, the ampoule was translated into the cold zone at 25 μm/sec. in order to provide a uniform temperature environment during cooling. The initial cooling rate for both zones was 0.25 °C/ minute. After approximately 14 hours, the hot zone cooling rate was increased to 0.35 °C/ minute and the cold zone cooling rate was increased to 0.30 °C/minute. The furnace was shut off after 30 hours and allowed to cool to room temperature.

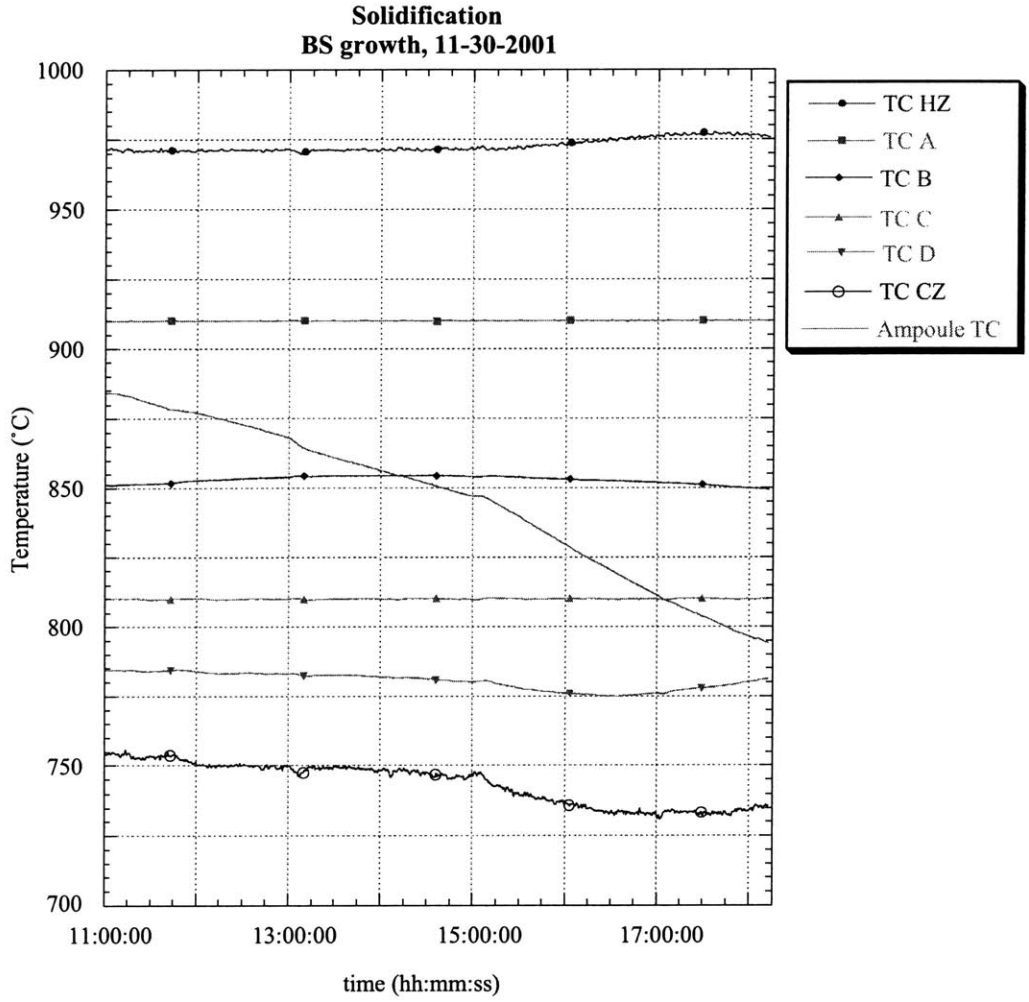

Figure 8-4: Thermocouple data from BS113001 growth during translation.

8.3.4 Results

The quartz ampoule cracked during the growth because melt leaked out of the platinum foil and reacted with the quartz. The processed ampoule is shown in Figure 8-5. The sample could easily be removed from the platinum foil, and the only evidence of adhesion was at the top of the sample. The sample was a single crystal, but it had cracked about 8 mm from the seeding interface. The material around the fracture was extremely brittle and continuously splintered off. The crystal is shown in Figure 8-6 with the seed on the left.

An axial slice was cut from the boule. Both sides were first lapped with a water, glycerol, alumina powder mixture and then polished with a 1:1 mixture of DI water and Syton solution. An image of the axial slice is shown in Figure 8-7. The diameter of the sample is 14

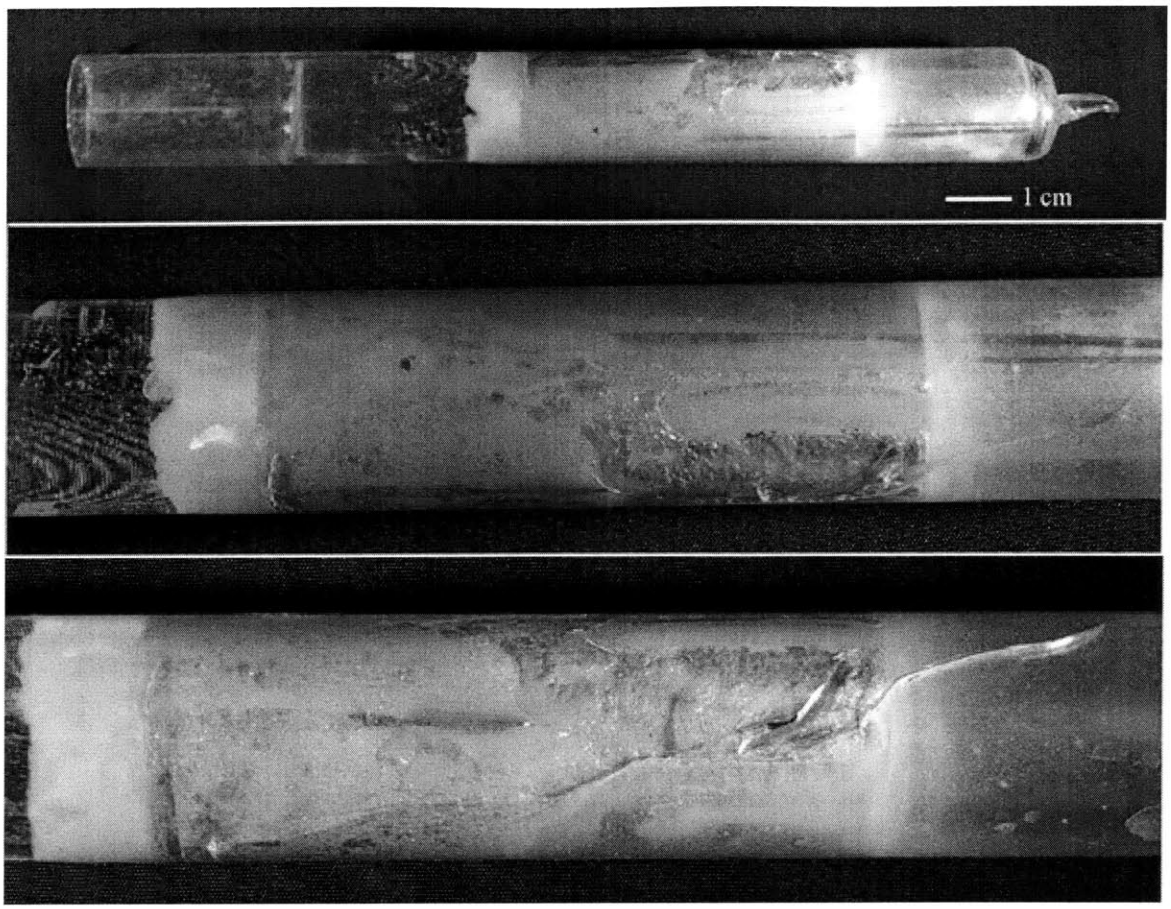

Figure 8-5: Processed ampoule from BS113001 growth. Close-up views show attack of ampoule from BSO melt as well as crack in ampoule.

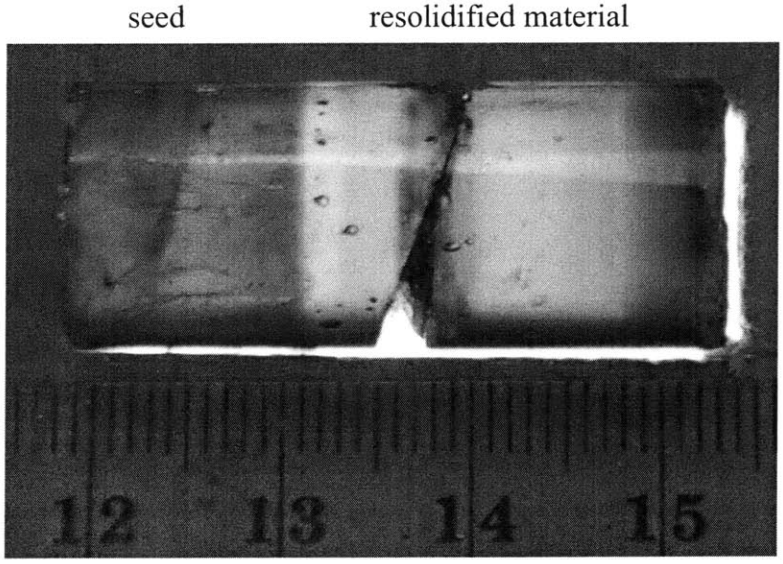

Figure 8-6: Uncut sample from BS113001 growth. Note cm scale.

mm and it is 35 mm long. The seeding interface was located at 12 mm from the bottom of the sample, which was 5 mm higher than the desired position. Thus, the ampoule TC should have indicated a temperature much closer to the actual melt temperature in order for the seeding interface to be located at the same height of the ampoule TC. A discussion of the location of the seeding interface for all of the growth runs is given in Section 8.6. The seeding interface is convex, and which is different from the concave interface that was predicted by the thermal profiling. The difference in interface shape is due to the fact that the quartz dummy does not adequately model the difference in absorption between the solid and the melt. Even if the melt is not opaque (no data is available for absorption properties of BSO melts), its absorption is assumed to be significantly higher than in the solid. As was discussed in the literature review

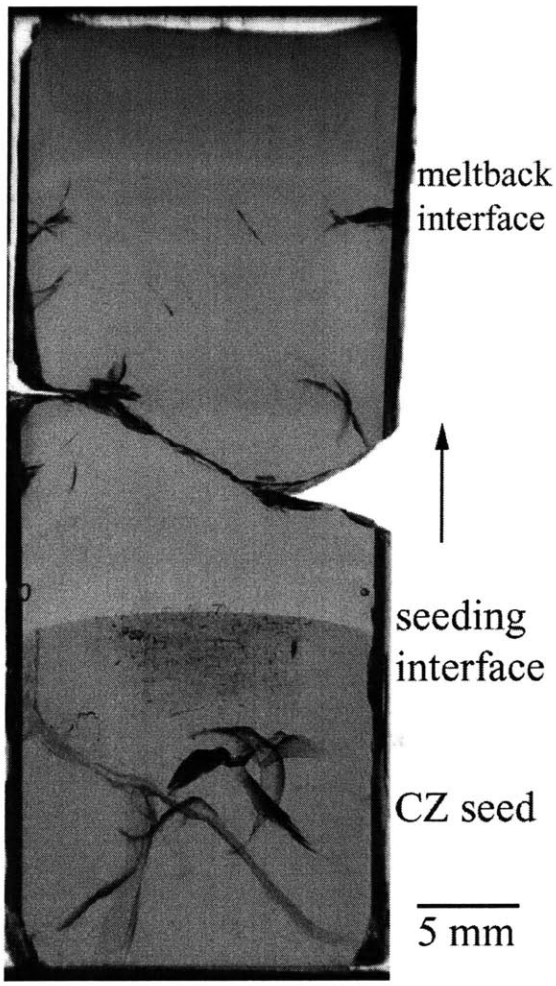

Figure 8-7: Polished axial slice from BS113001 boule.

(Section 2.4), the semi-transparency of the solid results in a convex interface shape due to the radiative heat flux in the solid. The most distinct interface demarcation was a result of translating the crystal upwards for a short period of time (*i.e.* remelting of the crystal), and it is labeled as the meltback interface in Figure 8-7. The absorption of the material was affected by changes in the growth rate as is seen by variations of the color of the regrown material that correspond to the different growth rates. Finally, the top of the crystal was much darker than the rest of the regrown portion.

Referring to Figure 8-7, the seed portion clearly shows striations from the Czochralski growth process. The regrown material is lighter in color and exhibits only faint non-uniformities on the periphery of the crystal. The seed material contained a number of inclusions and line defects that originated during the Czochralski growth. It was not known at the time of this first growth that these defects were present in the seed. However, the defects were not incorporated into the regrown Bridgman material.

8.4 Bridgman Stockbarger Growth #2 (BS122701)

8.4.1 Objective

The objective of the second growth run was to establish reproducibility of the first growth run, to refine the heat-up and cool-down procedure, and to establish a more accurate seeding interface location. Additionally, it was hoped to further investigate the relationship between growth rate and optical homogeneity. During the first growth run, when control was switched from the heatpipe thermocouples to the gradient zone thermocouples and vice versa, large temperature changes were observed as the system readjusted. Since rapid temperature changes introduce stresses into the crystal, it was also necessary to establish control procedures that avoided large temperature drops.

8.4.2 Ampoule configuration

The platinum foil from the first growth run was also used for the second ampoule. It was cleaned using HCl to remove residual BSO. The foil had been attacked in a few spots during the first run, but it was thought that by wrapping the foil such that these spots were on the outside it would not affect the run. The platinum foil is shown in Figure 8-8. The ampoule

was assembled in the same manner as the first ampoule. The ampoule configuration was the same as for the first run, and the details are given in Table 8-3.

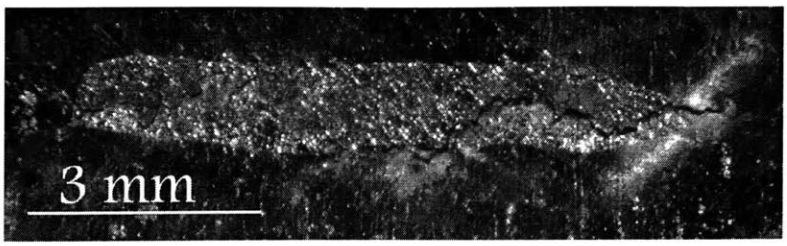

Figure 8-8: Close-up of platinum where it was attacked by the BSO melt.

charge length	39.28	mm
charge diameter	13.94	mm
charge weight	53.76	g
seed length	9.779	mm
seed weight	13.378	g
dopant type	none	
dopant concentration	n/a	
quartz thickness	1	mm
platinum foil thickness	0.17	mm
wrapped thickness	0.35	mm
inside surface	reflective	
outside surface	reflective	
atmosphere	20/80 O_2/Ar	
sealing pressure	~0.2	atm.

Table 8-3: Ampoule configuration for the second B-S growth (BS122701).

8.4.3 Experimental Procedure

Again, the ampoule was placed in the cold zone during heat-up to provide a more uniform thermal environment. Initial heat-up used manually controlled power settings that was then switched to PID control (TC A and TC C controlling HZ and CZ, respectively) after the first hour, and the ramping rate was 1.5 °C/minute. Once the setpoints (TC A =910 °C, TC C = 810 °C) were reached, the ampoule was translated upwards at 10-20 μm/sec. to the desired interface location. The sample thermocouple was used as a guide. The ampoule was positioned such that the sample thermocouple read 890 °C (as a comparison, in growth 1, the sample TC read 885 °C). This reading coincided with the theoretical location of the seeding interface as determined from the thermal profile.

The growth conditions and translation profile for the second growth run are given in Table 8-4. The second and fourth translation periods correspond to translation arrests which were expected to yield interface demarcation. Once translation was complete, the ampoule was translated into the cold zone heatpipe and cooled at 1 °C/minute to 650 °C. It was then annealed for 15 hours and subsequently cooled to room temperature.

HZ setpoint 1	910	C	
CZ setpoint 1	810	C	
translation rate 1	-1.00	μm/sec.	
translation time 1	3:00:00	hh:mm:ss	10.8
HZ setpoint 2	910	C	
CZ setpoint 2	810	C	
translation rate 2	0.00	μm/sec.	
translation time	0:10:00	hh:mm:ss	0
HZ setpoint 3	910	C	
CZ setpoint 3	810	C	
translation rate 3	-2.00	μm/sec.	
translation time 3	1:30:00	hh:mm:ss	10.8
HZ setpoint 4	910	C	
CZ setpoint 4	810	C	
translation rate 4	0.00	μm/sec.	
translation time 4	0:05:00	hh:mm:ss	0
HZ setpoint 5	910	C	
CZ setpoint 5	810	C	
translation rate 5	-0.50	μm/sec.	
translation time 5	6:00:00	hh:mm:ss	10.8
			32.4

Table 8-4: Experimental timeline for BS122701

8.4.4 Results

A severe breach in the quartz, due to attack from molten BSO, caused the ampoule to become attached to the thermocouple insert. It was necessary to disassemble the furnace in order to remove the ampoule. The processed ampoule is shown in Figure 8-9. As can be seen, a large amount of BSO material leaked out of the platinum confinement foil and reacted with the quartz. This was due to the fact that there were not enough wraps of the foil. It was concluded that a thinner foil was necessary that would have more wraps.

Analyzing the temperature data, there is a sudden drop in the reading of the ampoule thermocouple (Figure 8-10). Additionally, after the drop, the heat pipe thermocouples (TC HZ and TC CZ) no longer exhibit any variation due to thermal coupling with ampoule. These observations lead to the conclusion that the breach in the ampoule occurred around this time and that the ampoule got stuck in the gradient zone. The ampoule TC was attacked by the BSO; the top portion is can be seen in the close-ups in Figure 8-9. However, since the thermocouple did not go open circuit, it must have formed a new junction at a lower point in the thermocouple. Since the ampoule TC was attached to the stainless support rod, it continued to translate downwards with the rod and therefore, a decrease in temperature was still observed.

An axial slice was cut from the crystal and polished. It is shown in Figure 8-11. The seeding interface is non axisymmetric indicating that the ampoule might have already been leaking early on during the growth, thus affecting the thermal environment and convection in the melt. Like the first growth (BS11301), the seeding interface is again located above the expected location by 4-5 mm. Although the ampoule thermocouple temperature reading was increased, it was still not high enough. Since there should not be a significant temperature drop from the outside to the inside of the ampoule, it makes sense that the interface was not in the desired location. Refer to Section 8.6 for a more complete analysis. Because the thermal

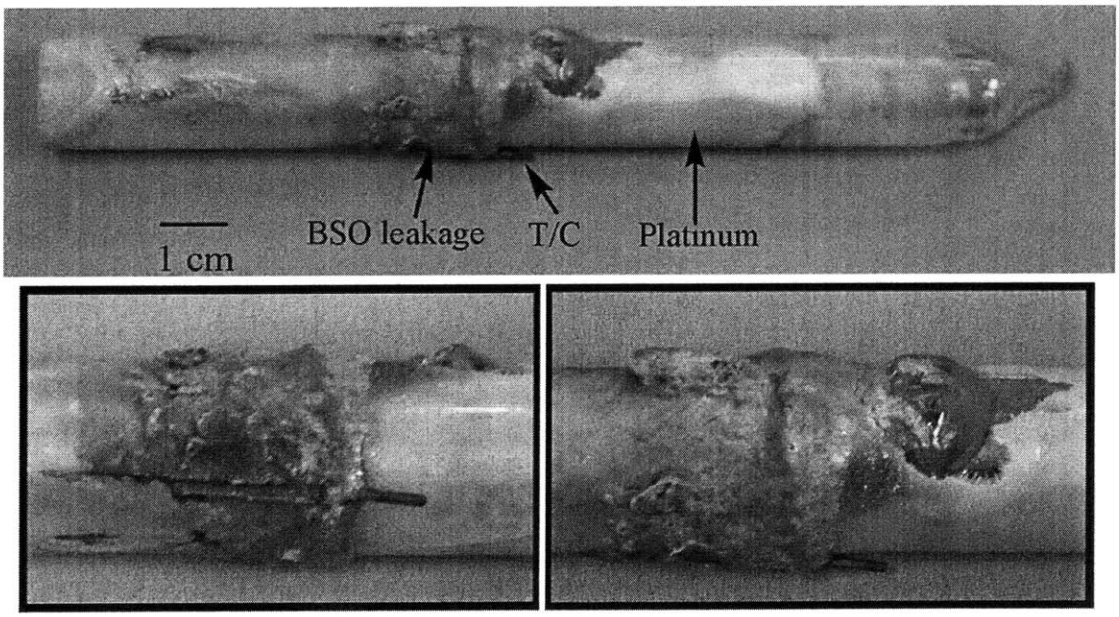

Figure 8-9: Processed ampoule from growth #2 (BS122701). Severe attack of the quartz occurred during growth as can be seen from close-up images.

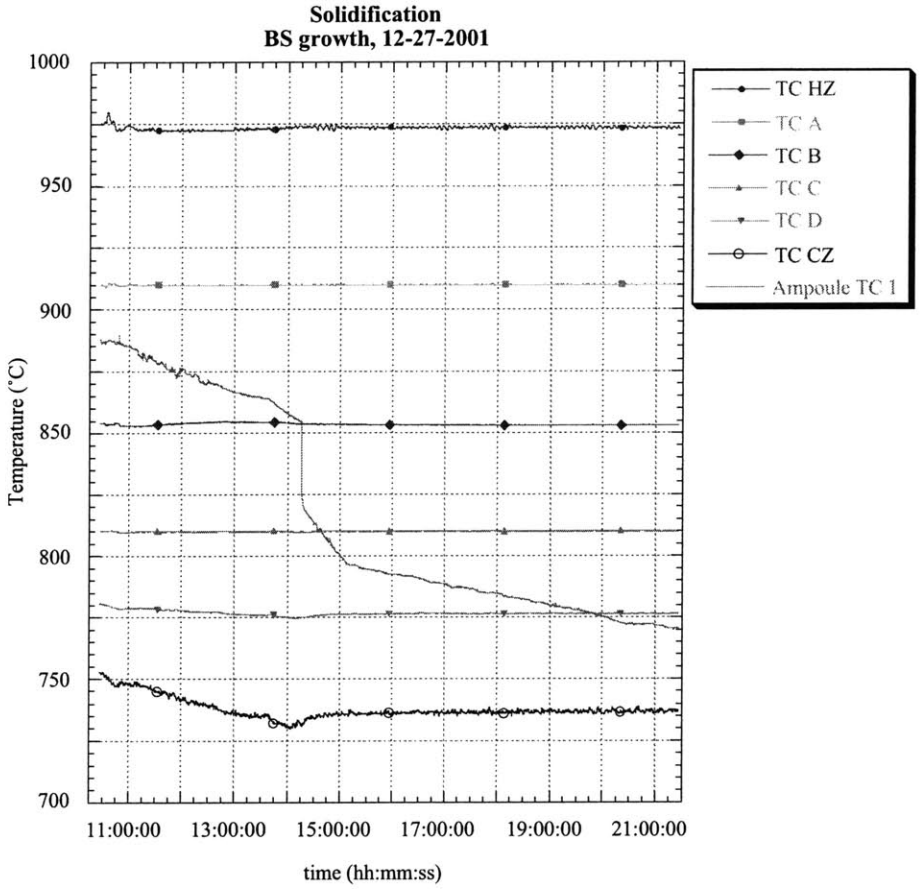

Figure 8-10: Temperature data from growth #2 (BS122701).

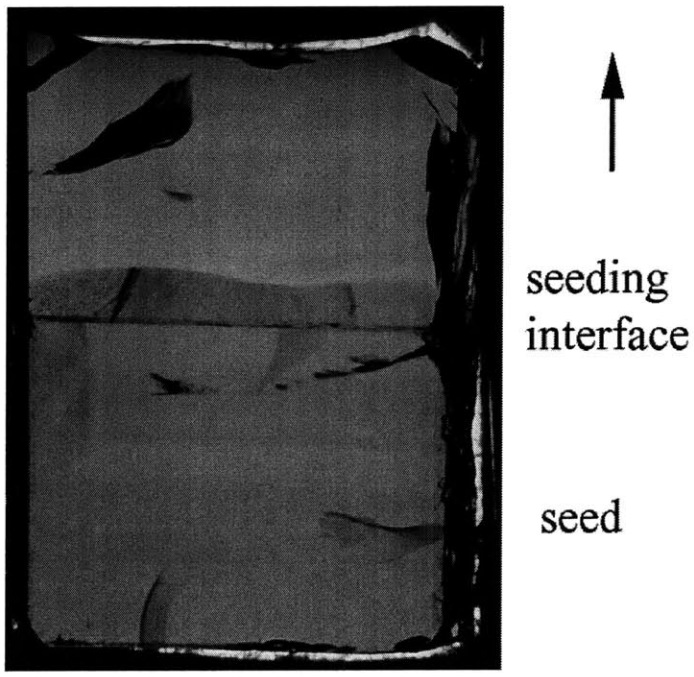

Figure 8-11: Axial slice of BS122701 boule.

environment and growth conditions are essentially unknown for this growth run due to the ampoule failure, no further analysis of this boule was. It was noted, that the top of the boule exhibited the same darkened material as was observed in the first growth (BS113001). The major conclusion from this growth experiment was the need to change the confinement material configuration.

8.5 Bridgman Stockbarger Growth #3 (BS020802)

8.5.1 Objective

The main objective of the third growth experiment was to investigate the effect of solidifying using a low axial gradient such that the melt temperature does not exceed 930 °C. The furnace had been reconfigured with the new gradient zone insulation (see section 6.4) as well as a new thermocouple insert.

8.5.2 Ampoule Configuration

In order to prevent another ampoule breach, a new, 0.075 mm platinum foil was used. This enabled 3 complete wraps around the material. Additionally, the thinner foil was more malleable than its thicker predecessor so that the layers had less empty space between them. Table 8-5 gives a summary of the ampoule configuration.

charge length	38.1	mm
charge diameter	13.95	mm
charge weight	53.3673	g
seed length	10.3	mm
seed weight	14.4135	g
dopant type	n/a	
dopant concentration	n/a	
quartz thickness	1	mm
platinum foil thickness	0.075	mm
wrapped thickness	0.23	mm
inside surface	reflective	
outside surface	reflective	
atmosphere	20% O2	
sealing pressure	0.25	atm.

Table 8-5: Ampoule configuration for BS020802.

8.5.3 Experimental Procedure

The ampoule was placed in the cold zone heat pipe during heat-up. The heaters were controlled by TC A and TC D and ramped at 5 °C/minute. Temperature oscillations experienced by the ampoule were reduced, but not eliminated completely. The thermal environment was allowed to stabilize for four hours before the sample was translated into the gradient zone for processing. The ampoule was translated until the sample thermocouple, located at the desired seeding interface location, read 892 °C. The translation rates, were 1 μm/s, 2 μm/s, and 0.5 μm/s; the experimental parameters are given in Table 8-6. Between each translation rate period, a 5 minute upwards translation period was employed so that meltback of the solid would occur and provide interface demarcation.

hot zone control TC	A		
cold zone control TC	D		
HZ setpoint 1	900	C	
CZ setpoint 1	860	C	
translation rate 1	-1.00	μm/sec.	
translation time 1	3:00:00	hh:mm:ss	10.8
HZ setpoint 2	900	C	
CZ setpoint 2	860	C	
translation rate 2	1.00	μm/sec.	
translation time	0:05:00	hh:mm:ss	-0.3
HZ setpoint 3	900	C	
CZ setpoint 3	860	C	
translation rate 3	-2.00	μm/sec.	
translation time 3	1:20:00	hh:mm:ss	9.6
HZ setpoint 4	900	C	
CZ setpoint 4	860	C	
translation rate 4	1.00	μm/sec.	
translation time 4	0:05:00	hh:mm:ss	-0.3
HZ setpoint 5	900	C	
CZ setpoint 5	860	C	
translation rate 5	-0.50	μm/sec.	
translation time 5	6:00:00	hh:mm:ss	10.8
			30.6

Table 8-6: Experimental timeline for BS020802.

8.5.4 Results

This experiment did not show any failure of the ampoule. Therefore, a key difference between the third experiment and the first two experiments was that the quartz ampoule did not lose integrity, and therefore the growth occurred in a closed system environment rather than one open to the furnace environment. The thinner platinum foil prevented the melt from leaking through the layers of platinum. The processed ampoule is shown in Figure 8-12. The platinum was found to be embrittled, however, and could not be used for another growth experiment.

An axial slice was cut from the boule and polished; it is shown in Figure 8-13. There was a very noticeable difference between this experiment and the first two. The entire crystal, including the seed, was much lighter in color. The seeding interface, although distinct, was not as clearly observable as in previous growths. Additionally, there appeared to be fewer inhomogeneities in the resolidified material. There were three major differences between this experiment and the first two experiments:

1. a low thermal gradient was employed
2. the ampoule did not crack during processing thus providing a sealed environment,
3. the Czochralski material used came from a different boule.

As will be discussed in Chapter 9, the sealed environment is the critical parameter responsible for the different appearance of the crystal. However, without further experiments where the only difference between experiments is the thermal environment, it is not possible to state whether the low thermal gradient also had an effect on the material properties.

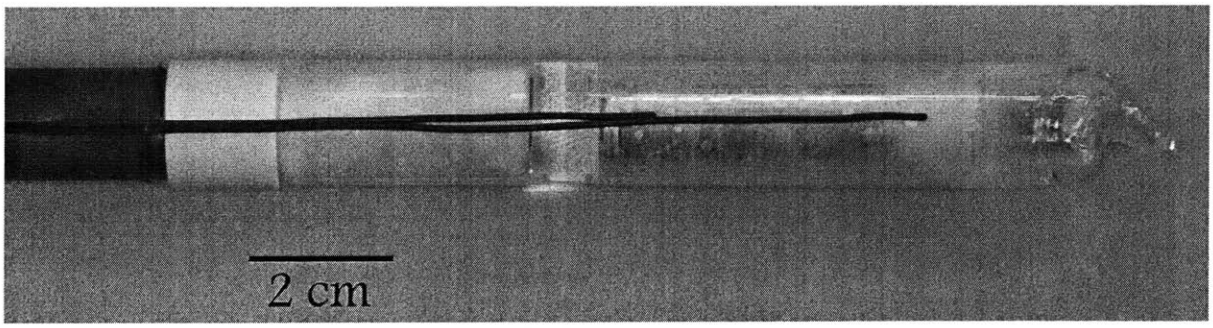

Figure 8-12: Processed ampoule from third growth experiment (BS020802) with ampoule thermocouples still in position.

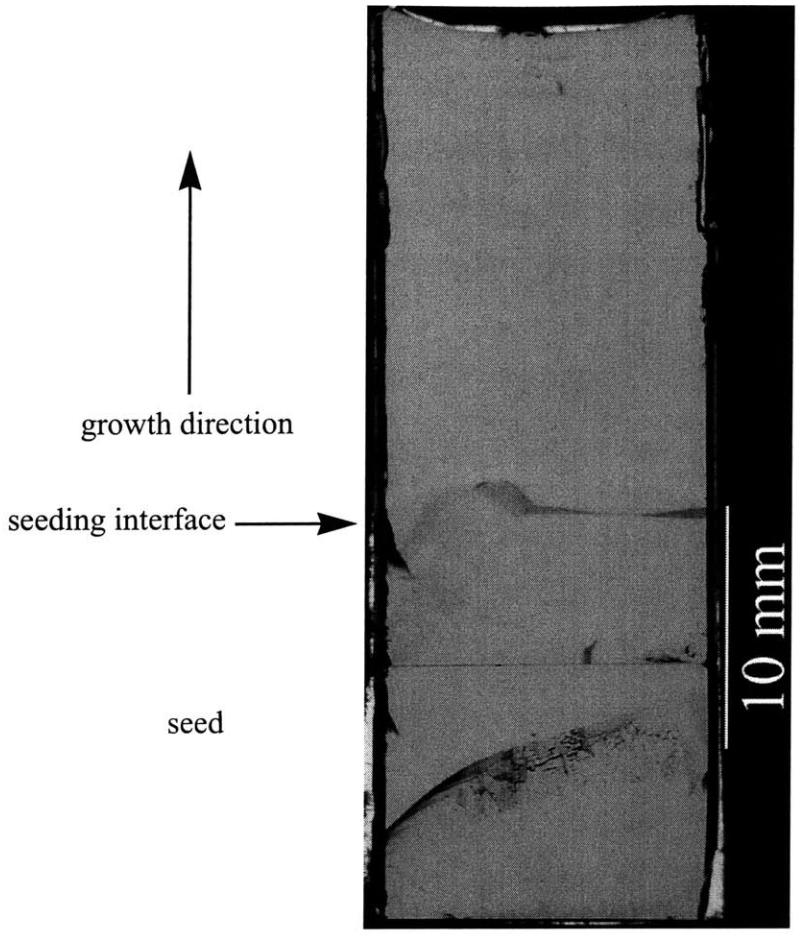

Figure 8-13: Axial slice from third growth experiment (BS020802).

8.6 Analysis of Seeding Interface Position

8.6.1 Experimental thermocouple data analysis

In all three B-S growth experiments, the seeding interface position was not at the desired location. The temperature data from the growths was examined to establish whether the actual location of the interface is in line with the axial profile in the furnace. A plot of the gradient zone thermocouple data at the start of translation is shown in Figure 8-14. The position of the gradient zone is marked by light shading. Initially, a linear fit through the gradient zone TC's was done in order to calculate where the 895 °C temperature was located, and if that position corresponded to where the seeding interface was in the growth experiments. Although the fit seems at first sight to be adequate, using a quadratic curve fit gave much better results, as can be seen in Figure 8-15 from the R^2 values.

For the first growth experiments, BS113001, the seeding interface was 5 mm higher than desired. However, ampoule TC only read 884 °C. The axial gradient was 2.63 °C/mm, and the temperature difference between the melting point and the ampoule thermocouple was 11 °C. This means that the 895 °C isotherm approximately lies 4.2 mm above the location of the ampoule thermocouple. Looking at the axial slice with the scale superimposed in Figure 8-16, the ampoule thermocouple was located 7 mm from the bottom of the crystal. At the edge, adding 4.2 mm to the 7 mm height, gives 11.2 mm, matching the edge of the seeding interface.

The same analysis was performed for the second growth experiment, BS122701. The seeding interface is 11.2 mm at the edge and 11.7 mm at the maximum from the bottom of the crystal (see Figure 8-11). The axial gradients in the furnace were almost identical to the BS113001 experiment, showing good reproducibility of the thermal environment in the growth system. The ampoule thermocouple read 887 °C. Again, using the computed gradient, 895 °C would have been 3.4 mm above the ampoule thermocouple, giving a 10.4 mm

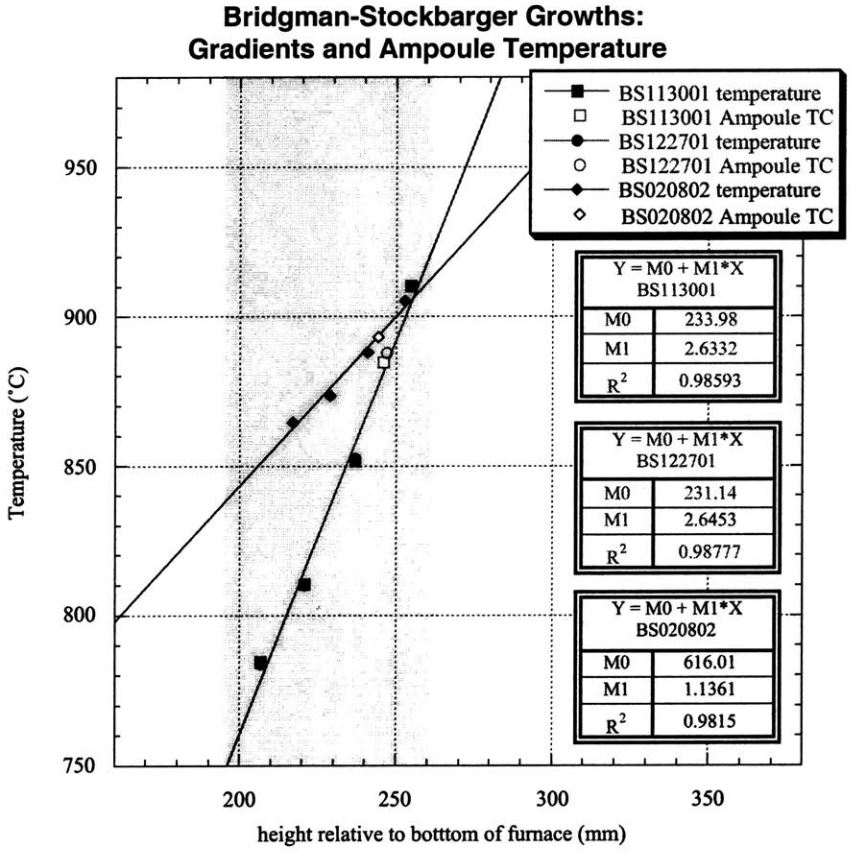

Figure 8-14: Linear fit through gradient zone thermocouple data at the start of translation

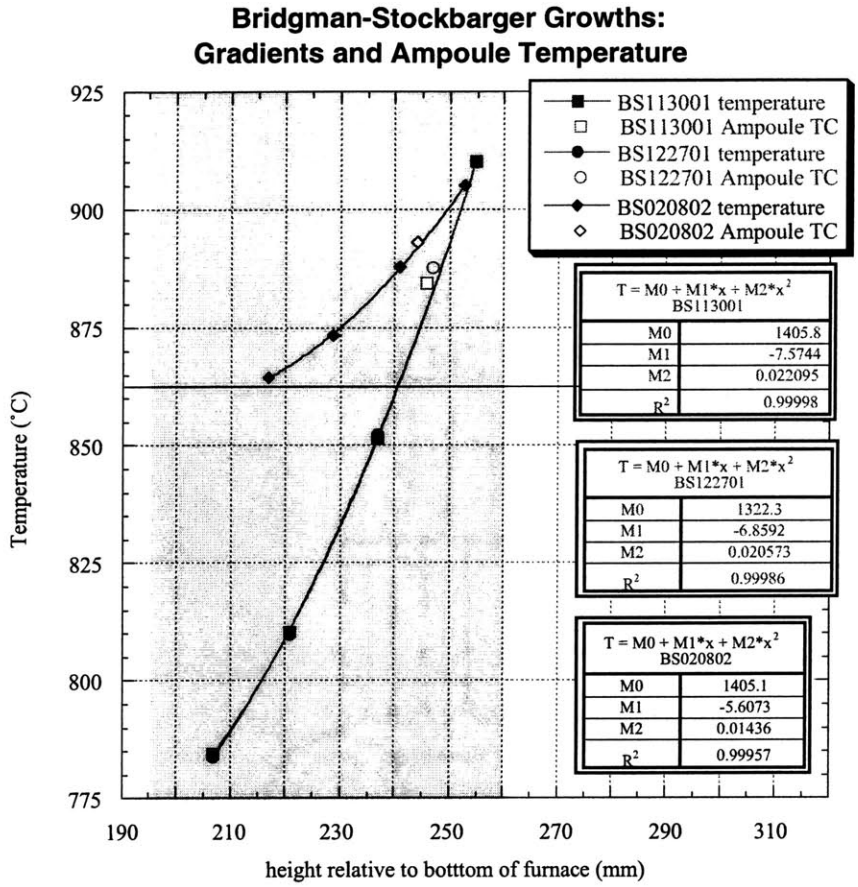

Figure 8-15: Gradient thermocouple data with quadratic curve fit.

interface position. This is less than 1 mm from the actual position and within experimental error. Both the reading from the scale used to establish the position of the ampoule and the exact location of the thermocouple relative to the sample had a minimum of 0.5 - 1 mm inaccuracy associated with them.

The last growth experiment was done with the new furnace insulation and the gradient thermocouples located in different positions. Additionally, the experiment was specifically intended to use a low axial gradient in order to keep the temperature of the melt below 930 °C in order to study the role of the thermal environment during growth on the formation of the native defect. The temperature of the ampoule thermocouple at the start of translation was 893 °C. The axial gradient for this growth run was only 1.1 °C/mm. This would have put the seeding interface at 1.8 mm above the desired location. The thermocouples have an accuracy on the order of several degrees, but that still does not account for the discrepancy. No adequate explanation could be found.

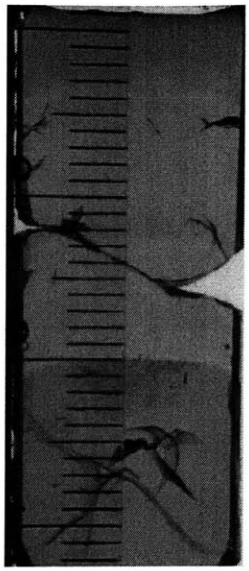

Figure 8-16: BS1113001 axial slice with superimposed scale.

8.6.2 Comparison with Modeling Results

In order to compare the modeling data with experimental results, simulation cases were run with the same setpoints as used for the Bridgman growth experiments. The agreement between the modeling and the experiments is excellent in the gradient zone, as seen in Figure 8-17. However, the predicted temperatures in the hot and cold zones differ. It was observed that the presence of the ampoule affected the temperature of the cold zone thermocouple, as is clearly shown in Figure 8-19. The furnace was therefore ramped to the setpoints of BS020802 without an ampoule or dummy in the furnace. This lowered the reading of the cold zone thermocouple by 7 °C, but this still does not account for all of the discrepancy. Running the setpoints from BS020802 with the additional platinum liner resulted in an increase of 5 degrees for the cold zone temperature (Figure 8-18). Hence, as was observed in earlier modeling work, the platinum liner used to emulate the platinum confinement material affects the heat pipe thermocouples.The thermal field for the BS113001/ BS122701 setpoints is shown in Figure 8-20, and the thermal fields with and without platinum for BS020802 setpoints are shown in Figure 8-21 and Figure 8-22, respectively. Although the platinum decreases the discrepancy between the modeling and the experimental data, the agreement in the hot zone decreased. The most likely cause for the discrepancy is additional losses in the real furnace that are not accounted for in the model.

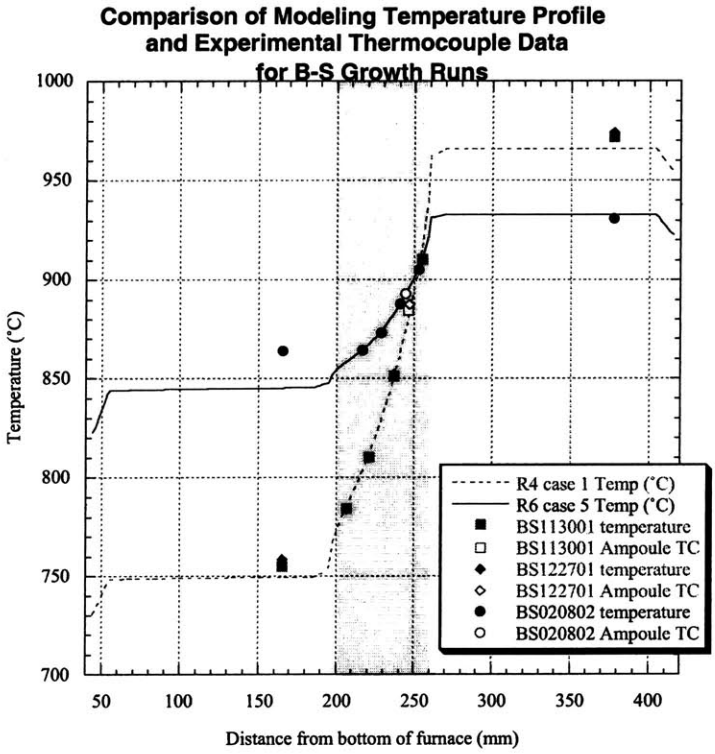

Figure 8-17: Comparison of modeling data (R4 case 1 and R6 case 5) with gradient thermocouple data from growth experiments.

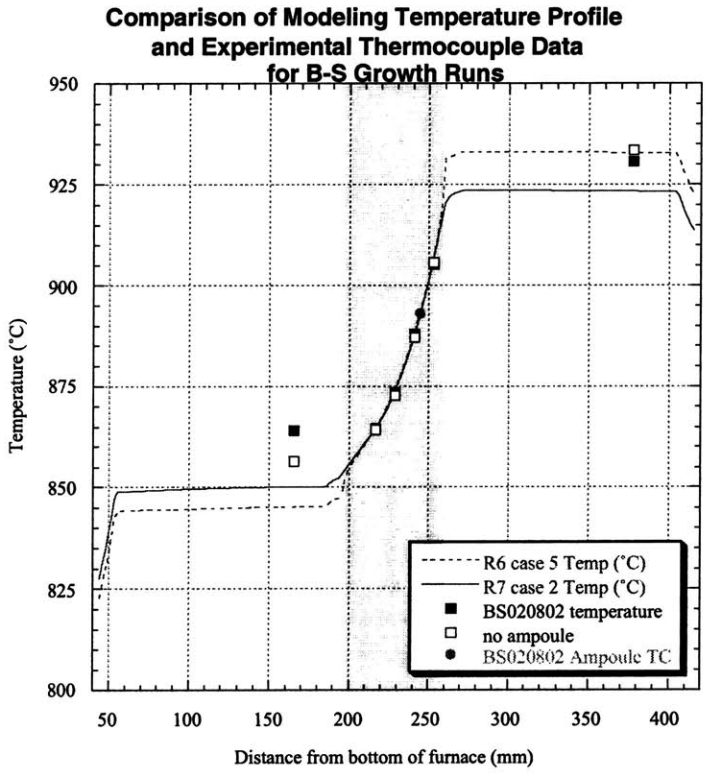

Figure 8-18: Comparison between BS020802 experimental data and modeling results with (R7 case 2) and without (R6 case 5) the platinum liner.

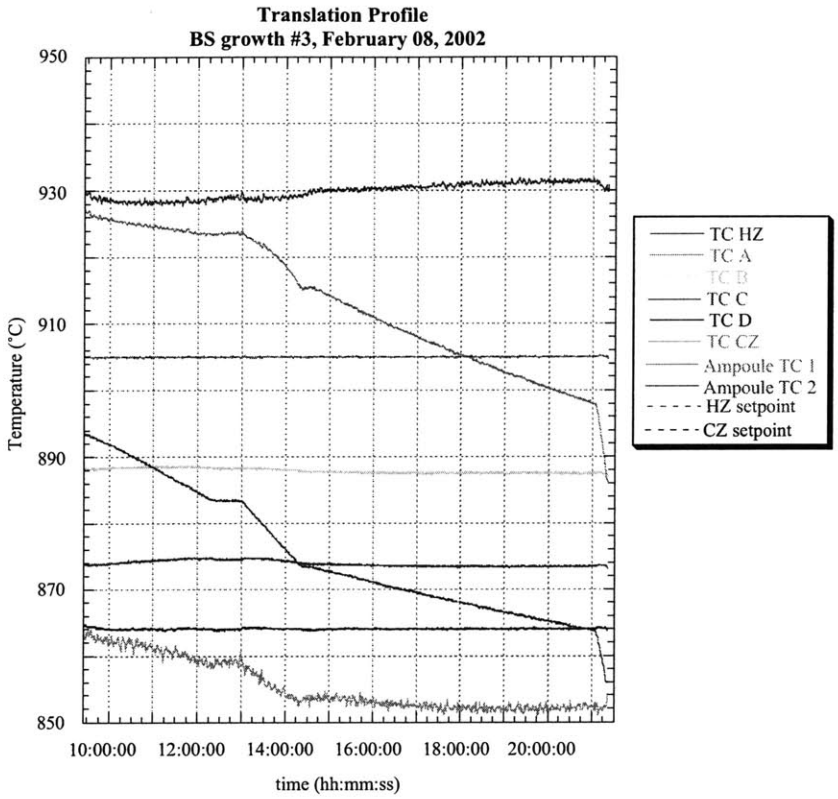

Figure 8-19: Coupling effect of ampoule and Cold Zone temperature.

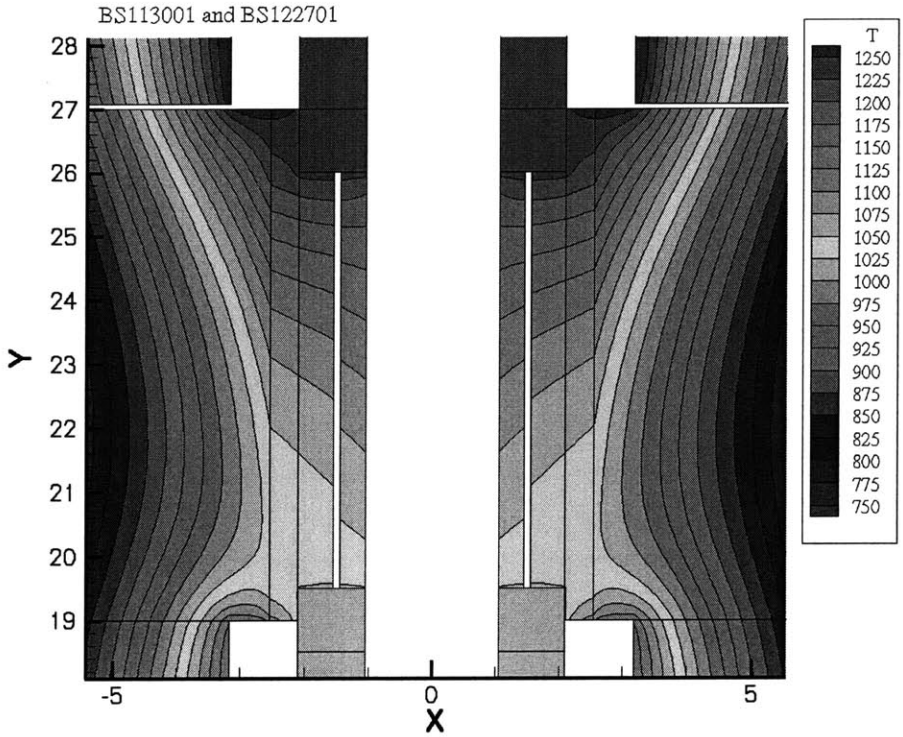

Figure 8-20: Temperature distribution in gradient zone for setpoints of BS113001 and BS122701 growth runs.

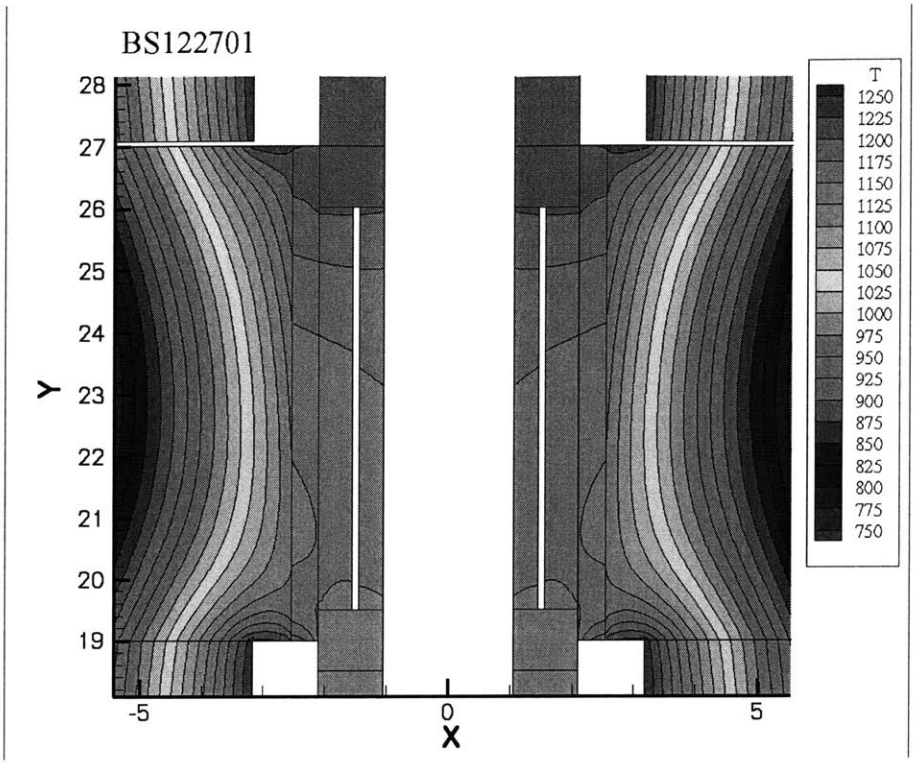

Figure 8-21: Temperature distribution in gradient zone for setpoints of BS020802 growth run without platinum liner.

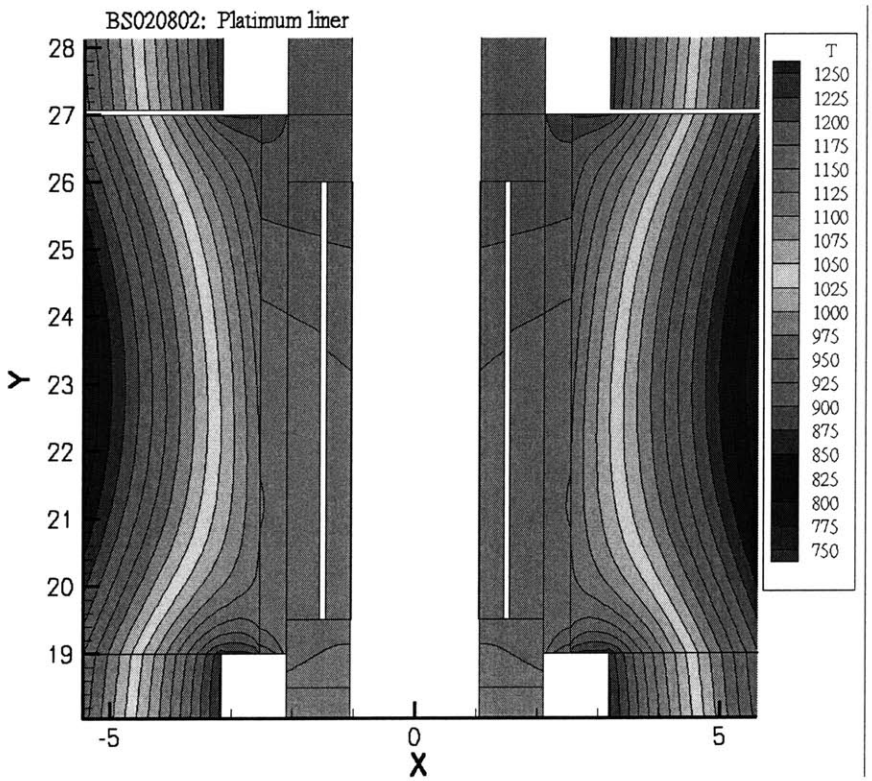

Figure 8-22: Temperature distribution in gradient zone for setpoints of BS020802 growth run with platinum liner.

CHAPTER 9: COMPARATIVE ANALYSIS OF BSO

9.1 Introduction

The fact that many of the electro-optic property measurement techniques are bulk in nature is one of the difficulties encountered in studying point defects in BSO. Observed optical variations, possibly due to fluctuations in the native defect concentration, are on the micron scale (e.g. striations); it is therefore desirable to have a technique that possesses excellent spatial resolution. Optical properties from samples grown under different conditions were analyzed in an effort to correlate variations in energy levels and trap densities to changes in growth conditions. It was hoped that variations in the optical properties of samples from Czochralski, Bridgman-Stockbarger, and hydrothermal grown crystals would help elucidate the origin of the native defect. Absorption, photoconductivity, and photoluminescence measurements were made. Subsequently, the photochromic property was chosen for more careful analysis of the effect of growth conditions on long lifetime traps. It was found that some samples did not exhibit any photochromicity as a result of a high temperature anneal in a sealed environment. Because the photochromic and the photorefractive effect are related, an analysis of the photorefractive response of both un-annealed and annealed samples was performed.

9.2 Absorption

In an extrinsic material, absorption from optical excitation occurs in three different ways: (1) band to band, (2) band to acceptor, and (3) donor to band. If the material has an indirect bandgap, the energy required for excitation is greater than the distance between the two states because of momentum conservation. A typical, full absorption spectrum for BSO is shown in Figure 9-1. Of interest is the portion of the spectrum that corresponds to where absorption occurs via the band to acceptor and/or donor to band mechanisms. This region was in the visible and near IR; therefore, all absorption measurements were made from 400 nm to 900 nm (1.4 - 3.2 eV). Initial absorption measurements were made using a Cary 500 Spectrophotometer with a one mm aperture. This small aperture increases spatial resolution,

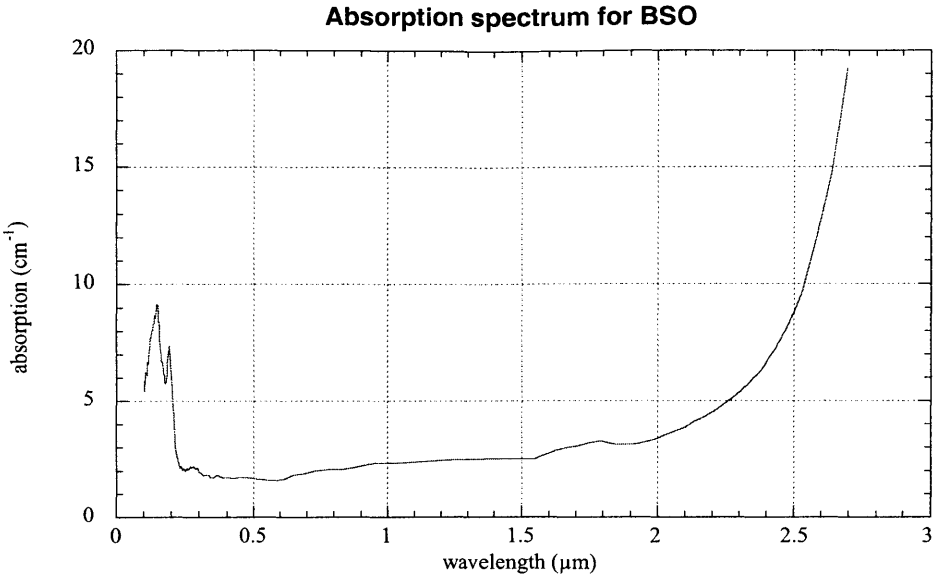

Figure 9-1: IR and visible absorption spectrum for Czochralski grown BSO.

but it decreases the sensitivity and increases the noise. Figure 9-2 shows absorption curves for BS113001 and BS020802. Approximate measurement points are indicated for both samples.

9.3 Photoconductivity

Photoconductivity measurements provide information regarding excitation of carriers from interband states into the conduction band. The transition mechanisms for photoconductivity, like absorption, comes from illumination exciting electrons from donor levels to energies higher than the conduction band edge. The energy required for excitation is greater than the distance a donor level is below the conduction band edge because of the barrier heights. Photoconductivity measurements show only transitions due to the excitation of carriers that produce conductivity (electrons and holes), whereas absorptions reveals all transitions that occur (lattice as well as electronic). Samples for photoconductivity measurements were cut to approximately 5 mm x 5 mm x 3 mm. Both sides and all the edges were polished using Syton solution on a Chemomet I (Buehler) polishing pad, and contacts were made using silver paste. The slit size during measurements was either 1 or 1.5 mm in order to accommodate the low signal intensity.

Photoconductivity was measured at 77 K on all three samples and at room temperature for the B-S and CZ samples. Figure 9-3 shows the difference in photoconductivity between

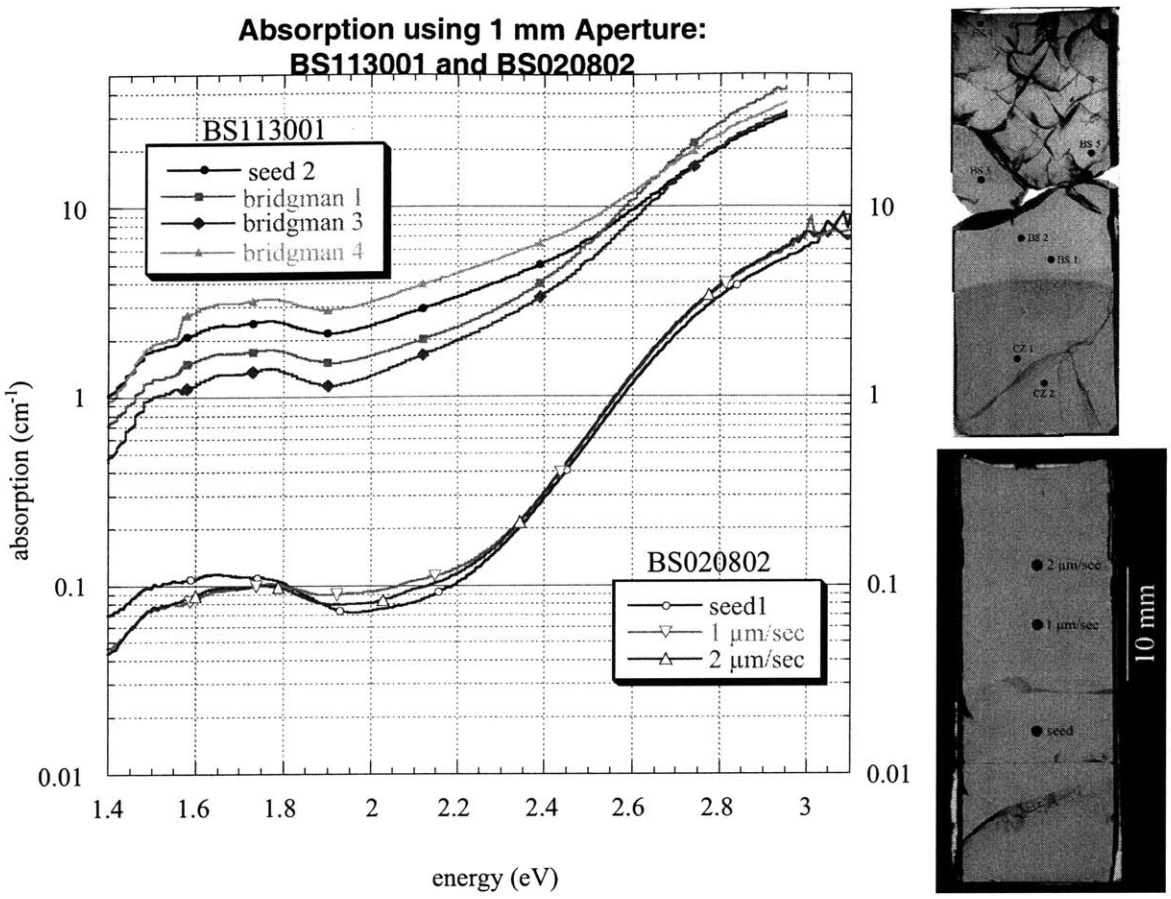

Figure 9-2: Initial absorption spectra for BS113001 and BS020802 with 1 mm aperture. Approximate measurement points shown on the right.

room temperature and 77 K for the B-S sample. At room temperature, shallow traps are partially filled and contribute to photoconductivity as indicated by the broad shoulder. At low temperatures, all the carriers are initially in the ground state and in the metastable trap after initial illumination excites carriers from the donor level.

Looking at Figure 9-4, it can be seen that the energy level of the peak position (1.4 eV) is the same for the Bridgman and Czochralski samples. The hydrothermal material does not exhibit a peak at this energy level, suggesting the absence of the defect that is responsible for the trap at that level. The absolute magnitude of the photoconductivity signal from the different samples (*i.e.* CZ vs. B-S vs. hydrothermal) cannot be directly compared because the current used to create the voltage difference across the electrodes was different for each sample in order to maximize signal to noise ratio.However, the current setting for the B-S sample was approximately 10 times smaller than the setting for the CZ sample. This is an

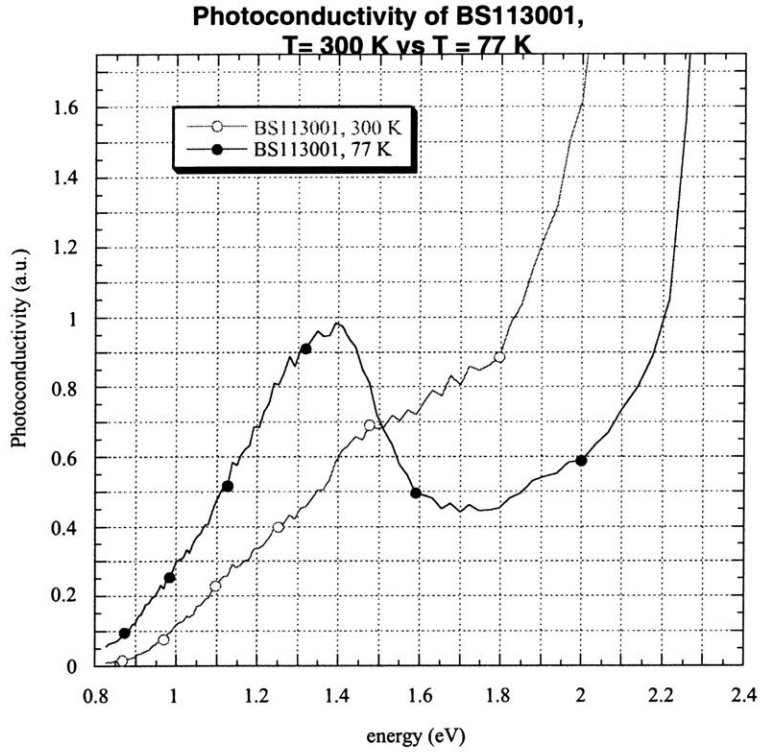

Figure 9-3: Comparison of photoconductivity for B-S material at room temperature and 77 K.

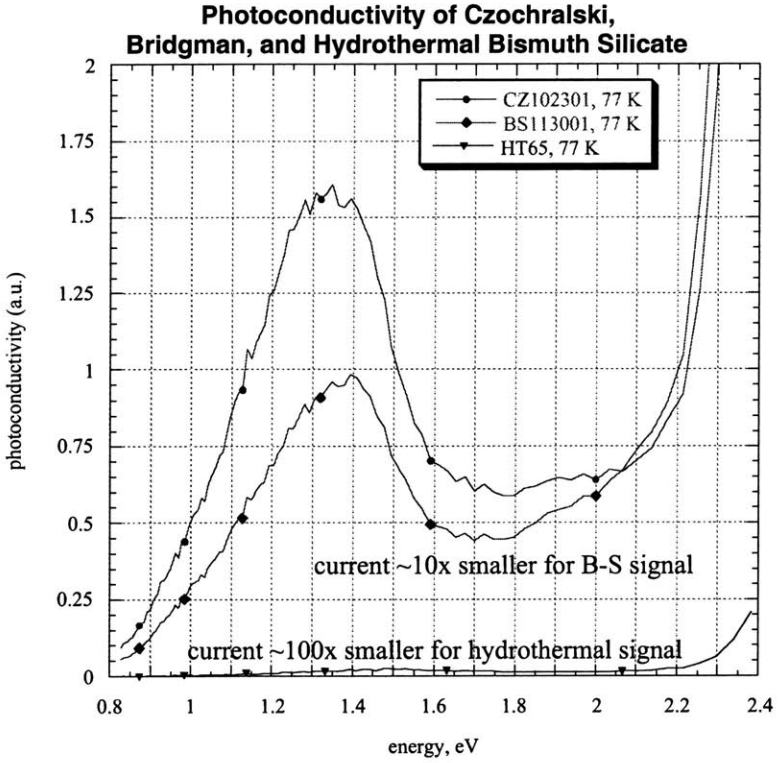

Figure 9-4: Photoconductive response for Czochralski, Bridgman, and hydrothermal material.

indication of increased resistivity due to a decreased trap density in the Bridgman type material. Since conductivity is proportional to carrier density, it can be concluded that the defect concentration is significantly lower in the Bridgman material and lowest in the hydrothermal material.

9.4 Photoluminescence

Photoluminescence (PL) was the third analysis technique used to analyze BSO samples. In PL, electrons are excited across the bandgap using high intensity illumination from a laser. As the electrons fall into interband states, they emit light. The PL mechanism is shown schematically in Figure 9-5. A HeCd laser (325 nm) was used for excitation. All samples were lapped by hand using a fine garnet abrasive mixed with glycerol and DI water. Samples were mounted and cooled with liquid helium to 4 K prior to data acquisition. Initial scans with a one nm spectral resolution were acquired for CZ, B-S, and hydrothermal samples, and the results are shown in Figure 9-6. The only detectable peak was located at 1.95 eV, and it corresponds to a deep donor level. This level is absent in the hydrothermal sample, and this is due to the fact that the hydrothermal material does not contain the native defect.

It was originally hoped that a line scan across the striations in the CZ sample would resolve variations in the donor level at 1.95 eV, and that these variations could be correlated to the striations observed optically. However, sample translation could only be achieved by manual repositioning of the sample holder. This resulted in movements on the order of 1 mm, which is much larger than the width of the striations. Additionally, the manual repositioning also introduced minute rotation of the sample holder with respect to the setup. The mirrors

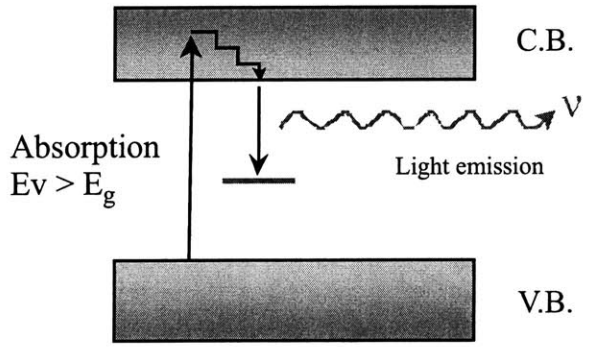

Figure 9-5: Schematic of photoluminescence process.

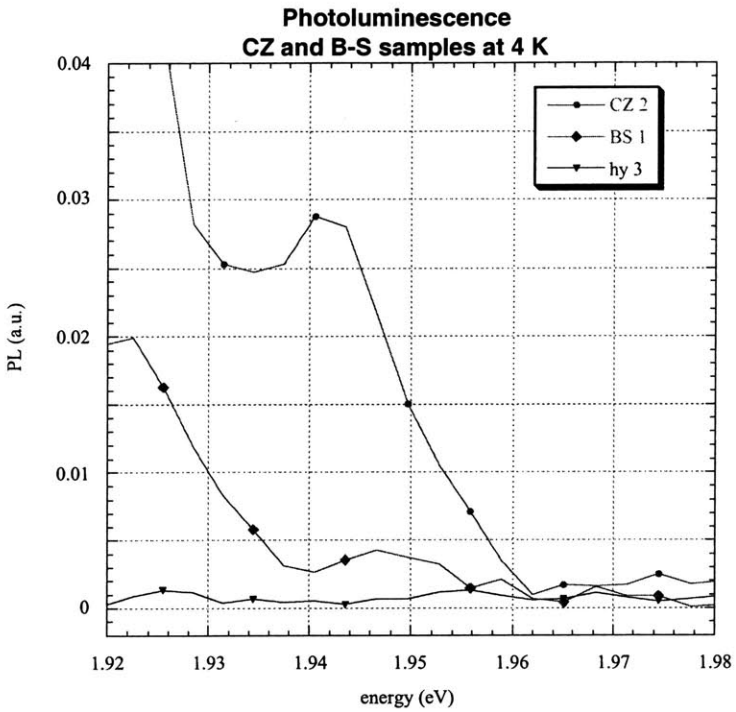

Figure 9-6: Photoluminescence signal for Czochralski, Bridgman-Stockbarger, and Hydrothermal material.

were therefore adjusted to maximize the signal at 637.5 nm prior to each scan. Another source of uncertainty came from the fact that the surface preparation between samples could have been slightly different, and this could also have affected the signal intensity. Therefore, quantitative comparison of the different curves is not possible. However, looking at Figure 9-6, a distinct difference in the maximum, attainable signal is observed between CZ and B-S samples. This suggests a lower defect concentration in the B-S material. Additionally, it can be seen that different areas of the same CZ sample had varying maximum signals.

9.5 Photochromic Effect

The photochromic effect occurs when carriers are excited into the conduction band, and the localized ground state transforms to a metastable delocalized excited state accompanied by a lattice relaxation[203]. This mechanism is schematically shown Figure 9-8. Samples from two Czochralski grown boules (identified as CZ102301 and CZ110501) and samples from two Bridgman-Stockbarger grown boules (labeled BS1130001 and BS020802) were prepared by mechanochemically polishing both sides. Sample thickness varied from 1.5

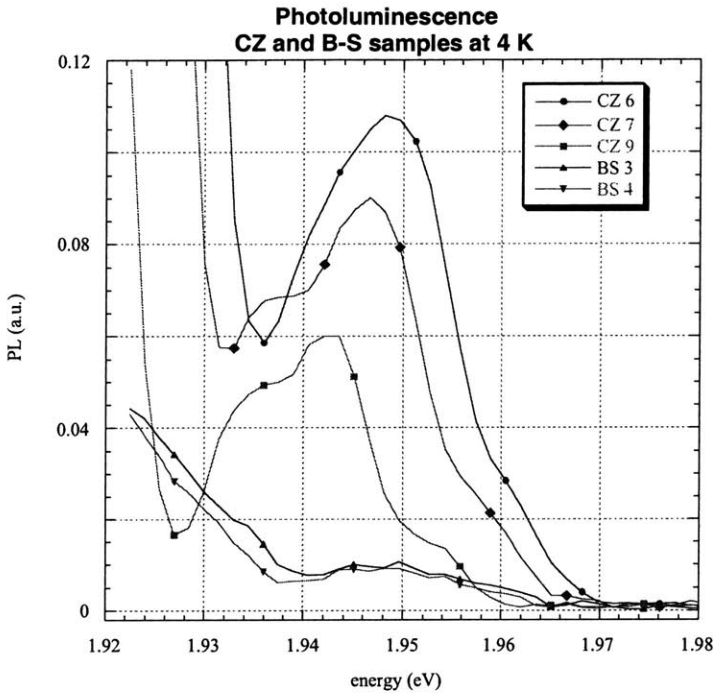

Figure 9-7: Variations of photoluminescence within Czochralski material as well as difference as compared to Bridgman material.

to 3 mm. Samples were dark annealed at elevated temperatures (200-300 °C) to thermally the empty traps. In order to have a consistent method for measuring the photochromic response, a number of identical sample holders were manufactured that would fit into a Cary 500 spectrophotometer. A two millimeter hole was chosen in order to balance the 'averaging' inherent in absorption measurements and the increasing errors incurred due to a weaker signal from small apertures. Samples were mounted on the plates prior to the dark anneal. Samples could then be loaded easily and reproducibly into the spectrophotometer with minimum exposure to the 'red' light used while mounting the samples.

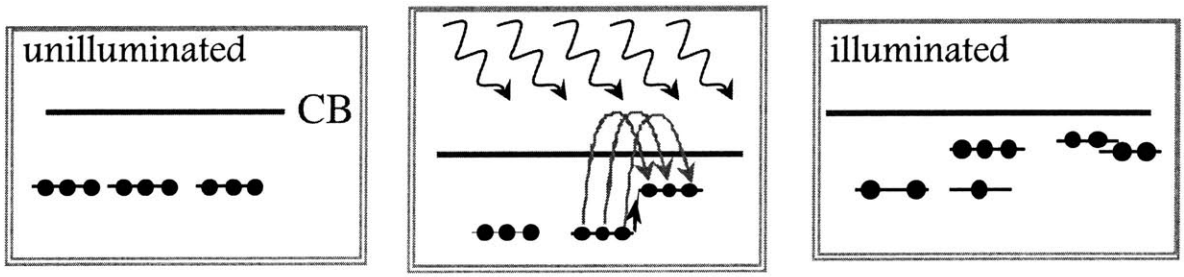

Figure 9-8: Phenomenological representation of the mechanism for the photochromic effect.

A 'dark' absorption spectrum (400-900 nm) was taken, and the sample was then exposed to light for one minute using a halogen lamp. Next, an 'illuminated' absorption spectrum (400-900 nm) was acquired. The change in the absorption behavior due to exposure to optical stimulation could be assessed by analyzing the ratio of the illuminated spectrum to the dark spectrum. Dark and light absorption spectra of CZ material and the change in absorption is shown in Figure 9-9.

Photochromic response was measured for samples CZ boules as well as from B-S samples. It was observed that the dark spectra of the Bridgman samples are different than the spectra from the Czochralski samples. In the CZ samples it appeared that several traps were emptied due to the dark anneal as is indicated by the absorption 'dark' spectra that does not show any peaks. Also noted was that the CZ102301 sample had a stronger photochromic response than the CZ110501 sample. The dark anneal did seem to have as marked an effect in the B-S samples. Moreover, the seed (BS113001-S) that was cut from the CZ102301 boule exhibits a reduced photochromic response due to the differences in the dark spectra. Figure 9-10 shows representative absorption spectra (a) before and (b) after illumination as well as (c)

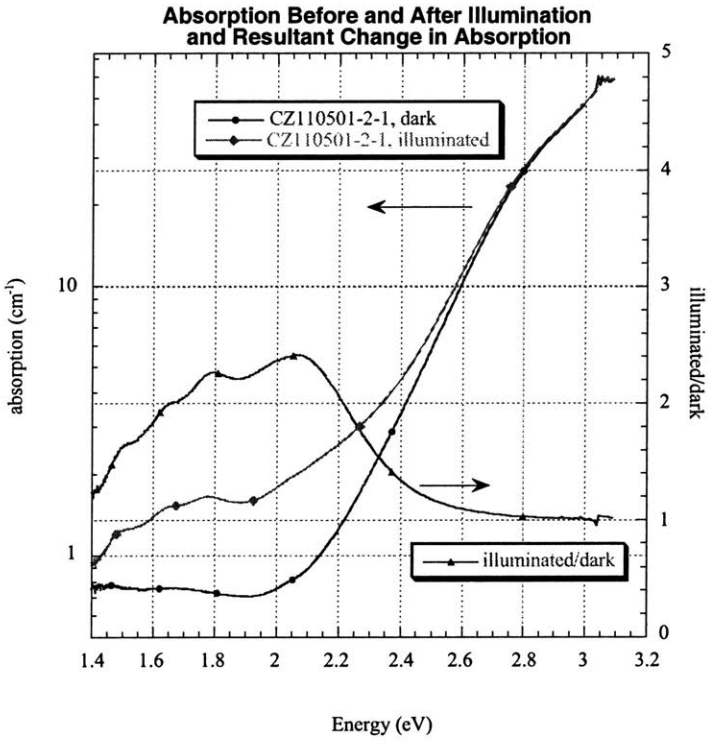

Figure 9-9: Typical absorption spectra before (dark) and after (illuminated) exposure to halogen light for 60 sec. Ratio of two spectra is also shown.

the ratio of illuminated to dark absorption from one of the CZ samples and two of the Bridgman samples. Looking at the ratio of illuminated to dark absorption (Figure 9-10c), there are five discernible peaks in the CZ spectrum. This indicates that the photochromic effect is not due to a a single trap, but rather, that several energy levels are involved. However, most unique is the fact that the BS020802 sample does not exhibit any photochromic response. This phenomena is discussed in the section 9.6.

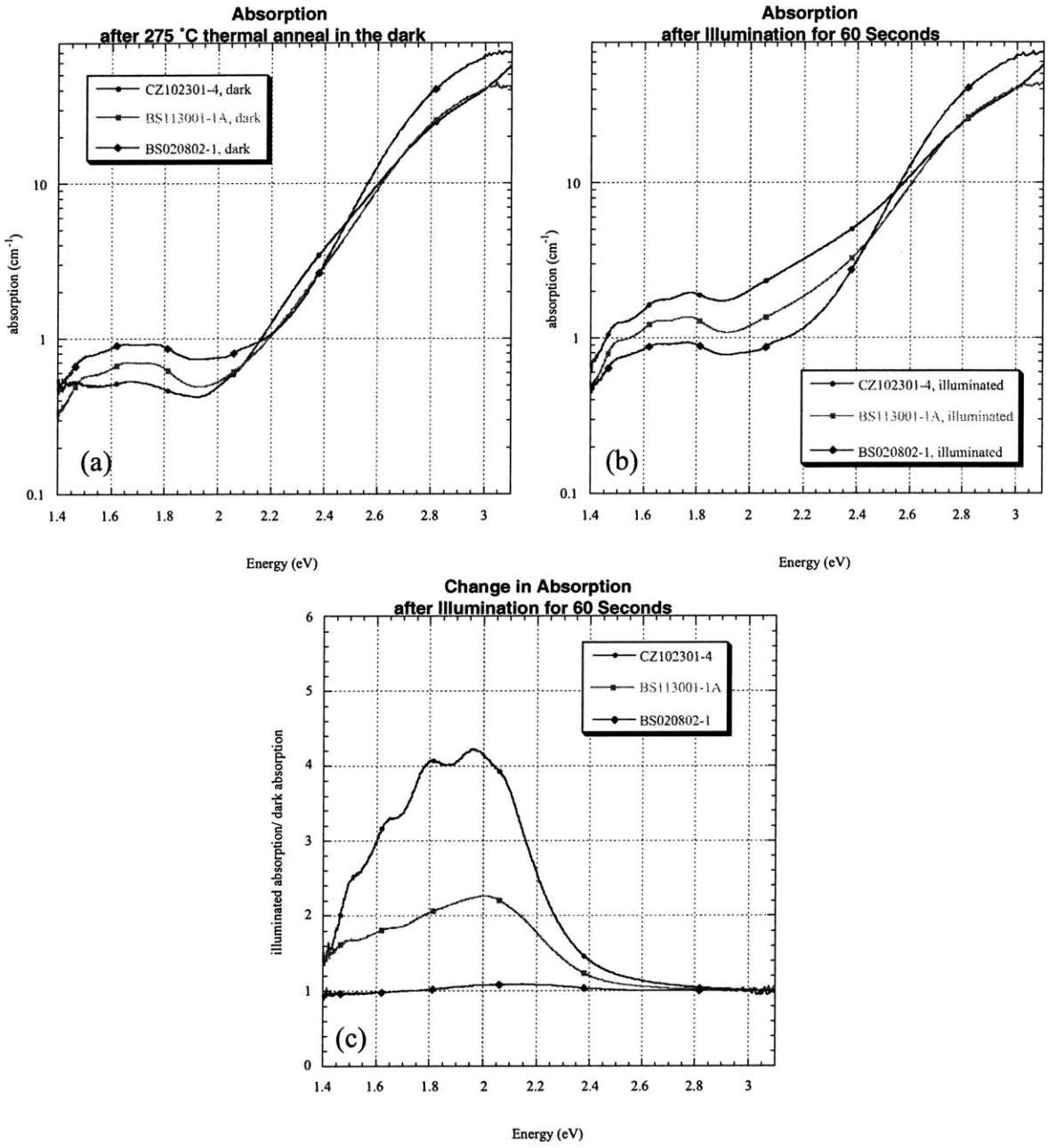

Figure 9-10: (a) Dark adapted absorption spectra (b) absorption spectra after illumination (c) ratio of illuminated to dark absorption.

Room temperature photochromism had been observed[19,153] by others. Although they could not unambiguously identify the cause, they found that very low levels of impurities of Cr and Fe were present in those samples. Mass spectrometry of both CZ boules was obtained in order to assess the level of unintentional impurities in these crystals. The results are shown in Figure 9-11 and Figure 9-12. Both boules have chromium levels above 1 ppm, and the CZ102301 boule has several ppm of iron as well. This boule exhibited a stronger darkening with exposure to room light than the CZ110501 boule.

cz102301					
Element	Conc	Element	Conc	Element	Conc
	[ppm wt]		[ppm wt]		[ppm wt]
Li	0.008	Ga	0.04	Nd	< 0.005
Be	< 0.001	Ge	4.8	Sm	< 0.005
B	0.01	As	0.09	Eu	< 0.005
C	-	Se	< 0.01	Gd	< 0.005
N	-	Br	< 0.01	Tb	< 0.005
O	Matrix	Rb	< 0.005	Dy	< 0.005
F	< 0.05	Sr	< 0.005	Ho	< 0.005
Na	0.02	Y	< 0.005	Er	< 0.005
Mg	0.006	Zr	< 0.005	Tm	< 0.005
Al	0.52	Nb	< 0.005	Yb	< 0.005
Si	Matrix	Mo	0.03	Lu	< 0.005
P	0.05	Ru	< 0.01	Hf	< 0.005
S	21	Rh	< 0.005	Ta	Source Mat.
Cl	0.02	Pd	< 0.005	W	< 0.01
K	0.02	Ag	< 0.005	Re	< 0.01
Ca	< 0.1	Cd	< 0.2	Os	< 0.005
Sc	< 0.005	In	Binder	Ir	< 0.005
Ti	0.08	Sn	< 0.05	Pt	0.63
V	0.02	Sb	0.01	Au	< 0.01
Cr	2.9	Te	< 0.01	Hg	< 0.01
Mn	0.01	I	< 0.005	Tl	< 0.01
Fe	2.6	Cs	< 0.005	Pb	< 0.2
Co	< 0.005	Ba	< 0.005	Bi	Matrix
Ni	0.03	La	< 0.005	Th	< 0.001
Cu	0.01	Ce	< 0.005	U	< 0.001
Zn	< 0.01	Pr	< 0.005		

Figure 9-11: Impurity analysis of CZ102301 boule.

cz110501					
Element	Conc	Element	Conc	Element	Conc
	[ppm wt]		[ppm wt]		[ppm wt]
Li	0.01	Ga	0.03	Nd	< 0.005
Be	< 0.001	Ge	0.12	Sm	< 0.005
B	< 0.005	As	0.01	Eu	< 0.005
C	-	Se	< 0.01	Gd	< 0.005
N	-	Br	< 0.01	Tb	< 0.005
O	Matrix	Rb	< 0.005	Dy	< 0.005
F	< 0.05	Sr	0.008	Ho	< 0.005
Na	0.02	Y	< 0.005	Er	< 0.005
Mg	0.01	Zr	< 0.005	Tm	< 0.005
Al	0.75	Nb	< 0.005	Yb	< 0.005
Si	Matrix	Mo	0.03	Lu	< 0.005
P	0.15	Ru	< 0.01	Hf	< 0.005
S	24	Rh	< 0.005	Ta	Source Mat.
Cl	0.02	Pd	< 0.005	W	< 0.01
K	< 0.01	Ag	< 0.005	Re	< 0.01
Ca	4.9	Cd	< 0.2	Os	< 0.005
Sc	< 0.005	In	Binder	Ir	< 0.005
Ti	0.06	Sn	< 0.05	Pt	0.59
V	0.006	Sb	0.07	Au	< 0.01
Cr	1.3	Te	< 0.01	Hg	< 0.01
Mn	< 0.005	I	< 0.005	Tl	< 0.01
Fe	0.76	Cs	< 0.005	Pb	1.1
Co	< 0.005	Ba	< 0.005	Bi	Matrix
Ni	0.01	La	0.02	Th	< 0.001
Cu	0.01	Ce	< 0.005	U	< 0.001
Zn	< 0.01	Pr	< 0.005		

Figure 9-12: Impurity analysis of CZ110501 boule.

9.6 High temperature annealing

The effect of high temperature annealing (near melting point – about 865 °C) was discovered as a result of photochromic response measurements. The first indication was the absence of any photochromic response in the Bridgman sample that was grown in a low thermal gradient (BS020802). Not only was there no difference between the dark and

illuminated spectra for the regrown material, more importantly, it was found that the seed material did not show any change either. Since samples from the Czochralski boule from which that seed was cut showed photochromic behavior, it was concluded that the seed material must have been modified during Bridgman growth process. Looking at the temperature data, it was observed that the seed material was exposed to temperatures near the melting point for over 12 hours. It was hypothesized that the defect concentration was permanently altered as a result of the high temperature anneal.

9.6.1 Annealing Effects on Photochromism

In order to test this theory, Czochralski material was sealed in an ampoule an annealed using the same thermal profile that was experienced by the seed of BS020802. The surface of the sample showed signs of re-crystallization as seen in Figure 9-13a. After re-polishing the sample, it was observed that dark striations had appeared while the bulk material was lighter in color. Figure 9-13b shows the annealed sample next to an un-annealed sample from the same boule.

The photochromic response is almost completely removed in the CZ sample that was annealed at the high temperature. Figure 9-14 shows the ratio of illuminated to dark spectra from several annealed samples on an expanded scale. The maximum lies in the vicinity of 585 nm (2.1 eV). In Figure 9-15, the dark and illuminated spectra for two samples is shown (a) before the high temperature anneal and (b) after the high temperature anneal. The

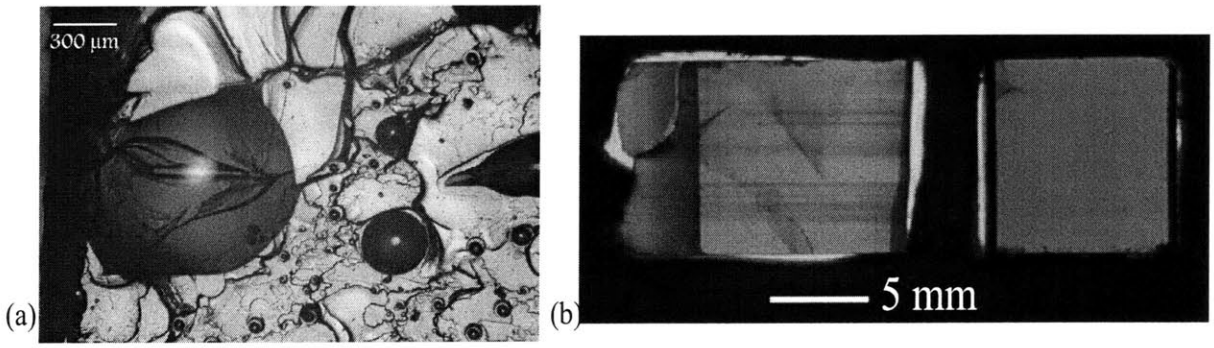

Figure 9-13: (a) surface of annealed sample (b) macroscopic view of annealed sample on left and unannealed sample on right.

difference for annealed samples lies in the spectra that is taken prior to illumination (the 'dark' spectra). The thermal anneal at 275 °C in the dark no longer empties the traps, *i.e.* the dark spectra is the same as the illuminated spectra.

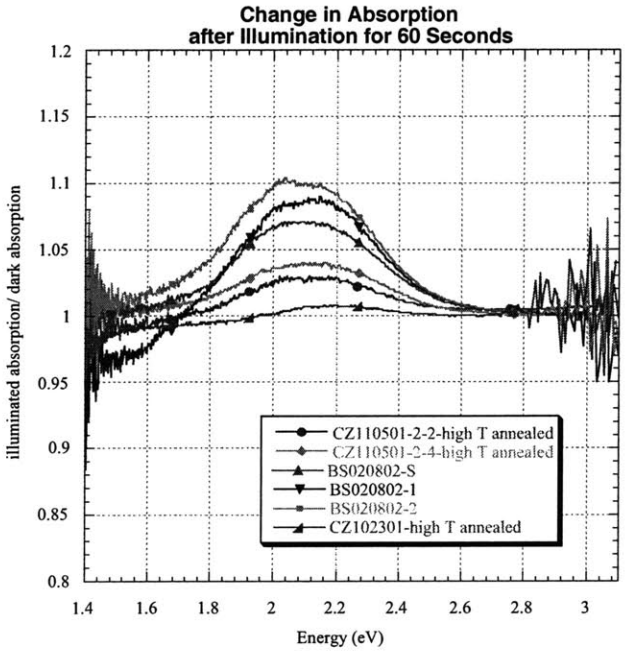

Figure 9-14: Photochromic response of samples annealed at high temperatures.

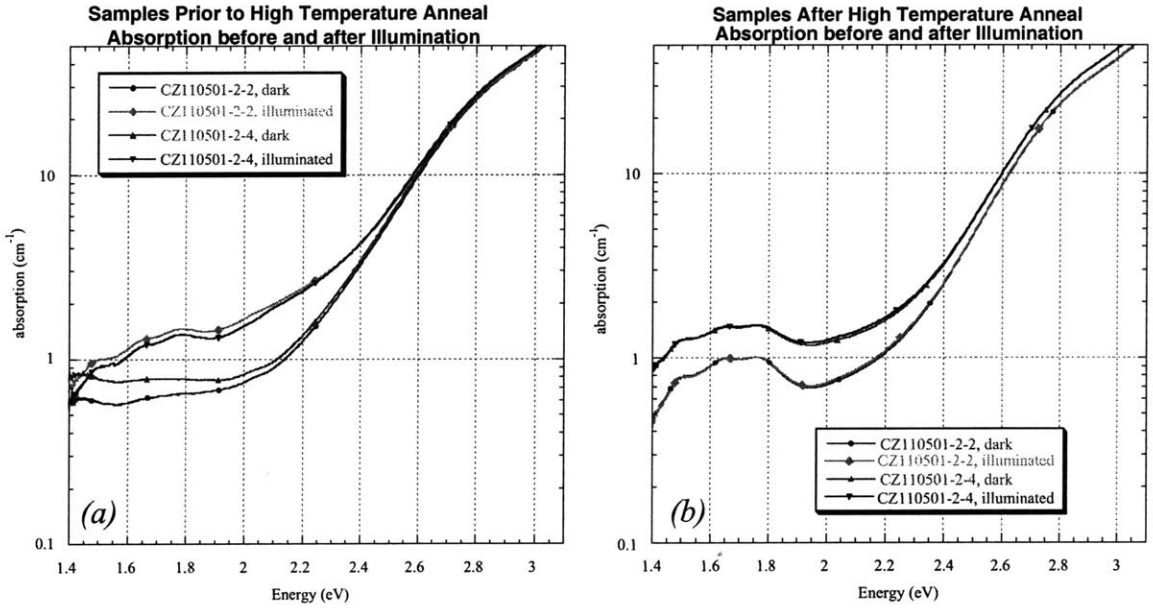

Figure 9-15: Difference in effect of 275 °C dark anneal and subsequent illumination (a) before high temperature anneal (b) after high temperature anneal.

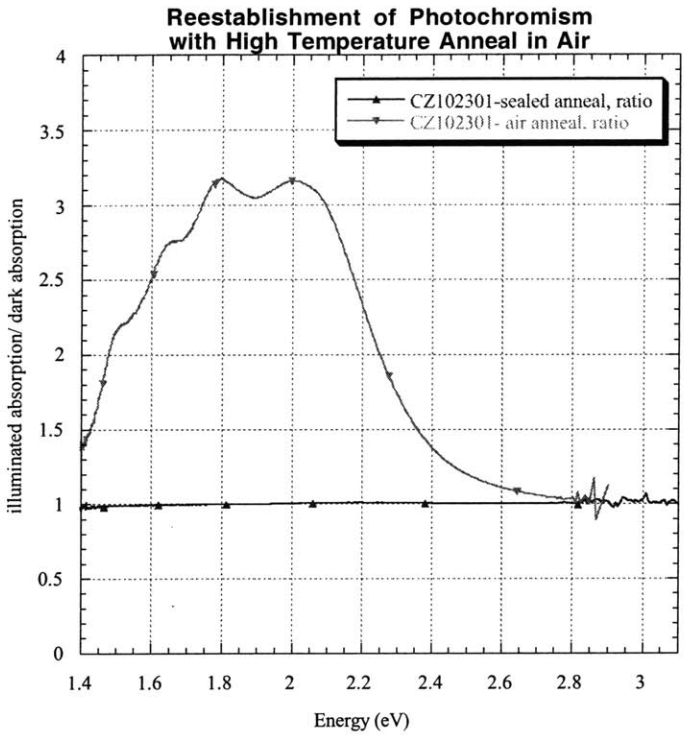

Figure 9-16: Reestablishment of photochromic response by annealing in air.

It is documented in literature that annealing chromium doped BSO[204] and Mn-doped BTO[150] in a vacuum removes the photochromic effect, but this process can be reversed by annealing the samples in air. A sample (CZ102301-high T anneal) that had been annealed at high temperatures and exhibited no photochromism was re-annealed in air. The photochromic response was restored, as can be seen in Figure 9-16. Therefore, it is concluded that oxygen vacancies are formed during annealing in a reduced oxygen environment and that this has a fundamental effect on the interband states. Panchenko[156] states that the number of oxygen vacancies is increased with vacuum annealing, and that as a result, the number of oxygen atoms available for ionization for light induced transitions decreases.

9.6.2 Annealing Effects on Photoconductivity

To further investigate the modification of the interband states, photoconductivity measurements of unannealed and annealed samples were taken. For these measurements, the geometrical configuration of the electrodes was changed from the earlier measurements. The

resistance was decreased by increasing the electrode size and decreasing the width of the sample. This resulted in a better signal to noise ratio and allowed for higher spectral resolution. Additionally, the new configuration allowed for the same current setting to be used for all samples. Direct comparison of signal strengths between samples was thus possible. The response in the annealed sample was approximately a factor of six weaker than for the unannealed sample as seen in Figure 9-17. Similar to the absorption measurements, samples were annealed in the dark at ~200 °C and a 'dark' photoconductivity spectrum was obtained. The sample was then illuminated while another spectrum was taken. The additional illumination acted as dynamic excitation and increased the photoconductivity signal. The signal decreased to its original value once the additional illumination was removed. This light induced photoconductivity was significantly less at 2.9 eV and absent at lower energies in the high temperature annealed samples. Figure 9-18 shows the spectra for dark and illuminated photoconductivity measurements of an unannealed and an annealed sample.

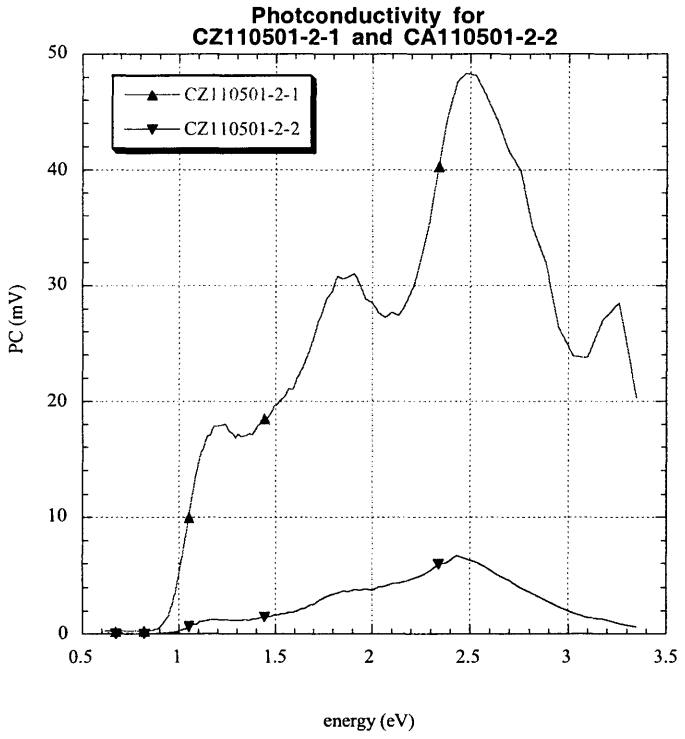

Figure 9-17: Difference in photoconductivity of unannealed and annealed samples.

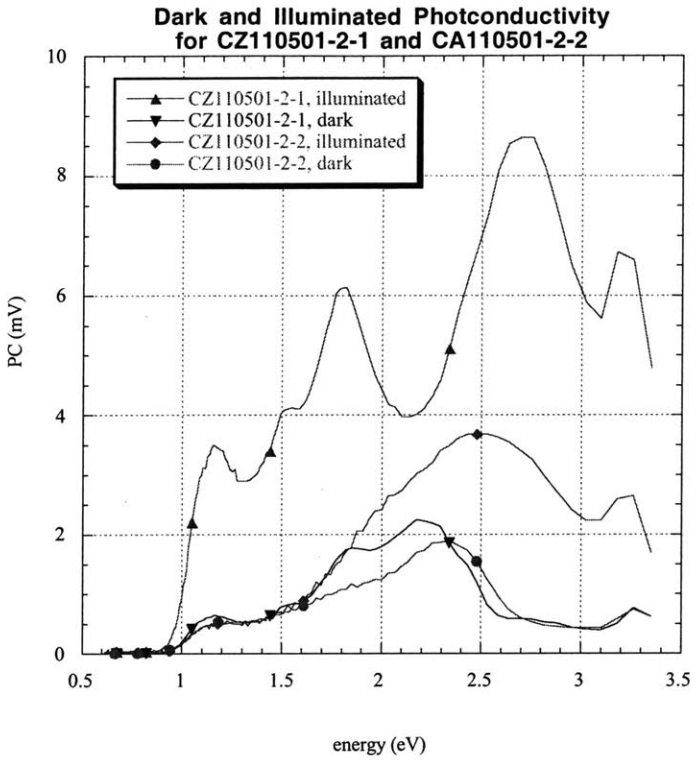

Figure 9-18: Light induced photoconductivity in unannealed BSO (CZ110501-2-1) and annealed BSO (CZ110501-2-2).

9.7 Photorefractive Response

Since photorefractivity and photochromicity are related, it was necessary to investigate the effect of high temperature annealing on the photorefractive response. In collaboration with Prof. Joel Martin at Oklahoma State University, photorefractivity measurements were performed on annealed and unannealed samples.

9.7.1 Experimental Set-up and Procedure

A four beam mixing set-up was used at Oklahoma State University. An argon laser (488 nm) was used for the write beams. The laser beam was attenuated and polarized before splitting it to produce the two write beams. The beams were crossed such that a two micron grating was created. The write beam power was set to 15 mW for all experiments. A HeNe laser (633 nm) was used for the read beam. In order to minimize erasing due to the read beam, a neutral density two filter reduced the signal strength by a factor of 100. The diffracted

read beam signal was measured with a photo multiplier tube (PMT) and the read beam was monitored with a silicon diode. For each sample, the PMT and Si diode had to be manually aligned with the beam due to the slightly different diffraction direction for each sample. The change in the diffracted beam direction arose from the varying sample thickness and the fact that not all faces were exactly parallel. This alignment procedure introduced unavoidable variance into the signal strength between samples. The signal was amplified and sent to an high precision digital voltmeter and an oscilloscope, and both signals were logged in a data file. The set-up is shown in Figure 9-19.

Gratings were written for 0.5 seconds and the subsequent decay was monitored for 20 seconds. In order to establish a baseline, data was recorded for 100 ms prior to triggering the write beams. The average of the baseline data was subtracted from the signal prior to storing the signal in the data file. The oscilloscope only recorded the first second (including the write cycle) but with a resolution of one millisecond. The higher resolution DVM recorded the full 20 seconds but only at 100 ms intervals. Samples were dark-annealed at 250 °C overnight to thermally empty traps.

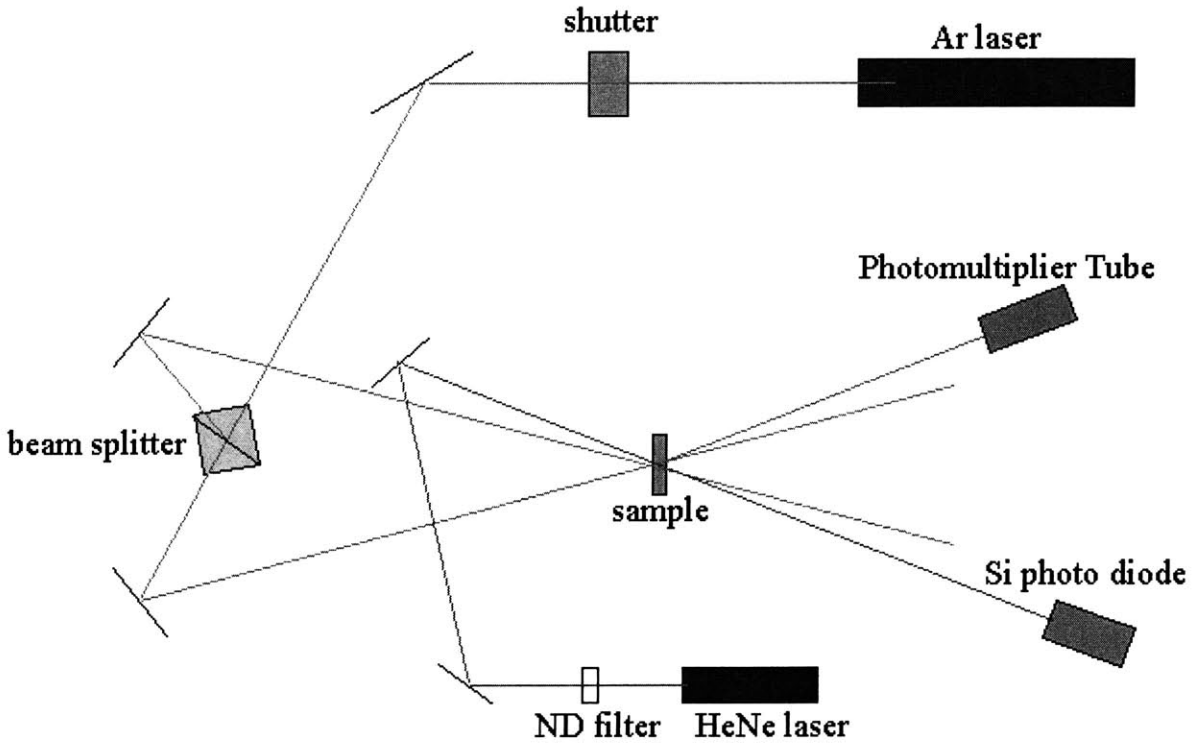

Figure 9-19: Experimental 4 wave mixing set-up used for photorefractivity measurements.

9.7.2 *Data Analysis*

The raw data had to be processed in order to be able to compare different scans. One of the initial observations was that annealed samples exhibited a persistent grating. This conclusion was made because some scans would drop below zero during the decay. By plotting the baseline average for different runs, shown in Figure 9-20, it can be seen that not all scan had the true baseline. This was due to the fact that the persistent grating in the sample would still diffract the read beam before the new grating was written and hence give a higher baseline. For the DVM, the normal baseline was very close to zero, and an average of all of the 'good' baselines was taken and used as the standard baseline. For scans with baselines that were too high, the standard one was used as a replacement. For the scope data, the 'normal'

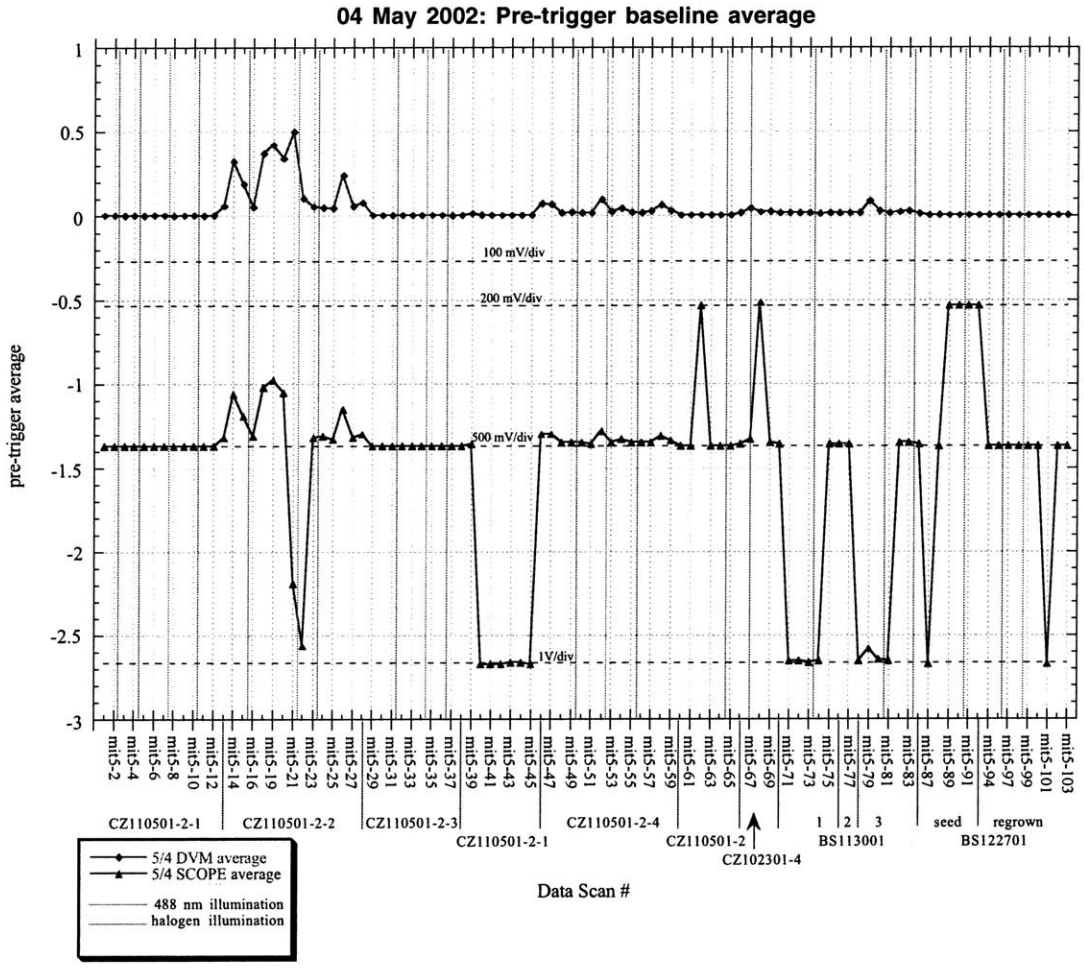

Figure 9-20: Baseline averages for all the runs.

baseline value also depended on the mV/division setting of the scope. For each mV setting, a 'standard' baseline was computed by averaging normal scans with that mV/div setting. Again, aberrant baselines were replaced with the 'standard' one. Next, the data was scaled by a factor of 10 to account for the neutral density two filter. In order to compare decay times, the DVM data was normalized using the last data value before the write beams were turned off. Since the scope data had a higher temporal resolution, the normalizing factor was taken from the scope data. For decay analysis, the last data point with the write beams on was used for t=0.

9.7.3 Results

The annealed samples showed a fundamentally different photorefractive response than the unannealed samples. The signal was weaker, had a different rise time, and exhibited a different decay behavior. The signal strength for annealed samples was reduced by a factor of approximately six as compared to un-annealed samples of comparable thickness. A comparison of the two signal strengths is shown in Figure 9-21.

The leading edge peak was narrower in annealed samples than in un-annealed samples. Figure 9-22 shows the scans from Figure 9-21 but with the leading peak of the annealed sample scaled to the same height as the leading peak of the un-annealed sample and translated such that the maximums coincide. This indicates that the response time has decreased through the high temperature anneal.

The decay of the read beam was substantially different in the annealed samples as compared to the un-annealed samples. The decay of the un-annealed sample was characteristic of the response for BSO as observed and published by Prof. Martin in his research. The attenuation of the signal strength is due to two factors: first, there is a natural decay inherent in the material due to the recombination of trapped charges back to the ground state; secondly there is decay that is due to the illumination from the read beam. In order to minimize the latter, the neutral density two filter was used. All data presented was scaled by a factor of 10 to account for the neutral density filter.

Figure 9-23 shows the differences in decay behavior for annealed vs. unannealed samples. The annealed samples exhibited decay in multi-step fashion. There was the initial, very fast, decay that was then followed by a very slow decay. Figure 9-24 is a plot of the read

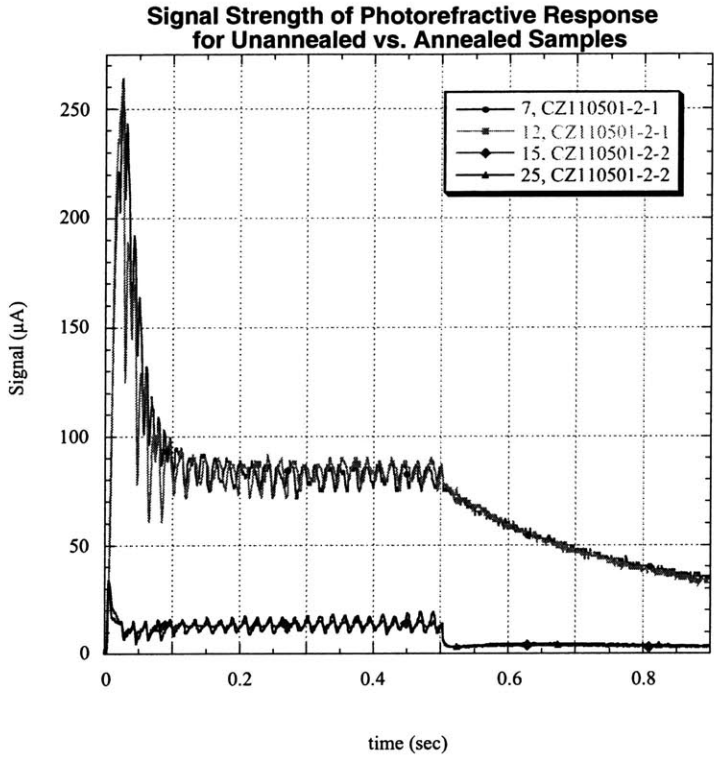

Figure 9-21: Strength of photorefractive response for unannealed and annealed samples.

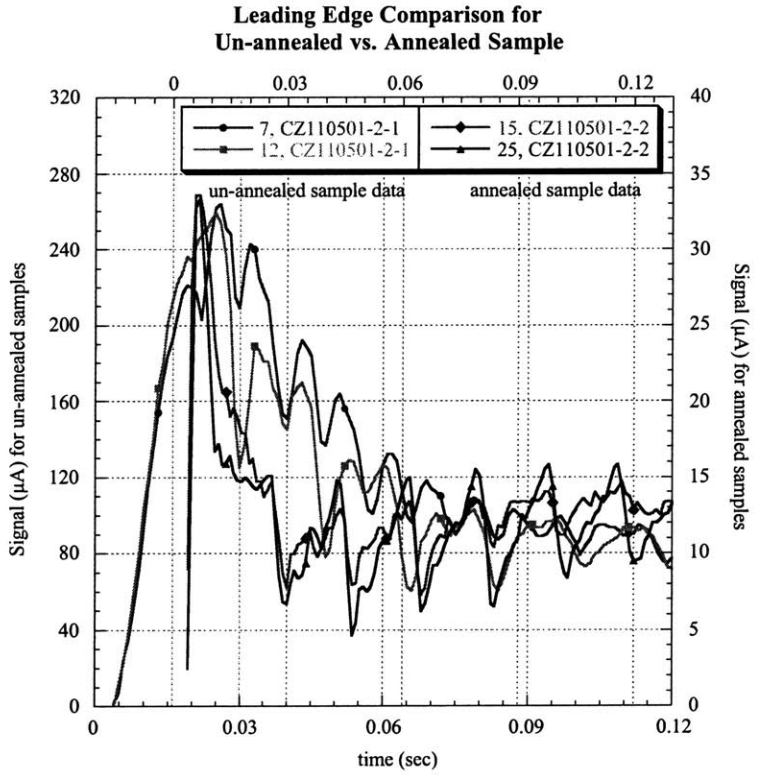

Figure 9-22: Differences in leading edge peak between unannealed and annealed samples (annealed peak has been scaled).

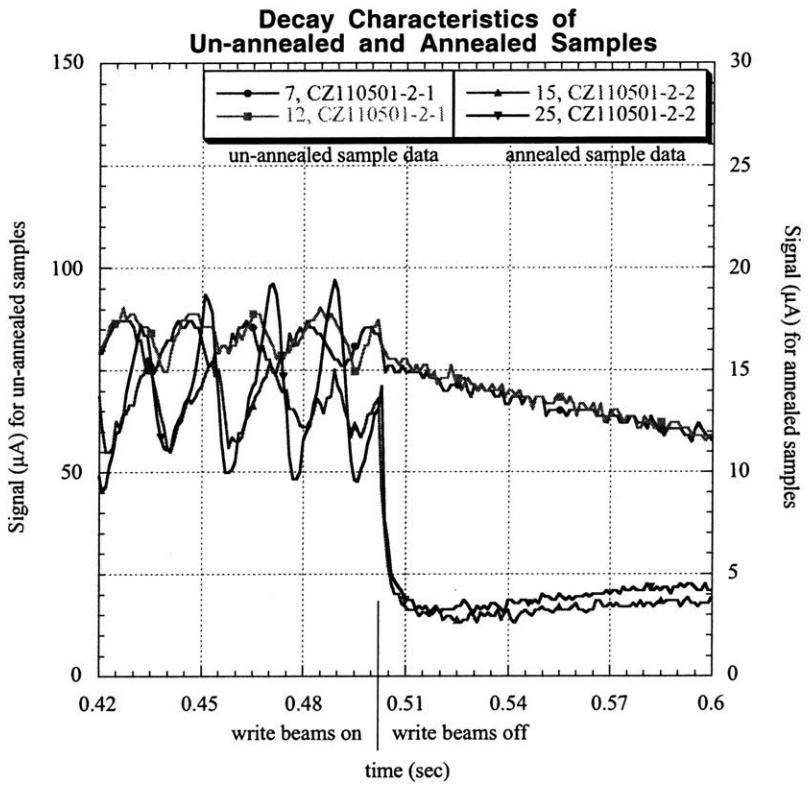

Figure 9-23: Difference in initial decay for unannealed and annealed samples after write beams are turned off (scope data). Annealed signal is scaled 5x.

beam strength after the read beam has been turned off. The signals have been normalized with the read beam signal strength just prior to the write beams being turned off so that the decay characteristics can be compared independent of the magnitude of the signal. By using a log-log plot of the decay curves (Figure 9-25), the different decay processes become apparent as changes in slopes between linear portions.

9.8 Discussion of Results

Each of the different analysis techniques - absorption, photoconductivity, photoluminescence, and photorefractivity - provides clues as to the changes in interband states from growth using different methods and by high temperature annealing. Comparing photoconductivity and photoluminescence for Czochralski, Bridgman, and hydrothermal material, the effect of varying growth conditions on the defect incorporation can be seen.

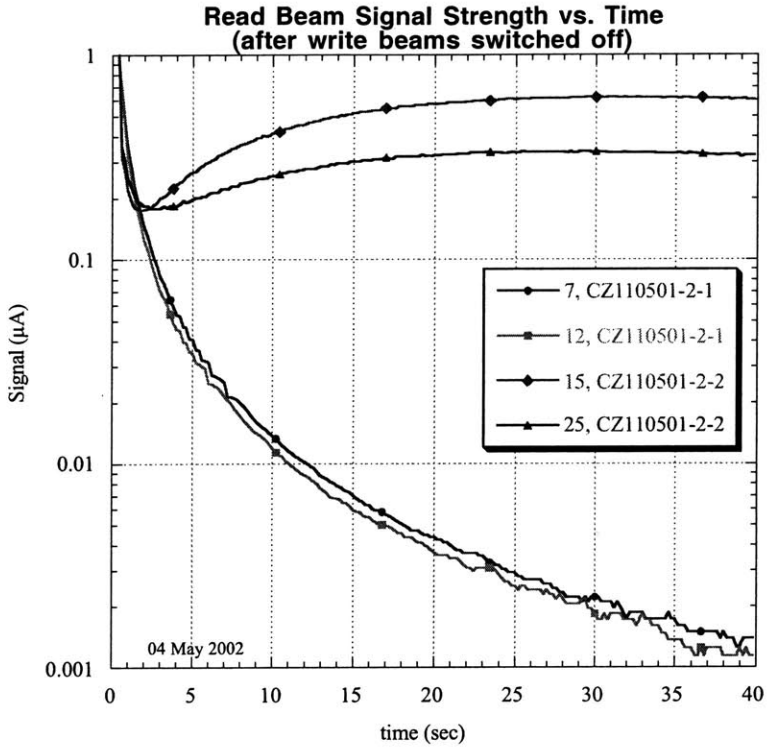

Figure 9-24: Difference in long decay for unannealed and annealed samples after write beams are turned off (DVM data).

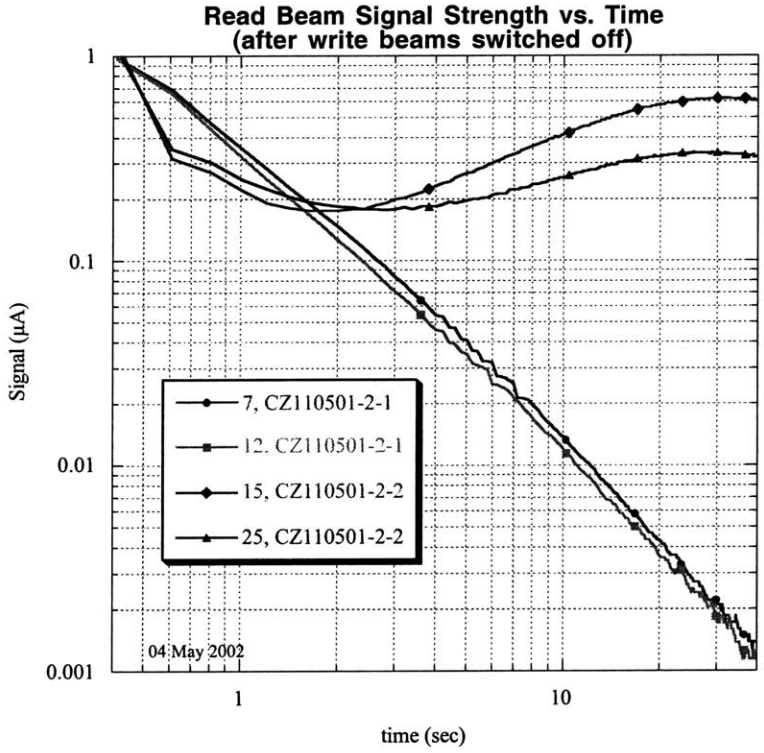

Figure 9-25: Log-Log plot of decay of unannealed samples (7,12) and annealed samples (15,25).

The first conclusion that can be drawn is that Bridgman material has a lower concentration of point defects that contribute carriers to photoconductivity than the Czochralski material. Optically, the B-S material appears lighter and has lower absorption than CZ material. Photoluminescence and photoconductivity both show significantly weaker signals for B-S material. The fact that the luminescence signal is weaker indicates that fewer interband levels exists to which the excited electrons can radiatively recombine. The hydrothermal material does not have the native defect and hence also does not exhibit photoconductivity or photoluminescence.

Examining the photoconductivity measurements clearly shows that there are fewer active carriers in B-S material. A schematic of the set-up for photoconductivity measurements is shown in Figure 9-26. A ~100 V potential was applied across each sample, and the current was controlled via an adjustable current source. Equation 9-1 gives the relationship for the photogenerated current.

Equation 9-1 $$I_{PC} = qN_{abs}\mu\tau V_{applied}$$

where q = charge (coul)
N_{abs} = number of absorbed photons (cm^{-2} sec^{-1})
μ = mobility (cm^2 V^{-1} sec^{-1})
τ = lifetime (sec)
$V_{applied}$ = voltage applied across the sample (V)

Since it is easy to measure the voltage drop across the sample as a result of illumination, the resistance of the sample (R_{sample}) is incorporated, as seen in the Equation 9-2. For this setup, the current was limited by the current source, and it had to be adjusted between different samples such that the overall applied voltage drop across the sample was approximately 100 V. Looking at Equation 9-3, if the resistance of a sample was significantly higher than another sample, the current had to be decreased in order to keep the applied voltage about the same.

Equation 9-2 $$V_{PC} = R_{sample}I_{PC} = qN_{abs}\mu\tau V_{applied}R_{sam}$$

Equation 9-3 $$V_{PC} = qN_{abs}\mu\tau(IR_{sample})R_{sample}$$
$$V_{PC} = qN_{abs}\mu\tau IR^2_{sample}$$

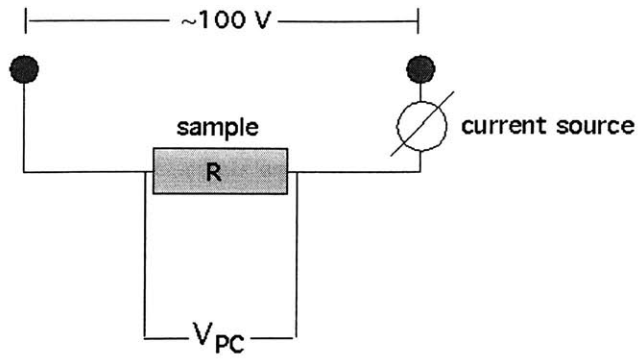

Figure 9-26: Schematic of set-up for photoconductivity measurements.

Referring to Figure 9-4, the photoconductivity signal of the B-S sample is 33% lower than that of C-Z; however, the current is also 10x lower. Using Equation 9-3, this corresponds to a resistivity that is ~2.6 higher than the resistivity of the CZ sample. For the hydrothermal material, the current is 100x lower than that for the CZ sample, indicating a very high resistance due to an extremely low defect concentration. Photoluminescence corroborates this conclusion since the luminescence signal is directly proportional to the trap density.

In contrast, the decreased signal observed in the high temperature annealed samples is not due to lower donor defect concentration. In these measurements, the current setting was the same for all samples. Therefore, resistance did not significantly vary between samples. The decrease in signal strength is concluded to be due to a decrease in carrier lifetime since the other terms in Equation 9-1 do not change between samples.

Photoconductivity determines the speed of photorefractive build-up as well as the decay of Δn[117]. Examining the photorefractivity data, this is clearly evident. The leading peak as well as the initial decay in the annealed samples are faster than in the unannealed case as seen in Figure 9-22 and Figure 9-23. Again, it is concluded that the time constant for these processes is smaller in the annealed sample.

The only explanation for the unusual decay behavior of the annealed samples is that the trap levels have been modified by the high temperature anneal and that carriers decay back to the ground state through a different pathway than in unannealed samples. However, the complexity of the energy band structure in BSO makes a detailed analysis beyond the scope of this work.

CHAPTER 10: CONCLUSIONS AND FUTURE WORK

All samples were nominally undoped, yet they exhibited behavior that is classically observed in doped semiconductors. Mass spectrometry revealed no impurity greater than a few ppm. It is known[19,153] that when chromium and iron are present at even these low levels, room temperature photochromism is observed and that low temperature photochromism is present in intrinsic BSO. However, the photorefractive property cannot be explained by any single impurity; it is observed in all crystals grown from the melt. The intrinsic defect that is present in melt-grown material is responsible for the photorefractive property. The main thrust of this work was to investigate the origin of this native defect by analyzing electro-optical properties as a function of growth conditions. Results from this work do not discount the hypothesis that the formation of the critical native defect is influenced by convective transport analogous to that of dopants in semiconductors. Literature indicates the presence of pre-crystalline structures in the melt that affect the phase formed upon solidification. It is therefore hypothesized that these clustering structures may act as precursors to formation of the critical native defect, and that they are subject to convective transport in the melt.

Microgravity experiments that would reduce the gravitational driving forces for convection by six orders of magnitude were proposed in order to study solidification under growth conditions not achievable in a terrestrial environment. This work is part of groundbased research in preparation for microgravity experiments. A number of growth related issues were investigated for the development of experimental designs and procedures that would be use in space flight experiments.

10.1 Clustering Literature

The first mention of clustering in the melts of sillenites is by Kagrin et al.[205]. They measured the viscosity, density, and surface tension of the melts of BSO and BGO. They observed marked deviations from linearity of the logarithmic curves for viscosity and are shown in Figure 10-1. This indicates the existence of pre-crystalline processes. The free energy of activation of viscous flow is given by

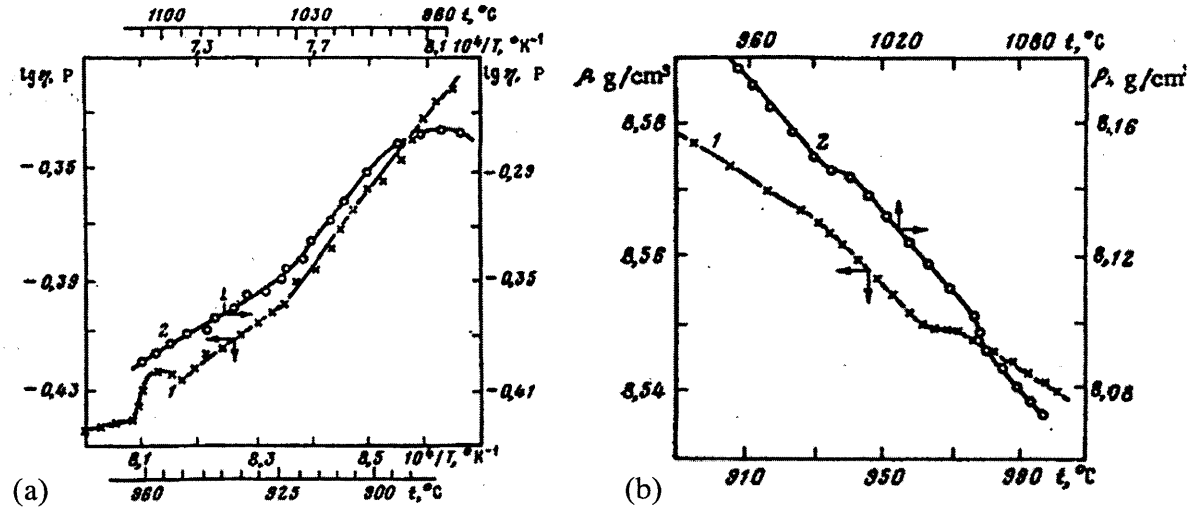

Figure 10-1: (a) Viscosity. 1: Bi_2O_3, 2: 14.3 mol% SiO_2 and (b) density measurements. 1: Bi_2O_3, 2: 14.3 mol% SiO_2 from Kagrin[205].

Equation 10-1

$$F_v = RT \cdot \ell n\left(\frac{Mv}{Nh}\right)$$

where R = gas constant (J $mole^{-1}$ K^{-1})
T = temperature (K)
M = molar volume (m^3)
v = viscosity (kg m^{-1} sec^{-1})
N = Avogadro's number
h = Planck's constant (J sec)

The rapid increase in viscosity due to the formation of clusters in the melt has a greater effect on the activation energy than the decrease in temperature, and this accounts for the nonlinear behavior observed. They conclude that the properties of the melt are governed by structures of the anionic complexes.

Tananaev et al.[206] investigated the formation of the metastable phases in BSO and BGO and also found marked deviations from linearity in density and viscosity polytherms. They divide the melt into three different regions which they denote as Zone A, B, and C. Zone A is the low temperature regime, zone B the intermediate, and Zone C the high temperature region. They found that solidification from zone A yielded the stable gamma phase while solidification from zone B produced the metastable δ* phase. Figure 10-2 shows the phase diagram for BSO with the melt zones as well as the metastable phases.

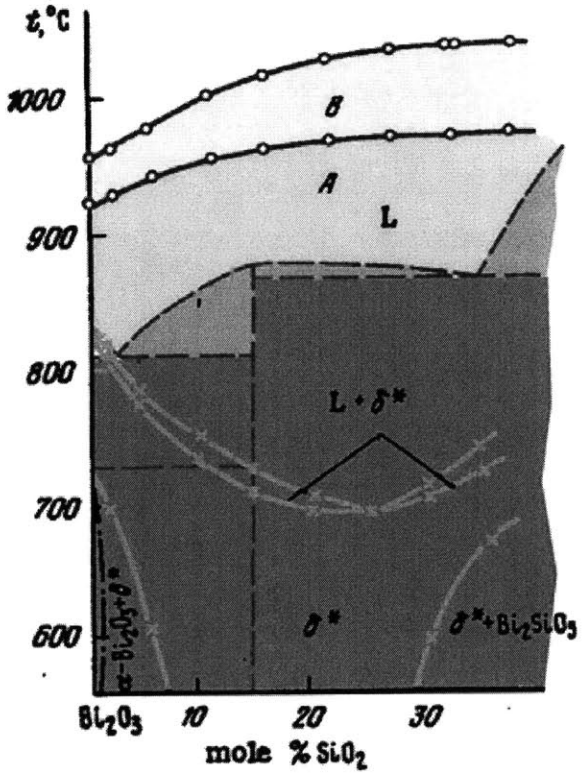

Figure 10-2: Stable and metastable phase diagram after Tananaev[206] with melt divided into low and high temperature zones.

In continuation of the above work, Zhereb et al.[207] gives a model of the clusters that are found in each of the three zones. The first assumption is that the structure of the melt near the melting point resembles the solid. Likewise, as the temperature approaches the boiling point, the melt structure resembles the vapor phase. Figure 10-3 shows the different clusters for each zone as described by Zhereb. In zone A, there are two types of clusters, crystallizable and non-crystallizable. The crystallizable clusters are SiO_4 tetrahedra surrounded by deformed BiO_6 octahedra. The noncrystallizable structures are formed from layers of Bi_2O_2 elements. As the temperature is increased to zone B, the bismuth-oxygen envelope decomposes and the SiO_4 tetrahedra polymerize and form long chains. The noncrystallizable structures from zone A are also found in zone B and are very stable because the depolymerization of these chains is very difficult in the absence of free oxygen. With uniform cooling, these structures remain until the crystallization temperature of the metastable phase. They conclude that the principal cause of metastability is caused by the polymerization of the

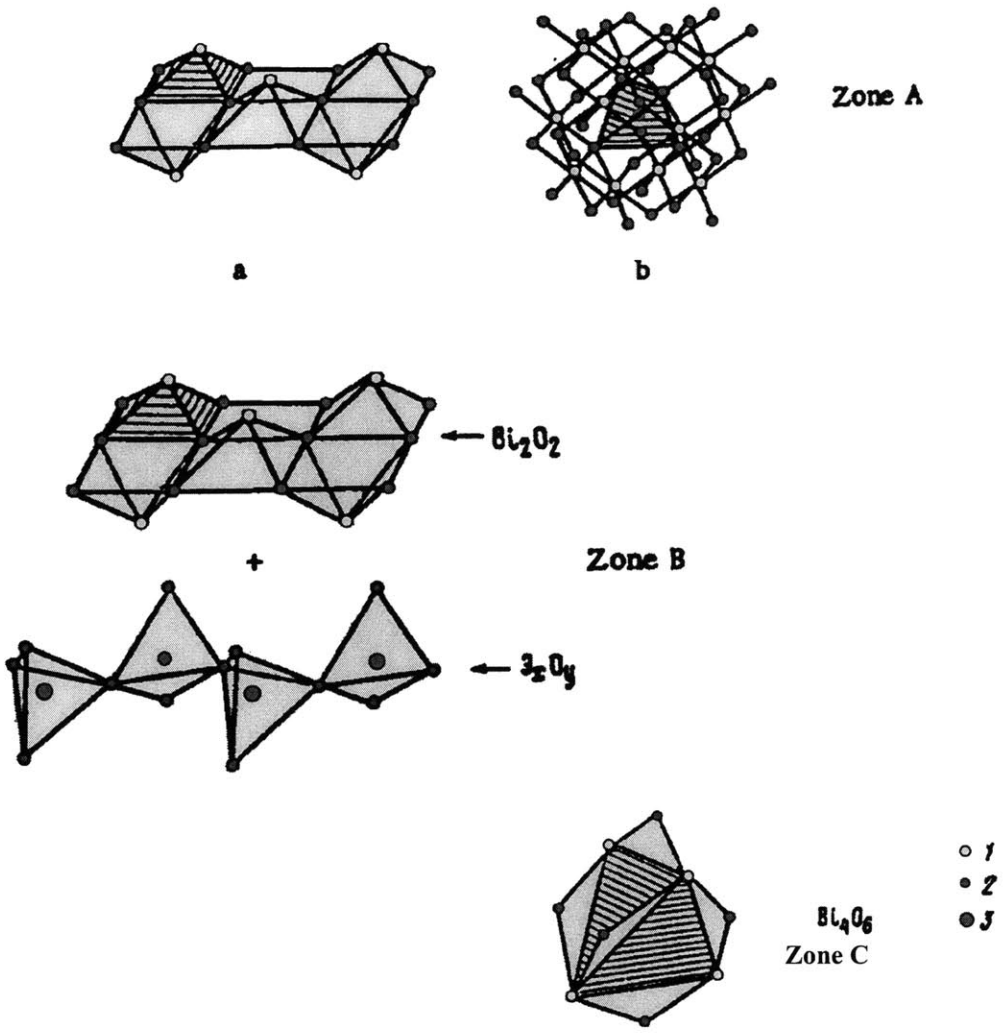

Figure 10-3: Model of clusters found in the different temperature zones as proposed by Zhereb[207]. In zone A, (a) non-crystallizable (b) crystallizable.

Bi_2O_2 elements and the SiO_4 tetrahedra, and that this occurs in the melt as some of the oxygen ions are transferred to the space between the clusters and to the gas phase.

Fu and Ozoe investigated the formation of metastable vs. stable BSO as a function of melt temperature[208,209]. They cooled BSO melts at 20°C/min. from temperatures varying from 908 °C to 966.5 °C. They found that no δ-BSO was formed at temperatures less than 948.5 °C. In quenching experiments, however, with extremely high cooling rates, δ-BSO was formed at lower temperatures. Using x-ray diffraction, they studied the effect of melt temperature on fraction of δ-BSO found in the quenched material. Their data is shown in Figure 10-4.

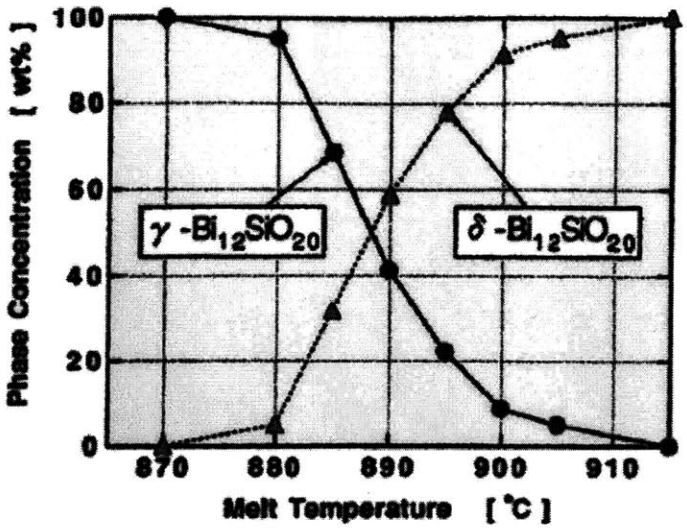

Figure 10-4: Fraction of δ-BSO formed as a function of temperature of the melt in quenching experiments.

More recently, Fei et al.[20] also studied the crystallizing behavior of the Bi_2O_3-SiO_2 system, and they attribute the formation of the metastable phase to the fact that the melt has distinct structures. They note the similarity between the clusters proposed by Zhereb and the structure of Bi_2O_5 as determined by Aurivillius et al.[14]. They conclude that the large amount of energy needed for depolymerization of the SiO_4 polymer chains is responsible for their existence at large undercooling provided by crystallizing the metastable phase. Takeda et al.[210] also conclude that the GeO_4 structure remains in tact in their investigations using x-ray diffraction of BGO melts at different compositions.

10.2 Clustering Hypothesis

The above data strongly support that clustering structures present in the melt affect the subsequent crystalline state. It is possible that the incorporation of nonequilibrium cluster structures, formed at high temperatures, leads to the critical native defect. How this happens is as yet unclear. Cluster formation and incorporation into the solid will depend on a number of factors: solidification temperature, composition, thermal history, and cluster lifetime. Additionally, exactly how clusters are formed, how they are transported to the interface, and the kinetics of incorporation into the crystal matrix are as yet unknown. Because the optical

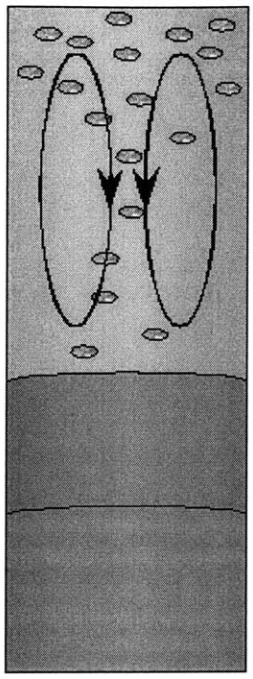

Figure 10-5: Schematic of convective transport of clusters to the interface.

variations observed in nominally undoped BSO are analogous to that of doped semiconductor behavior, it is hypothesized that transport of the nonequilibrium clusters from superheated melt to the interface could be due to gravitationally induced convection, as schematically represented in Figure 10-5.

The thrust of this work was to perform growth experiments under controlled conditions such that the role of the growth environment on the formation of the critical intrinsic defect could be elucidated. However, due to the effects of the high temperature anneal, an extra variable was changed between experiments such that the effect of the temperature environment could no longer be independently analyzed. Additionally, the role of unintentional impurities in the ppm range are cited to significantly affect the photochromic response, and therefore impurities cannot be discounted as being a possibility as the source of variations observed. For all of the above stated reasons, it is not possible to draw unambiguous conclusions about the role of clusters on the incorporation of the native defect and the subsequent effect on optoelectronic processes. However, it can be concluded that the data from this work is consistent with the clustering hypothesis. Therefore the question of the role of clustering in the origin of the native defect remains open and subject to further research.

There are a number of important conclusions that can be drawn from this work regarding wetting behavior, growth system requirements, experimental growth using Czochralski and Bridgman-Stockbarger methods, and dependence of optoelectronic properties of BSO on growth conditions. Moreover, the role of the ambient atmosphere at the time of processing has been shown to fundamentally change the optoelectronic response and must be carefully monitored.

10.3 Conclusions

10.3.1 Interaction of BSO with Confinement Material

Work on the interaction of BSO melts with platinum and platinum/5% gold was studied in both a terrestrial and a low gravity environment. Results led to the following conclusions:

1. Assumptions required for the applicability of the sessile drop theory are not met due to nonhomogenous surfaces as well as pinning at the grain boundaries of the substrate
2. Due to the low contact angles of the platinum-BSO system, the Laplacian curve used for modeling is not adequate because not enough of the curve is available for accurate curve fitting.
3. Although the contact angle data is within experimental error between the computational model and the experimental results, the surface tension varies widely. Statements (1) and (2) are the cause of the fluctuation in the values.
4. A low gravity environment does not fundamentally change the wetting behavior.
5. The embrittlement of platinum in a closed environment is attributed to bismuth vapor that attacks the foil. A lack of sufficient oxygen atoms in the system allows bismuth vapor to form that subsequently attacks the grain boundaries.

10.3.2 Modification and Thermal Characterization of Bridgman-Stockbarger Growth System

Design, Implementation, and thermal characterization of a modified, heat-piped based Bridgman-Stockbarger furnace was successful and provided the following information:

1. Design considerations of axial alignment between hot and cold zones as well as the need for easy and reproducible assembly were met with new design.
2. Thermal profiling indicated that interface inversion from convex to concave always occurs. This is in contradiction to previous work at MIT in the old system[72]. The discrepancy is attributed to the old system having larger heat losses in the hot zone region.
3. Gradient zone insulation from the initial design did not have a low enough thermal conductivity. This led to the inability to control the morphology of the seeding interface due to excessive heat flux radially outward in the gradient zone. Modeling data was in agreement with experimental work. A new gradient zone with lower thermal conductivity was designed and implemented. Control of the interface was achieved with the new insulation.
4. A finite element computational model was developed by CapeSim, Inc. and was found to be in excellent agreement with experimental data in the gradient zone. Hot and cold zone temperatures were found to be different by up to 18 °C with the ampoule in the furnace. The discrepancy was reduced to 7 °C in the cold zone by removing the ampoule from the furnace. The remainder of the difference in values is attributed to additional losses in the system during experimental work that are not accounted for in the model.

10.3.3 Czochralski Growth Experiments

Czochralski growth experiments were originally intended to produce charge material for Bridgman-Stockbarger experiments. In addition to fulfilling this role, Czochralski material provided direct evidence of macro and micro segregation of point defects as a result of convective interference. It provided a useful basis of comparison of electro-optic properties of B-S and hydrothermal material. Lastly, unique macroscopic defects helped elucidate the nature of fluid flow in the melt during growth.

1. Large boules cracked during annealing due to a combination of using heating rates that were too large for the given diameter and additional facet induced strain.

2. Macroscopic defects were identified as voids and platinum inclusions. Incorporation of these defects was orientation dependent with the <100> being almost void and platinum free.
3. Convection in the melt was found to dominate the interface morphology. Both of the large boule exhibited a strongly convex and faceted initial interface with a subsequent interface inversion. Both boules eventually exhibited a flat growth interfaces due to a single, large facet.
4. Faceted growth led to a higher incorporation of point defects as observed by the higher absorption of material grown with a faceted versus a non-faceted interface.
5. Both rotational and non-rotational striations are observed in CZ grown crystals. Non rotational striations are attributed to the periodic remelting and solidification due to thermal fluctuations in the melt.

10.3.4 Bridgman-Stockbarger Growth Experiments

The main focus of the thesis was Bridgman-Stockbarger growth experiments. Three growths were done to establish reproducibility as well as investigate the effect of growth conditions on the incorporation of point defects. The following conclusions are drawn:

1. The thermal environment in the redesigned furnace is reproducible. Experiments done with the same setpoints led to identical axial gradients and interface behavior. Overall, the crystal growth system was found to be highly successful.
2. The platinum confinement foil needs to as thin as possible in order to maximize the number of wraps around the sample. This decreases the likelihood of ampoule failure due to attack from molten BSO that has leaked out of the confinement material.
3. Interface location can best be established based on the gradient established by the gradient zone thermocouples. The thermocouple located on the ampoule should be at 895 °C.
4. Bridgman-Stockbarger material was found to possess a much higher degree of uniformity than Czochralski grown material. No voids or platinum inclusions were observed.

5. Macroscopic defect segregation was observed. Higher translation rates yielded darker material associated with higher defect concentration. The end portions of BS113001 and BS122701 both were considerably darker with higher absorption as compared with material at the beginning of the growth indicating macroscopic segregation of point defects and/or impurities.
6. Interface demarcation is possible by reversing translation for a short period of time, thus remelting a portion of the crystal. A thin line of lighter material is produced. This is further evidence that supports the notion that absorption and thus defect incorporation is subject to segregation.

10.3.5 Comparative Analysis of Electro-Optic Properties

A comparative analysis of electro-optic properties of Czochralski, Bridgman-Stockbarger, and hydrothermal material was done in order to investigate the origin of the critical native defect. The following conclusions can be made:

1. Material appearing darker in color exhibited higher overall absorption indicating a higher defect concentration.
2. Absorption, photoconductivity, and photoluminescence data all indicate a lower defect concentration in Bridgman-Stockbarger material as compared to Czochralski material.
3. Photoconductivity and photoluminescence confirm that hydrothermal material is near intrinsic with no measurable trap levels.
4. Mass spectrometry indicated that ppm levels of Cr and Fe were present in both Czochralski crystals. The room temperature photochromism is attributed to these unintentional impurities.
5. The atmosphere during growth was found to be a critical factor. Room temperature photochromism was absent in BS020802, the only sample to be processed in a sealed environment. Subsequent high temperature annealing experiments showed that this effect was only observed in sealed ampoules and not in flowing atmospheres. The photochromic effect could be re-established by annealing in air.

6. The leading edge peak as well as the initial grating decay in annealed samples indicate a faster dynamic response. However, long time decay slows drastically and persistent gratings are left in annealed material that can be erased with 488 nm uniform exposure. Comparison of decay curves for annealed and unannealed samples leads to the conclusion that several traps are involved in the decay process.
7. High temperature annealing decreases the lifetime of photogenerated carriers. The decrease in photoconductivity as well as the photorefractive response support this conclusion. The exact mechanism of defect modification that is responsible could not be unambiguously identified.
8. Variations in the electro-optic properties show a strong dependence on growth conditions including the thermal environment, the growth technique used, and the atmosphere. Additionally, post growth processing can affect material response. For this reason, in order to perform valuable analysis of sillenite electro-optic properties, growth conditions must be known and controllable.
9. Analysis of grown crystals and comparison of the optical properties is consistent with the clustering theory.

10.4 Suggestions for Future Work

The question of the origin of the critical native defect remains unanswered. As a result of this work, however, it is clear that growth conditions critically affect material properties in resultant material. For this reason, it is absolutely necessary to use a growth system with well characterized and reproducible growth conditions. Additionally, the thermal environment must be controlled accurately.

1. Refine heat-up and cool-down procedures for B-S growth in order to minimize thermal fluctuations experienced by the ampoule. The most stable portion of furnace is the gradient zone. It is suggested that the ampoule should be placed in the gradient zone while heating the furnace isothermally to the cold zone temperature. The hot zone should then be incrementally ramped to the final temperature.

2. The thermocouple at the seeding interface location should read 895 °C. In order to ensure a steady state thermal environment, a thermal soak should be added into the growth procedure before the start of translation.
3. Analysis of ampoule translation system for deviations from vertical should be done. These deviations cause the ampoule not to be centered within the furnace chamber and therefore produce thermal asymmetries. Redesign the interface mechanism between translation system and the ampoule in order to ensure it stays vertical.
4. Analysis of electro-optic properties needs to be accompanied by chemical analysis of residual impurities of all boules. Since the impact of these residual impurities is as yet unclear, the concentration present in samples needs to be known so that it can be one of the variables considered when assessing changes in measured properties.
5. The effect of the ambient atmosphere in the ampoule needs to be investigated since it was shown that it can drastically effect the properties of the grown material. A method of sealing ampoules at a known pressure and composition therefore needs to be developed. Alternatively, the growth system could be modified to have a controlled atmosphere within the furnace cavity. The last option is to design an ampoule that has a controllable flowing atmosphere and is not sealed.
6. Further growth experiments should be done to determine the relationship between growth environment and native defect incorporation. Variables that need to be considered independently include thermal environment, growth rate, and ambient atmosphere. It is suggested that a matrix of experiments be developed to map the parameter space of growth conditions and the resultant defect incorporation.
7. Characterization techniques for growth experiments should include absorption, photochromic response, photoconductivity, photorefractivity, and photoluminescence. Low temperature measurements (77 K) as well as room temperature response should be investigated.

REFERENCES

1. Ashkin, A., G. D. Boyd, et al. (1966). Appl. Phys. Letters **9** (1), 72-4.
2. Fainman, Y., J. Ma, et al. (1993). Materials Science Reports **9** (2-3), 53-139.
3. Witt, A. F. (2001). draft of SCR report for NASA, Massachusetts Institute of Technology.
4. Huignard, J. and F. Micheron (1976). Applied Physics Letters **29** (9), 591-593.
5. Peltier, M. and F. Micheron (1977). Journal of Applied Physics **48** (9), 3683-3690.
6. Yeh, P. (1987). Applied Optics **26** (16), 3190-3191.
7. Jones, A. D. W. (1983). Journal of Crystal Growth **61**, 235-244.
8. Sillen, L. G. (1937). Ark. Kemi, Mineral. Geol. **12A** (18), 1-15.
9. Abrahams, S., P. Jamiesen, et al. (1967). Journal of Chemical Physics **47** (10), 4034-4041.
10. Feldman, A., W. J. Brower, et al. (1970). Applied Physics Letters **16** (5), 201-202.
11. Witt, A. F. (1991). NASA proposal.
12. Speranskaya, E. I. and A. A. Arshakuni (1964). Russian Journal of Inorganic Chemistry **9** (2), 226-230.
13. Speranskaya, E. I. and V. M. Skorikov (1967). Inorganic Materials **3** (2), 303-307.
14. Aurivillius, B., L. Claes-ivar, et al. (1964). Acta Chem. Scand. **19** (6), 1555-1557.
15. Speranskaya, E. I., V. M. Skorikov, et al. (1968). Inorganic Materials **4** (8), 1208-1209.
16. Levin, E. and R. S. Roth (1964). Journal of Research of the National Bureau of Standards **68A** (2), 197-206.
17. Kargin, Y. F. and V. M. Skorikov (1995). Ferroelectrics **167**, 257-265.
18. Takamori, T. (1990). Journal of the American Ceramics Society **73** (1), 158-160.
19. Brice, J., M. Hight, et al. (1977). Phillips Technical Review **37** (9/10), 250-262.
20. Fei, Y. T., S. J. Fan, et al. (2000). Journal of Material Science Letters **19**, 893-895.
21. Abrahams, S., J. Bernstein, et al. (1979). Journal of Chemical Physics **71** (2), 788-792.
22. Chevrier, V., J. Dance, et al. (1996). Journal of Material Science Letters **15** (4), 363-365.
23. Babonas, G., E. Zhogova, et al. (1982). Soviet Physics Solid State **24** (6), 921-925.
24. Radaev, S. and V. Simonov (1992). Soviet physics, crystallography **37** (4), 484-499.
25. Radaev, S. F., V. I. Simonov, et al. (1992). Acta Crystallographica Section B-Structural Science **48**, 604-609.

26. Radaev, S. F., V. I. Simonov, et al. (1992). European Journal of Solid State and Inorganic Chemistry **29** (2), 383-392.
27. Ballman, A. (1967). Journal of Crystal Growth **1**, 37-40.
28. Brice, J., T. Bruton, et al. (1974). Journal of Crystal Growth **24/25**, 429-431.
29. Hill, O. and J. Brice (1974). Journal of Material Science **9**, 1252-1254.
30. Whiffin, P. A. C., T. M. Bruton, et al. (1976). Journal of Crystal Growth **32** (2), 205-210.
31. Brice, J. C. and P. A. C. Whiffin (1977). Journal of Crystal Growth **38**, 245-248.
32. Lin, C. (1994) PhD, Massachusetts Institute of Technology.
33. Gospodinov, M. and D. Doshkova (1994). Material Research Bulletin **29** (6), 681-686.
34. Kravchenko, V., V. Kucha, et al. (1980). Soviet Physics - Cryst. **25** (5), 638-641.
35. Rojo, J. C., C. Marin, et al. (1998). Journal of Crystal Growth **183** (4), 604-613.
36. Kobayashi, N. (1981). Journal of Crystal Growth **52**, 425-434.
37. Xiao, Q. and J. J. Derby (1995). Journal of Crystal Growth **152** (3), 169-181.
38. Iliev, K., M. Berkowski, et al. (1991). Journal of Crystal Growth **108** (1-2), 219-224.
39. Jones, A. D. W. (1989). Journal of Crystal Growth **94**, 421-432.
40. Brandle, C. D. (1977). Journal of Crystal Growth **42**, 400-404.
41. Gopalakrishnan, R., D. Krishnamurthy, et al. (1994). Mat Chem and Phys **37**, 90-93.
42. Tada, K. and M. Tatsumi (1986). Sumitomo Technical Review (25), 97-103.
43. Carruthers, J. R. and K. Nassau (1968). Journal of Applied Physics **39** (11), 5205-5214.
44. Carruthers, J. R. (1976). Journal of Crystal Growth **36**, 212-214.
45. Kobayashi, N. and T. Arizumi (1975). Journal of Crystal Growth **30**, 177-184.
46. Kobayashi, N. (1978). Journal of Crystal Growth **43**, 357-363.
47. Kimura, H. (1986). Journal of Crystal Growth **78** (1), 19-23.
48. Nikolov, V., K. Iliev, et al. (1988). Journal of Crystal Growth **89**, 313-323.
49. Nikolov, V., K. Iliev, et al. (1988). Journal of Crystal Growth **89**, 324-330.
50. Berkowski, M., K. Iliev, et al. (1991). Journal of Crystal Growth **108**, 225-232.
51. Picone, P. J. and J. G. L. Terlet (1986). Journal of Materials Science Letters **5** (8), 829-831.
52. Jasinski, T., W. M. Rohsenow, et al. (1983). Journal of Crystal Growth **61** (2), 339-354.
53. Jasinski, T., A. F. Witt, et al. (1984). Journal of Crystal Growth **67** (2), 173-184.
54. Fu, T. and W. Wilcox (1980). Journal of Crystal Growth **48**, 416-424.

55. Chang, C. and W. Wilcox (1974). Journal of Crystal Growth **21**, 135-140.
56. Naumann, R. J. (1982). Journal of Crystal Growth **58** (3), 554-568.
57. Naumann, R. J. (1982). Journal of Crystal Growth **58** (3), 569-584.
58. Naumann, R. J. and S. L. Lehoczky (1983). Journal of Crystal Growth **61** (3), 707-710.
59. Matsushima, H. and R. Viskanta (1990). International Journal of Heat and Mass Transfer **33** (9), 1957-1968.
60. Brandon, S. and J. Derby (1991). Journal of Crystal Growth **110**, 481-500
61. Brandon, S. and J. Derby (1992). Journal of Crystal Growth **121**, 473-494.
62. Lin, C. and S. Motakef (1993). Journal of Crystal Growth **128**, 834-841.
63. Gryvnak, D. A. and D. E. Burch (1965). Journal of the Optical Society America **55** (6), 625.
64. Nason, D., C. Yen, et al. (1990). Journal of Crystal Growth **106**, 221-226.
65. Vizman, D., I. Nicoara, et al. (1996). Journal of Crystal Growth **169** (1), 161-169.
66. Nicoara, I., A. Pusztai, et al. (1997). Crystal Research and Technology **32** (3), 413-422.
67. Virozub, A. and S. Brandon (1998). Journal of Crystal Growth **193** (4), 592-596.
68. Lu, W. Q. (2000). Materials Science and Engineering a-Structural Materials Properties Microstructure and Processing **292** (2), 219-223.
69. Vizman, D., I. Nicoara, et al. (2000). Journal of Crystal Growth **212** (1-2), 334-339.
70. Xu, X., J. Liao, et al. (1993). Journal of Crystal Growth **133** (3-4), 267-272.
71. Xu, X., J. Liao, et al. (1994). Crystal Research and Technology **29** (2), 207-213.
72. Zheng, Y. (1999). PhD, Massachusets Institute of Technology.
73. Larkin, J., M. Harris, et al. (1993). Journal of Crystal Growth **128**, 871-875.
74. Harris, M. and J. Larkin (1992). Journal of Applied Physics Letters **60** (17), 2162-2163.
75. Harris, M., J. Larkin, et al. (1994). Journal of Crystal Growth **137**, 128-131.
76. Larkin, J., M. Harris, et al. (1995). Proceedings of SPIE - Int Society for Optical Engineering **2481**, 216-226.
77. Klebanskii, E. O., A. Y. Kudzin, et al. (1999). Physics of the Solid State **41** (6), 913-915.
78. Jain, M., A. K. Tripathi, et al. (1999). Journal of Material Science Letters **18**, 479-481.
79. Quon, D., S. Chehab, et al. (1993). Journal of Crystal Growth **134** (3-4), 266-274.
80. Fu, S. and H. Ozoe (1996). Material Research Bulletin **31** (11), 1341-1354.
81. Fu, S. and H. Ozoe (1997). Journal of Material Science **32** (14), 3667-3674.

82. Fu, S. and H. Ozoe (1999). Journal of Materials Science **34** (2), 371-377.
83. Maffei, N., D. Quon, et al. (1997). Journal of Crystal Growth **181** (4), 382-389.
84. Maffei, N., D. Quon, et al. (1997). Journal of Crystal Growth **180** (1) , 105-112.
85. Saghir, M. Z., M. R. Islam, et al. (1998). Journal of Crystal Growth **193** (4), 623-635.
86. Prokofiev, V., J. Andreeta, et al. (1994). Journal of Crystal Growth **137** (3-4), 528-534.
87. Prokofiev, V. V., J. P. Andretta, et al. (1995). Optical Materials **4** (4), 521-527.
88. Prokofiev, V. V., J. P. Andreeta, et al. (1995). Optical Materials **4** (2-3), 433-436.
89. Prokof'ev, V. V. (1997?). SPIE **3178**, 14-21.
90. Miyamoto, K., H. Miyamoto, et al. (1980). Material Research Bulletin **15** (6), 729-734.
91. Wang, J. H., D. H. Kim, et al. (1997). Journal of Crystal Growth **174** (1-4), 13-18.
92. Maida, S., M. Higuchi, et al. (1999). Journal of Crystal Growth **205** (3), 317-322.
93. Krishnamurthy, D., R. Gopalarishnan, et al. (1993). Journal of Material Science Letters **12** (15), 1218-1220.
94. Shimura, F. and Y. Fujino (1977). Journal of Crystal Growth **38**, 293-302.
95. Nassau, K. and A. M. Broyer (1962). Journal of Applied Physics **33** (10), 3064- .
96. Miyazawa, S. (1980). Journal of Crystal Growth **49**, 515-521.
97. Miyazawa, S. and H. Iwasaki (1970). Japanese Journal of Applied Physics **9** (5), 441-445.
98. Cockayne, B. (1977). Journal of Crystal Growth **42**, 413-426.
99. Kobayashi, N. (1981). Journal of Crystal Growth **54**, 414-416.
100. Brice, J. C. (1970). Journal of Crystal Growth **6**, 205-206.
101. Jackson, K., D. Uhlman, et al. (1966). Journal of Crystal Growth **1**, 1-36.
102. Brice, J. C. (1977). Journal of Crystal Growth **42**, 427-430.
103. Picone, P. J. (1988). Journal of Crystal Growth **87** (4), 421-424.
104. Aggarwal, M., W. Wang, et al. (1994). Journal of Crystal Growth **137**, 132-135.
105. Santos, M. T., L. Arizmendi, et al. (1996). Materials Research Bulletin **31** (4), 389-396.
106. Tu, H., X. Xu, et al. (1994). Crystal Research and Technology **29** (3), K43-K46.
107. Gospodinov, M., V. Tassev, et al. (1996). Crystal Research and Technology **31** (5), 595-600.
108. Hou, S., R. Lauer, et al. (1973). Journal of Applied Physics **44** (6), 2652-2658.
109. Aldrich, R., S. Hou, et al. (1971). Journal of Applied Physics **42**, 493-494.
110. Lauer, R. (1970). Applied Physics Letters **17** (4), 178-179.

111. Lauer, R. (1971). Journal of Applied Physics **42** (5), 2147-2149.
112. Nesheva, D., Z. Aneva, et al. (1993). Journal of Physics and Chemistry of Solids **54** (7), 857-862.
113. Panchenko, T. and Z. Yanchuk (1996). Physics of the Solid State **38** (10), 1663-1665.
114. Panchenko, T. and Z. Yanchuk (1996). Physics of the Solid State **38** (7), 1113-1129.
115. Kostyuk, V., A. Kudzin, et al. (1980). Soviet Phys Solid State **22** (8), 1429-1432.
116. Oberschmid, R. (1985). Phys Stat Sol (A) **89**, 263-270.
117. Vogt, H., K. Buse, et al. (2001). Journal of Applied Physics **90** (7), 3167-3173.
118. McCullough, J. S., A. M. Georgalas, et al. (2001). Journal of Applied Physics **89** (10), 5276-52281.
119. Ennouri, A., M. Tapiero, et al. (1993). Journal of Applied Physics **74** (4), 2180-2191.
120. Plyaka, S. N. and G. K. Sokolyanskii (1998). Physics of the Solid State **40** (11), 1859-1860.
121. Efendiev, S., V. Gavryushin, et al. (1990). Phys Stat Sol (B) **162**, 281-288.
122. Takamori, T. and D. Just (1990). Journal of Applied Physics **73** (1), 848-851.
123. Just, D. and T. Takamori (1991). Material Science and Engineering (B) **B9** (4), 469-474.
124. Takamori, T. (1991). Journal of Applied Physics **69** (12), 8222-8226.
125. Efendiev, S. M., V. E. Bagiev, et al. (1982). Ferroelectrics **43** (3-4), 217-221.
126. Attard, A. (1989). Applied Optics **28** (23), 5169-5174.
127. Zakharov, I. S., P. A. Petukhov, et al. (1986). Inorganic Materials **22** (3), 379-382.
128. Panchenko, T., S. Kopylov, et al. (1995). Physics of the Solid State **37** (9), 1415-1419.
129. Panchenko, T., V. Kostyuk, et al. (1996). Physics of the Solid State **38** (1), 84-89.
130. Garrett, M. (1991). Journal of the Optical Society America (B) **8** (1)7, 8-87.
131. Babu, S. M., K. Kitamura, et al. (1999). Journal of the Optical Society of America B-Optical Physics **16** (8), 1243-1249.
132. Briat, B., H. J. Reyher, et al. (1995). Journal of PhysicsCondensed Matter **7**, 6951-6959.
133. Reyher, H. J., U. Hellwig, et al. (1993). Physical Review B **47** (10), 5638-5645.
134. Lenzo, P., E. Spencer, et al. (1966). Applied Optics **5** (10), 1688-1689.
135. Vachss, F. and L. Hesselink (1987). Optics Communications **62** (3), 159-165.
136. Lemaire, P. C. and M. P. Georges (1995). Optical Materials **4** (2-3), 182-187.

137. Solymar, L., D. J. Webb, et al. (1996). The Physics and Applications of Photorefractive Materials. Oxford, Clarendon Press.
138. Biaggio, I., R. Hellwarth, et al. (1997). Physics Review Letters **78** (5), 891-898.
139. Murillo, J. G. (1999). Optics Communications **159** (4-6), 293-300.
140. Kobozev, O. V., S. M. Shandarov, et al. (1998). Physics of the Solid State **40** (11), 1844-1849.
141. Attard, A. (1991). Journal of Applied Physics **69** (1), 44-55.
142. Attard, A. (1989). Journal of Applied Physics **66** (7), 3211-3216.
143. Attard, A. (1988). Applied Optics **27** (2), 232-238.
144. Attard, A. and T. Brown (1986). Applied Optics **25** (18), 3253-3259.
145. Strohkendl, F. and R. Hellwarth (1987). Journal of Applied Physics **62**(6)2, 450-2455.
146. Cedilnik, G., M. Esselbach, et al. (1999). Applied Physics B-Lasers and Optics **68** (5), 983-987.
147. Foldvari, I., J. Martin, et al. (1993). Optical Materials **2**, 25-32.
148. dos Santos, P. A. M., P. M. Garcia, et al. (1989). Journal of Applied Physics **66** (1), 247-251.
149. Mullen, R. and R. Hellwarth (1985). Journal of Applied Physics **58** (1), 40-44.
150. Volkov, V. V., A. V. Egorysheva, et al. (1993). Inorganic Materials **29** (11), 1364-1374.
151. Panchenko, T. V. (2000). Physics of the Solid State **42** (4), 657-663.
152. McCullough, J. S., A. L. Harmon Bauer, et al. (2001). Journal of Applied Physics **90** (12), 6022-6025.
153. Tanguay, A. R., S. Mroczkowski, et al. (1977). Journal of Crystal Growth **42**, 431-434.
154. Hart, D. W., C. A. Hunt, et al. (1993). Journal of Applied Physics **73** (3), 1443-1448.
155. Martin, I. Foldavi, et al. (1991). Journal of Applied Physics **70** (12), 7554-7559.
156. Panchenko, T. V. and N. A. Truseyeva (1991). Ferroelectrics **115** (1-3), 73-80.
157. Wardzynski, W., T. Lukasiewicz, et al. (1979). Optics Communications **30** (2), 203-205.
158. McCullough, J. S., A. L. Harmon Bauer, et al. (2001). Journal of Applied Physics **90** (1 2), 6017-6021.
159. Wardzynski, W., H. Szymczak, et al. (1985). Journal of Physics and Chemistry of Solids **46** (10), 1117-1129.

160. Wardzynski, W., H. Szymczak, et al. (1982). Journal of Physics and Chemistry of Solids **43** (8), 767-769.
161. Hamri, A., M. Secu, et al. (1995). Optical Materials **4**, 197-201.
162. Grabmaier, B. and R. Oberschmid (1986). Physica Status Solidi (A) **96**, 199-210.
163. Kopylov, Y., V. Kravchenko, et al. (1991). Proceedings of the Indian National Science Acadamy **54A** (2), 145-151.
164. Petrova, D. and M. Gospodinov (1996). Ceramics International **22** (1), 45-47.
165. Petrova, D., M. Gospodinov, et al. (1995). Materials Research Bulletin **30** (10), 1201-1206.
166. Kopylov, Y., V. Kravchenko, et al. (1982). Soviet Technical Physics Letters **8** (2), 88-89.
167. Petrova, D., M. Gospodinov, et al. (1996). Crystal Research and Tech. **31** (5), 577-581.
168. Gospodinov, M. and D. Doshkova (1994). Crystal Research and Tech. **29** (5), 603-611.
169. Nesheva, D., Z. Aneva, et al. (1995). Journal of Physics and Chemistry of Solids **56** (2), 241-250.
170. Lukasiewicz, T. and J. Zmija (1980). Kristall und Technik **15** (3), 267-269.
171. Mihailova, B., L. Konstantinov, et al. (1997). Solid State Communications **102** (6), 441-444.
172. Tassev, V., G. Diankov, et al. (1995). Materials Research Bulletin **30** (10), 1263-1267.
173. Tassev, V., G. Diankov, et al. (1996). Optical Materials **6** (4), 347-351.
174. Tassev, V., M. Gospodinov, et al. (1999). Optical Materials 13 (2), 249-253.
175. Tanguay, A. R. (1985). Optical Engineering **24** (1), 2-18.
176. Allegretti, F., B. Borgia, et al. (1989). Journal of Crystal Growth **94** (2), 373-380.
177. Mechev, V., V. Kutvitskiy, et al. (1982). Izv. Akad. Nauk SSSR **3**, 37-39.
178. Robertson, J. (1969). Englehard Industrial Technical Bulletin **10**, 77-79.
179. Kutvitskii, V., V. Skorikov, et al. (1979). Inorganic Materials **15** (10), 1453-1456.
180. Miller, R., G. Boyd, et al. (1965). Applied Physics Letters **6** (4), 77-79.
181. Paffett, M., C. Cambell, et al. (1986). Journal of Chemical Physics **85** (10), 6176-6185.
182. Okamoto, H. (1991). Journal of Phase Equilibria **12**, (2) 207-210.
183. Shi-ji, F., S. Guan-shun, et al. (1991). Crystal Properties and Preparation **36-38**, 42-45.
184. Takamori, T. and J. J. Boland (1991). Journal of Materials Science Letters **10** (16), 972-974.

185. Chongfan, H., F. Shiji, et al. (1985). Progress in Crystal Growth and Characterization **11**, 253-262.
186. Voskresenskaya, E. N., Y. F. Kargin, et al. (1982). Inorganic Materials **18** (1), 84-88.
187. Sobolev, A., Y. Kopylov, et al. (1978). Soviet Physics, Crystallography **23** (1), 93-96.
188. Aesar, A. (2002). Platinum Labware and Select Analytical Products, 12.
189. Lahooti, S., O. Del Rio, et al. Axisymmetriic Drop Shape Analysis, 441-507.
190. Duffar, T., I. Harter, et al. (1990). Journal of Crystal Growth **100**, 171-184.
191. Duffar, T., P. Boiton, et al. (1997). Journal of Crystal Growth **179**, 397-409.
192. Duffar, T., P. Dusserre, et al. (2000). Journal of Crystal Growth **211**, 434-440.
193. Duffar, T. and B. Drevet (2000). private communications.
194. Witt, A. F., H. C. Gatos, et al. (1978). Journal of the Electrochemical Society **125** (11), 1832-1840.
195. Courtney, T. H. (1990). Mechanical Behavior of Materials. New York, McGraw-Hill, Inc.
196. Shaw, E. (1999). private communications.
197. Jasinski, T. (1982). PhD, Massachusetts Institute of Technology.
198. Wang, C. (1984). PhD, Massachusetts Institute of Technology.
199. Rao, P. (1997). PhD, Massachusetts Institute of Technology.
200. Horowitz, A. and G. Kramer (1986). Journal of Crystal Growth **78** (1), 121-128.
201. Gopalakrishnan, R., D. Krishnamurthy, et al. (1993). Ferroelectrics **142**, 161-165.
202. Burton, J. A., R. C. Prim, et al. (1953). Journal of Chemical Physics **21**, 1987.
203. Becla, P. (2002). private communications.
204. Coya, C., J. L. G. Fierro, et al. (1997). Journal of Physics and Chemistry of Solids **58** (9), 1461-1467.
205. Kargin, Y. F., V. P. Zhereb, et al. (1977). Inorganic Materials **13** (1), 114-117.
206. Tananaev, I., V. Skorikov, et al. (1978). Inorganic Materials **14** (11), 1576-1579.
207. Zhereb, V. P., Y. F. Kargin, et al. (1978). Inorganic Materials **14** (11), 1580-1581.
208. Fu, S. and H. Ozoe (1996). Journal of Materials Research **11** (10), 2575-2582.
209. Fu, S. L. and H. Ozoe (1996). Journal of Physics D-Applied Physics **29** (7), 2032-2043.
210. Takeda, S., K. Sugiyama, et al. (1993). Japanese Journal of Applied Physics Part 1-Regular Papers Short Notes & Review Papers **32** (12A), 5633-5636.